Scuola Normale Superiore di Pisa

A sensitive search for lepton-flavor violation: the MEG experiment and the new LXe calorimetry

Giovanni Signorelli

Advisor

Dr. Alessandro M. Baldini

Ph.D. Thesis

Autumn 2004

Contents

Introduction

After more than forty years since its introduction, the Standard Model of electro-weak interactions is still *the* answer that physicists give to their question on how the elementary building blocks of the universe are put together to form the world everybody lives in. This answer is supported by an extraordinary series of milestone measurements that traced the route towards it in the past, and that now try to put it under trial, without success hitherto.

Since proving that neutrinos are not massless, with little or no distress for the model (which could accommodate even this) a more and more important role is being played by the search for rare processes, such as proton decay or lepton flavor violation, both forbidden by symmetries that should not be there. Despite their smallness, these processes, if found, could open an amazing window on a completely unknown physics realm.

It is in this endeavor that the search for the $\mu^+ \to e^+\gamma$ decay beyond the present limit, $BR(\mu^+ \to e^+\gamma) < 1.2 \times 10^{-11}$, is being undertaken at the Paul Scherrer Institut (PSI, Switzerland) by the MEG collaboration, composed of physicists from Italian, Japanese, Swiss and Russian institutions. But whereas one sets for an unknown challenge, he must face it with the proper instruments: an experiment has been designed around an innovative cryogenic calorimeter, in which xenon has been chosen as the active scintillating material.

This thesis deals with the tests performed on a large calorimeter prototype, by itself the largest liquid xenon calorimeter in the world, towards the design of the full-scale calorimeter for the experiment. After a brief introduction on the Standard Model, its possible extensions and the phenomenology of lepton flavor violation (Chapter 1÷3) and a description of the MEG experiment (Chapter 4) we will discuss the properties of xenon as a radiation detection medium (Chapter 5). The simulation of the detector will be the subject of Chapter 6, while Chapter 7 deals with the operation of the calorimeter large prototype which brought us to reach a xenon purification sufficient for our purposes. From Chapter 8 to 10 we will describe a beam test performed at PSI, in which we measured the energy and timing resolution of the prototype by means of photons coming from the decay of π^0s produced in a charge exchange reaction of negative pions on protons. In Chapter 11 we will describe the operation of a cryogenic PMT test facility installed at INFN Pisa which was used to study problems related to the PMT response at high rates that emerged during the beam test. Chapter 12 contains statements on the MEG experiment sensitivity, in the light of the last results obtained.

Part I

Theory and phenomenology

Chapter 1

The Standard Model and beyond

The Standard Model of electroweak and strong interactions[1] (SM) is presently the most successful theory in explaining and predicting the elementary particle phenomenology. Nonetheless it is believed to be a low energy approximation of some more fundamental theory, mainly because of its many free parameters.

In this Chapter we will review the main characteristics of the model, together with its pitfalls, and we will discuss some of its proposed extensions. In particular, the recent evidence for neutrino oscillations implies that a hitherto believed symmetry of the Standard Model, namely lepton flavor conservation, no longer holds.

1.1 The Standard Model

The SM is based on the gauge symmetry group $SU(3)_C \times SU(2)_L \times U(1)_Y$ of color, weak isospin and hypercharge invariance, spontaneously broken at the Fermi scale $M_{\mathrm{F}}(\sim 100$ GeV) to $SU(3)_C \times U(1)_{e.m.}$.

The model accommodates three generations of fermion matter fields (quarks and leptons) $8 \oplus 3 \oplus 1$ gauge bosons and an elementary scalar (the Higgs boson) necessary to accomplish the spontaneous symmetry breaking down to $SU(3)_C \times U(1)_{e.m.}$.

The Lagrangian of a free fermion field $\psi(x)$ can be written as

$$\mathcal{L}_F = \bar{\psi} i \partial\!\!\!/ \psi - \bar{\psi} m \psi \tag{1.1}$$

where ψ and $\bar{\psi}$ are Weyl spinors, the first is the kinetic term and the second is the mass term. The Lagrangian is said to have a gauge symmetry (or to be symmetric under a gauge group $\mathcal{G}$) if it is invariant with respect to a local transformation of the fields (ψ can in general be a k-dimensional multiplet)

$$\psi \quad \rightarrow \quad e^{i\theta^a(x)T^a}\psi = U(x)\psi \tag{1.2}$$

[1] As general reference for this Chapter one may take, besides the original papers, [1, 2, 3, 4, 5].

$$\bar{\psi} \quad \to \quad \bar{\psi} e^{-i\theta^a(x) T^{*a}} = \bar{\psi} U^\dagger(x) \tag{1.3}$$

where T^a $(a = 1, \dots, N)$ are the k-dimensional representations of the N generators of the group $\mathcal{G}$ and $\theta^a(x)$ are the (x-dependent) parameters of the transformation. For the Lagrangian (1.1) to be invariant under such a transformation it is necessary to introduce N vector fields A^a_μ (gauge fields) which transform in the following way

$$A_\mu \quad = \quad \sum_a A^a_\mu T^a \tag{1.4}$$

$$A_\mu \quad \to \quad U^\dagger A_\mu U - i U^\dagger \partial_\mu U. \tag{1.5}$$

It is customary to introduce the notation of covariant derivative

$$D_\mu = \partial_\mu + i g A_\mu \tag{1.6}$$

where g is a scalar parameter (the coupling constant) from which follows that

$$\bar{\psi} \not{D} \psi = \bar{\psi} \not{\partial} \psi + i g \bar{\psi} \gamma^\mu T^a \psi A^a_\mu \tag{1.7}$$

is invariant under gauge transformations. To allow the propagation of the gauge bosons their kinetic term must be added.

$$\mathcal{L}_{\text{vb,kin}} = -\frac{1}{4} \text{Tr}_a F_{\mu\nu} F^{\mu\nu} \tag{1.8}$$

where $F^{\mu\nu}$ is the field tensor

$$F^{\mu\nu} = \partial^\mu A^\nu - \partial^\mu A^\nu + g[A^\mu, A^\nu]. \tag{1.9}$$

From Equation 1.7 it follows that the requirement of gauge invariance introduces couplings between the fermion current $J^\mu = \bar{\psi} \gamma^\mu T^a \psi$ and the vector bosons A^a_μ, all with the same strength g.

The assignment of a fermionic field to some representation of the gauge group automatically determines its interactions with the gauge fields. It is well known that parity is maximally violated in weak interactions *i.e.* only left-handed (LH) fermions take part in weak phenomena. From this phenomenology it is natural to speak of LH and RH (right-handed) fields, and group the LH fermions in SU(2) doublets. All RH particles are $SU(2)_L$ singlets, there is no RH neutrino, and only quarks transform non-trivially under $SU(3)_C$. Here we present the quantum numbers of the first generation fermions.

$$L \quad = \begin{pmatrix} \nu_L \\ e_L \end{pmatrix} \quad (1, 2, -1) \tag{1.10}$$

$$e_R \qquad\qquad (1, 1, -2) \tag{1.11}$$

$$Q^i \quad = \begin{pmatrix} u^i_L \\ d^i_L \end{pmatrix} \quad (3, 2, 1/3) \qquad (i = \text{colour}) \tag{1.12}$$

$$u^i_R \qquad\qquad (3, 1, 4/3) \tag{1.13}$$

$$d^i_R \qquad\qquad (3, 1, -2/3) \tag{1.14}$$

Three replicas of these particles exist, one for each generation, for a total of 45 elementary fields (or a 45-dimensional reducible field).

The gauge group possesses twelve gauge bosons which are usually indicated with λ_μ^i ($i = 1, \ldots, 8$; the gluons) W_μ^a ($a = 1, \ldots, 3$; the weak bosons) and B_μ.

A mass term for the vector bosons, *e.g.* $\frac{1}{2}m^2 B_\mu B^\mu$, as well as for the fermion fields, $m\bar{\psi}_L\psi_R$, would spoil the gauge invariance, hence all the particles in this model are massless.

In this respect the theory is in open contrast to the experiment. To overcome the problem without throwing away the theoretical beauty of a gauge symmetry, particle masses are introduced via the so-called Higgs mechanism.

1.1.1 The Higgs field and mass generation mechanism

A scalar field (the Higgs boson) is included in the Lagrangian, together with its interactions with all the other particles and a Mexican hat shaped potential term (self-coupling). The field is different from zero at the potential minimum, and it is said to develop a non-null vacuum expectation value (VEV). The effect of this is twofold: (1) generating particle masses and (2) reducing the unobserved $SU(2)_L \times U(1)_Y$ symmetry down to the electromagnetic $U(1)_{e.m.}$ gauge symmetry.

The Higgs field is a scalar complex $SU(2)_L$ doublet with $Y = 1$

$$\phi = \begin{pmatrix} \phi^+ \\ \phi^0 \end{pmatrix}. \tag{1.15}$$

Its kinetic and potential term are added to the Lagrangian

$$\mathcal{L}_H = (D_\mu\phi)^\dagger(D^\mu\phi) - V(\phi) \tag{1.16}$$

where the most general, renormalizable form for the potential is

$$V(\phi) = -\mu^2\phi^\dagger\phi + \lambda(\phi^\dagger\phi)^2, \quad \mu^2 > 0 \tag{1.17}$$

Together with the kinetic and potential part the Lagrangian can now include terms describing the interactions of the fermion fields with the scalar field (Yukawa couplings). All terms which are singlets under the gauge group can, and must, be written:

$$\mathcal{L}_Y = \sum_{\text{generations}} \bar{Q}_L^i \lambda_u^{ij} \phi^\dagger u_R^j + \bar{Q}_L^i \lambda_d^{ij} \phi d_R^j + \bar{L}_L^i \lambda_e^{ij} \phi e_R^j, \tag{1.18}$$

where $\lambda_{u,d,e}^{ij}$ are arbitrary 3×3 matrices.

Two things are worth noticing: (1) $\phi^\dagger$ is used in the first term in order to build a $Y = 0$ term. (2) Due to the lack of a ν_R singlet we cannot write a term of the form $\bar{L}_L\phi^\dagger\nu_R$.

1.1.2 Spontaneous symmetry breaking

The potential (1.17) has infinite, degenerate minima for the Higgs field corresponding to a non-zero vacuum expectation value:

$$v = \sqrt{\frac{\mu^2}{2\lambda}}. \tag{1.19}$$

We can choose a gauge in which

$$\langle\phi\rangle = \begin{pmatrix} 0 \\ v \end{pmatrix}. \tag{1.20}$$

Notice that the vacuum state is no longer invariant under $SU(2)_L \times U(1)_Y$. It is however invariant under the $U(1)$ symmetry generated by $Q = T_3 + Y/2$ (which in particular annihilates the $\langle\phi\rangle$ state) which is identified with the residual $U(1)_{e.m.}$ gauge symmetry.

To see the effects of the spontaneous symmetry breaking we must replace ϕ with its vacuum expectation value in the SM Lagrangian.

1.1.3 Masses for the vector bosons

In the gauge (1.20) the kinetic term of the Higgs sector of the Lagrangian generates the following mass term for the gauge bosons

$$\mathcal{L} = \frac{v^2}{4}\left(gW_3^\mu - g'B^\mu\right)^2 + \frac{v^2}{2}g^2 W_\mu^- W^{+\,\mu} \tag{1.21}$$

where $W^{\pm\,\mu} = 1/\sqrt{2}(W_1^\mu \pm iW_2^\mu)$ are the fields mediating the weak charged current interactions. W_3^μ and B^μ can be rotated in the two mutually orthogonal fields

$$Z^\mu = \frac{1}{\sqrt{g^2+g'^2}}(gW_3^\mu - g'B^\mu) = \cos\theta_w W_3^\mu - \sin\theta_w B^\mu \tag{1.22}$$

$$A^\mu = \frac{1}{\sqrt{g^2+g'^2}}(g'W_3^\mu + gB^\mu) = \sin\theta_w W_3^\mu + \cos\theta_w B^\mu \tag{1.23}$$

where θ_w is the Weinberg angle. With the new notation the A^μ boson remains massless (photon) and the Z^μ acquires a mass term of the form

$$\frac{v^2}{4}\sqrt{g^2+g'^2}\,Z_\mu Z^\mu, \tag{1.24}$$

from which follows

$$m_W = gv \qquad m_Z = \sqrt{g^2+g'^2}\,v \qquad m_\gamma = 0 \qquad \frac{m_W}{m_Z} = \cos\theta_W. \tag{1.25}$$

1.1.4 Fermion masses

The replacement of ϕ with $\langle\phi\rangle =^t(0,v)$ generates the following form for the Yukawa couplings:

$$\mathcal{L}_Y = \sum_{\text{generations}} v\lambda_u^{ij}\bar{u}_L^i u_R^j + v\lambda_d^{ij}\bar{d}_L^i d_R^j + v\lambda_e^{ij}\bar{e}_L^i e_R^j + \text{h. c.} \tag{1.26}$$

The interactions now mimic a mass term which can be diagonalized in the flavor space with bi-unitary transformations

$$U_L^\dagger \lambda_{u,d,e} U_R = \lambda_{u,d,e}^{\text{DIAG}}, \tag{1.27}$$

to make the masses for the three generations of quarks and leptons explicit. It is important to notice that these rotations affect also the kinetic term, which contains the fermion interactions with the vector bosons. The neutral and electro-magnetic currents remain flavor diagonal also in the mass eigenbasis. The charged current, instead, it is no longer diagonal and can be expressed as

$$J^\mu = \bar{d}'_L \gamma_\mu U_L^{d\,\dagger} U_L^u u'_L + \bar{e}'_L \gamma^\mu U_L^{e\,\dagger} \nu_L, \tag{1.28}$$

where the primed fields are the rotated ones. Since neutrinos are massless (and hence degenerate) we can rotate the ν_L field in such a way as to make the second term in Eq. (1.28) flavor diagonal. It is not possible however to perform such a rotation in the first term without changing the quark mass term. Therefore the 3×3 unitary matrix $U_L^{d\,\dagger} U_L^u$ retains a physical meaning, describing the inter-generation flavor transitions between quarks, and is known as the Cabibbo, Kobayashi and Maskawa matrix V_{CKM}.

Flavor transitions in the lepton sector, on the contrary, are exactly forbidden. For every global phase transformation of the fields $\psi \to \psi e^{iL\theta}$ a corresponding quantum number is conserved. The SM Lagrangian is invariant under four such global symmetries, which are not dictated by gauge invariance and are therefore called "accidental". They correspond to the conserved quantum numbers B, the barion number, and L_i, $i = e, \mu, \tau$, the lepton family number of each generation.

1.2 Neutrino masses

In the SM, lepton flavor is preserved because of the vanishing neutrino masses. How this compares with the evidence of neutrino oscillations? How do neutrino masses affect the picture described above? Recall that we are interested in lepton flavor violation, hence we have to search for all its possible sources!

It is possible to supplement the SM just inserting the field for the RH neutrino, ν_R, which could pair with the SM ν_L giving rise to the neutrino masses. In a way completely analogous to the quark sector we can now introduce in the Lagrangian the Yukawa coupling of the RH neutrino:

$$\mathcal{L}_Y^\nu = \bar{L}_L^i \lambda_n^{ij} \phi^\dagger \nu_R \tag{1.29}$$

which becomes, after spontaneous symmetry breaking, the following mass term for the neutrino

$$\mathcal{L}_Y^m = v \bar{\nu}_L^i \lambda_n^{ij} \phi^\dagger \nu_R. \tag{1.30}$$

This can be diagonalized to give the neutrino mass eigenstates. Consequently, also for the leptons, the mass basis is different from the flavor basis, which gives rise to flavor violation also in the lepton sector.

The introduction of the right handed neutrino however does not account for the lightness of neutrinos with respect to all the other fermions. To accomplish this the coupling constants λ_N^{ij} should be orders of magnitude smaller than $\lambda_{u,d,e}^{ij}$, but there is no fundamental reason for that in the model.

One possible explanation comes from the see-saw model: a new field for the RH neutrino is included. Up to now we have treated a neutrino as a Dirac particle, *i.e.* different from its anti-particle, in analogy with the charged fermions. The neutrinos being electrically neutral does not exclude the possibility for them to be their own anti-particle: neutrinos and anti-neutrinos are just opposite chiral states of the same particle. In this case it is possible to write in the Lagrangian additional mass terms of the form

$$m_L \nu_L \nu_L^c + M_R \nu_R \nu_R^c. \tag{1.31}$$

The RH neutrinos are completely neutral under the SM gauge group. Consequently they can acquire Majorana masses M_R which are unrelated to the electro-weak symmetry breaking scale.

Let us restrict to the one generation case. The complete mass term for the neutrino is written as

$$\begin{aligned} \mathcal{L}_m^\nu &= m_D \bar{\nu}_L \nu_R + M_R \bar{\nu}_R^c \nu_R + \text{h.c.} \qquad (1.32) \\ &= (\bar{\nu}_L \bar{\nu}_R^c) \begin{pmatrix} 0 & m_D \\ m_D & M_R \end{pmatrix} \begin{pmatrix} \nu_L \\ \nu_R \end{pmatrix}. \end{aligned}$$

It is natural to have m_D comparable with the other lepton masses. If $M_R \gg M_Z$ the eigenvalues of the matrix, *i.e.* the neutrino physical masses, are

$$m_1 \sim M_R \qquad m_2 \sim \frac{m_D^2}{M_R}. \tag{1.33}$$

One neutrino remains super-heavy while the other gets a tiny mass. For example if M_R is 10^{15} GeV and the Dirac mass is of the order of 100 GeV, the neutrino mass becomes naturally $\mathcal{O}(10^{-2})$ eV.

1.2.1 Neutrino Mixing

If neutrinos are not massless the mass basis is in general different from the flavor basis. For example, in the two neutrino flavor scheme, we have

$$\begin{pmatrix} \nu_e \\ \nu_\mu \end{pmatrix} = \begin{pmatrix} \cos\theta & \sin\theta \\ -\sin\theta & \cos\theta \end{pmatrix} \begin{pmatrix} \nu_1 \\ \nu_2 \end{pmatrix} \tag{1.34}$$

where ν_1 and ν_2 are the mass eigenstates, while ν_e and ν_μ are flavor eigenstates. In this scheme the transition probability between one flavor and the other is

$$P(\nu_e \to \nu_\mu) = \sin^2 2\theta \sin^2 \left(1.27 \frac{\Delta m^2 (\text{eV}^2)\, L(\text{m})}{E(\text{MeV})} \right) \tag{1.35}$$

where θ is the mixing angle, Δm^2 is the square mass difference of the two neutrinos, E is their energy and L is the traveled distance.

Recent experimental results [6, 7, 8, 9, 10, 11, 12, 13] strongly confirmed the existence of oscillations in solar, atmospheric and reactor neutrinos, proving that indeed neutrinos have masses different from zero.

Atmospheric neutrino experiments prove a $\nu_\mu \leftrightarrow \nu_\tau$ oscillation with a $\Delta m^2 \approx 3 \times 10^{-3}$ eV^2 and an almost maximal mixing ($\sin^2 2\theta_{\text{Atm}} > 0.92$). Solar neutrino experiment, recently confirmed by the KamLAND reactor neutrino experiment, suggest a ν_e disappearance in a $\nu_\mu \div \nu_\tau$ mixed state with a $\Delta m^2 \approx 7 \times 10^{-5}$ eV^2 and a nearly maximal mixing here, too [14].

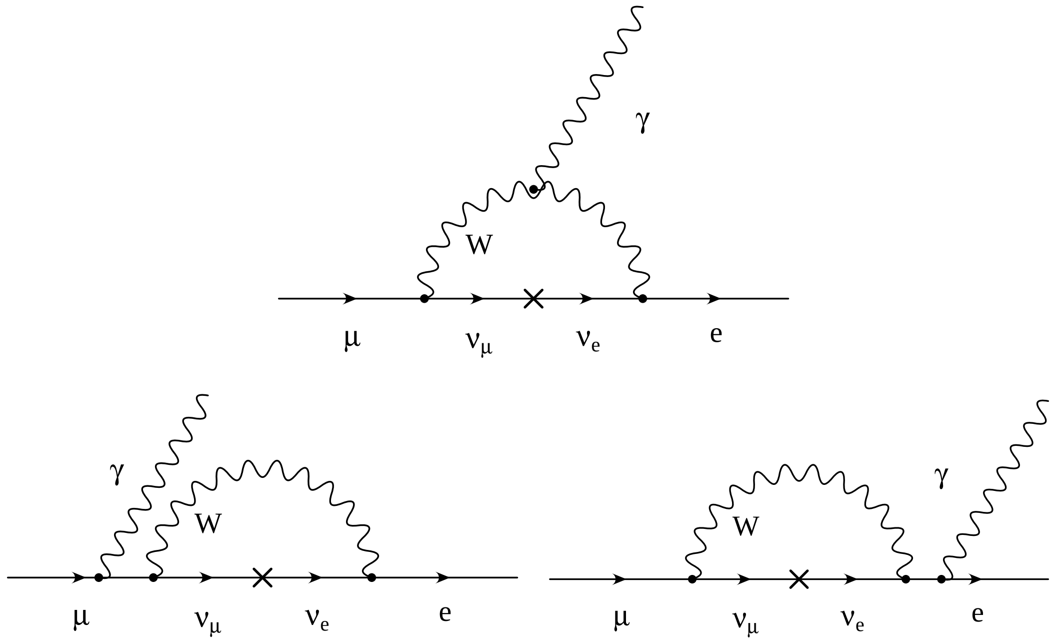

Figure 1.1: Diagrams describing the $\mu^\pm \to e^\pm\gamma$ decay in the Standard Model.

Neutrino oscillations show that lepton flavor is not conserved in the phenomenology of particle physics. This implies the existence of other LFV processes, such as $\mu^\pm \to e^\pm\gamma$ decay, due to the diagrams shown in Figure 1.1. The calculation of this amplitude is straightforward applying the usual Feynman diagram calculations, anyway a crude estimation of the transition rate is easily done observing that the oscillation $\nu_\mu \to \nu_e$ should take place over a distance $L \sim 1/M_W$, the energy flowing in the loop is of order M_W and, otherwise, the diagram is the same as the muon Michel decay with one more photon leg.

$$\begin{aligned}
\Gamma(\mu \to e\gamma) &\approx \underbrace{\frac{G_F^2 m_\mu^5}{192\pi^3}}_{\mu-\text{decay}} \quad \underbrace{\left(\frac{\alpha}{2\pi}\right)}_{\gamma-\text{vertex}} \quad \underbrace{\sin^2 2\theta \sin^2\left(\frac{1.27\Delta m^2}{M_W^2}\right)}_{\nu-\text{oscillation}} && (1.36)\\
&\approx \frac{G_F^2 m_\mu^5}{192\pi^3}\left(\frac{\alpha}{2\pi}\right)\sin^2 2\theta_\odot\left(\frac{\Delta m^2}{M_W^2}\right)^2, && (1.37)
\end{aligned}$$

that gives, normalized to the normal muon decay

$$\begin{aligned}
\frac{\Gamma(\mu \to e\gamma)}{\Gamma(\mu \to e\nu\bar{\nu})} &\approx \left(\frac{\alpha}{2\pi}\right)\sin^2 2\theta_\odot\left(\frac{\Delta m^2}{M_W^2}\right)^2 \\
&\approx \frac{1}{2\times 137\times\pi}\left(\frac{7\times 10^{-5}\ \text{eV}^2}{80\ \text{GeV}^2}\right)^2 \\
&\approx 10^{-55}, && (1.38)
\end{aligned}$$

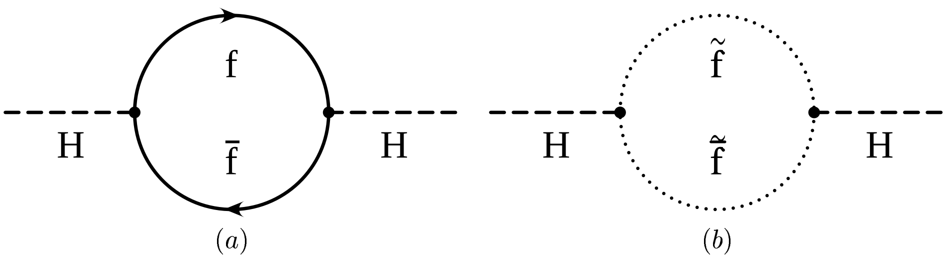

Figure 1.2: (a) One-loop diagrams responsible for the quantum correction to the Higgs mass, which give a divergent contribution in the Standard Model; in generic super-symmetric theories this diagram is partly canceled by the diagram (b) involving the sfermion partner.

which is an exceedingly small branching ratio (the correct evaluation differs by a factor of 3/64).

The SM is, in conclusion, successful in embedding all the observed phenomenology of elementary particles, giving a correct description of vector boson masses, of the observed symmetries and of the quark sector (including CP violation, which is accounted for by a complex phase in $V_{\rm CKM}$). It can be quite easily extended to include the observed neutrino mass pattern. Yet lepton flavor violation outside the neutrino sector is extremely small.

1.3 Beyond the Standard Model

Despite its success in describing particle phenomenology the SM is unsatisfactory from many points of view, most of them of theoretical nature. To begin with it is a theory which describes the world but does not explain why the world is at it stands.

To be more precise the SM does not account for the existence of three generations of quarks and leptons, nor for the quark and lepton masses and mixing pattern.

It is also appealing to think of a unification of the strong and electro-weak forces with gravitation. In this way a new energy scale, $M_{\rm Pl} \approx 10^{19}$ GeV, the scale at which the three forces become comparable, enters the game.

In the SM the parameters of the Higgs potential are arbitrary and unrelated to other energy scales, yet quantum corrections to the Higgs mass $m_{\rm H}$, induced by loop diagrams, as in Figure 1.2a, give contributions of order

$$\delta m_{\rm H}^2 \sim \Lambda^2 \tag{1.39}$$

where Λ is the cut-off energy of the theory ($\Lambda \sim M_{\rm Pl}$) making Λ as the natural scale for the Higgs boson mass.

This poses the problem of *naturalness*[2] and stability of the Fermi scale because an extreme

[2]Naturalness can be defined by the statement that every small parameter ξ in the SM is dictated by some symmetry, which is restored in the limit $\xi \to 0$. This is true for all parameters (*e.g.* fermion masses kept small by the chiral symmetry) except for the Higgs parameter μ. No symmetry controls its smallness with respect to super-heavy scales.

fine-tuning of the parameters to every order in perturbation theory is necessary to keep m_{H} at the Fermi scale.

1.3.1 Supersymmetry

The technical way to solve the naturalness problem of the Higgs mass is the introduction of a new symmetry that is able to keep the scalar mass under control. The only known symmetry able to do that is supersymmetry.

Supersymmetry (SUSY) is a symmetry which commutes with the gauge and the other internal symmetries and relates bosons and fermions with the same quantum numbers (apart, obviously, from spin, which is a "Poincarè" quantum number). In particular it predicts, along with every particle, its super-symmetric counterpart with, in the limit of non-broken SUSY, the same mass. The two particles are said to belong to the same super-multiplet. In this way the Higgs mass is kept under control by the following mechanism: for each fermion in the loop of Figure 1.2 there is a contribution from its scalar partner, of the opposite sign due to the difference in Fermi-Bose statistics. The one-loop contribution to the Higgs mass is given by

$$\delta m_H^2 \sim \sum_i g_i^2 \left(m_{B_i}^2 - m_{F_i}^2\right) \tag{1.40}$$

where B_i and F_i are the Bosons and Fermion belonging to the same super-multiplet and g_i is their (common) coupling to the Higgs scalar.

Supersymmetry is clearly broken, since we do not observe any partner of the known fermions. Furthermore, equation (1.40) does something more than simply controlling the divergence of the scalar mass: it establishes that the scale at which we expect to find SUSY particles is the same as the Higgs boson mass, *i.e.* the Fermi scale.

It is customary to express the non-kinetic part of the Lagrangian by means of a super-potential. The super-potential is an analytic function, cubic at most, of the super-multiplets. We will make use of this convenient way of writing in the following Chapter. The Yukawa coupling between the matter fields and the Higgs is written as

$$W = y_u H_1 QU + y_d H_2 QD + y_e H_2 LE \tag{1.41}$$

where the contractions which render all the terms singlets are understood.

Being the super-potential an analytic function of the super-fields it is not possible to give mass to all fermions via Yukawa interactions with one Higgs doublet only ($\phi^\dagger$ cannot be included). Two doublets with opposite hypercharge are introduced which develop two different VEVs. The ratio of the two VEVs is called

$$\frac{v_1}{v_2} = \tan\beta$$

and it is always assumed $\tan\beta > 1$.

1.3.2 The Grand-Unified Theories

Supersymmetry is an appealing feature, yet there are other problems in the SM which it does not address: the existence of three gauge groups with independent coupling constants is not theoretically appealing. Furthermore the hypercharge assignment to the particles is completely arbitrary, and adjusted to reproduce the measured particle charges.

There is no theoretical motivation (yet an astonishing experimental piece of evidence for something deeper) for the quark charges being related to the lepton charges, or for the charge being quantized at all[3].

In fact the values of the other quantum numbers (weak isospin, etc.) are strictly dictated by the commutation relations of the gauge group generators (exactly in the same way as the momentum of a free particle can be arbitrary, while its angular momentum is quantized). Charge quantization would occur if Q were a generator of the gauge group.

SU(5): the magic of quantum numbers

$SU(3) \times SU(2) \times U(1)$ possesses four independent commuting (*i.e.* diagonal) generators: Y, T_3, λ_3 and λ_8 (λ_3 and λ_8 are the diagonal generators of SU(3), the colorless gluons).

The number of mutually commuting generators of a group is called the *rank* of the group. It is normal to try to embed $SU(3) \times SU(2) \times U(1)$ in a rank= 4 group $\mathcal{G}$ which is broken at some energy to $SU(3) \times SU(2) \times U(1)$.

The only rank= 4 group is $SU(5)$, whose fundamental representation is five-dimensional. It possesses 24 generators (gauge bosons). There is an obvious embedding of the eleven $SU(3) \times SU(2)$ generators in $SU(5)$ which is

$$(\lambda_i)_{3\times 3} \rightarrow \left(\begin{array}{c|c} \lambda_i & 0 \\ \hline 0 & 0 \end{array}\right)_{5\times 5} \qquad (\sigma_i)_{2\times 2} \rightarrow \left(\begin{array}{c|c} 0 & 0 \\ \hline 0 & \sigma_i \end{array}\right)_{5\times 5} \tag{1.42}$$

with the last diagonal generator being

$$Y = y \begin{pmatrix} 1 & & & & \\ & 1 & & & \\ & & 1 & & \\ & & & -{}^3/_2 & \\ & & & & -{}^3/_2 \end{pmatrix} . \tag{1.43}$$

[3]Apart from the request to the theory of being anomaly-free, which anyway relates quark and lepton charges but does not explain charge quantization

There are twelve generators left, which are of the form

$$\left(\begin{array}{ccc|cc} & & & 1 & 0 \\ & & & 0 & 0 \\ & & & 0 & 0 \\ \hline 1 & 0 & 0 & & \\ 0 & 0 & 0 & & \end{array}\right), \quad \left(\begin{array}{ccc|cc} & & & i & 0 \\ & & & 0 & 0 \\ & & & 0 & 0 \\ \hline -i & 0 & 0 & & \\ 0 & 0 & 0 & & \end{array}\right), \quad \text{etc.} \tag{1.44}$$

The SM particles of each generation are placed in a $\bar{5} \oplus 10$ representation in the following way

$$\bar{5} = \bar{F} = \begin{pmatrix} \bar{d}^r \\ \bar{d}^y \\ \bar{d}^b \\ e^- \\ \nu_e \end{pmatrix}_L \qquad 10 = T = \left(\begin{array}{ccc|cc} 0 & u^b & u^y & -u^r & -d^r \\ & 0 & u^r & -u^y & -d^y \\ & & 0 & -u^b & -d^b \\ \hline & & & 0 & -e^+ \\ & & & e^+ & 0 \end{array}\right). \tag{1.45}$$

The representations are also called $\bar{F} = \bar{5}$ (from "five") and $T = 10$ (from "ten").

The gauge bosons of the SM are associated with block diagonal generators, thus act in the same way as before. Conversely the twelve new gauge bosons are associated to generators[4] connecting leptons and quarks, mediating quark-lepton transitions, giving rise to processes such as proton decay.

Their masses must be very large in order to make proton instability acceptably small, hence $SU(5)$ must be broken at a very high energy. The spontaneous symmetry breaking of SU(5) is accomplished by a 24-dimensional Higgs multiplet.

$SU(5)$ unification has two remarkable properties: it predicts charge quantization (and the correct relation between quark and lepton electric charge) and the unification of all coupling constants at an energy $M_{\rm GUT} \sim 10^{15}$ GeV (as well as a prediction of $\sin\theta_W$ consistent with measurements).

It removes all the SM accidental symmetries but preserves $B - L$, $(L = L_e + L_\mu + L_\tau)$. Unfortunately the prediction of the proton decay rate in the minimal SU(5) model is in conflict with the experiment.

SO(10): the gauging of $B - L$

The possibility of $SO(10)$ as a grand-unification group for the Standard Model was first noted by Georgi [15] and Fritsch & Minkowski [16]. Unlike $SU(5)$, $SO(10)$ is a rank= 5 group with the extra diagonal generator being $B - L$. It is worth noticing that $SO(10) = SU(5) \otimes U(1)$ and that it possesses a 16-dimensional representation which decomposes, under $SU(5) \otimes U(1)$ as $16 = 10 \oplus 5 \oplus 1$. This is theoretically appealing because it can be regarded as a natural explanation of the fact that in the framework of $SU(5)$ the fermions belong to a reducible representation. In fact it is possible to accommodate all the fermions of one generation within a single 16-dimensional chiral multiplet with the extra singlet field easily associated with a right handed neutrino.

[4]Note that these new bosons are color triplets and SU(2) doublets; they are conventionally called $X^{\pm}$ and $Y^{\pm}$, whose charge are 4/3 and 1/3.

1.3.3 SUSY + GUT = SUSY GUTs

In Grand Unified Theories the problem of naturalness is still present, since it is not possible to explain the existence of two energy scales which differ by so many orders of magnitude (M_{GUT} and m_H). They retain all the bad divergence properties of the Higgs mass.

The natural solution is provided by the SUSY generalization of GUT theories, the so-called SUSY-GUTs, which are, for all the reasons explained above, among the most appealing candidates for the extension of the SM to date.

1.4 Conclusions

In the SM lepton flavor violation is forbidden by an "accidental" symmetry. This symmetry is removed in all its viable extensions. The presence of a lepton-flavor violating signal, other than neutrino oscillation, can really indicate the existence of new physics beyond the Standard Model.

Chapter 2

Phenomenology

2.1 Introduction

As shown in Chapter 1, the detection of lepton-flavor violating processes would clearly indicate the existence of physics beyond the SM. Among the various channels, those involving muon decays are the most appealing, due to the comparative ease to have high fluxes of low energy muons at dedicated beams. Recent theoretical developments calculate rates for some LFV processes involving muon decays that are just below the present experimental limit. In the present Chapter we will review the phenomenology of lepton flavor violation, concentrating on the $\mu^+ \to e^+\gamma$ decay.

2.2 Main LFV processes and limits

In Table 2.1 the upper limits of various lepton-flavor violating processes are listed. They involve decays of muons and tau leptons in neutrinoless final states, as well as those of heavy bosons, π, K and Z^0, in pairs of leptons of different generations. The sensitivity to LFV is superb in the muon system, mostly because of the large number of muons (of about $10^{14} \div 10^{15}$/year) available for experimental searches today.

The processes involving muon decays can be grouped in three categories:

1. Direct muon decays ($\mu^+ \to e^+\gamma$ and $\mu \to eee$);
2. Muon conversion on heavy elements, as Titanium or Gold;
3. Muonium—anti-muonium conversion.

As apparent from Table 2.1 the best limits are obtained for $\mu \to eee$ and muon conversion on heavy elements. This is due to the clear signature of the processes which allows for a search in a background-clear environment. However the exclusion power on $\Delta L_i = \pm 1$ processes due to their limits is comparable to that of the $\mu^+ \to e^+\gamma$ decay, since, in most theoretical models, the

Reaction	Present limit	Reference
$\mu^+ \to e^+\gamma$	$< 1.2 \times 10^{-11}$	[17, 18]
$\mu \to eee$	$< 1.0 \times 10^{-12}$	[19]
$\mu^- Ti \to e^- Ti$	$< 6.1 \times 10^{-13}$	[20]
$\mu^+ e^- \to \mu^- e^+$	$< 8.3 \times 10^{-11}$	[21]
$\tau \to e\gamma$	$< 2.7 \times 10^{-6}$	[22]
$\tau \to \mu\gamma$	$< 1.0 \times 10^{-6}$	[23]
$\tau \to \mu\mu\mu$	$< 1.9 \times 10^{-6}$	[24]
$\tau \to eee$	$< 2.9 \times 10^{-6}$	[24]
$\pi^0 \to \mu e$	$< 8.6 \times 10^{-9}$	[25]
$K_L^0 \to \mu e$	$< 4.7 \times 10^{-12}$	[26]
$K^+ \to \pi^+ \mu^+ e^-$	$< 2.1 \times 10^{-10}$	[27]
$K_L^0 \to \pi^0 \mu^+ e^-$	$< 4.4 \times 10^{-10}$	[28]
$Z^0 \to \mu e$	$< 1.7 \times 10^{-6}$	[29]
$Z^0 \to \tau e$	$< 9.8 \times 10^{-6}$	[29]
$Z^0 \to \tau\mu$	$< 1.2 \times 10^{-5}$	[30]

Table 2.1: Limits for the branching ratio of the lepton-flavor violating processes involving muons, taus, pions, kaons and Z bosons. For the muon capture processes the limit of the relative probability with respect to the SM predicted processes is given.

two former processes are suppressed by one power of α, the fine structure constant, with respect to the latter. There are however theories in which $\mu \to eee$ and muon conversion are enhanced with respect to the $\mu^+ \to e^+\gamma$ decay. The existence of $\Delta L_i = \pm 2$ processes, on the other way, is constrained by limits on the muonium anti-muonium conversion.

The search of lepton-flavor violating muon decays is important *per se*, inasmuch it is able to test the validity of the Standard Model. However there has been a recent revival of the subject after the discovery of the top quark, and the realization of its heaviness, $m_t = (174.3 \pm 5.1)$ GeV. The presence in the model of such a huge parameter leads to an enhancement of LFV processes [31, 32, 33].

Furthermore the evidence for neutrino oscillations can be related to amplitude predictions for SM-forbidden muon decays.

We want to review in this Chapter the recent theoretical speculations on muon rare decays, with a particular emphasis on the predictions for the $\mu^+ \to e^+\gamma$ decay.

2.3 The $\mu^+ \to e^+\gamma$ decay: predictions

As stated in Chapter 1, the $\mu^+ \to e^+\gamma$ decay amplitude induced by non-zero neutrino masses is negligible. For a model-independent description of the phenomenon we turn to the formalism of effective field theory. If we expect the SM to be valid up to some energy scale M, the effects of physics above this scale may be accounted for by shifts in the SM couplings and by a series of non-renormalizable terms suppressed by powers of M. In this view, the effective Lagrangian for the $\mu^+ \to e^+\gamma$ process is given by [34]

$$\mathcal{L}_{\mu^+\to e^+\gamma} = \frac{g}{M^2}\left[m_\mu A_R \bar{\mu}_R \sigma^{\mu\nu} e_L F_{\mu\nu} + m_\mu A_L \bar{\mu}_L \sigma^{\mu\nu} e_R F_{\mu\nu}\right] + \text{h.c.} \tag{2.1}$$

where A_L and A_R are the coupling constants that correspond to $\mu^+ \to e_R^+\gamma$ and $\mu^+ \to e_L^+\gamma$ respectively, $F^{\mu\nu}$ is the usual electro-magnetic field tensor and $\sigma^{\mu\nu} = -i/2[\gamma^\mu, \gamma^\nu]$.

The general mechanism that generates a $\mu^+ \to e^+\gamma$ amplitude in the Standard Model extensions is the following: SM particles possess heavy partners whose interactions are in general non flavor-diagonal. Flavor transitions in the heavy sector of the theory induces flavor transitions in the sector of the SM particles, suppressed by powers of the energy scale at which the symmetry between the light and the heavy sector is restored.

In a way analogous to the Fermi theory of weak interactions in which the coupling constant G_F is related to the inverse of M_W^2, the processes occurring at a energy scale M can be summarized in the low energy Lagrangian by effective couplings (*e.g.* A_R and A_L in Equation (2.1)) suppressed by powers of M.

We will briefly describe the predictions for three most popular models: SU(5) SUSY-GUTs, SO(10) SUSY GUTs, and SU(5) unification with heavy right-handed Majorana neutrinos.

2.3.1 SU(5) SUSY GUTs with R-parity

The SM accidental symmetries (B, L, L_i) which forbid processes such as proton decay, neutrino masses and $\mu^+ \to e^+\gamma$ decay respectively, are removed at the unification scale M_G. In the effective theory beneath M_G (the Standard Model) the three phenomena are suppressed by powers of M_G. If the effective theory is super-symmetric at a scale $M_F \sim 100$ GeV, the energy scale which plays a role in the effective Lagrangian is M_F, hence the processes are suppressed by powers of M_F. Such interactions induce proton decay at unacceptable rate unless a new symmetry, called R-parity or matter parity, is introduced[1]. R-parity forces all interactions to have an even number of quarks and leptons and their super-partners (a consequence of this is that the lightest SUSY particle, called neutralino, is stable, allowing for the existence of SUSY dark matter). Thus all B and L-violating processes are forbidden at a scale M_F and remain suppressed by powers of M_G, while processes which violate L_i are still suppressed only by powers of M_F. In other words, in the most general form of super-potential

$$\begin{aligned} W = \quad & y_e H_d L E + y_d H_d Q D + y_u H_u Q U + \\ + \quad & \lambda L L E + \lambda' L Q D + \lambda'' U D D \end{aligned} \tag{2.2}$$

which include the couplings between the Higgs field and the matter fields, as in Equation (1.41) as well as the couplings between the matter fields alone, the interactions of the second line are forbidden by R-parity.

[1] For the particles of the low energy sector $R = (-1)^{B+L+2S}$, where B is the Baryon number, L the lepton number and S is the particle spin.

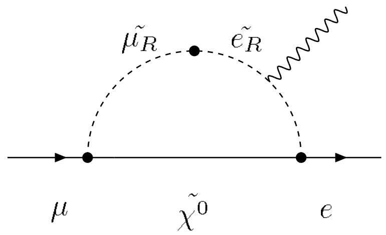

Figure 2.1: Possible diagram for the $\mu^+ \to e^+\gamma$ decay in SU(5) SUSY GUT. The $\tilde{\chi}^0$ particle is a heavy neutralino mediating the flavor changing process.

The large Yukawa coupling of the top quark further enhances the lepton flavor transitions, as a consequence of the combined action of SUSY and unification. This results in a large transition rate between the scalar partners of the muon and the electron, $\tilde{\mu}$ and $\tilde{e}$, which enhances the $\mu^+ \to e^+\gamma$ process through diagrams of the type depicted in Figure 2.1. The predicted rate depends on several parameters of the theory. In [32] the following expression is given

$$BR(\mu^+ \to e^+\gamma) = 2.4 \times 10^{-12} \left(\frac{|V_{ts}|}{0.04}\frac{|V_{td}|}{0.01}\right)^2 \left(\frac{100 \text{ GeV}}{m_{\tilde{e}}}\right)^4 . \tag{2.3}$$

In Figure 2.2 predictions are given as a function of slepton masses. It has been calculated that, since up-type quarks and down-type quarks and leptons belong to different representations of SU(5), the left handed sleptons are not significantly mixed, and the branching ratio $\mu^+ \to e^+_R\gamma$ is negligible, therefore only $\mu^+ \to e^+_L\gamma$ occurs in SUSY GUT SU(5). This asymmetry can be easily seen if we write the Yukawa couplings (2.2) as a function of the SU(5) matter fields

$$W_{SU(5)} = \quad (y_u)_{ij} \quad T_i T_j H(5) + (y_d)_{ij}\bar{F}_i T_j \bar{H}(5) \tag{2.4}$$

$\nwarrow$

The large top quark Yukawa
coupling is here

where $H(5)$ and $\bar{H}(5)$ are the Higgs fields associated with the 5 and $\bar{5}$ representations, and T and F are the representations containing the matter fields as in Equation (1.45). Since the large top Yukawa coupling enters in $(y_u)_{ij}$ left-handed and right-handed fields are treated differently[2].

2.3.2 SO(10) SUSY GUT

In SO(10) SUSY GUT models both left-handed and right-handed (s)leptons receive LFV contributions, since the super-potential is now written as

$$W_{SO(10)} = (y_u)_{ij}16_i \; H_u(10) \; 16_j + (y_d)_{ij}16_i \; H_d(10) \; 16_j \tag{2.5}$$

[2]This point could be used in a future, since studies of the correlation between the muon spin and the direction of the $\mu \to e\gamma$ photon will distinguish between SU(5) and SO(10). As we shall see in the next Section, in SO(10) leptons of both helicities take part in the $\mu^+ \to e^+\gamma$ amplitude.

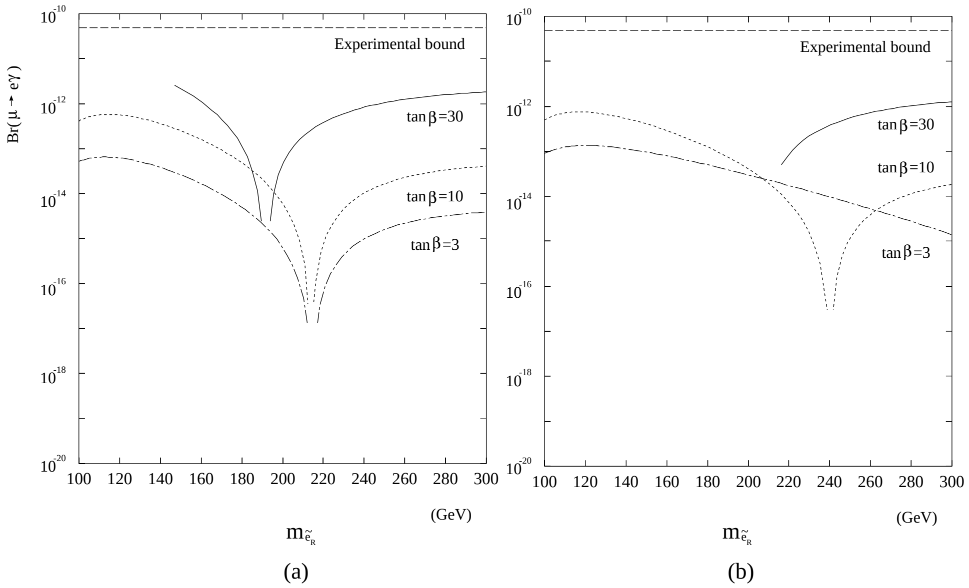

Figure 2.2: Branching ratio for the process $\mu^+ \to e^+\gamma$ as a function of the right-handed selectron mass $m_{\tilde{e}_R}$ for a reasonable choice of electro-weak breaking parameters (after [35]).

where in the 16 representation all particles are included. In particular, the diagrams shown in Figure 2.3 give a large contribution because they are proportional to m_τ, hence the $\mu^+ \to e^+\gamma$ branching ratio is enhanced by a factor $(m_\tau/m_\mu)^2$ compared to the minimal SU(5) SUSY GUT. In Figure 2.4 the $\mu^+ \to e^+\gamma$ branching ratio is plotted versus the top-quark Yukawa coupling at GUT scale for a wide range of the SUSY parameter space.

2.3.3 Super-symmetric models with right-handed neutrinos

Another independent source of LFV comes from SUSY models with right-handed neutrinos [37]. As seen in Chapter 1, the smallness of neutrino masses can be explained by the see-saw mechanism induced by right-handed Majorana neutrinos. Rewriting Equation (1.32) taking all three generations into account a second Yukawa coupling matrix, which in general is not generation-diagonal, is introduced, inducing flavor mixing in the high energy sector of the theory between heavy Majorana neutrinos.

The expected magnitude of LFV processes depends on the Yukawa coupling constants but under the assumption that the observed neutrino mixing arises mostly from the Yukawa coupling constants [34] the information from atmospheric and solar neutrinos can be related to slepton mixing, which enhances the $\mu^+ \to e^+\gamma$ decay. Figure 2.5 shows the predicted BR($\mu^+ \to e^+\gamma$) for the LMA solution of the solar neutrino mixing, as a function of the Majorana neutrino mass scale. A large fraction of the range for M_R is already excluded by the present experimental limit.

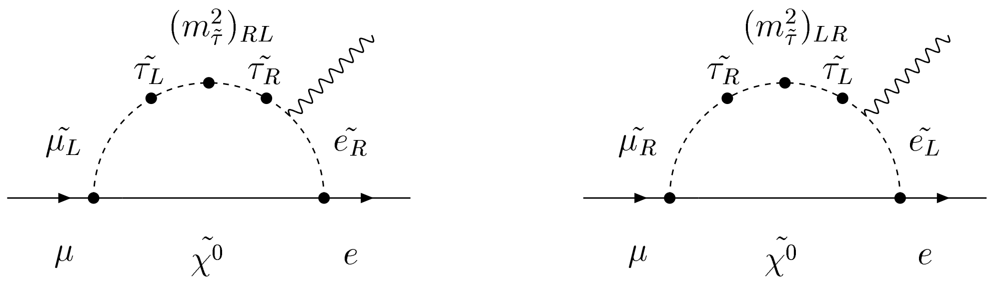

Figure 2.3: Feynman diagrams in SO(10) SUSY GUT which give dominant contributions to the $\mu^+ \to e^+\gamma$ process. The $\tilde{\chi}^0$ particle is a heavy neutralino mediating the flavor changing process.

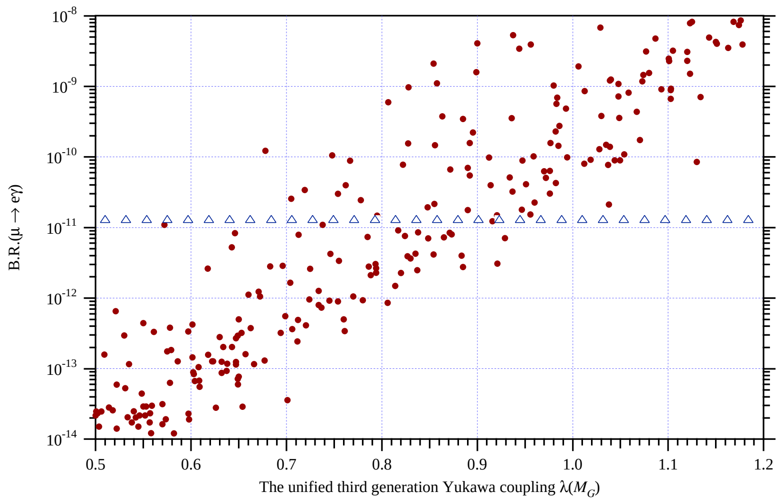

Figure 2.4: Branching ratio of the $\mu^+ \to e^+\gamma$ decay as a function of the unified top-quark Yukawa coupling. The line denotes the present experimental bound (after [36]). The compatibility with the large top quark mass requires $\lambda(M_G) > 0.6$.

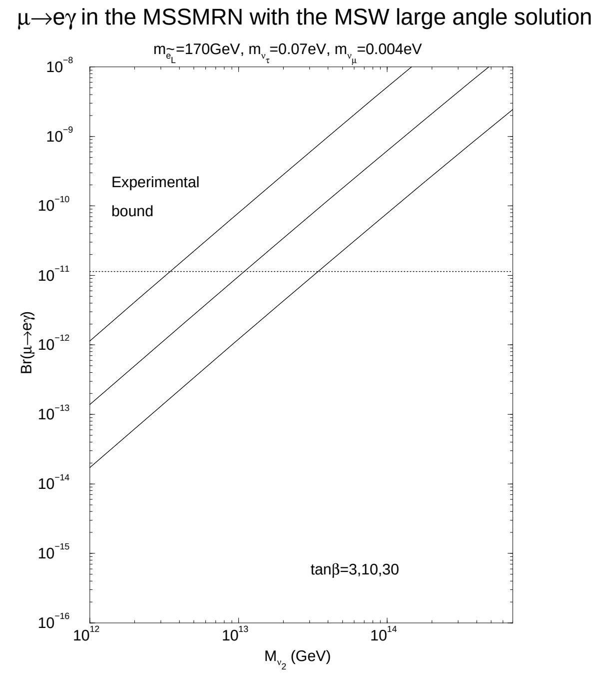

Figure 2.5: Predicted branching ratio of $\mu^+ \to e^+\gamma$ decay as a function of the Majorana mass of the second-generation right-handed neutrino in the MSSM model with right-handed neutrino, for the MSW large mixing angle solution. The three lines correspond to $\tan\beta = 30, 10, 3$ from top to bottom respectively.

2.3.4 Connections with other parameters

Connection with $\tan\beta$

In all the predictions the $\mu^+ \to e^+\gamma$ decay rate increases with increasing $\tan\beta$, the ratio of the two SUSY Higgs boson VEVs as is shown, *e.g.* in Figure 2.5. It is worthwhile to notice that the non-discovery of super-symmetry at LEP and TeVatron excludes most of the small $\tan\beta$ region [38]

Connection with a_μ

The branching ratio of the $\mu^+ \to e^+\gamma$ process is naturally linked to the value of the muon anomalous magnetic moment. In fact the general term of the Lagrangian (2.1) is written, taking the three generations into account, as

$$\mathcal{L} = g\frac{m_{l_j}}{M^2}\left(A^R_{ij}\bar{l}^R_i\sigma_{\mu\nu}F^{\mu\nu}l^L_j + A^L_{ij}\bar{l}^L_i\sigma_{\mu\nu}F^{\mu\nu}l^R_j\right) \tag{2.6}$$

where the same notation as Eq. (2.1) is used. The real diagonal parts of A^L_{ij} and A^R_{ij}, which are now 3×3 matrices, contribute to the anomalous magnetic moment of the charged leptons,

$$a_{l_i} \equiv \frac{g-2}{2} = m^2_{l_i}\left(A^R_{ii} + A^L_{ii}\right) \tag{2.7}$$

while the flavor transitions are produced by the off-diagonal terms, *e.g.*:

$$BR(\mu^+ \to e^+\gamma) \propto \left(\left|A^R_{\mu e}\right|^2 + \left|A^L_{\mu e}\right|^2\right). \tag{2.8}$$

The relations among the elements of $A^{R,L}_{ij}$ are dictated by the model. The latest result for the anomalous magnetic moment for the muon [39] is

$$a^{\mathrm{exp}}_\mu = (116\,593\,023 \pm 151) \times 10^{-11} \tag{2.9}$$

while the SM prediction is

$$a^{\mathrm{SM}}_\mu = (116\,592\,768 \pm 65) \times 10^{-11}. \tag{2.10}$$

The present measurement is 1.6σ away from the SM prediction.

Using Equation (2.6) non-SM contributions to a_μ can be related, in a model-dependent way, to the branching ratio of the $\mu^+ \to e^+\gamma$ decay. Figure 2.6 shows for instance the relation between a_μ and BR($\mu^+ \to e^+\gamma$) in a super-symmetric see-saw model [40].

2.4 Conclusion

The phenomenology of lepton flavor violation is very sensitive to the possible extensions of the Standard Model; research in the muon sector is promising because of the large number of such particles produced each year at dedicated beams.

We reviewed three popular models in which the predictions for the $\mu \to e\gamma$ decay branching ratio, due to different independent sources, is generally above $10{-}14$, almost independently from the model parameters: it is therefore worthwhile to try to push down the present limits toward this level.

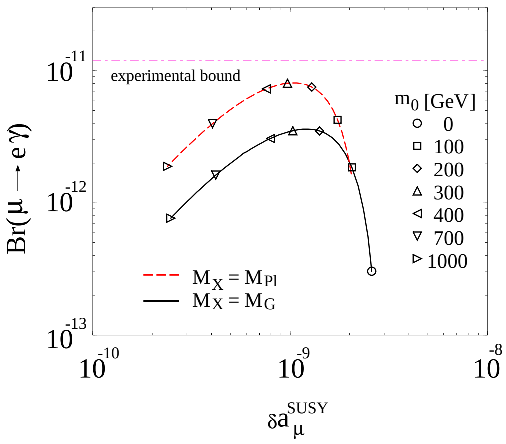

Figure 2.6: Dependence of BR($\mu^+ \to e^+\gamma$) and of the SUSY contribution to the muon anomalous magnetic moment on the universal scalar mass m_0 in the super-symmetric see-saw model. The solid and dashed lines are for cases where the scale of the generation of the SUSY-breaking terms in the SUSY SM (M_X) are the GUT scale or the Plank scale, respectively (after [40]).

Chapter 3

Search for the $\mu^+ \to e^+\gamma$ decay.

3.1 Introduction

The $\mu^+ \to e^+\gamma$ decay was searched for soon after the muon discovery. Its absence was a key ingredient for the formulation of the Standard Model. We want to review in this Chapter the early experiments and their importance, emphasizing the key points to be addressed by future $\mu^+ \to e^+\gamma$ search experiments.

3.2 Experimental status of $\mu^+ \to e^+\gamma$ decay search

The muon role in the spectrum of elementary particles has been a mystery since its discovery in cosmic radiation [41] (1937). For over a decade the muon was thought to be the quantum mediating the strong nuclear force, as predicted by Yukawa [42]. Yet the famous experiment by Conversi, Pancini and Piccioni [43] demonstrated that the muon did not interact through strong force, therefore it could not be the Yukawa meson. It was thought that if the muon were a heavy electron, it would also decay into an electron and a γ-ray. The first search for $\mu^+ \to e^+\gamma$ was made by Hincks and Pontecorvo in 1947 [44]. They stopped cosmic ray muons in a lead absorber (Figure 3.1) and measured the rate of the discharge coincidence of two Geiger-Müller tube trays. With an expected rate of 1.0 ± 0.3 counts/h they measured $0.01^{+0.06}_{-0.01}$ counts/h, setting an upper limit of less than 10% on the $\mu^+ \to e^+\gamma$ branching ratio.

The search was significantly improved when muons became artificially produced at accelerators, first by using stopped pion beams, later directly with muon beams from the meson factories. In 1955, the upper limit of $B(\mu \to e\gamma) < 2 \times 10^{-5}$ [45] was set at the Columbia University Nevis cyclotron.

After the discovery of parity violation, it was suggested that the weak interaction takes place through the exchange of charged intermediate vector bosons. In 1958, Feinberg [46] pointed out that the intermediate vector boson, if it existed, would have led to $\mu^+ \to e^+\gamma$ at a branching

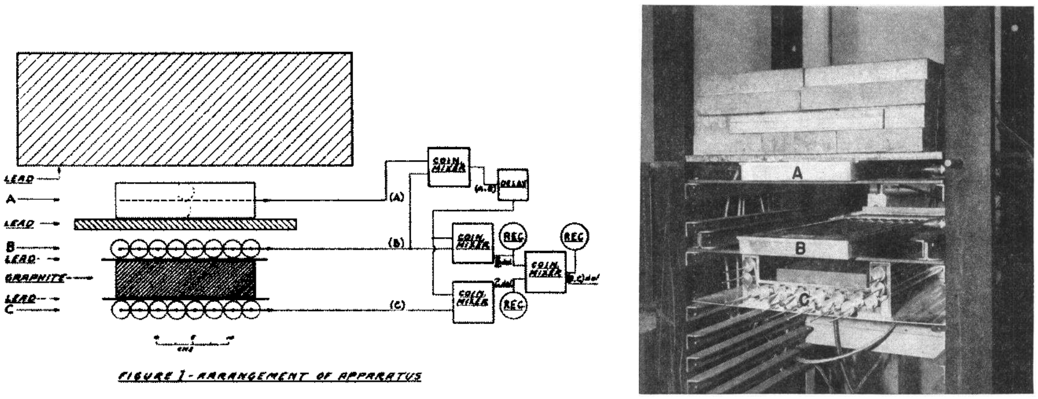

(a) (b)

Figure 3.1: Drawing (a) and photograph (b) of the apparatus used by Hinks and Pontecorvo for the first search of the decay of cosmic ray mesons into an electron plus a photon.

Place	Year	ΔE_e	ΔE_γ	$\Delta t_{e\gamma}$	$\Delta\theta_{e\gamma}$	Upper limit	References
TRIUMF	1977	10%	8.7%	6.7ns	–	$< 3.6 \times 10^{-9}$	[48]
SIN	1980	8.7%	9.3%	1.4ns	–	$< 1.0 \times 10^{-9}$	[49]
LANL	1982	8.8%	8%	1.9ns	37mrad	$< 1.7 \times 10^{-10}$	[50]
Crystal Box	1988	8%	8%	1.8ns	87mrad	$< 4.9 \times 10^{-11}$	[51]
MEGA	1999	1.2%	4.5%	1.6ns	15mrad	$< 1.2 \times 10^{-11}$	[17]

Table 3.1: Historical Progress of search for $\mu^+ \to e^+\gamma$ since the era of meson factories with 90 % C.L. upper limits. The resolutions quoted are given as a full width at half maximum (FWHM).

ratio of 10^{-4}. In fact the process is described by the same diagrams as in Figure 1.1, but without neutrino oscillation, because at that time ν_e and ν_μ were thought to be the same particle.

The absence of any experimental observation of the $\mu^+ \to e^+\gamma$ process with $B(\mu \to e\gamma) < 2 \times 10^{-5}$ led directly to the two-neutrino hypothesis, which was verified experimentally at Brookhaven National Laboratory (BNL) by confirming muon production, and no electron production, from the scattering of neutrinos coming from pion decays [47].

Over the years, the search for the $\mu^+ \to e^+\gamma$ decay was pursued at the intense muon beams available, *e.g.* at TRIUMF, PSI (formerly SIN) and Los Alamos National Laboratories. Limits on the $\mu^+ \to e^+\gamma$ branching fraction were constantly tightened by improving detector resolutions of the four relevant variables: positron and photon energy resolution, relative timing and direction. In Table 3.1 the historical progress of the $\mu^+ \to e^+\gamma$ search is summarized and in figure 3.2 a graphical view of the limit as a function of the year is given. The groupings of points in the plot reflect innovation in muon source and instrumentation.

The largest steps towards an improvement in the $BR(\mu^+ \to e^+\gamma)$ determination were due to improvements in the muon source. From cosmic ray muons (whose rate is $\sim$Hz) to stopped pion

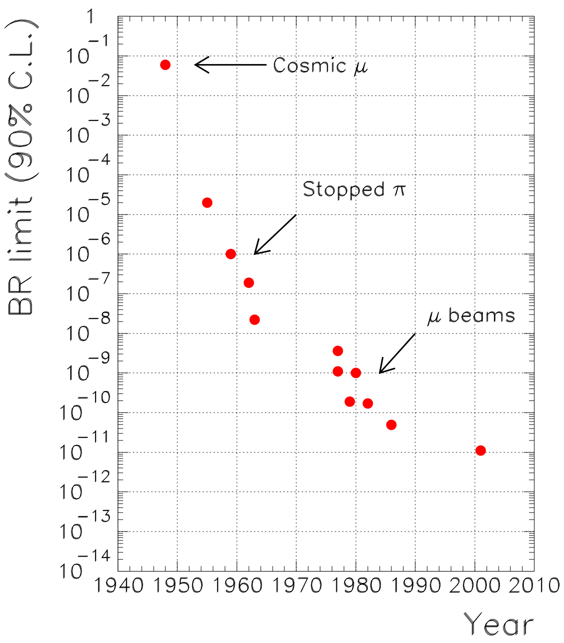

Figure 3.2: Improvement of the 90% CL upper limit on the $\mu^+ \to e^+\gamma$ decay branching fraction over the years

beams the improvement was over four order of magnitudes, and two further orders of magnitude were gained in the passage from pion to muon beams.

The limit improved essentially as the number of observed muons, and within each beam configuration improvements of the detectors were fundamental. The quality of a detector is judged by its capability of discriminating a signal event from the background, composed of spurious particles which mimic a $\mu^+ \to e^+\gamma$ decay. With the increased muon rate the number of background events was enormously increased, hence the design of new apparatuses depend essentially on their background rejection capabilities.

For this reason we will briefly describe the $\mu^+ \to e^+\gamma$ decay properties and kinematics, and discuss the main background sources.

3.3 Event signature and backgrounds

The event signature of $\mu^+ \to e^+\gamma$ decay at rest is an e^+ and a photon in coincidence, moving collinearly back-to-back with their energies equal to half of the muon mass ($m_\mu/2 = 52.8$ MeV). The searches are carried out by using positive muon decay at rest to fully utilize its kinematics. A negative muon cannot be used, since it is captured by a nucleus when it is stopped in the target. There are two major backgrounds in the search for $\mu^+ \to e^+\gamma$. One is a physics (prompt) background from radiative muon decay, $\mu^+ \to e^+\nu_e\overline{\nu}_\mu\gamma$, when the e^+ and the photon are emitted back-to-back with the two neutrinos carrying off little energy. The other background is an accidental coincidence of an e^+ in a normal muon decay, $\mu^+ \to e^+\nu_e\overline{\nu}_\mu$, accompanied by a high energy photon. The sources of the latter might be either $\mu^+ \to e^+\nu_e\overline{\nu}_\mu\gamma$ decay, or annihilation-in-flight or external bremsstrahlung of e^+s from normal muon decay. These backgrounds are described in more detail in the following.

3.3.1 Physics background

One of the major physics backgrounds to the search for $\mu^+ \to e^+\gamma$ decay is radiative muon decay, $\mu^+ \to e^+\nu_e\overline{\nu}_\mu\gamma$ (branching ratio = 1.4 % for $E_\gamma > 10$ MeV), when the e^+ and photon are emitted back-to-back with two neutrinos carrying off little energy. The differential decay width of this radiative muon decay was calculated as a function of the e^+ energy (E_e) and the photon energy (E_γ) normalized to their maximum energies, namely $x = 2E_e/m_\mu$ and $y = 2E_\gamma/m_\mu$ [52, 53]; therefore the kinematical ranges are $0 \leq x, y \leq 1$. As a background to $\mu^+ \to e^+\gamma$, the kinematic case when $x \approx 1$ and $y \approx 1$ is important. The differential decay width of $\mu^+ \to e^+\nu_e\overline{\nu}_\mu\gamma$ has been computed (see [54]) as a function of x, y, and $z = \pi - \theta_{e\gamma}$, and expanded in the region $x \approx 1$, $y \approx 1$ and $z \approx 0$.

When $x = 1$ and $y = 1$ exactly, this differential decay width vanishes. However, in a real experiment, finite detector resolutions introduce background events which would ultimately limit the sensitivity of a search for $\mu^+ \to e^+\gamma$.

Given the detector resolution, the sensitivity limitation from this physics background can be estimated by integrating the differential decay width over the kinematic signal box. It is given by [34]

$$\begin{aligned} dB(\mu^+ \to e^+\nu\overline{\nu}\gamma) &= \frac{1}{\Gamma(\mu^+ \to e^+\nu\overline{\nu})}\int_{1-\delta x}^{1} dx \int_{1-\delta y}^{1} dy \int_{0}^{\min(\delta z, 2\sqrt{(1-x)(1-y)})} dz \ \frac{d\Gamma(\mu^+ \to e^+\nu\overline{\nu}\gamma)}{dxdydz}, \\ &= \frac{\alpha}{16\pi}\Big[J_1(1-P_\mu\cos\theta_e) + J_2(1+P_\mu\cos\theta_e)\Big]d(\cos\theta_e), \end{aligned} \quad (3.1)$$

where δx, δy and δz are a half width of the $\mu^+ \to e^+\gamma$ signal region for x, y and z, respectively, θ_e is the angle between the muon spin and the e^+ momentum direction, and $\Gamma(\mu^+ \to e^+\nu\overline{\nu})$ is the total muon decay width. J_1 and J_2 are given as the sixth power of a combination of δx and δy. For the case of $\delta z > 2\sqrt{\delta x \delta y}$, they are presented by

$$J_1 = (\delta x)^4(\delta y)^2 \quad \text{and} \quad J_2 = \frac{8}{3}(\delta x)^3(\delta y)^3. \quad (3.2)$$

While if $\delta z \leq 2\sqrt{\delta x \delta y}$, they are given by[1]

$$J_1 = \frac{8}{3}(\delta x)^3(\delta y)(\frac{\delta z}{2})^2 - 2(\delta x)^2(\frac{\delta z}{2})^4 + \frac{1}{3}\frac{1}{(\delta y)^2}(\frac{\delta z}{2})^8, \quad (3.3)$$

$$J_2 = 8(\delta x)^2(\delta y)^2(\frac{\delta z}{2})^2 - 8(\delta x)(\delta y)(\frac{\delta z}{2})^4 + \frac{8}{3}(\frac{\delta z}{2})^6. \quad (3.4)$$

Experimentally, the resolution of the e^+ energy is better than that of the photon energy, *i.e.* $\delta x < \delta y$. Figure 3.3 shows the $\mu^+ \to e^+\nu_e\overline{\nu}_\mu\gamma$ decay fraction for the given δx and δy values with unpolarized muons in the case of $\delta z \geq 2\sqrt{\delta x \delta y}$. From Figure 3.3, it can be seen that both δx and δy on the order of 0.01 are needed to achieve a sensitivity limit at the level of 10^{-15}.

3.3.2 Accidental background

With a very high rate of incident muons, the accidental background becomes more important than the physics background. This is usually the case for the present and future experiments. The event rate of the accidental background normalized to the total decay rate ($B_{\rm acc}$) can be estimated by

$$B_{\rm acc} = R_\mu \cdot f_e^0 \cdot f_\gamma^0 \cdot (\Delta t_{e\gamma}) \cdot (\frac{\Delta\Omega_{e\gamma}}{4\pi}), \quad (3.5)$$

where R_μ is the instantaneous muon intensity. f_e^0 and f_γ^0 are the integrated fractions of the spectrum of e^+ in the normal muon decay and that of photon (such as from $\mu^+ \to e^+\nu_e\overline{\nu}_\mu\gamma$ decay) within the signal region, respectively. $\Delta t_{e\gamma}$ and $\Delta\Omega_{e\gamma}$ are, respectively, the full widths of the signal regions for timing coincidence and angular constraint of the back-to-back kinematics.

Given the sizes of the signal region, B_{acc} can be evaluated. Let us take δx, δy, $\delta\theta_{e\gamma}$, and $\delta t_{e\gamma}$ to be the half width of the signal region for e^+, photon energies, angle $\theta_{e\gamma}$, and relative timing

[1] We shall see in Chapter 12 that this is indeed the situation for the MEG experiment.

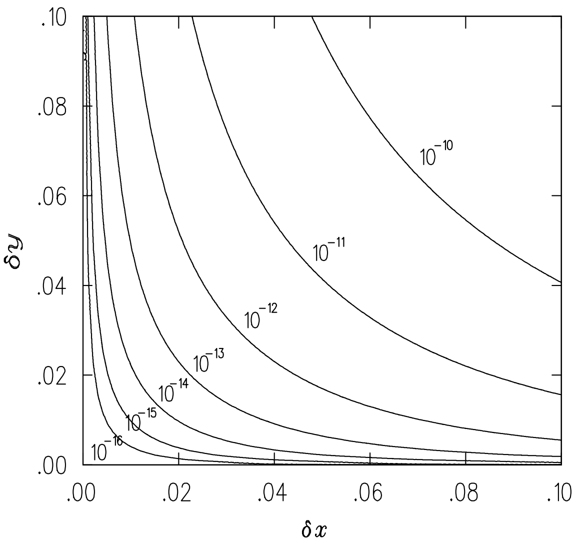

Figure 3.3: Branching ratio of the physics background from the muon radiative decay as a function of the e^+ energy resolution (δx) and photon energy resolution (δy). After [34].

between e^+ and photon, respectively. f_e^0 can be estimated by integrating the Michel spectrum of the normal muon decay over $1 - \delta x \leq x \leq 1$, yielding $f_e^0 \approx 2(\delta x)$, since the Michel spectrum is constant at $x \approx 1$. Given the angular resolution, $\delta\theta_{e\gamma}$, the back-to-back resolution $(\Delta\Omega_{e\gamma}/4\pi)$ is given by $(\Delta\Omega_{e\gamma}/4\pi) = (\delta\theta_{e\gamma})^2/4$.

As for f_γ^0, if the radiative muon decay $\mu^+ \to e^+\nu_e\overline{\nu}_\mu\gamma$ is considered as a source of the 52.8 MeV photon, it can be given by integrating the photon energy spectrum (shown in Figure 3.4*a*) within the width of the signal region ($1 - \delta y \leq y \leq 1$). For unpolarized muons, it is given by [34]

$$f_\gamma^0 = \int_{1-\delta y}^{1} dy \int d(cos\theta_\gamma) \frac{dB(\mu^+ \to e^+\nu\overline{\nu}\gamma)}{dy d(cos\theta_\gamma)} \approx \left(\frac{\alpha}{2\pi}\right)(\delta y)^2 \Big[\ln(\delta y) + 7.33\Big]. \tag{3.6}$$

From Equation (3.6), it is shown that f_γ^0 for $\mu^+ \to e^+\nu_e\overline{\nu}_\mu\gamma$ decay is roughly proportional to $(\delta y)^2$.

The other sources of high-energy photons are annihilation in flight of e^+s in the normal muon decay and external bremsstrahlung. The contribution from annihilation of e^+ in flight depends on the materials along the e^+'s track path. Figure 3.4*b* shows, for instance, the contribution of annihilation in flight for the case of e^+s passing through a muon-stopping target of 150 μm of Mylar in thickness. It indicates that its contribution from the target is smaller than the radiative muon decay, and only becomes important if the photon energy resolution becomes extremely good. However, it is dependent on the total amount of materials in an experimental setup.

From the above, the effective branching ratio of accidental background is given by

$$B_{acc} = R_\mu \cdot (2\delta x) \cdot \left[\frac{\alpha}{2\pi}(\delta y)^2(\ln(\delta y) + 7.33)\right] \times \left(\frac{\delta\theta^2}{4}\right) \cdot (2\delta t). \tag{3.7}$$

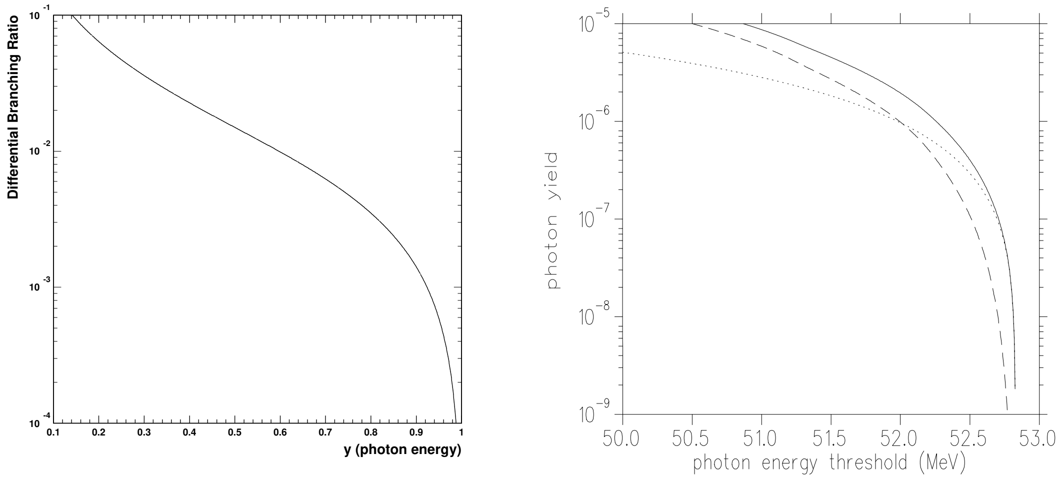

(a) (b)

Figure 3.4: (a) Energy spectrum of the photon coming from the muon radiative decay ($y \equiv 2E_\gamma/m_\mu$). (b) Integrated rates of background from annihilation-in-flight (dotted line) and radiative muon decay (dashed line) as a function of the photon energy. The solid line shows the sum of the two. Both Figures are from [34].

For instance, take some reference numbers such as the e^+ energy resolution of 1% (FWHM), the photon energy resolution of 6% (FWHM), $\Delta\Omega_{e\gamma} = 3 \times 10^{-4}$ steradian, $\Delta t_{e\gamma} = 1$ nsec, and $R_\mu = 3 \times 10^8$ μ^+/sec, $B_{\rm acc}$ is 3×10^{-13}. It is critical to make significant improvements in the detector resolution in order to reduce the accidental background.

3.4 Background rejection

The capability for an experiment to reject background events is related to its experimental resolutions on the photon and positron four momenta measurement.

The first experiments used spark chambers to detect the presence of both the positron and the photon [44, 55]; later on the configuration with two back-to-back large NaI crystals, as in Figure 3.5, became common [48, 49, 56, 57] allowing for a better energy and timing determination. This technique was pursued to an extreme by the Crystal Box experiment where an almost 4π segmented NaI calorimeter surrounded the target region [51].

The number of produced pions and muons increases with their energy, hence a larger particle flux requires a higher momentum for the particles, which in turn, imply a thick target to bring them to a stop. An extremely good positron energy resolution was therefore not necessary because the target thickness usually contributed heavily to the positron energy loss. In the experiment at SIN [49] the energy loss in the target alone introduced a 4 MeV uncertainty in the positron

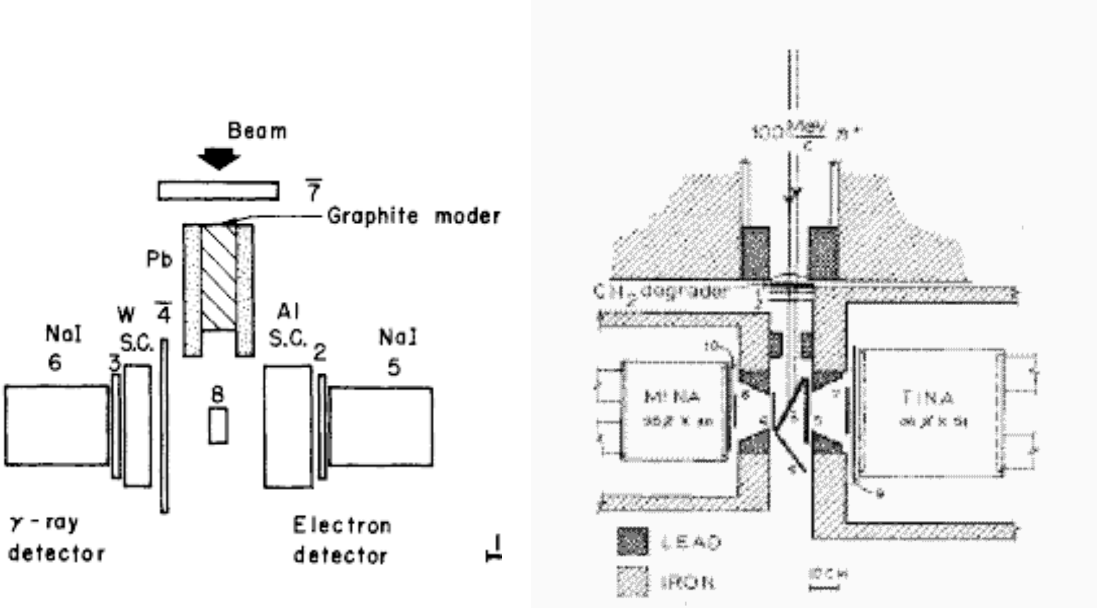

Figure 3.5: Experimental configuration of the early $\mu^+ \to e^+\gamma$ search experiment [56] and [48]

momentum.

The introduction of "surface" muon beams [58, 59], originating from pions decaying on the surface of a secondary target, brought low energy muon beams (p = 28 MeV) of high intensity, which could be stopped in thinner targets.

The use of a dipole spectrometer coupled to a hodoscope counter for the determination of positron momentum and timing was introduced in the $\mu^+ \to e^+\gamma$ search experiment at LAMPF [60]; in the MEGA experiment the photon was converted and measured with a pair spectrometer, and the positron with cylindrical tracking chambers in a solenoid magnetic field, hence the better energy resolutions shown in Table 3.1.

3.5 Future of LFV searches

With a high intensity muon beam the capability of recognizing two coincident monochromatic photon and positron becomes essential. A thin target is the necessary choice for the precise measurement of the positron momentum with a magnetic spectrometer, while fast scintillators are able to provide extremely good timing for the positron.

The photon momentum and direction are well determined by a pair spectrometer, as in MEGA, but a thin converter is needed not to degrade the photon energy, therefore a low conversion efficiency is attained.

The timing information provided by a NaI calorimeter is insufficient, because of its large decay time constant (470 ns). For this reason the design of a new $\mu^+ \to e^+\gamma$ search experiment cannot be disentangled from the design of a new kind of photon detector. For this reason the MEG experiment proposes to use a novel liquid Xe calorimeter, whose characteristics are comparable to NaI as far as luminosity and uniformity are concerned, but with far better timing capabilities.

In the following we will describe the MEG experiment with particular emphasis on the studies regarding the newly proposed liquid Xe scintillation calorimeter.

Part II

The MEG experiment

Chapter 4

The MEG experiment

4.1 Introduction

In this Chapter we will describe the MEG experiment. This experiment, proposed by an Italian-Japanese-Russian-Swiss collaboration, will operate on a low-energy muon beam line at the Paul Scherrer Institut (CH). Its aim is to reach a sensitivity on the $\mu^+ \to e^+\gamma$ decay of 5×10^{-14} [61].

The description needs a reference frame choice: the coordinate system is such that the z-axis lies along the incoming beam direction. The plane perpendicular to this direction is called the $r - \phi$ plane, and we will use rectangular (x, y, z), cylindrical (r, z, ϕ) or spherical (ρ, θ, ϕ) coordinates to refer to the detector, depending on the convenience of the choice. In any case the origin of the reference system is in the center of the target, placed in the center of the experiment $(x = y = z = 0)$. The detector is designed to cover approximately 10% of the solid angle, which, in our reference system, covers, for the photon acceptance, $-60 < \phi < 60$ and $0.08 < \cos\theta < 0.35$.

4.2 Concept of the MEG experiment

The sensitivity of an experiment searching for rare muon decays improves linearly with the number of observed muons, if the background is lower than the possible signal.

For a beam intensity of $R_\mu \sim 10^7 \div 10^8$ μ^+/sec and a typical observation period of one year (10^7 sec) at a 10% efficiency, it is possible to observe $\mathcal{O}(10^{13} \div 10^{14})$ μ^+ decays, being therefore sensitive to branching fractions of $\mathcal{O}(10^{-13} \div 10^{-14})$.

Two types of muon beam operation exist in present muon factories: a pulsed operation or a continuous one. In a pulsed beam the muons are grouped in bunches of definite time width separated by some delay in which (almost) no muon is present. The ratio of the bunch width to the total period is called *duty cycle* of the beam. In a continuous muon beam the muons are generated in order to have a duty cycle approximately one. For a given muon flux the peak rate is higher in a pulsed beam. In a $\mu^+ \to e^+\gamma$ search experiment the dominant background source, the accidental

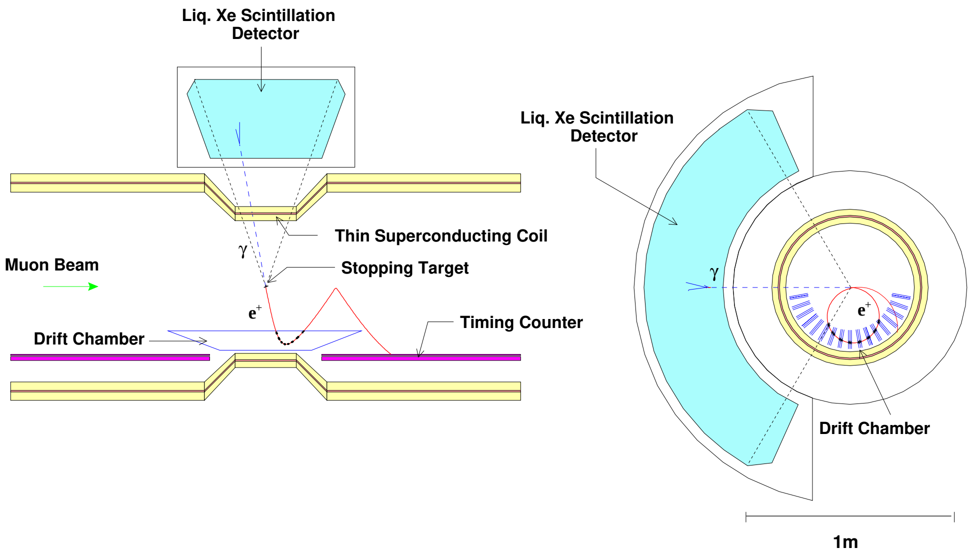

Figure 4.1: Schematic view of the MEG detector

coincidence of a high energy photon and a high energy positron from two different muon decays, increases quadratically with the *instantaneous* muon rate, because each daughter particle comes from a different muon. The $\mu^+ \to e^+\gamma$ signal and the physics (prompt) background, conversely, grow only linearly because the two daughter particles have the same parent. Hence a continuous muon beam is preferred with respect to a pulsed beam.

A $\mu^+ \to e^+\gamma$ search experiment beyond the present limit requires the highest intensity, continuous muon beam presently available in the world: the one at the Paul Scherrer Institute (PSI) in Villigen AG, Switzerland.

This high intensity, continuous beam of low energy muons will be stopped in a thin polyethylene target. The MEG apparatus, covering ten percent of the solid angle, is optimized for the detection of a coincidence of a back-to-back, high energy positron and photon pair: the positron momentum is measured by a set of drift chambers placed in a inhomogeneous magnetic field and its timing is given by a scintillating bar timing counter.

The photon energy and timing are measured by a ~ 0.8 m^3 liquid Xe scintillating calorimeter read by more than 800 photo-multiplier tubes (PMTs).

A schematic view of the detector is show in in Figure 4.1. We give in the following a detailed description of all sub-detectors.

4.3 Beam and target

Protons are accelerated by a ring cyclotron up to an energy of 590 MeV. The proton beam, whose current is approximately 1.8 mA, is transported to two meson production carbon targets

solid angle acceptance	150 msr
momentum range	$20 \div 120$ MeV/c
length	10.4 m
momentum band (FWHM)	10%
momentum resolution (FWHM)	2%
horizontal emittance	15.3 cm·rad
vertical emittance	3.6 cm·rad
spot size	4×4 cm^2

Table 4.1: Main properties of the $\pi E5$ beam line

in sequence, a thinner one called M-target and a thicker one called E-target, before being stopped in a high power beam dump or refocused on the target of a high-flux spallation neutron source (SINQ).

The two targets are rotating truncated cones made of isotropic graphite, of semi-aperture α, slanted at an angle α with respect to the beam axis in order to allow the incoming proton beam to uniformly hit the target surface, and the target surface to cool down by thermal radiation. The M-target is 7 mm thick while the E-target can be 40 mm or 60 mm thick, in the direction of the proton beam. Protons mainly produce charged pions which decay either in flight or in the target region, in turn generating muons and electrons of both charges. Seven beam lines branch out of the targets, and are named after the parent target (M, E). All secondary beam lines are available simultaneously.

The $\pi E5$ channel extracts low energy pion and muon beams from the thick (E) production target at an angle of 175° with respect to the primary proton beam. The main characteristics of the beam are listed in Table 4.1. The $\pi E5$ beam line can be tuned to collect the so-called "surface" muons, coming from pion decays [58, 59]. For pions decaying at rest in the target, daughter muons have only 4 MeV kinetic energy and 29 MeV momentum, and are therefore trapped in the proton target, unless for π^+ decays occurring on the target "skin". Surface muons are muons produced by pion decaying on the target surface and have quite well determined momentum and polarization.

In Figure 4.2 the measured fluxes of several particles are shown for the $\pi E5$ beam line at various momenta. The kinematic enhancement condition due to surface muons is clearly visible at a momentum ~ 29 MeV/c.

Muons of such a low energy can be stopped in a thin target therefore reducing to a minimum the multiple scattering of decay positrons in the target, which was one of the limiting features of early $\mu^+ \to e^+\gamma$ search experiments, as seen in the previous Chapter.

The $\pi E5$ beam line can be operated in two modes, called U-version and Z-version, depending on the sign of the current in the bending magnet AST (cfr. Figure 4.3 and 4.4).

The positron content of the beam at production is a factor of ten higher than the muon content, mostly because of the low energy positrons coming from the decays of the muons trapped in the E-target and from the conversion of photons from neutral pion decays.

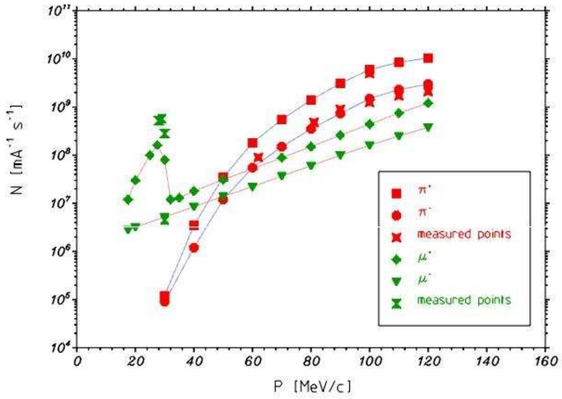

Figure 4.2: Particle fluxes for the $\pi E5$ beam line

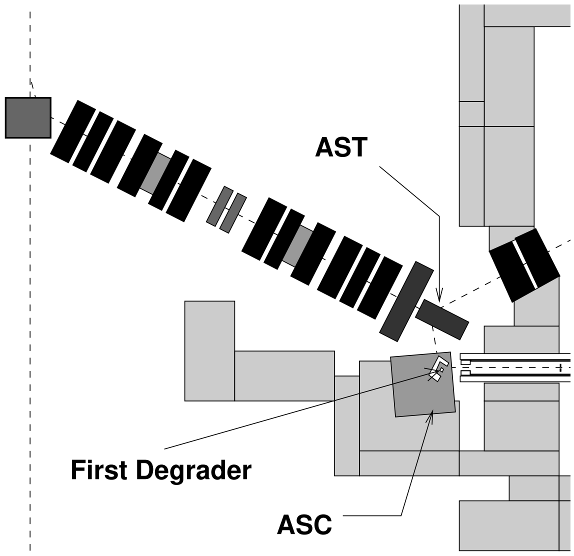

Figure 4.3: $\pi E5$ beam-line and experimental area, showing the two branches: U-branch, leading to the $\pi E52$ area and Z-branch, leading to the $\pi E51$ zone. The promary proton beam comes along the dashed line from the bottom of the figure, and the secondary particles produced backward in the target are transported along the beam line through quadrupoles and sextupoles.

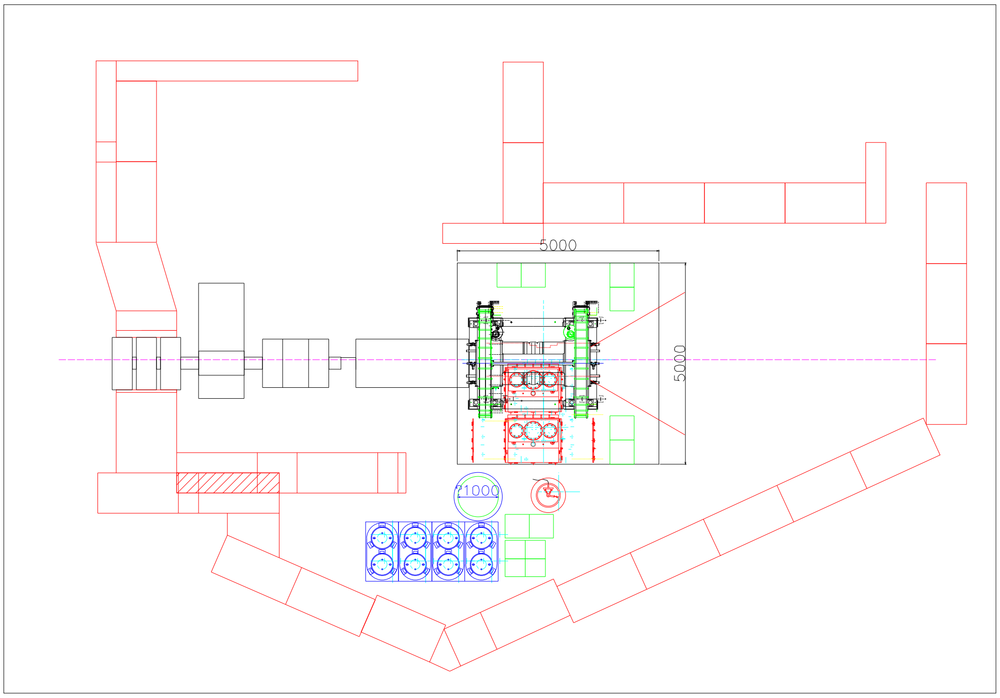

Figure 4.4: The layout of the MEG experimental area shows the muon beam coming from the left through a quadrupole triplet, a Wien filter and a second quadrupole triplet before entring the beam transport solenoid (BTS) which couples with the COBRA magnet, standing on a platform together with the calorimeter (visible with its three chimneys in the bottom part of the platform). The position of the xenon storage bottles in the lower part of the area is also shown.

The positron content must be reduced because positrons can either show up in the positron spectrometer, leading to a high rate in the chambers, or, stopping somewhere in the experimental hall, leading to a huge background of annihilation photons, which could degrade the calorimeter performance.

4.3.1 Beam line completion

The beam must be manipulated before reaching the thin MEG target in order to accomplish two features:

1. Reducing the positron content to a fraction of the muon flux;
2. Reducing the muon momentum in order to stop them in a 150 μm target.

Studies have been made with both configurations (U and Z) and with several degrader/particle selector devices. Each time the beam line properties have been studied both with a third order beam optic simulator (TRANSPORT [62]) and with a second order ray-tracing program (TURTLE [63]) before performing the experimental measurements on flux, contamination and beam spot size [64]

The studies converged towards the choice of the Z-version in which some elements are added between the end of the beam line and the MEG solenoid:

- A quadrupole triplet, partly placed in the wall separating the experimental area from the beam line is used to re-focus the beam after the ASC bending magnet;
- An electrostatic separator (Wien filter) with a 19 mm gap is used as a velocity selector, thus enabling a spatial separation of muons and electrons. The vertical separation at the output of the filter amounts to 11 σ, where σ is the combined rms of the muon and positron beam envelope;
- A second quadrupole triplet refocuses the muon beam after positron separation;
- A transport solenoid is used as a coupling element between the last quadrupole triplet and the MEG solenoid. A momentum degrader is placed in the solenoid intermediate focus, in order to reduce the μ^+ momentum.

In these conditions up to 1.2×10^8 μ^+/sec/mA can be focused in a ellipsoidal spot, whose axes measure $\sigma_x = 5.5$ mm and $\sigma_y = 6.5$ mm. In the presence of the drift chamber gas the multiple scattering degrades the spot to a $\sigma_x = 10$ mm, $\sigma_y = 10$ mm.

4.3.2 The target

The target will be placed at a slant angle of 22°, corresponding to a slant ratio of 1 : 2.5 in an atmosphere of gaseous He. Various materials were considered, namely polyethylene $(CH_2)_n$, Mylar $(C_5H_4O_2)_n$ and Kapton $(C_{22}H_{10}N_2O_5)_n$, both for their stopping power and their short radiation length.

Polyethylene was found to be the best material from both a background suppression and a beam quality point of view, mainly because of its larger radiation length [64].

Since the range of 29 MeV/c muons in polyethylene is about 1.1 mm, a 150 μm thick CH_2 target requires a $\sim$ 700 μm thick polyethylene degrader to be placed along the beam line, in the last solenoid intermediate focus (the target is slanted, therefore the average muon path in a 150 μm target is of the order of 400 μm). The energy loss for positrons in a 150 μm polyethylene target is about 30 keV.

De-polarization characteristics of these materials are being checked, as well as the suspension device. The use of calibrating targets as in MEGA and Crystal Box is being investigated.

4.4 The positron detector

Positron tracks are measured by drift chambers inside an inhomogeneous magnetic field. The positrons eventually hit the scintillating bars of a timing counter.

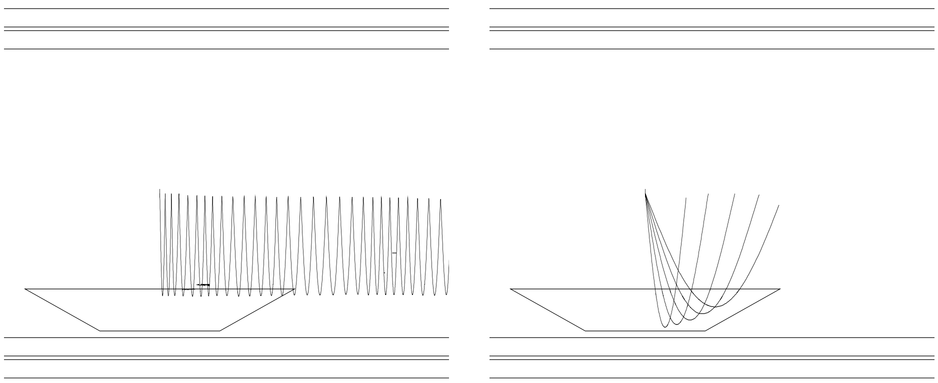

(a) (b)

Figure 4.5: Problems with a uniform solenoidal magnetic field:
(a) $r - z$ view of the solenoid shown with the trajectory of a particle emitted at 88° making many turns inside the detector.
(b) Trajectories of monochromatic particles emitted at various angles. The bending radius depends on the emission angle.

The inhomogeneous field has a maximum at the center, where its value is 1.28 T, and decreases towards the spectrometer edges. The purpose of having a non-homogeneous field is two-fold (see Figure 4.5 and 4.6):

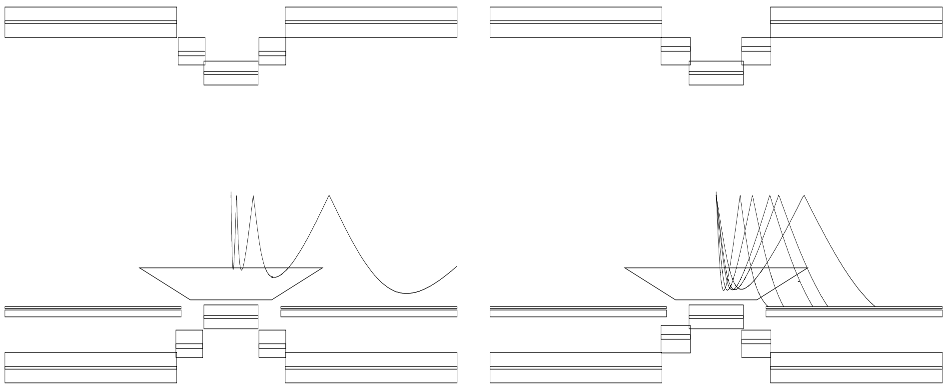

Figure 4.6: Advantages of a gradient magnetic field:
(a) $r - z$ view of the COBRA spectrometer shown with the trajectory of a particle emitted at 88°. The particle is swept away much more quickly than in Fig. 4.5(a).
(b) Trajectories of monochromatic particles emitted at various angles. The bending radius is independent of the emission angle.

1. In a conventional solenoid, positrons with high transverse momentum (p_t), emitted with a pitch angle close to 90° with respect to the solenoid axis, spiral inside the spectrometer and, making multiple turns, leave multiple hits on the drift chambers, therefore degrading the detector performance.

   Conversely, in a decreasing magnetic field, also high-p_t positrons are quickly swept away from the detector center, after one or two turns in the drift chamber zone.

2. In a conventional solenoid the radius of the positron trajectory on the transverse plane (projected radius) is determined by its p_t. In an inhomogeneous solenoid the field can be shaped so as to make the projected radius depend on the *absolute* value of the momentum, p, and not on its transverse part only, over a wide angular range. In this way low momentum tracks are confined inside a cylindrical shell and the reconstruction of higher momentum tracks is greatly simplified by this feature, since the spread in the projected radius for particles with the same momentum depends almost exclusively on the beam spot on the thin target.

Coil	Central	Gradient	Inner end	Outer end	Compensation
Conductivity	Super	Super	Super	Super	Resistive
Inner dia. (mm)	700	810	920	920	2210
Outer dia. (mm)	712.4	820.6	929.5	929.5	2590
Length (mm)	240.3	110.4	189.9	749.2	265
Layers	4	4	3	3	14
Winding	edge-wise	edge-wise (1st) flat-wise (2nd-4th)	flat-wise	flat-wise	double pancake
Inductance(H)	1.64	0.62	0.35	2.29	0.54
$I_{\rm op}$(A)	360	360	360	360	360
Energy E (kJ)	106	40	23	148	35
Weight M (kg)	9	4	7	28	1620
E/M (kJ/kg)	11.8	10.0	3.3	5.3	0.02

Table 4.2: Parameters of the COBRA magnet

4.4.1 The COBRA magnet

The inhomogeneous field is generated by a thin superconducting magnet called COBRA (COnstant Bending RAdius). This magnet was designed in order to be as transparent as possible to 52.8 MeV γ-rays directed towards the photon calorimeter.

The COBRA magnet is composed of five coils of three different radii: a central coil, two gradient coils and two end coils. The parameters of the super-conducting cable and of the three types of coils are summarized in Table 4.2. The cable consists of a Niobium-Titanium multi-filament wire embedded in a copper matrix, extruded in a rectangular, 1.2×0.9 mm^2, aluminum support cable. The varying current density in the coils is obtained by varying the winding pitch, the number of winding layers and the orientation of the super-conducting wire, as summarized in Table 4.2.

To reduce the stray field in the calorimeter zone to a level tolerable by the calorimeter photomultipliers, two resistive (*i.e.* non super-conducting) compensation coils are used. These are two large (120 cm radius) coils placed at both extremities of the COBRA magnet as shown in Figure 4.7. They reduce the field in the calorimeter zone to less than 50 Gauss.

The total equivalent thickness of the central part of the magnet is 3.83 g/cm^2 which corresponds to 0.197 radiation lengths. Therefore the conversion probability on the magnet for a 52.8 MeV photon is 18%. The COBRA magnet is already built and placed in the $\pi E5$ experimental area, and it is presently undergoing a series of tests aiming at mapping precisely its magnetic field.

4.4.2 The Drift Chambers

Positron tracks are measured with 17 trapezoidal drift chamber sectors aligned radially at 10° intervals in azimuthal angle (Figure 4.8). Each sector consists of two staggered arrays of drift cells, as shown in Figure 4.9. The sensitive area of the chamber extends from a radius of 19.3 cm to

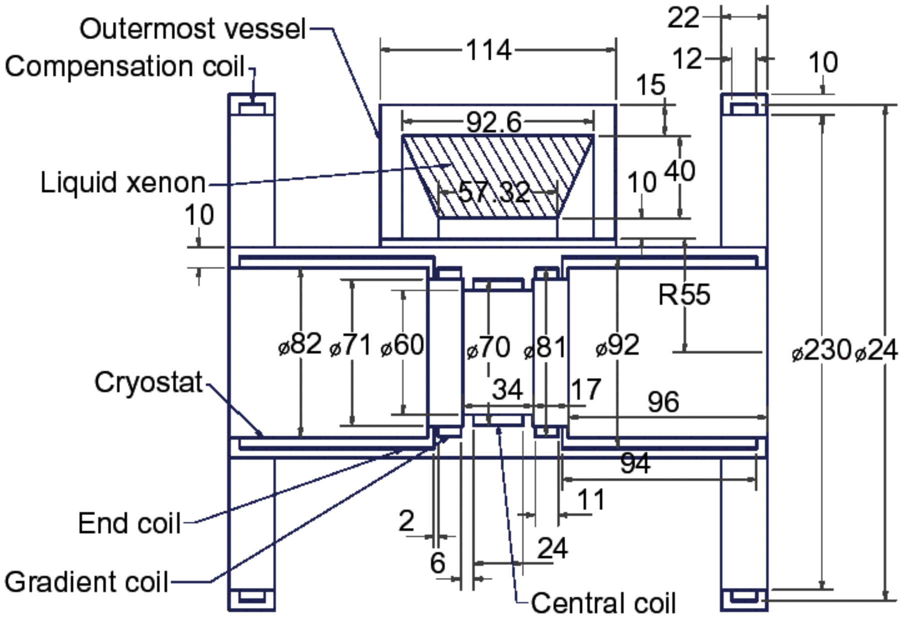

Figure 4.7: Layout of the COBRA magnet with the compensation coils.

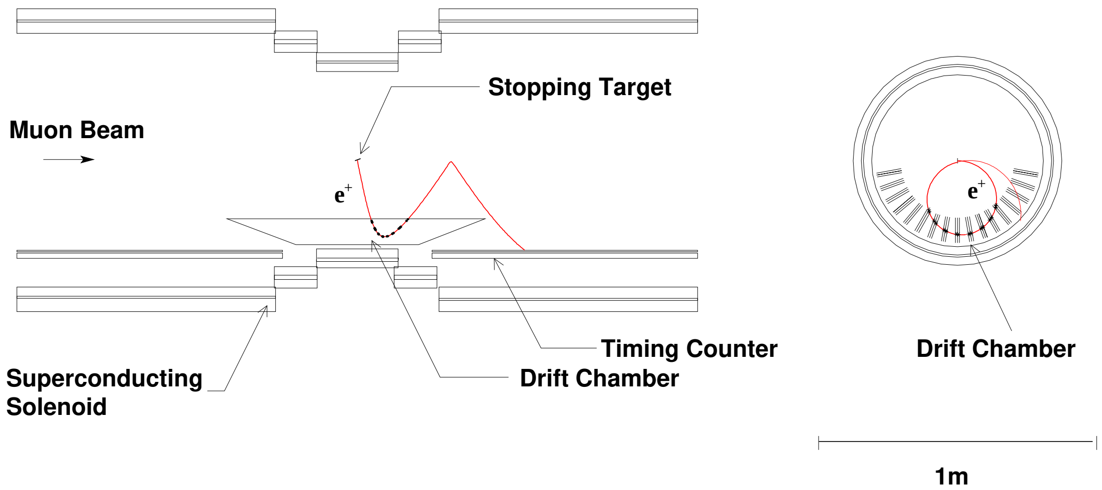

Figure 4.8: Schematic view of the positron spectrometer

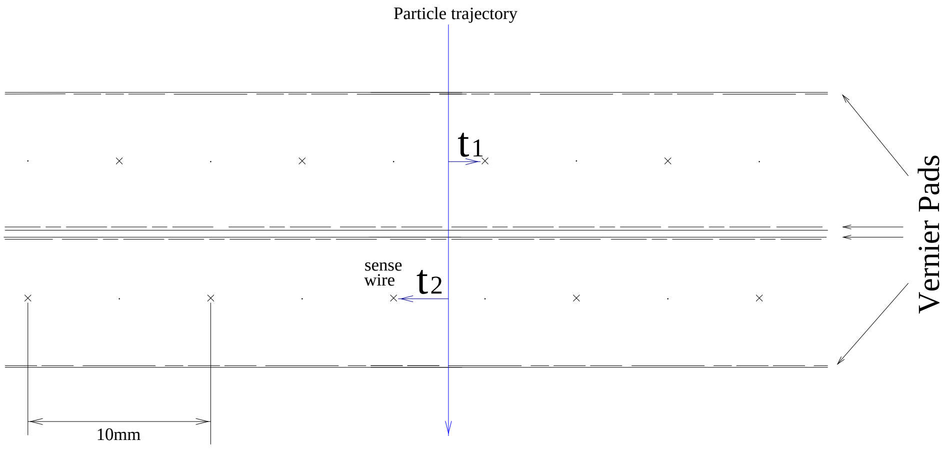

Figure 4.9: Cross sectional view of a part of a chamber sector. It consists of two layers of drift cells staggered by a half-cell.

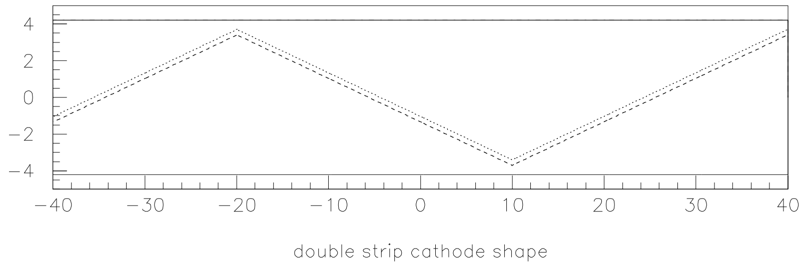

Figure 4.10: Shape of the aluminum coating of the cathode foils (Vernier pads)

27.0 cm. In the z-direction the active region extends up to $z = \pm 50$ cm at the innermost radius and $z = \pm 21.9$ cm at the outermost. The chamber walls are made of thin plastic foils. A thin aluminum deposit is shaped on the four cathode foils in order to make a so-called "Vernier pad" (Figure 4.10) A comparison between the induced charges on different pads considerably improves the resolution in the longitudinal direction.

The staggered-cell configuration allows for the measurement of the radial coordinate and the absolute time of the track simultaneously. The difference between the drift times $(t_1 - t_2)$ in two adjacent cells gives the r-coordinate of the track with a $\sim 150\ \mu$m accuracy, while the mean time $(t_1 + t_2)/2$ gives the absolute time of the track with ~ 5 ns accuracy. This excellent timing resolution is important for the pattern recognition.

The ratio of the charges observed at both ends of a sense wire gives the z-coordinate with a ~ 1 cm accuracy. The ratio of the charges on the Vernier pads allows to refine the z-coordinate determination with an accuracy of about 300 μm [65].

The chambers are filled with a 50% Helium, 50% Ethane mixture, chosen to have sufficient ionization loss in the gas and to minimize the multiple scattering. In fact as long as the position

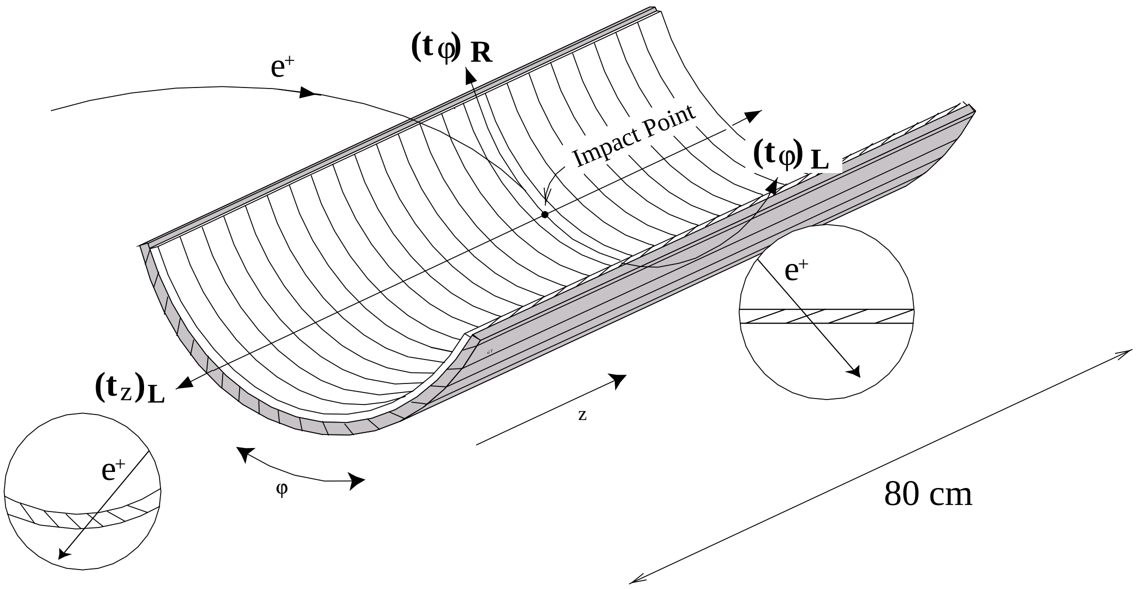

Figure 4.11: The timing counter configuration

resolutions are at the 300 μm level, momentum and angular resolutions are primarily limited by multiple scattering. Several drift chamber prototypes are being tested at PSI.

Expected resolutions

The expected resolutions of the spectrometer have been studied with GEANT simulations by incorporating detailed material distribution. 52.8 MeV positrons were generated and their trajectories reconstructed using several methods. The fractional momentum resolution turns out to be $\Delta E/E = 0.9\%$ FWHM and the angular one 12 mrad. The positron origin on the target can be reconstructed with a 2.5 mm resolution.

4.4.3 The Timing Counter

The timing counter detector is designed to provide the timing of the positrons with a 100 ps resolution FWHM, at the end of their path through the drift chambers. It also provides a fast determination of the positron direction for triggering purposes.

Hodoscope arrays are placed at both sides of the drift chambers at a radius of 29.5 cm, covering an azimuthal angle of 145° and their position along the beam is 25 cm $< |z| <$ 95 cm. The $\mu^+ \to e^+\gamma$ positrons emitted in the angular range $0.08 < \cos\theta < 0.35$ impinge on the timing counter after completing about 1.5 turns in the $r - \phi$ plane.

Figure 4.11 shows the configuration of one of the two timing counters (placed symmetrically with respect to the $z = 0$ plane) which consists of two layers of plastic scintillator bars orthogonally placed along the z and ϕ directions. The bars of the outer layer are 5 cm wide and 2 cm thick, are approximately 90 cm long and are read at both sides by photo-multiplier tubes which measure the pulse heights as well as the arrival time of the scintillation light. The inner (curved) layer is made of 5×5 mm^2 scintillating fibers read by avalanche photo-diodes (APDs) and it is mainly used for trigger purposes, while the outer (longitudinal) layer provides the positron timing.

Photo-multipliers have a limited life-time in He atmosphere. For this reason the area surrounding the timing counters will be separated from the drift chamber region by metal-coated plastic bags. Nitrogen will flow inside the plastic films embedding the timing counter.

Tests performed with cosmic ray muons (at Pisa) and electron beams (at PSI and Frascati) demonstrated a timing resolution of 100 ps FWHM [66, 67, 68]

4.5 The photon detector

The photon detector in undoubtfully the most challenging and innovative part of the experiment. Its characteristics will be thoroughly examined in the following Chapters. We give here a quick look at this device.

The precise measurement of the photon four-momentum is the key role of the MEG experiment photon detector, which is a ~ 0.8 m^3, C-shaped homogeneous scintillating liquid Xe calorimeter. Xe is a rare gas which is liquid at a comparatively high temperature (165 K), has a high atomic number, $Z = 54$, hence small radiation length $X_0 = 2.7$ cm, and its light yield is comparable to that of sodium iodide, but with a significantly lower emission time, of the order of tens of nanoseconds. Its scintillation peak is at 178 nm, in the vacuum ultra violet (VUV). Details on the scintillation mechanism and on liquid Xe physical properties will be treated in details in Chapter 5.

The MEG calorimeter cryostat is placed just outside the COBRA magnet (Figure 4.7). It has a C-shape in order to minimize its volume and to have the photon impinging as perpendicularly as possible on its front face (see Figure 4.12). Its volume is read by more than 800 VUV-sensitive PMTs.

The photon parameters to be measured are its energy, direction and timing. The energy is provided by the scintillation light collected by all PMTs. The photon is supposed to come from the same vertex of a companion positron on the target, and its direction is determined by looking at the interaction point on the calorimeter, extracted from the light distribution on the calorimeter front face. The light arrival time on all PMTs is used to extract the photon timing.

Since the calorimeter has a big homogeneous volume we expect a high rate of low energy photons: it is therefore necessary to collect the waveform of every PMT to reject events in which pile-up between different γ-rays occur.

This detector is the most technologically advanced of the experiment, and its performance is crucial for the successful search for the $\mu^+ \to e^+\gamma$ decay. The characteristics of 52.8 MeV electro-magnetic showers are different from those at high energy, namely they are subject to larger fluctuations. In this condition the optical properties of liquid Xe enter the determination of the calorimeter response. In particular the liquid Xe transparency to scintillation light could strongly

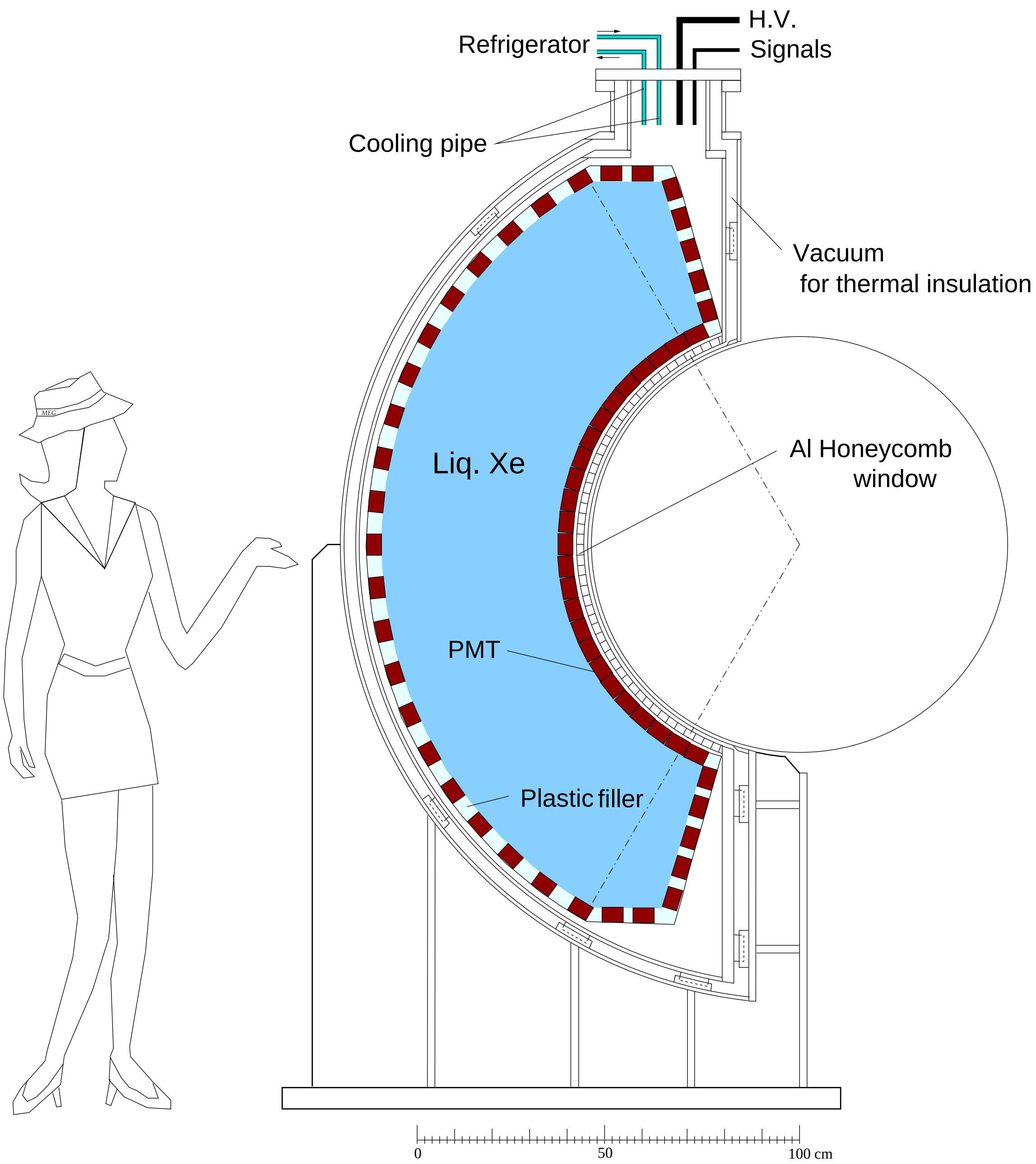

Figure 4.12: Schematic view of the liquid Xe photon detector

affect its energy resolution.

For these reasons detailed Monte Carlo simulation of the liquid Xe detector have been performed, and are presented in Chapter 6. A 0.1 m^2 prototype, called "large prototype" (presently the largest liquid Xe calorimeter in the world) has been built and tested, to demonstrate the performances of the full-scale detector.

This thesis predominantly deals with the characterization of such prototype, describing all the expertise which has been gained during almost four years of operation, demonstrating the feasibility of the final detector.

4.6 Trigger and DAQ

The signature of a $\mu^+ \to e^+\gamma$ decay is a back-to-back photon-positron pair coincident in time, each carrying half of the muon mass of energy. The experiment trigger therefore requires the presence of two high-energy particles with opposite momenta.

4.6.1 Trigger algorithm

The information available at trigger level comes from the liquid Xe detector and from the timing counter. The information from the drift chambers is too slow due to the electron drift time in the cells. Trigger rates have been estimated taking into account the main sources of background.

All the trigger system is based on VME boards equipped with Field Programmable Gate Arrays (FPGAs), which digitize the output of both the photon detector and the timing counter photomultipliers and perform basic event reconstruction. The trigger boards perform PMT equalization and a 100 MHz waveform digitization, necessary in particular for the signal from the calorimeter in order to perform an on-line subtraction of the pedestal and rejection of the common noise.

The photon energy is determined by the sum of the light collected by all PMTs, while its direction is determined by the position of the PMT with the largest signal. The photon conversion time is extracted from the rising edge of this PMT wave-form. The estimated trigger rate for photons with energy larger than 45 MeV is $R_\gamma \approx 2$ kHz for a muon stopping rate of $R_\mu = 10^8\ \mu^+/\text{sec}$.

The presence of a time-coincident positron is provided by the timing counter: its radial position already excludes most of low momentum positrons. The overall rate on each of the two timing counters due to Michel positrons is estimated to be $R_{TC} = 2 \times 10^6$ Hz for a muon stopping rate of $R_\mu = 10^8\ \mu^+/\text{sec}$ (4% of the Michel positrons hit either timing counter). The azimuthal segmentation of the timing counter allows for a correlation of the positron direction with that of the photon, with a rejection factor of $f_\phi \simeq 5$.

If we define a coincidence window of $\Delta T = 10$ ns the trigger rate for the uncorrelated background is

$$R_{\text{trig}} = 2\Delta T\, R_\gamma\, \frac{R_{TC}}{f_\phi} \left(\frac{R_\mu}{10^8}\right)^2 \simeq 20 \text{ Hz} \left(\frac{R_\mu}{10^8}\right)^2 \tag{4.1}$$

The estimated trigger rate is quite low compared to the present-day DAQ and storage capabilities. This gives some margin in case of possible contributions not taken into account (e.g. photons coming from the experiment shielding) and/or of inclusion of calibration trigger during the normal runs.

4.6.2 Front-end electronics and DAQ

The signals from all PMTs and from the drift chambers will be individually digitized by a custom chip, called Domino Sampling Chip (DSC). A "domino" wave runs circularly along a loop of 1024 capacitors which are sequentially cleared and opened to sample the incoming signal. When a trigger occurs, the domino wave is stopped and the charges collected on all capacitors are sequentially read out and digitized. This digitization method constitutes a sort of analog pipeline which minimizes the use of delay cables.

The PMT signals will be digitized at 2 GHz (500 ps bin width) in order to be able to obtain a timing resolution of 50 ps by bin interpolation.

Wave-form digitizing on all channels gives an excellent handle on event pile-up and noise suppression, although the amount of data is large ($\sim$ 1.8 Mb per event). Studies are under way to reduce or compress the raw data.

4.7 Conclusion

The concept and layout of the MEG experiment has been described. Presently all detector subdevices are under engineering design or construction. The rest of this thesis will present the R&D work on the photon detector prototype, and statements on its energy, timing and position resolution will be made. Those will be used in Chapter 12, together with the resolutions of the other sub-detectors, to evaluate the MEG experiment sensitivity to the $\mu^+ \to e^+\gamma$ decay.

Chapter 5

Liquid xenon as a scintillation medium

Liquid rare gases have been considered as optimum radiation detectors since the discovery of their scintillating properties. A fast decay component and a high photon yield, comparable to that of NaI(Tl), are among their appealing characteristics, though the scintillation light wavelength is in the vacuum ultraviolet (VUV): 128 nm for liquid Ar, 147 nm for liquid Kr and 178 nm for liquid Xe. The high atomic number of Xe (*i.e.* short radiation length) together with a comparatively high boiling temperature (see Table 5.1) and freedom from radioactive isotopes makes it the optimum choice for homogeneous calorimetry.

In the following we will describe the characteristics of noble liquid detectors, focusing on homogeneous scintillating Xe calorimeters. We will describe Xe properties and scintillation mechanisms, and we will state requirements on its purity for building a large volume detector.

5.1 Homogeneous scintillation calorimeters

Homogeneous liquid rare gas detectors can be divided in two groups [69]: (1) liquid Ar or liquid Xe time projection chambers (TPC) and (2) homogeneous rare liquid calorimeters. The homogeneous calorimeters in category (2) may be operated in ($2a$) ionization mode and ($2b$) scintillation mode. The idea of category (1) was originally proposed by Rubbia for liquid Ar detectors [70] and is now successfully applied in liquid Ar and Xe detectors, and homogeneous calorimeters operating in ionization mode have already been developed and applied to some elementary particle physics experiments. A homogeneous non-segmented liquid Xe calorimeter operated in scintillation mode was first proposed by Doke *et al.* [69] to be applied to the MEG experiment.

Recently there have been proposals for hybrid ionization-scintillation liquid noble gas detectors [71] in which a better energy resolution is expected due to the reduction of energy loss fluctuations, since both light and ionization are used.

	Ar	Kr	Xe
ρ (g/cm^3)	1.39	2.45	2.98
Z	18	36	54
λ_{peak}	128 nm	147 nm	178 nm
boiling $T(K)$	87.3	119.9	167.1
dE/ dx (m.i.p.) (MeV/cm)	2.11	3.45	3.89
X_0 (cm)	14.3	4.76	2.77
Molière radius (cm)	7.3	4.7	4.1
τ_1 (ns)	6	2	4
τ_3 (ns)	1000	91	22
τ_{r} (ns)	–	–	45

Table 5.1: Main characteristics of Ar, Kr and Xe. τ_1, τ_3 and τ_r are the singlet, triplet and recombination de-excitation time constants (see the text for details).

The characteristics of Ar, Kr and Xe are presented in Table 5.1. Liquid Xe is the most interesting, having the largest wavelength, the fastest response and the shortest radiation length. For this reason we will use it to discuss in detail the scintillation mechanism, yet most of the consideration apply to Ar and Kr as well.

5.2 Liquid xenon properties

Liquid Xe is an optimal choice for homogeneous scintillating detectors because its short radiation length (2.77 cm) allows small self-shielding detectors. All noble gases have boiling points well below the STP, therefore suitable cryogenic and vacuum facilities are necessary for their handling. The comparative high boiling point of Xe makes easier to deal with cryogenics for this particular gas, whose phase diagram is shown in Figure 5.1.

On the other hand Xe is the least abundant among the three considered rare gases: presently it is produced together with Kr as a by-product in giant air separation stations at metallurgical factories mainly in Russia and Ukraine [72]. Using commonly accepted techniques most of these stations produce a KrXe mixture containing approximately 93% Kr and 7% Xe. The rare gases are separated at special separation factories. The annual production of Xe in the former USSR amounts to approximately 3000 m^3 of (gaseous) Xe, *i.e.* 5 m^3 of liquid Xe per year. Usual purities of Xe are, among the others, O_2 <5 ppm and H_2O <5 ppm, and we will see in the following sections that Xe purity level reflects heavily on the performance of a Xe-based detector.

Measurements of Xe emission yield gave, in the past, contradictory results. It will be apparent that Xe purity for various experiments is likely to be the cause of such differences. In the experimental part we will present measurements of gaseous and liquid Xe light yield.

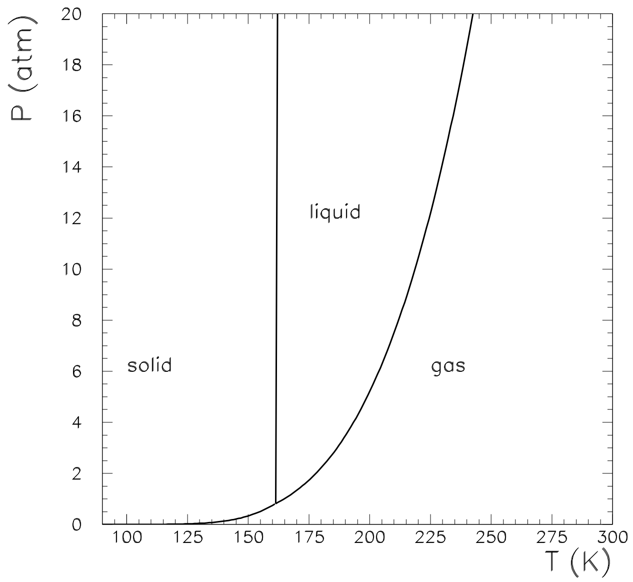

Figure 5.1: Phase diagram of xenon.

5.2.1 Emission mechanism

The luminescence emitted by rare gases excited by vacuum ultraviolet radiation or particles has been rather well studied for gas, condensed and solid phases [69, 73, 74, 75, 76, 77]. A remarkable feature is the close similarity between the emission of gaseous and condensed noble gases. Such a behavior is basically due to the fact that in both cases the last relaxation step before the radiative decay is the formation of an "excimer-like" state. An *excimer* is a bound state or molecule which exists only in excited electronic state, the fundamental level being a repulsive ground state (see Figure 5.2 for a schematic representation of the phenomenon). It is also well known that the decay occurs from the two different ${}^1\Sigma_u^+$ and ${}^3\Sigma_u^+$ to the ${}^1\Sigma_g^+$ repulsive ground state giving rise to the "fast" and the "slow" components of the excimer emission, whose spectra practically coincide in width and wavelength [77].

The scintillation mechanism, which involves excited atoms Xe^* and Xe^+ produced by ionizing radiation, can be summarized as follows:

$$\mathrm{Xe}^* + \mathrm{Xe} \rightarrow \mathrm{Xe}_2^* \rightarrow 2\mathrm{Xe} + h\nu \tag{5.1}$$

or

$$\begin{array}{llll} \mathrm{Xe}^+ + \mathrm{Xe} \rightarrow & \mathrm{Xe}_2^+, & & \\ & \mathrm{Xe}_2^+ + e \rightarrow \quad \mathrm{Xe} + & \mathrm{Xe}^{**}, & \\ & & \mathrm{Xe}^{**} \rightarrow & \mathrm{Xe}^* + \text{heat} \\ & & & \mathrm{Xe}^* + \mathrm{Xe} \rightarrow \mathrm{Xe}_2^* \rightarrow 2\mathrm{Xe} + h\nu, \end{array} \tag{5.2}$$

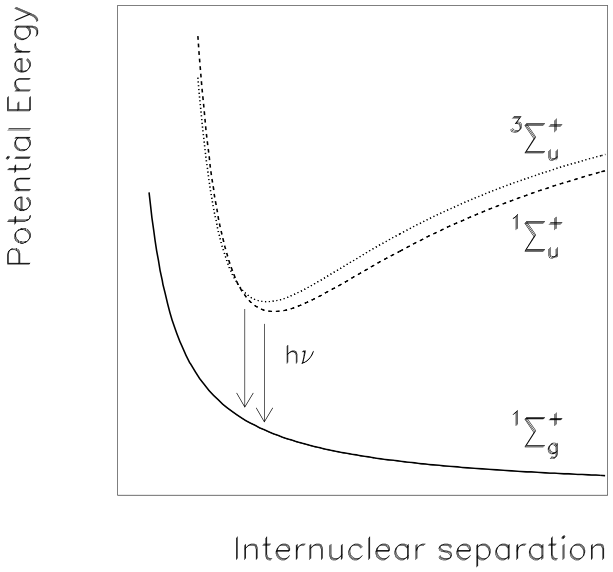

Figure 5.2: Schematic representation of photo-emission by a Xe_2^* excimer to the unbound ground state of the diatomic molecule.

where $h\nu$ is the ultraviolet photon (see table 5.2).

Two things are worth noticing:

1. The emission of the scintillation photon is due either to excitation or to ionization of Xe atoms, and the two processes exhibit a different time behavior, as discussed later;

2. Due to the lack of a bound Xe_2 ground state, the inverse transition $h\nu$+ $Xe_2 \rightarrow Xe_2^*$ is absent. This peculiarity of the excimeric emission is a strong hint for the transparency of noble liquids to self-scintillation light. However a short attenuation length of scintillation light in liquid xenon has been reported by several authors. Photo-attenuation arises in principle from both photo-absorption and coherent scattering. There exists strong evidence that at least in the gaseous phase, in the frequency range around that of scintillation, the attenuation is dominated by Rayleigh scattering [79].

5.2.2 Emission yield and decay timing constants

As apparent from the decay schemes (5.1) and (5.2), two different mechanisms contribute to convert energy loss to scintillation light in liquid and gaseous Xe, with different time characteristics. A fast component with two short time constants (τ_1 = 4.2 ns, τ_3 = 22 ns) comes from the de-excitation of singlet and triplet states of excited dimers ($Xe_2^* \rightarrow$ 2 Xe $+h\nu$). This mechanism is excited

Phase	Peak value (nm)	FWHM (nm)	Ref.
liquid (175 K)	176.1	12.0	[74]
dense gas ($\rho = 1.13 \times 10^{22}$ cm^{-3})	174.6	10.8	[75]
liquid (160 K)	178.1	13.0	[76]
gas (300 K)	175.1	16.1	[76]
liquid	176.3	7.3	[77] in turn from [78]

Table 5.2: A compilation of the experimental results on xenon scintillation spectra. For all the references the peak is Gaussian in shape.

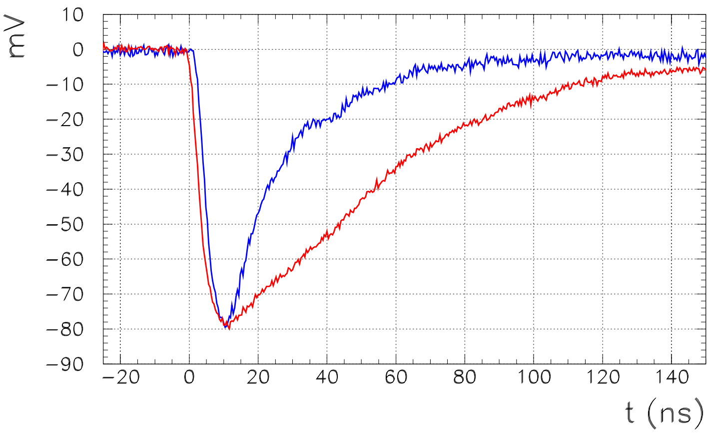

Figure 5.3: Pulse shape of a signal in liquid Xe induced by α-particles (narrow spectrum) or cosmic ray muons (wide spectrum)

mainly by α sources and fission fragments. Scintillation from relativistic electrons gives on the other hand a (comparatively) slow component (τ_r = 45 ns) which is presumably due to the slow recombination between electrons and ions, since this component disappears if some electric field is applied. An example of pulse shapes registered with a UV-sensitive photo-multiplier is shown in Figure 5.3 where a clear distinction between the time profile of the α-source and cosmic ray muon pulse is apparent. This feature could prove its usefulness in pulse-shape discrimination for particle recognition.

The light emission yield for noble gas liquids is usually given in terms of $W_{\rm ph}$, defined as the average energy needed to produce a scintillation photon. This is related to $W_{\rm i}$, the average energy to create an electron-ion pair, and to $N_{\rm i}$ and $N_{\rm ex}$, the number of ionized and excited Xe atoms produced for a deposited energy E_0, by simple relations [69]. The total number of emitted

	$W_{\mathrm{ph}}(eV)$
relativistic e/γ	23.7 ± 2.4
α-particle	19.6 ± 2.0

Table 5.3: Average energy needed to produce a scintillation photon in liquid Xe for different particles (adapted from [69])

scintillation photons comes from either ionized or excited Xe atoms:

$$N_{\mathrm{ph}} = N_{\mathrm{i}} + N_{\mathrm{ex}} \tag{5.3}$$

hence the average energy release is

$$W_{\mathrm{ph}} = \frac{E_0}{N_{\mathrm{ph}}} = \frac{E_0}{N_{\mathrm{i}}} \frac{1}{(1 + N_{\mathrm{ex}}/N_{\mathrm{i}})} = W_{\mathrm{i}} \frac{1}{(1 + N_{\mathrm{ex}}/N_{\mathrm{i}})} \tag{5.4}$$

where we single out the energy to produce an ion-electron pair $W_i = 15.10$ eV.

From Equation (5.4), which can be amended including quenching effects and subtracting the contribution of escaping "late" electrons, it is apparent that different ionizing particles could in principle have different $N_{\mathrm{ex}}/N_{\mathrm{i}}$ yield due to their different ionization density, hence having different W_{ph}. Several values of W_{ph} for electrons, photons and α-particles are reported in literature, and are summarized in Table 5.3.

5.2.3 Xe optical properties

In ideal homogeneous fluids light suffers neither absorption nor scattering: in fact all the waves propagating in a direction different from that of the incoming wave vector are canceled by an equal and opposite contribution coming from somewhere inside the liquid [80]. In pure real fluids, on the other hand, the Rayleigh scattering is determined by density fluctuations through the change in the dielectric constant, which prevent the perfect cancellation of the contributions coming from different parts of the volume. The inverse of the scattering length can be written as [80, 81]

$$h = \frac{8\pi^3}{3\lambda^4} \left[kT \varrho^2 \kappa_T \left(\frac{\partial \epsilon}{\partial \varrho} \right)_T^2 + \frac{kT^2}{\varrho c_v} \left(\frac{\partial \epsilon}{\partial T} \right)_\varrho^2 \right] \tag{5.5}$$

where λ is the wavelength of the scattered photon, k s the Boltzmann's constant, T the temperature, ϱ the liquid density, κ_T is the isothermal compressibility (proportional to the inverse square of the sound speed in the liquid), c_v is the heat capacity at constant volume and ϵ is the (real part of the) dielectric constant. The second term in eq. (5.5) can be neglected [81] and the derivative of the dielectric constant with respect to the density can be re-expressed via the Clausius-Mossotti equation

$$\frac{\epsilon - 1}{\epsilon + 2} = \frac{4\pi}{3} \frac{N_a \alpha_0}{M} \varrho = A_\varrho(\lambda, T) \varrho \tag{5.6}$$

where the last step is made using the virial expansion where terms in ϱ of order higher than one are embedded in A_ϱ. Using data from literature one finds that equation 5.6 is rather well obeyed with $A_\varrho(\lambda, T)$ independent of the density, and values for $\lambda_{\rm Ray}$ and for the liquid Xe refractive index at 178 nm can be obtained: $\lambda_{\rm Ray} \sim 45$ cm and $n \sim 1.65$. It is remarkable that these values are linked by the relation [82]:

$$\frac{1}{\lambda_R} = \frac{\omega^4}{6\pi c^4}\left\{kT\kappa_T \frac{[n^2(\omega)-1]^2[n^2(\omega)+2]^2}{9}\right\}. \tag{5.7}$$

For non-pure fluids there exist an additional contribution to the scattering length due to fluctuations in the concentrations of the impurities. For sufficiently diluted impurities this contribution can be written as [80, 81, 84]:

$$h_{\rm Imp.} = \frac{8\pi^3}{3\lambda^4}\left[\frac{xM}{N_a}\left(\frac{\partial\epsilon}{\partial x}\right)^2\right] \tag{5.8}$$

where x is the solute concentration, M its molecular weight and N_a is Avogadro's number. Using the approximation $\epsilon \approx x\epsilon_{\rm Imp.} + (1-x)\epsilon_{\rm Xe}$, equation (5.8) gets rewritten as:

$$\frac{8\pi^3}{3\lambda^4}\frac{xM}{N_a}\left(\epsilon_{\rm Xe} - \epsilon_{\rm Imp.}\right)^2. \tag{5.9}$$

As far as the impurities level is low and the difference in dielectric constants is of order unity the contribution due to (5.9) remains negligible, *i.e.* of the order of

$$h_{\rm Imp.} \sim 10^{-8}\left(\frac{x}{1\ \rm ppm}\right)\ \rm cm^{-1} \tag{5.10}$$

5.2.4 Absorption

Due to the scintillation mechanism in xenon the self-absorption should be small. Light attenuation is due to (Rayleigh) scattering and absorption processes. The photo-absorption is dominated by impurities in the liquefied gas. Two important absorbers are water vapor and molecular oxygen both of which exhibit important absorption lines in the range of interest (VUV).

As far as the O_2 is concerned in the 120-200 nm range the absorption spectrum is composed by what is commonly referred to as the Schuman-Runge continuum and the Schuman-Runge bands which occur because of photo-dissociation of the O_2 molecule [85, 86, 87].

The H_2O absorption cross section (Figure 5.4*b*) is dominated by the photo-dissociation of the water molecule

$$H_2O + h\nu \rightarrow H_2 + O^* \tag{5.11}$$

which has a threshold of ≈ 176 nm. The absorption spectrum of water vapor and liquid water is slightly different because water has a polar molecule, hence the spectrum is distorted at high density [88, 89, 90]. Since we are considering very small concentrations of water in the non-polar liquid Xe, we believe that the correct choice is to use the water vapor absorption spectrum.

We plot in Figures 5.4 the attenuation coefficient $\mu = 1/N\sigma$ of a 1 ppm in weight of oxygen and water in liquid xenon, as a function of the wavelength with the Xe scintillation spectrum

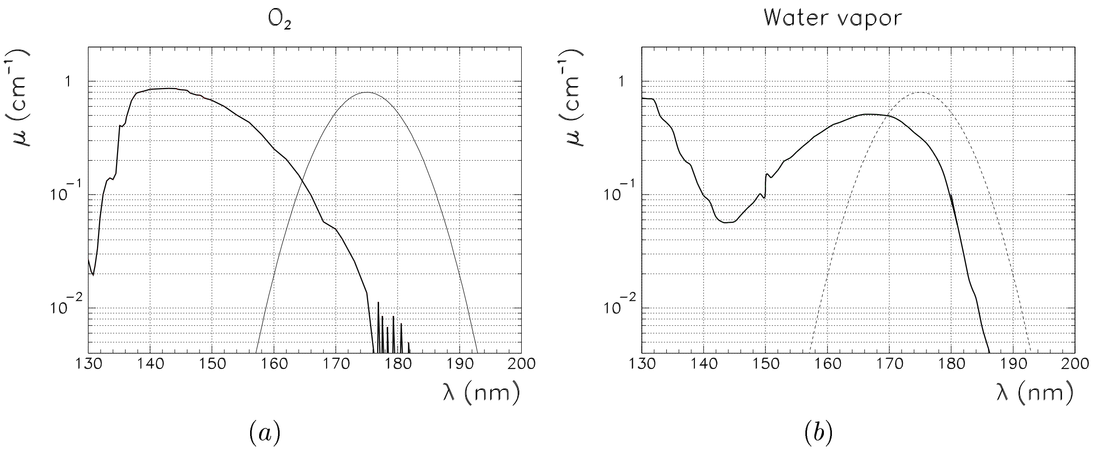

Figure 5.4: Oxygen (a) and water (b) attenuation coefficient with superimposed the Xe scintillation spectrum (at an arbitrary scale).

superimposed. The effect is dramatic, especially for water. It is readily seen that a purity much better than 1 ppm is needed and some 10 ppb should suffice.

We computed the effect of absorption by water and oxygen in LXe for different concentrations of impurities. In a regime in which the light attenuation is absorption-dominated and not diffusion-dominated ($\lambda_{\rm abs} < \lambda_{\rm R}$) the intensity $I(x)$ of the light collected by a PMT at a distance x from a source is given by

$$I(x) = I_0 \int_0^{+\infty} S(\lambda) Q_e(\lambda) T(\lambda) e^{-x\sigma(\lambda)N} \mathrm{d}\lambda \tag{5.12}$$

where $S(\lambda)$ is the normalized Xe scintillation spectrum, $Q_e(\lambda)$ is the PMT quantum efficiency, $T(\lambda)$ is the PMT quartz window transmittance, N is the number of contaminant molecules per cm^3, and $\sigma(\lambda)$ is the contaminant absorption cross section.

In Figure (5.5) the computation results are shown for both contaminants at a concentration (in mass) of $10, 5, 1$ ppm, 200 and 100 ppb. We will see in Chapter 7 that the attenuation of scintillation light in Xe is dominated by water absorption.

The non-exponential shape is due to selective absorption of shorter wave-lengths (for which the absorption cross section is larger) hence the surviving component of the scintillation light is slightly red-shifted. This fact could explain the discrepancies among Xe refractive index measurements, since n rapidly varies as a function of frequency in the region close to the Xe absorption resonance at 147 nm. The red-shift is the main effect, but the presence of contaminants might also correspond to a different $n(\omega)$ behavior for the LXe–contaminant compound.

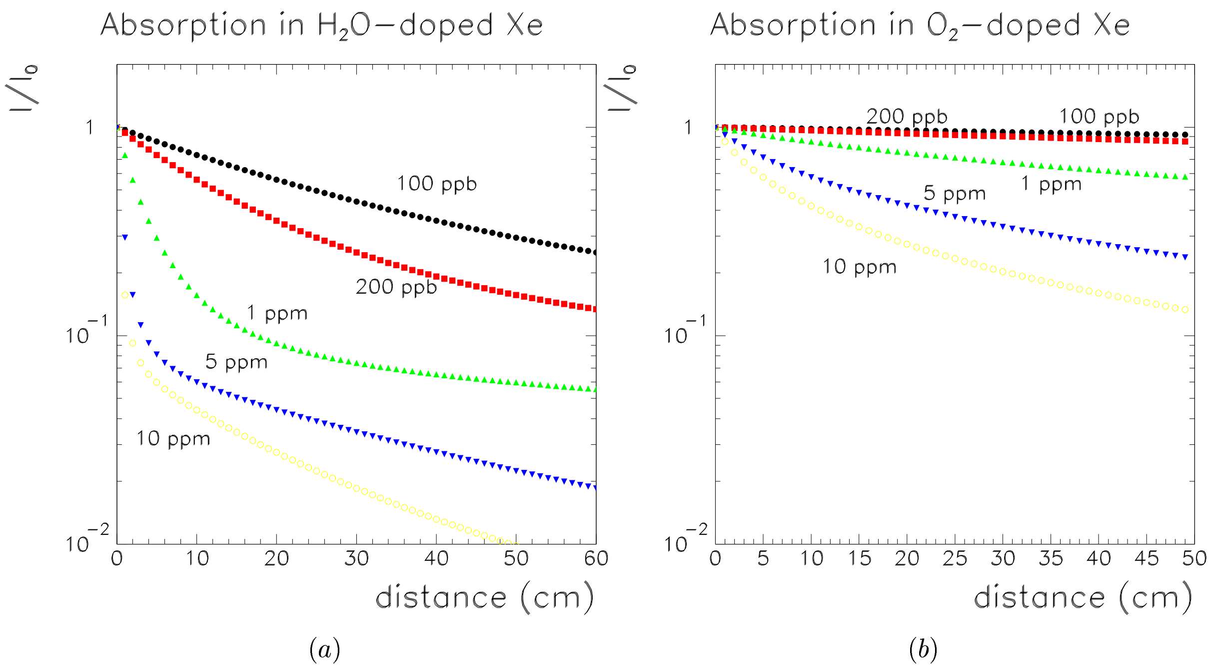

Figure 5.5: Calculated intensity of the transmitted light through liquid xenon doped with different concentrations of water (a) and oxygen (b).

5.3 Conclusion

Liquid rare gases possess remarkable properties which make them suitable for scintillating radiation detectors. Among them xenon is the natural choice for a compact detector. A liquid scintillator has the advantage of uniformity but its optical properties must be well understood. In particular Xe purity against UV-absorbing contaminants must be well monitored.

Chapter 6

Liquid Xenon calorimeter simulation

6.1 Introduction

In the design and construction of a novel detector an important role is played by the Monte Carlo simulation. In fact it is possible to predict the behavior of a complex device from the knowledge of simple facts and numbers such as, for instance, photon cross sections, optical properties of the scintillation medium, etc. This means that a Monte Carlo simulation cannot be trusted unless supported by strong experimental inputs. In the simulation of a novel detector this step is made harder by the fact that the knowledge of some material properties (Xe in this case) may be poor. The interplay between simulation and measurements is therefore necessary, and makes the simulation code a "living" object, continuously evolving on the base of new experimental facts. The Monte Carlo results help in understanding the data and, conversely, data that can be confidently explained by the Monte Carlo simulation imply a thorough comprehension and confidence in the device.

We performed a GEANT based simulation of the liquid Xenon calorimeter. The photon detector for the MEG experiment should be optimized for comparatively low energy photons (~ 50 MeV). At these energies one cannot really speak of elecro-magnetic shower: the photon loses energy in few steps and large fluctuations are implied.

In section 6.2 we will study the characteristics of a low energy shower in liquid Xe. We will then analyze the response of the MEG detector, in particular the determination of the parameters of the incoming photon, such as its conversion point and its energy. We will study the effect of a finite Xe absorption length on the detector energy resolution. Studies will be presented on the simulation of a box-shaped calorimeter prototype, which will be the subject of extensive measurements reported in the following chapters.

6.2 Simulation of the shower development

The simulation is based on GEANT v. 3.21 [91]. The properties of the liquid Xenon were discussed in the previous chapter and those used in the Monte Carlo simulation are summarized in Table 6.1. We simulated both 52.8 MeV photons and photons coming from known background sources (radia-

Density	2.98 g/cm^3
Light Yield	$42,000$ photons/MeV
Light Absorption Length	variable
Rayleigh Scattering Length	variable, generally used $30 \div 50$ cm
Scint. Decay Time	45 nsec (e.m. shower)
Refractive Index @178 nm	1.65
Scintillation wavelength	178 nm ($\approx$ 10 nm FWHM)

Table 6.1: Liquid Xenon properties used in the simulation.

tive decay and positron annihilation in flight). For any photon we follow the shower development within the calorimeter: all relevant electromagnetic processes (pair production, bremsstrahlung, Compton scattering, photo-electric effect, ionization losses, multiple scattering and positron annihilation) are included and the secondary particles are traced down to 10 keV. Examples of "electromagnetic showers" induced by 52.8 MeV photons are shown in fig. 6.1. The simulation of other particles entering the detector, alpha sources, electrons or neutrons, is also possible.

Every time some energy is released inside the calorimeter, we generate the corresponding number of scintillation photons, whose wavelength is randomly extracted from a Gaussian spectrum centered at 178 nm, and propagate each scintillation photon up to the calorimeter walls, where the wavelength dependence of the PMT quantum efficiency is considered. The time distribution of the scintillation photons is exponential, with de-excitation constant shown in table 6.1. The absorption and Rayleigh scattering (angular distribution $\propto \left(1 + \cos^2 \vartheta\right)$) are included, but can be short circuited, if needed, to disentangle the different effects which determine the detector performances. We then check if a photo-multiplier is hit by a scintillation photon and, if so, we increase the collected charge and record the arrival time of the photon on that PMT. We can choose to take reflections on the PMT window or on the calorimeter walls into account. At the end of each event, an unformatted data stream is produced, which contains the starting position and momentum of the primary photon, the energy release in all traversed materials (aluminum, liquid xenon etc.), the coordinates of the first interaction point and the charge recorded by each PMT. If needed, we also store the time development of the PMT signals. This data stream is the input for any charge-based reconstruction program.

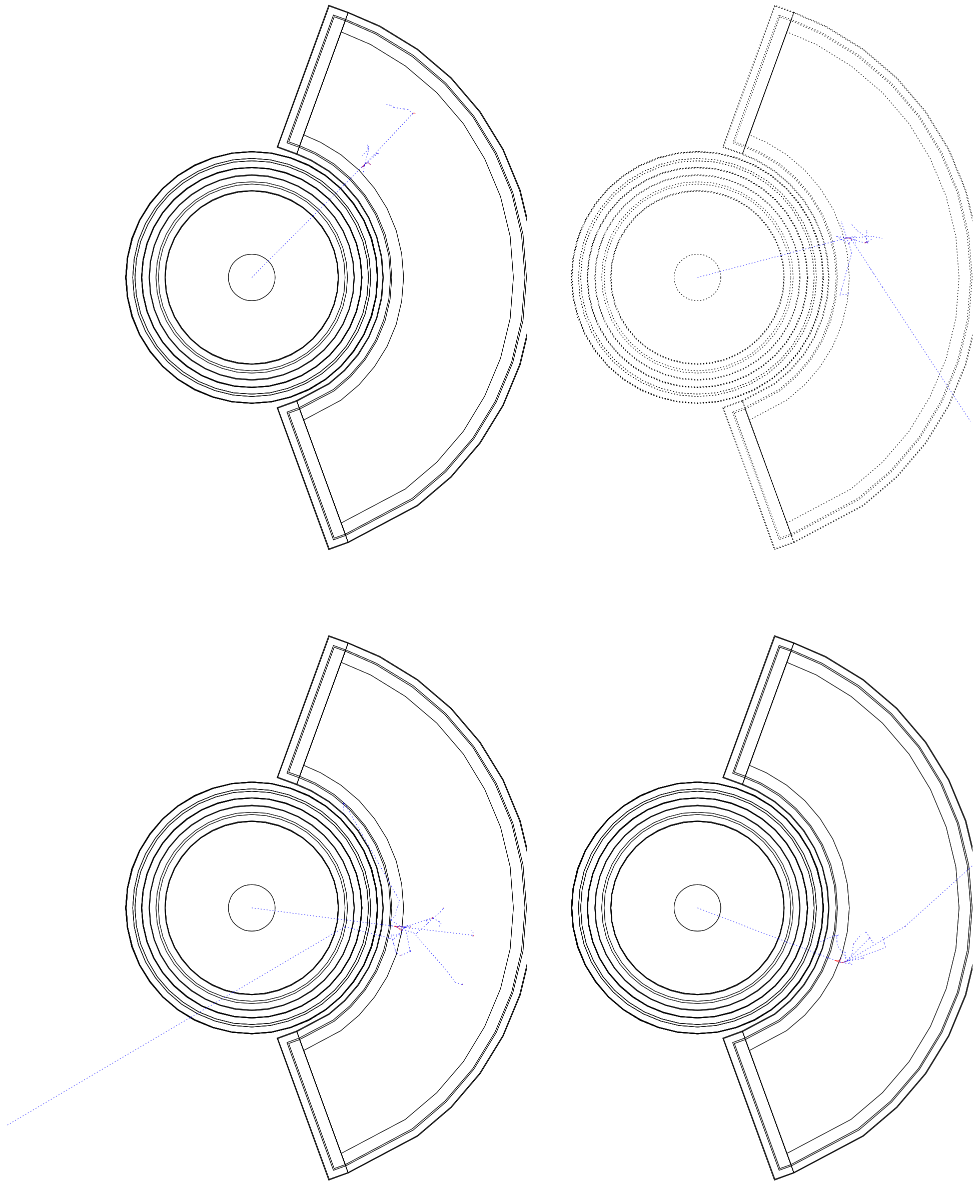

Figure 6.1: Examples of four simulated electromagnetic showers induced by 52.8 MeV photons inside the calorimeter. The dotted lines are the priamry and secondary photon trajectories while the solid (short) lines are secondary electrons and positrons.

6.3 The shape of the shower

In this section we describe the main characteristics of the simulated 52.8 MeV photon-initiated electromagnetic shower. We speak of “shower” even though at these energies we are in a regime of transition from single processes to shower development, as can be understood noticing that the Xe critical energy is of $\sim$ 14 MeV.

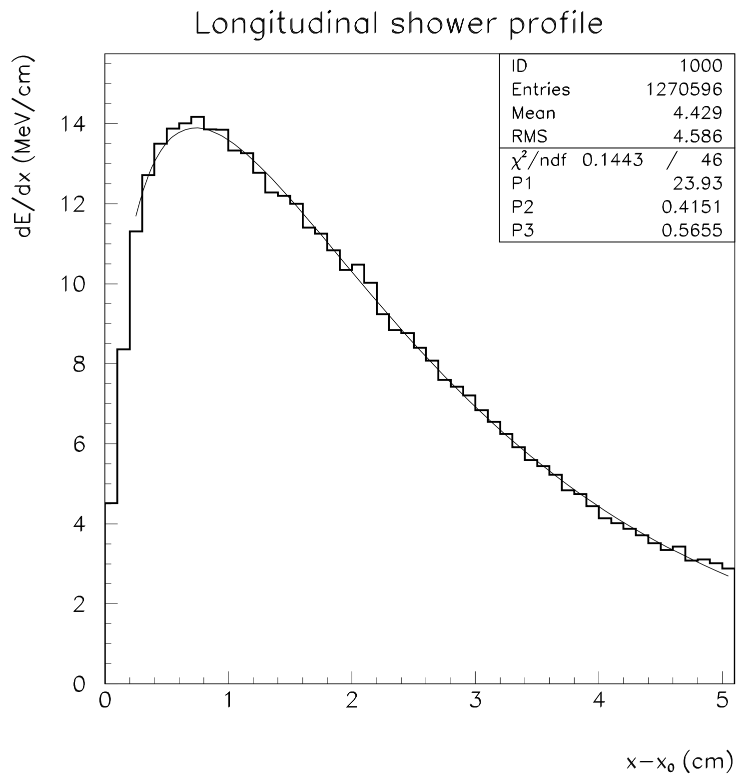

Figure 6.2: Longitudinal profile of a sample of 10000 showers. The fitting function is the product of a power law (x^{α}) and an exponential tail $\exp(-\beta x)$.

- The mean longitudinal shower profile is shown in fig. 6.2; x_0 is the coordinate of the interaction point of the gamma along the shower axis. The average longitudinal spread is $\sim$ 5 centimeters;
- The transverse spread is of the order of a couple of centimeters, as one can see from fig. 6.3;
- despite those mean properties, the energy deposit occurs at several positions along the development of the shower (as one can see in fig. 6.4), with large fluctuations.

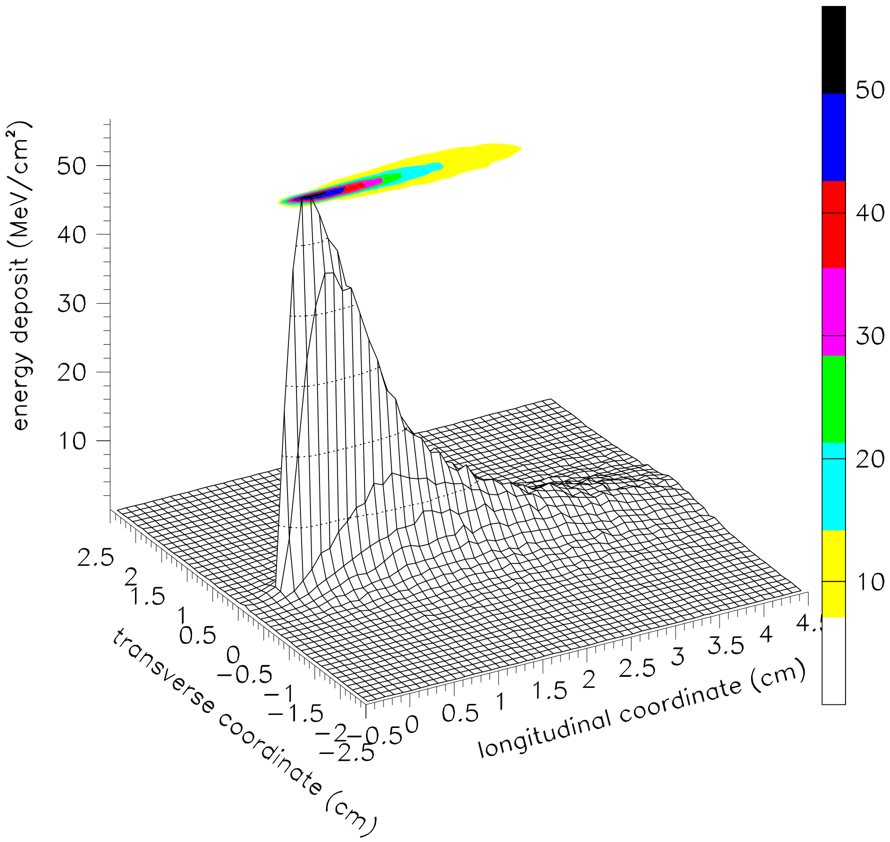

Figure 6.3: Bidimensional profile of a sample of 10000 showers, showing that the transverse spread is of order of 2 cm.

6.4 Detector geometry

We simulated the detector behavior in two different geometrical configurations: the MEG calorimeter and the "Large Prototype".

6.4.1 The MEG calorimeter

The MEG calorimeter is simulated following the cylindrical sector design. The main parameters of the detector geometry are reported in table 6.2. The beam is oriented along the positive z axis. The calorimeter is contained in the $x > 0$ half-plane; $y = 0$ and $z = 0$ are the symmetry planes of the detector. The curved surface next to the target is called the INNER and the outermost the OUTER; the surfaces on the (x, y) plane are called the LEFT and RIGHT sides and the radial caps are called the UP and DOWN plugs. The polar angles ϑ and φ are defined in the usual way. 848 PMTs are positioned on the various surfaces according to Table 6.3, and have an average photocathode coverage of 32%. The coverage is maximum on the INNER face (48%).

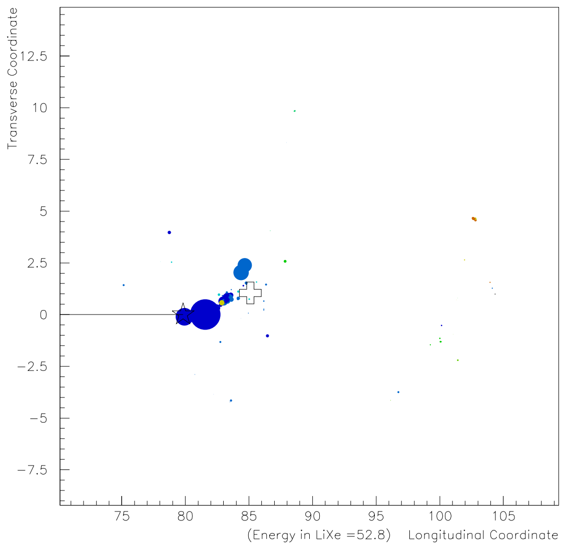

(a)

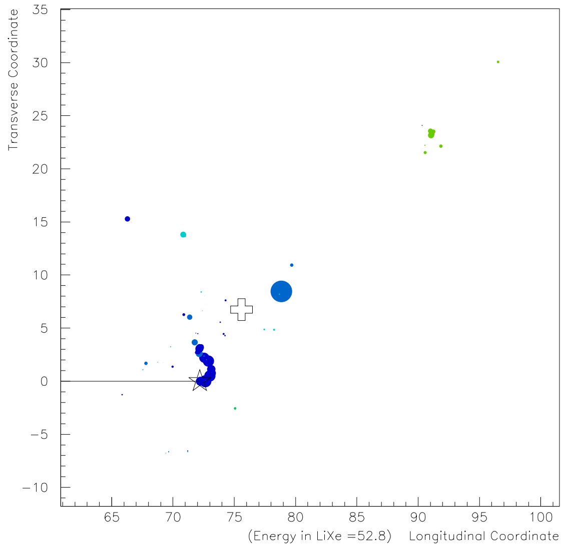

(b)

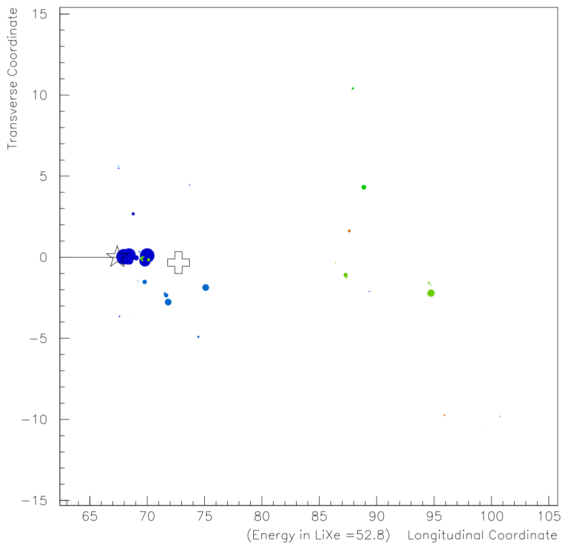

(c)

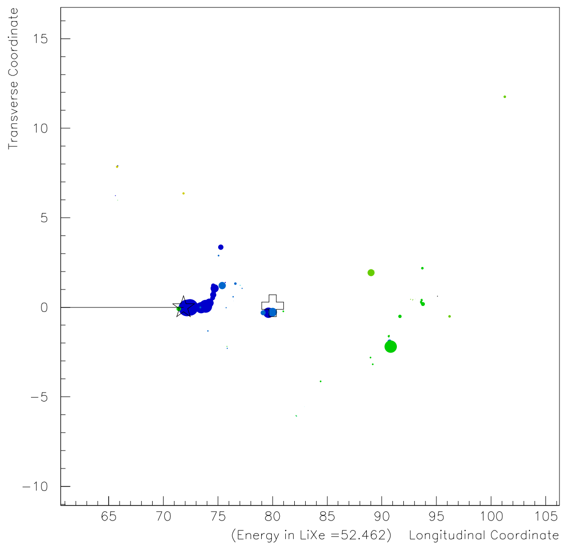

(d)

Figure 6.4: Examples of energy deposit along the shower. The photon is entering from the left and its first interaction position is marked with a star. Each energy deposit is marked by a spot. The spot radius is proportional to the energy deposit. The cross indicates the position of the center of energy of the shower (the weighted mean of all deposits). The color scale stands for the time of the energy release (blue = early, red = late). All the quotes are in centimeters.

Inner Radius	65 cm
Outer Radius	112 cm
Height	80 cm
Angular Coverage (ϑ)	$-0.35 < \cos\vartheta < 0.35$
Angular Coverage (φ)	$-60° < \varphi < 60°$

Table 6.2: Main parameters of the MEG liquid Xenon calorimeter.

Surface	**Number of PMTs**
INNER	312
OUTER	216
LEFT/RIGHT side	120
UP/DOWN plug	40
Total	848

Table 6.3: PMT positioning scheme.

The calorimeter mechanical structure was simulated in this way: the liquid Xenon fills an internal 0.6 cm thick Aluminum container, which is also the mechanical support for the plastic vessel where the PMTs are positioned; this internal container is separated by a 3 cm vacuum chamber from an external container, 0.3 cm thick. The detector partially surrounds the coils (assumed to be built in Aluminum) which generates the magnetic field of the COBRA spectrometer; the PMT is simulated as a mixture of quartz and copper (to take into account the presence of the dynodes). A pictorial view of the calorimeter structure is shown in fig. 6.5.

6.4.2 The Large Prototype

The geometry of the large prototype, which will be extensively described in the next Chapter, is simulated in the following way: the sensitive volume is a box which measures $40 \times 40 \times 50$ cm^3 and is viewed by 264 PMTs (6×6 on the square faces and 6×8 on the lateral ones), placed in a 4.5 cm thick plastic container (see fig. 6.6a). Two Aluminum containers are separated by a vacuum chamber and are 6 mm and 3 mm thick, the innermost and the outermost respectively.

A 52.8 MeV photon impinges normally on the central 2×2 PMT window, and this window is populated uniformly. We call (x, y) the coordinates on the entrance face and z the coordinate along the initial direction of the photon, *i. e.* along the shower. Note that this axis definition is different from that used for the curved calorimeter (see section 6.4.1).

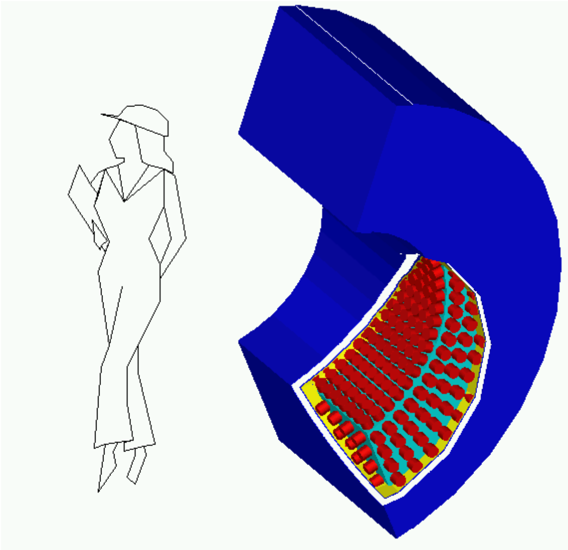

Figure 6.5: Cut view of the liquid Xenon calorimeter structure.

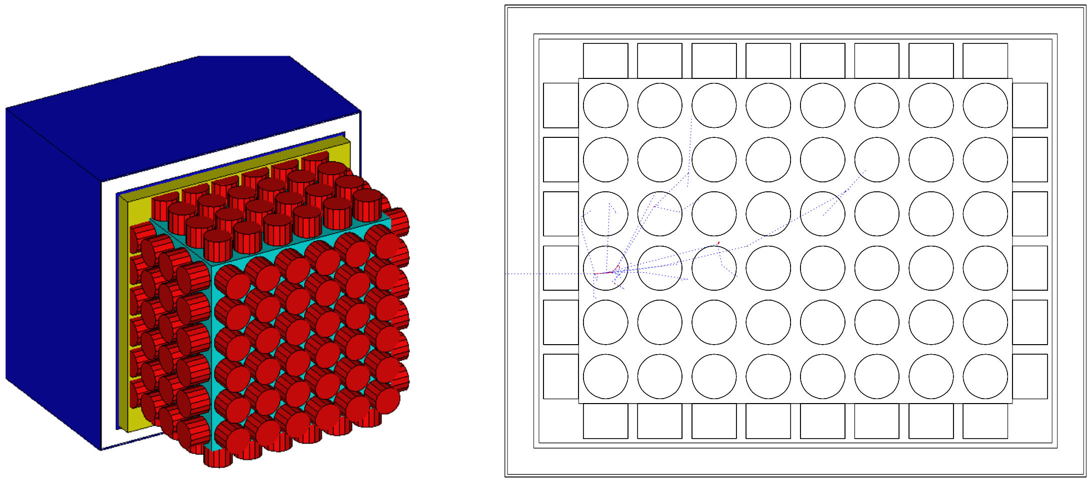

(*a*) (*b*)

Figure 6.6: The simulated geometry of the large prototype. In (*b*) a typical shower is shown.

6.5 Event Reconstruction

The signature of a $\mu \to e\,\gamma$ decay is a back-to-back electron-gamma pair, both these particles having ≈ 52.8 MeV energy. A good identification of this process requires a high resolution measurement of the energy of the particles, of the relative angle between them and of the time difference between the positron and γ signal. Therefore, we have to reconstruct the photon direction and the photon energy from the liquid Xenon information.

The photon direction is defined as the line-of-flight between the emission point and the point where the first interaction of the photon (mainly, but not always, a pair production) takes place. Note that, because of the transverse fluctuations, the angular separation between the axis of the e.m. shower[1] and the photon direction is $\sim 1°$; such an axis is generally not a satisfactory measurement of the γ direction and we need to determine (at its best) the position of the first interaction point or (equivalently) of the entrance point in the calorimeter.

From now on, we shall distinguish between "ideal" and "realistic" events: the former are events where Rayleigh scattering and light absorption mechanisms were switched off, the latter are events where all these mechanisms are included using the absorption and scattering lengths dependent on the scintillation photon wavelength. "Ideal" events give us a measure of the maximum performances attainable using the various reconstruction procedures, the "realistic" ones a first idea of the problems we will have to cope with during the experiment. Rayleigh scattering and light absorption are not expected to produce large effects on the charge distribution of INNER face PMTs, since most of these PMTs are close to the region where the bulk of the energy is deposited; however, they can significantly reduce the charge on far PMTs and therefore the total collected charge. The total amount of the collected charge is a first estimate of the energy release, fast enough to be useful at a trigger level, but important distortions are expected (and observed: see later) in energy reconstruction if such effects are not compensated at all.

We discuss here the results obtained by using the PMT charge information: spatial distribution of the collected charge and total amount of charge. The described methods apply to both the curved detector and the large prototype. For both position and energy resolution we will state the general reconstruction procedure and then specify the differences between the two detectors.

6.6 Position reconstruction

6.6.1 General considerations

The shower originating from 52.8 MeV photons has a very complex shape and the energy is not directly emitted at the conversion point but at several points along the shower (see fig. 6.4). However the first energy release has a stronger memory of the interaction point, and is almost always the closest to the entrance face. Solid angle effects further enhance this first deposit on the entrance face. That is why we used only the PMT signals of the entrance face. The charge on the other faces is heavily affected by later (sparse) energy deposits and is sensitive to the center of the shower energy, which is a point different from the one we are looking for.

Two different approaches are used to exploit the information provided by the INNER (in case of the curved detector) or FRONT (in case of the LP) face PMTs:

[1] Defined, *e.g.*, as the axis passing through the first interaction point and the center of energy released.

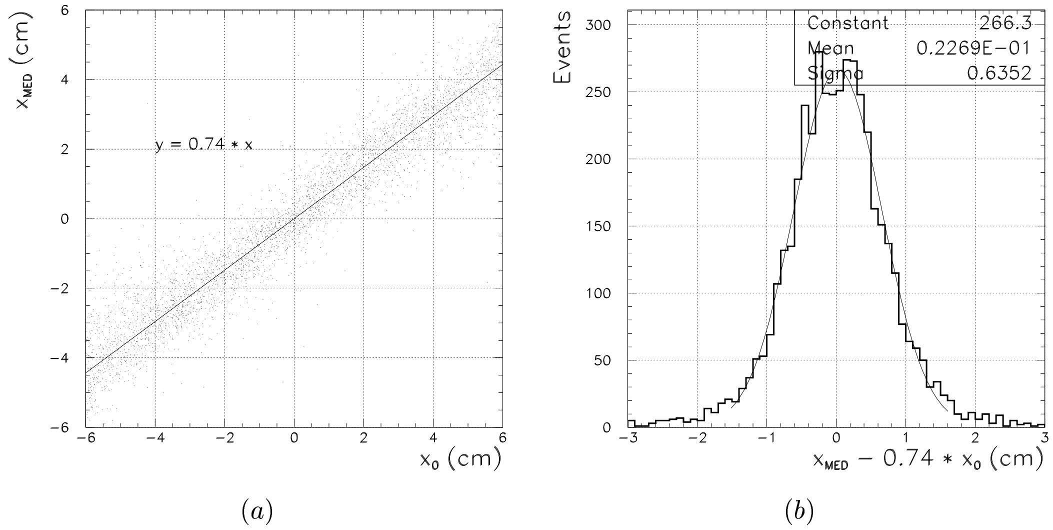

Figure 6.7: (a) Correlation between weighted average (x_{med}) and x of entrance of the photon. (b) Distribution of reconstructed entrance point using the weighted mean technique.

1. weighted mean of charge deposit;
2. a fit to PMT amplitudes.

Method (1) is by far the simplest and fastest: the position of each PMT is weighted with the corresponding charge.

$$\begin{aligned} \bar{x} &= \frac{\sum_i Q_i\, x_i}{\sum_i Q_i} \\ \bar{y} &= \frac{\sum_i Q_i\, y_i}{\sum_i Q_i} \\ \bar{z} &= \frac{\sum_i Q_i\, z_i}{\sum_i Q_i} \end{aligned} \tag{6.1}$$

where (x_i, y_i, z_i) are the coordinates of the $i-$th PMT on the INNER surface and Q_i are the corresponding collected charges.

This method, however, presents a drawback. The weighted average reconstructed photon interaction point is biased towards the detector center. For this reason a correcting factor must be applied to evaluate the photon entry position correctly.

This can be seen in fig. 6.7a, where we plot a coordinate on the INNER face (called x) calculated with the weighted mean x_{med} versus the true entrance point x_0. Once we know the correction coefficient we can use it to determine the entrance point (fig. 6.7b). The resulting position resolution is $\sigma_x = 6.3$ mm.

Method (2) takes into account the solid angle subtended by each PMT for a point-like source

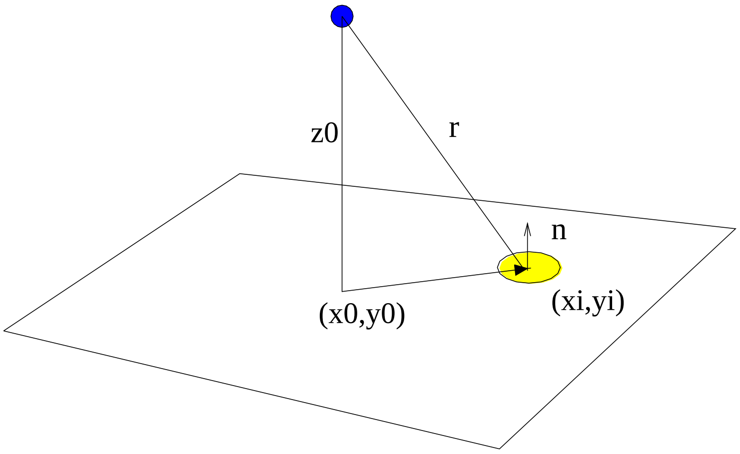

Figure 6.8: Sketch of a point-like source in front of a wall. The solid angle subtended by an infinitesimal surface dxdy around point (x_i, y_i) is, by definition, $\frac{\mathrm{d}x\mathrm{d}y}{|r|^3}\vec{r}\cdot\hat{n}$, $\vec{r}$ and $\hat{n}$ being the distance from the source and the unit vector normal to the plane in (x_i, y_i), respectively.

at a distance z_0 from the front face. With reference to fig. 6.8, the charge collected by the $i-$th PMT is proportional to

$$C_i \propto \frac{z_0}{(z_0^2 + (x_i - x_0)^2 + (y_0 - y_i)^2)^{3/2}} \cdot \pi R^2, \tag{6.2}$$

R being the radius of the PMT. For each event we use MINUIT to find the best value for (x_0, y_0, z_0) given the C_i. A refined version of this method uses the correct (tabulated) solid angle for each PMT, and only part of the INNER face PMTs is used: starting from an initial estimate of the γ conversion point $\vec{r}_0$ using all PMTs, only the PMTs within a certain distance from this estimate are used to fit expression (6.2). A new estimate of the conversion point $\vec{r}_1$ is obtained and used as a new circle center. The procedure is iterated until it converges (*i.e.* $|\vec{r}_i - \vec{r}_{i+1}| < 0.5$ mm). In this way one gets rid of the tails of the light distribution on the front face.

6.6.2 Resolution of the large prototype

The results of the fit for x and y are shown in fig. 6.9a and b. The superimposed Gaussian fits have $\sigma \lesssim 5.5$ mm. With the refined version (tabulated solid angle) we obtain a resolution of $\sigma_{x,y} \sim 5$ mm over the whole incidence region of the γ-ray ($|(x, y)| < 6.2$ cm). As far as the determination of the shower depth is concerned, we can see that the correlation between z_0 and z is quite strong (fig. 6.10a) though the best fit line does not pass through the origin. This is due to the fact that the bulk of the energy deposit takes place ≈ 2 cm after the photon interaction point. By making use of this strong correlation we have a determination of z_{int} with $\sigma \approx 6$ mm (see fig. 6.10b). The knowledge of the photon conversion point depth is essential to evaluate its timing precisely, as will be seen in Chapter 10.

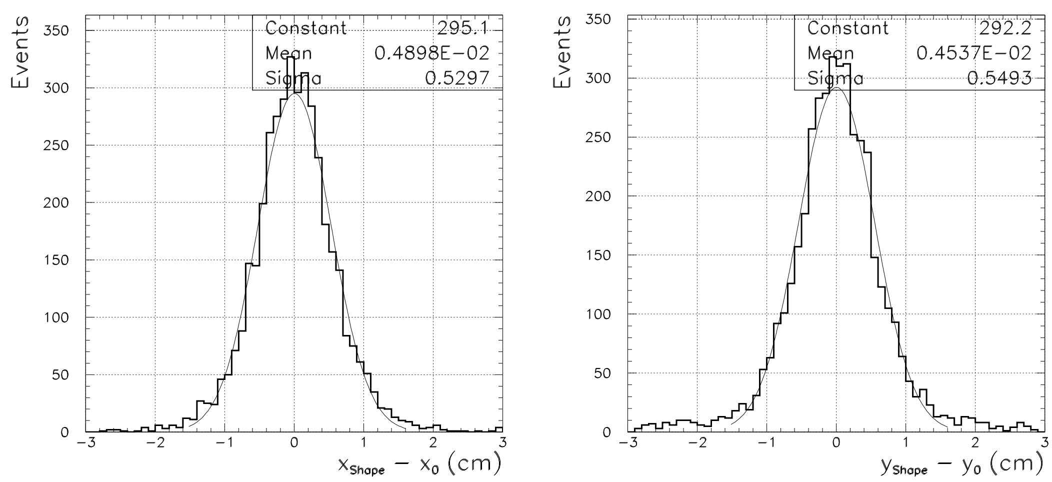

(a) (b)

Figure 6.9: Reconstruction of the entrance point of the photon on the front face using the fit of the entrance face PMT charge. x and y are two arbitrary orthogonal directions on the detector face.

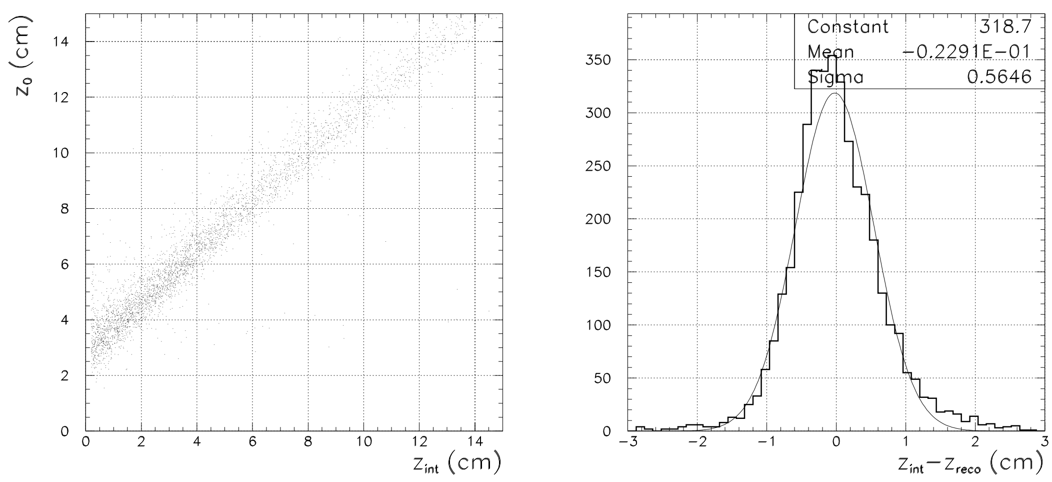

(a) (b)

Figure 6.10: (a) Correlation between the z_0 parameter in the shape fit (see eq. (6.2)) and the Monte Carlo distance of the gamma conversion point from the front face. Note that the main energy release takes place some centimeters after this first conversion. (b) Distribution of the z coordinate of the γ interaction point reconstructed with the fit to the PMT outputs.

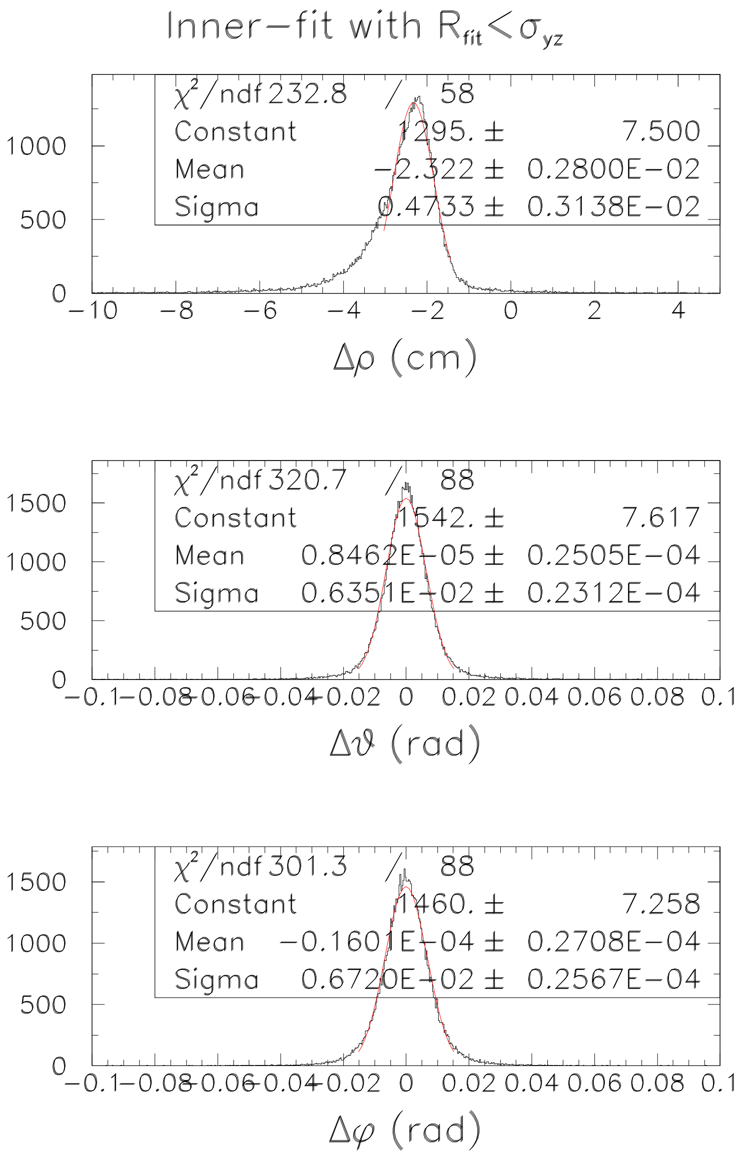

Figure 6.11: Angular resolutions (in radians) obtained applying a "large prototype-like" fit to the inner (curved) surface of the proposed calorimeter, with all the physics effects taken into account.

6.6.3 Resolution of the curved calorimeter

The results of the refined version of the fit applied to the PMTs of the INNER face of the MEG curved calorimeter are shown in Figure 6.11. The resolutions are $\sigma_\theta \approx 6.4$ mrad, $\sigma_\phi \approx 6.8$ mrad on the whole acceptance of the calorimeter. The reconstruction of the shower depth shows a small bias also for the curved calorimeter (upper plot of the same figure) anyway the resolution is comparable to that obtained in the large prototype.

6.6.4 Investigations on the position resolution

In order to understand the ultimate reason that affects the position resolution we made the following simulations:

1. we simulated a calorimeter with smaller PMTs, with radius one half of the R6041Q, *i.e.* 1-inch radius, quadruplicating the number of PMTs in the inner face;
2. a point-like 52.8 MeV energy deposit with the exponential depth in LXe which mimics the real gamma interaction point (both with 1" and 2" PMTs).

The results obtained are the following:

2" PMT	shower	4.5 mm σ
1" PMT	shower	3.3 mm σ
2" PMT	point-like	1.0 mm σ
1" PMT	point-like	0.7 mm σ

We can conclude that the position resolution is mainly limited by the transverse fluctuations of the shower and can be only slightly improved by using smaller PMTs.

6.7 Energy resolution

6.7.1 General considerations

The following considerations apply equally to the curved calorimeter and to the large prototype. In the idealized situation in which neither absorption nor scattering exist in liquid Xe, an estimate of the deposited energy is given by the sum of all PMT charges, weighted for the different PMT density on the calorimeter wall, to take the non-sphericity of the detector into account.

$$Q_{sum} = \sum_i W_i Q_i \tag{6.3}$$

where $W_{1,\ldots,6}$ are the PMT densities on the six detector faces.

The distribution of the total PMT charge (Q_{sum}) for the idealized detector ($\lambda_{\mathrm{Ray}} = \lambda_{\mathrm{Abs}} = \infty$) is shown in Figure 6.12; the photon energy spectrum can be interpolated with a pseudo-Gaussian fit, with an energy-dependent sigma. The resulting FWHM is $\approx 2.5\,\%$ at 52.8 MeV.

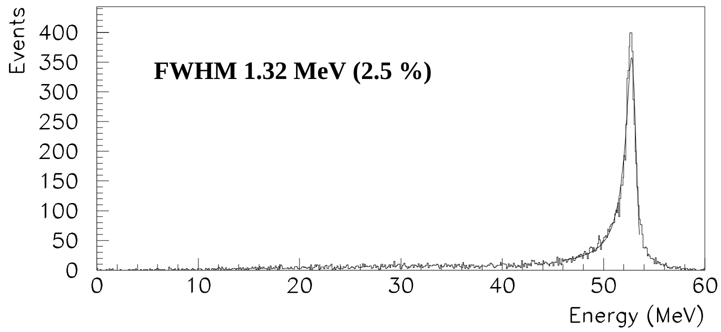

Figure 6.12: Weighted mean reconstruction of "ideal" events: total sum of PMT charge in units of energy.

If we now look at "realistic" events, the situation becomes more problematic: we considered the situations in which Rayleigh scattering is taken into account, or absorption or both. The results of the simulations for the curved detector are shown in Figure 6.13.

Rayleigh diffusion does not seem in itself really dangerous (see the upper-right plot): since no photons are absorbed and the angular distribution of the scattered photons is forward-backward symmetric, the amount of charge collected by the various surfaces is only slightly different with respect to the "ideal" case and the "$Q_{\rm sum}$"is still a good measurement of the energy.

When the light absorption is taken into account (see the lower plot on the left), the energy resolution begins to degrade. This is due to the fact that light absorption has different effects on the surfaces far from the bulk of energy deposit (OUTER, UP and DOWN plugs) than on the INNER one: the light directed towards the OUTER surface is more frequently absorbed than that directed towards the INNER surface. So, the different light collection efficiencies of the various surfaces are no more compensated by the weighting factors, which equalize the photo-cathodic coverage only.

Finally, when one combines Rayleigh scattering and light absorption, the resulting distribution is even broader (see the lower plot on the right); this is not surprising since, because of multiple Rayleigh scattering, the real path traveled by a photon to reach a PMT is larger than the distance between this PMT and the photon emission point. This effect enhances the differences between the various surfaces, since the more distant the surface, the longer the effective path of a photon and the higher the probability of absorption.

The situation for the large prototype is slightly better mainly because of two reasons: the smaller size of the detector which implies that the light reaches the PMTs after a shorter average path, and the absence of portion of detector which are sometimes shadowed by others, as the region close to one of the two end-caps in the curved detector.

For what concerns energy measurements we investigated three different ways of reconstructing the energy of $\sim$ 50 MeV photons as a function of the light absorption length used in our Monte

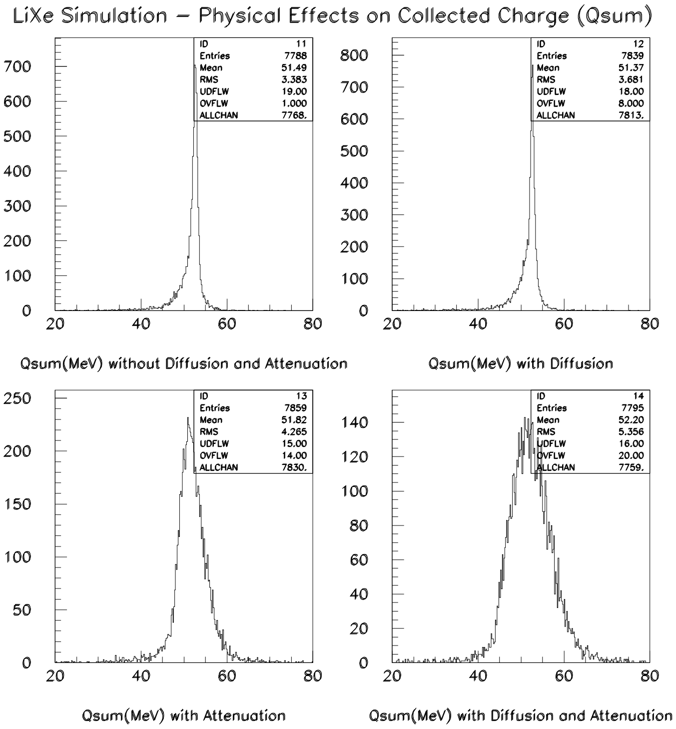

Figure 6.13: Comparison of the weighted sum of the PMT charges in various cases. From left to right, from top to bottom: "ideal" events, events with only Rayleigh diffusion applied, events with only light absorption applied, events with both Rayleigh scattering and light absorption. Light absorption length was held fixed at 100 cm and Rayleigh scattering length at 30 cm.

Carlo simulation:

1. A simple sum of the charges seen by all the PMTs (Q_{SUM}) taking into account the different PMT densities on the various surfaces;
2. a minimization procedure based on the assumption that the light be emitted at two different points along the photon direction (dipole fit);
3. an algorithm derived by the so–called "principal component analysis" [92] which exploits the information seen by the individual PMTs (linear fit) which is described right below.

In the linear fit case, the γ-ray energy is written in a linear approximation as a weighted sum of the charges Q_i seen by each PMT:

$$E_l = c + \sum_i c_i Q_i \tag{6.4}$$

The coefficients c_i and the constant c are determined as follows: a sample of N ($\sim 10^4$) Monte Carlo events is used to compare the linearized value of the energy, E_l, with the true deposited energy, E_t; a χ^2 expression can be formed:

$$\chi^2 = \sum_{\text{MC events}}^{N} (E_l - E_t)^2 \tag{6.5}$$

and the coefficients are obtained requiring that this χ^2 is a minimum. The minimization procedure is analytical and yields the following results:

$$c = \langle E_t \rangle - \left\langle \sum_j c_j Q_j \right\rangle \tag{6.6}$$

$$c_i = \frac{\mathcal{M}^{-1}}{N-1}\left[\sum_{\text{MC events}}^{N} E_t Q_i\right] - \frac{1}{N}\sum_{\text{MC events}}^{N} E_t \sum_{\text{MC events}}^{N} Q_i \tag{6.7}$$

where the averages are calculated over the event sample and $\mathcal{M}$ is the covariance matrix (computed using the Monte Carlo simulated events):

$$\mathcal{M}_{kl} \simeq \Big\langle \big(Q_k - \langle Q_k \rangle\big)\big(Q_l - \langle Q_l \rangle\big) \Big\rangle \tag{6.8}$$

6.7.2 Resolution for the curved detector

The resolutions obtained by the three different methods are shown in Figure 6.14 as a function of the absorption length used in the Monte Carlo simulation. For small absorption lengths the best resolutions are obtained by the "linear fit" method while in the limit of large absorption lengths the three methods tend to give equivalent results.

Assuming a 100 cm absorption length, this method yields an average of 5% (FWHM) resolution (Fig. 6.15) for γ-rays uniformly entering the detector with energy of 52.8 MeV. This resolution

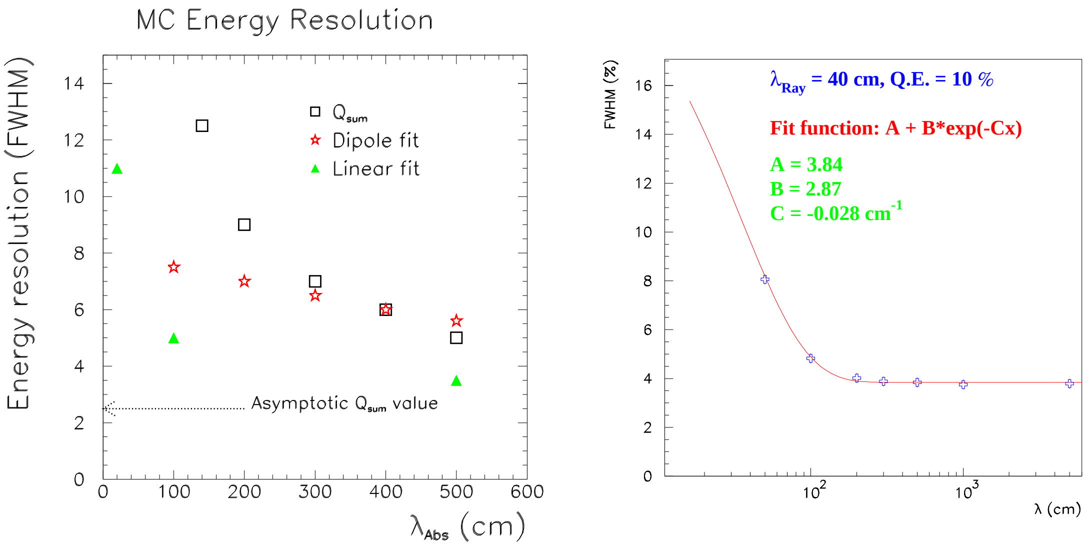

(a) (b)

Figure 6.14: (a) Resolutions obtained by the three different methods used for the energy reconstruction of $\sim$ 50 MeV photons as a function of the absorption length used in the Monte Carlo simulation; (b) Resolution obtained with the linear fit as a function of the absorption length λ_{Abs}.

can be further improved by exploiting the knowledge of the photon conversion point: if we prepare different sets of the coefficients c_i for different incident positions in 5×5 cm^2 bins, it improves to 4% (FWHM).

6.7.3 Resolution of the large prototype

As already mentioned the charge collection for the large prototype in the presence of absorption and Rayleigh scattering is slightly better than that of the curved calorimeter. The resolution obtained with the linear fit with $\lambda_{\mathrm{Abs}} = 100$ cm is 4% FWHM with a single set of coefficients, as in the case of the curved detector with position dependent coefficients. This is easily understood since the photon incidence region on the large prototype is limited. The simple Q_{SUM} method gives also better results in the LP, once a correction for the z_{fit} dependence of the collected charge is made (see Figure 6.16) but it does not perform like the linear fit method.

6.8 Importance of Xenon purity

The performances of the detector as a calorimeter ($i.$ $e.$ for the energy measurement) seems strongly dependent on the properties of the liquid Xenon, mainly on the absorption length, as clearly visible

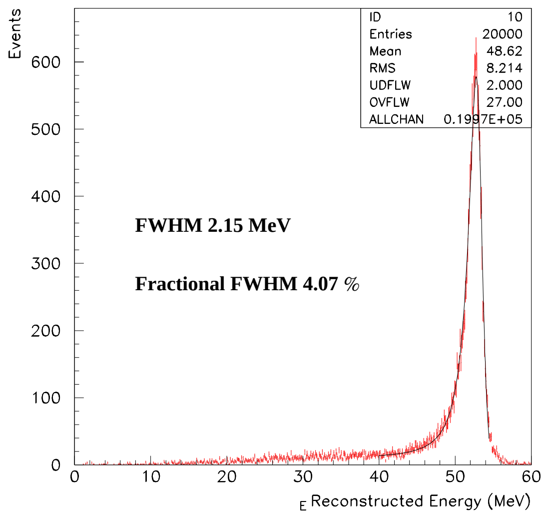

Figure 6.15: Reconstructed energy distribution for photons from $\mu^+ \to e^+\gamma$.

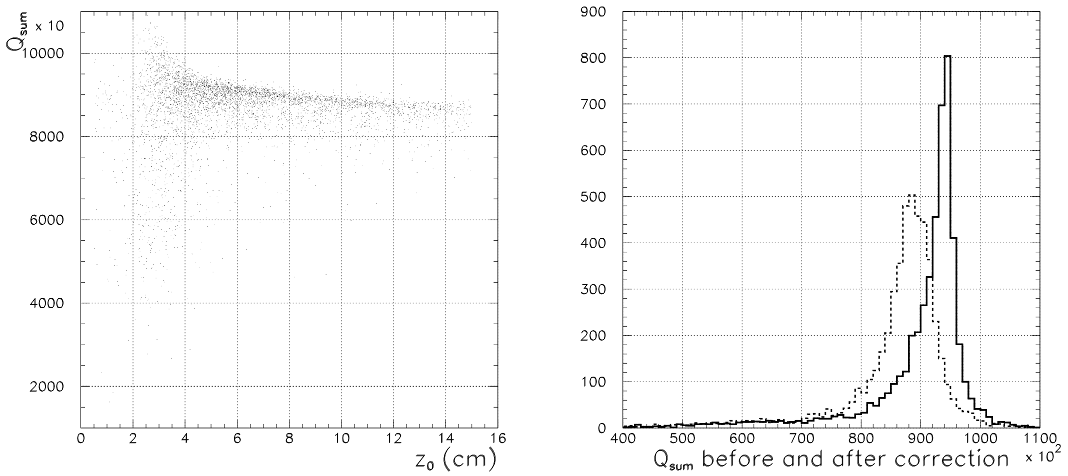

(a) (b)

Figure 6.16: (a) Correlation between the charge collected on the PMTs and the shower depth as measured by the parameter z_0 of the shape fit. The effect of attenuation is apparent. In (b) the charge distribution is corrected by taking this effect into account (continuous line histogram).

from Figure 6.14*b*. The combined effect of light scattering and absorption produces a PMT charge distribution which cannot be predicted analytically; this produces an intrinsic limiting performance for any charge-based reconstruction algorithm. Apart from possible refinements of the shower model and of the algorithms (which are under study), we stress the importance of a long (some meters) light absorption length, which implies a high purity for Xenon. In the following we will show measurements regarding the large prototype. It is not obvious, *a priori*, that the results obtained apply to the curved calorimeter as well. But if the results are close to the Monte Carlo predictions we can confidently extrapolate them to the final shape.

Chapter 7

The Large Prototype

7.1 Introduction

In this Chapter the operation of the MEG liquid Xe calorimeter large prototype (LP) is described.

This prototype of the final calorimeter has been assembled and is still under test. The purpose of the construction of the LP is twofold: operation and material study, and physics measurement study. In the first category are included, for instance, the Xe liquefaction and recovery procedures, the mechanical stability and compatibility of all materials, including PMTs operation and calibration at low temperature, Xe handling and purification etc. In the second category measurements such as the detector response to alpha sources, cosmic rays are implied, as well as measurements of the performances of a large liquid Xe homogeneous calorimeter, *i.e.* energy, position and timing resolution, which play a key role in determining the ultimate sensitivity of the MEG experiment in view of the $\mu^+ \to e^+\gamma$ decay search.

At the early stages of the LP operation it was soon realized that the purity of liquid Xe is crucial for scintillation light collection. More than one year was needed to fully understand and solve this problem, with the ultimate introduction of a Xe circulation and purification system to guarantee a sufficient transparency of Xe to its scintillation light.

Only after this was accomplished we were able to start reliable measurements of the LP performance, including timing and energy resolution.

This Chapter is divided as follows: after a description of the LP, the procedures of Xe liquefaction/recovery are briefly reviewed. The establishment of an on-line gain monitoring procedure for the PMTs, which is essential to reach an excellent energy resolution in treated in detail. The Xe purification is then described and measurements of some optical properties of liquid Xe are presented.

The study of the detector performances are deferred to the following Chapters.

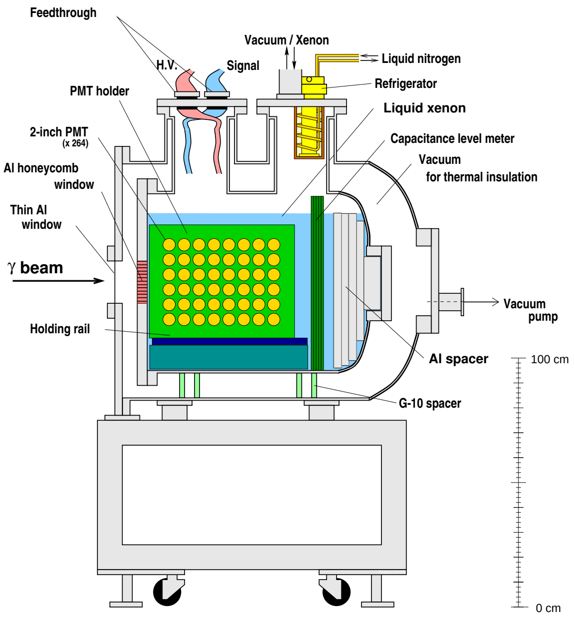

Figure 7.1: Schematic view of the large prototype

7.2 Mechanical description

The LP was built in close similarity to the final calorimeter. Both the prototype itself and the cryostat were intensively studied. Various technical issues were faced and solved and testing of important parts, such as signal and high-voltage feed-through, were carried out.

7.2.1 Mechanics and materials

A schematic view of the LP is shown in Figure 7.1. The LP is a rectangular box whose internal volume measures $37.2 \times 37.2 \times 49.6$ cm^3. The direction along the longer side is named z-direction, while the other two (shorter) sides are named x (horizontal) and y (vertical) directions. Five out of six walls are made of stainless steel, the remaining one, one of the two square-shaped, is designed as the photon entrance face and therefore made of G10, for a shorter radiation length. The LP walls (holders) present array of holes in order to accommodate the photo-multiplier tubes, whose windows are in direct contact with the liquid Xe. The lateral faces can fit 6×8 PMTs, while the front and back faces can accommodate 6×6 PMTs, hence a maximum of 264 PMTs can be assembled on the LP.

The LP is placed inside its cryostat, which is composed of two cylindrical chambers: an inner and an outer vessel. The inner vessel thermal insulation is guaranteed by the vacuum between the two chambers and by a super-insulation.

Part of the inner vessel front wall is made of an aluminum honeycomb structure, in order

PMT size	57 mm ϕ
Photo-Cathode material	Rb-Cs-Sb
Effective area	46 mm ϕ
Q.E. at 165 K	$\sim$5% (@ 175 nm)
Dynode type	Metal channel
Number of stages	12
Typical H.V.	900 V
Current amplification	$\sim 10^6$
Transit time spread	750 ps (FWHM)

Table 7.1: Properties of the Hamamatsu R6041Q photo-multiplier tube

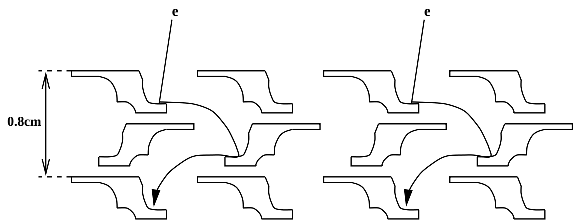

Figure 7.2: Dynode structure of a metal channel PMT

to exhibit the lowest possible material to incoming photons. Correspondingly a thin aluminum window, (150 μm, 10 cm diameter) is flanged on the outer vessel.

Two chimneys out of the inner chamber contain the signal and HV feed-troughs and the Xe cooling device. A pulse-tube refrigerator [93] is installed on top of the chamber for Xe condensation. A liquid nitrogen cooling pipe is also present in order to provide additional cooling power. Xe is liquefied in the inner chamber and permeates the LP. Dead volumes are filled with inert material, such as acrylic, Teflon and stainless steel.

7.2.2 Photo-multipliers

The LP is equipped with 2″ UV-sensitive photo-multipliers especially developed for the MEG experiment by Hamamatsu Photonics (R6041Q). The main characteristics of the R6041Q PMT are shown in Table 7.1. It is a metal-channel photo-multiplier (see Figure 7.2 for a schematics of its dynode structure) embedded in a cylindrical metal case. The fused silica window is glued at one end with an epoxy resin specially suited to resist the mechanical stress due to the different thermal contractions of the PMT case and window. After an initial bunch of comparatively low ($\sim$ 5%) quantum efficiency (QE) photo-multipliers, a different photo-cathode material (Rb-Cs-Sb instead of K-Cs-Sb) was employed. A special aluminum pattern was also deposited on the PMT window to decrease the photo-cathode resistivity at low temperature. The improvement in QE is up to a factor of 5 for the last bunch of delivered PMTs, but the PMTs mounted on the LP so far

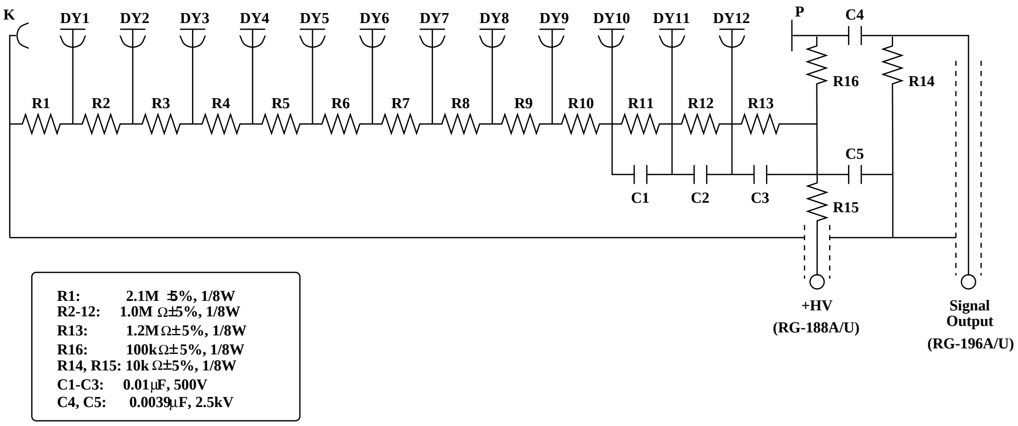

Figure 7.3: The voltage divider circuit used for the R6041Q PMTs

have been all of the old type.

The PMTs are supplied with positive voltage and the divider circuit, schematically shown in Figure 7.3, is optimized to avoid local boiling of Xe and to minimize Xe convection due to heat dissipation. The total resistance of the divider circuit is ≈ 14 MΩ hence, for a typical applied voltage of 1000 V the average divider current is of the order of 70 μA.

7.2.3 Calibration devices

The LP is equipped with radioactive sources and LEDs for calibration and monitoring purposes. On each lateral face two blue LEDs and one ^{241}Am α-source are placed for a total of eight LEDs and four α-sources. The alpha sources are made of an aluminum flat cylinder onto which ^{241}Am is electro-chemically deposited, and coated with a 2 μm protection gold film.

During operation three pairs of trigger counters (TC1, TC2 and TC3, one member of the pair above the cryostat and one member below it) are placed along the LP, in the z-direction, to select vertical, through going cosmic ray muons.

The positions of LEDs, α-sources and cosmic-ray trigger counters are shown in Figure 7.4. Temperature and pressure sensors inside the vessel continuously monitor the LP status.

7.3 Operation

The LP operation requires lengthy procedures: it takes about half a month to complete Xe liquefaction. After inserting the LP into the chamber, the inner and the outer vessels are evacuated. Baking of the detector is done at a relative low temperature ($\approx 70°$) because of the PMTs and acrylic parts. After ten days of evacuation the inner pressure reaches $\sim 10^{-3}$ Pa.

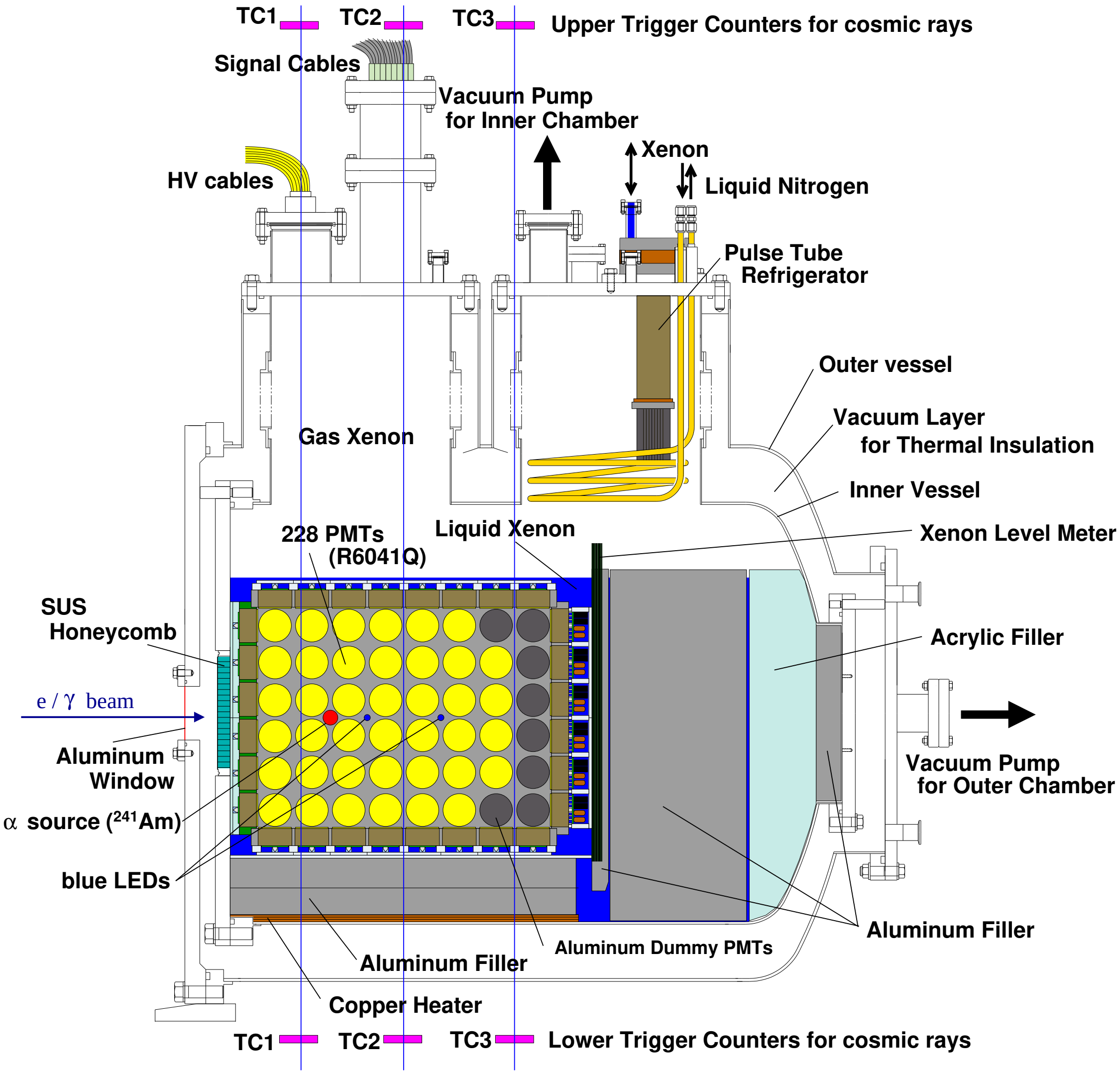

Figure 7.4: LED, α-source and cosmic-ray trigger counter positions on the large prototype

7.3.1 Cryogenics

In the phase called "pre-cooling" liquid nitrogen is flushed through the copper coil and the pulse-tube refrigerator is started, while gaseous Xe is continuously poured inside the inner vessel. Before reaching the chamber, the gaseous Xe passes through a gas purifier (SAES getter [94]) and a molecular filter (Oxisorb [95]), which can absorb gas contaminants such as water, oxygen, carbon dioxide, nitrogen and methane down to a ppb level.

When the inner temperature reaches $\sim$ 165 K the Xe liquefaction starts: gaseous Xe condenses on the copper serpentine and fills the inner volume. It takes about two days to liquefy 100 l Xe; Xe is then kept in a steady state ($\sim$165 K, $\sim$1.3 atm) by the pulse-tube refrigerator only.

After completing all the measurements, Xe is recovered to a storage tank. The refrigerator is turned off and the outer vessel is filled with gas nitrogen to accelerate Xe evaporation, favored also by a heater inside the inner vessel. The storage tanks are immersed in a liquid nitrogen bath to re-condense Xe. The recovery procedure takes one additional week.

7.3.2 HV, electronics and DAQ

PMT high voltages are supplied by two LeCroy HV power supplies (LRS 1458 and 1454) through a HV feed-through developed for the ATLAS experiment. The power supplies are controlled through a RS232 LAN interface and have a resolution of $\pm$1 V.

Each PMT charge is digitized by 15-bit FASTBUS ADCs (CIAFB, specially developed for the OPAL experiment, 20 fC resolution [96]). The anode output of 100 PMTs is fed directly to the ADCs, while the signal of the remaining 128 photo-multipliers, those of the front face and most of the PMTs on the lateral faces, is split[1]: one output goes to the ADCs, while the other one is discriminated and fed into FASTBUS TDCs (LRS 1875A 25 ps least count). This DAQ configuration was continuously upgraded. During the charge exchange experiment, for instance, all PMTs had both ADC and TDC information.

Apart from experiment-dependent triggers (*e.g.* coincidence with a particular beam RF) there are common trigger sources, selectable via a NIM or CAMAC module, or from the acquisition programme. For triggering purposes the discriminated PMTs are divided into 4 patches (see Figure 7.5): each patch is composed of the PMTs on one lateral face, surrounding a particular α-source, and one fourth of the PMTs on the front face, those pointing towards the same α-source. The four central PMTs of the inner face belong to four different patches. The common triggers are:

1. A pedestal (random) trigger;

2. A so-called "photon" trigger, requiring at least one PMT of three different patches to be over threshold, used to select photons entering the center of the detector;

[1] At the early stages of the tests the signal were passively split. Since passive splitting added consistent noise to the PMT output, active splitter developed for the MACRO experiment were used for later tests.

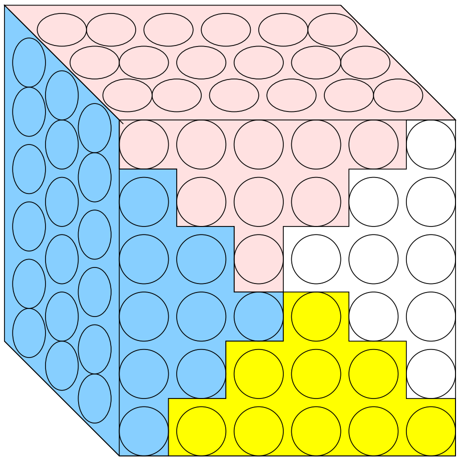

Figure 7.5: Patches of PMTs used to realize the various LP triggers

3. The “alpha” trigger, requiring at least three PMTs in one single patch to be over threshold, used to trigger on alpha sources;
4. The “cosmic” trigger, independent of the LP PMT output but requiring a coincidence in either TC1, TC2 or TC3, used to trigger on cosmic-ray muons going through the detector.

A scheme of the DAQ used for the measurements shown in this Chapter is shown in Figure 7.6

7.3.3 QE measurement

During usual operation only 228 PMTs are inserted in the LP, leaving vacancies on the last backward PMT row of the lateral faces (see Figure 7.4). The PMT Quantum Efficiencies (QE) were evaluated comparing the signal from α-sources in gas to the Monte Carlo simulation. Cold Xe gas was used in order to minimize absorption and scattering effects which are present in the liquid phase. As seen in Chapter 5, the scintillation spectrum in gas in not much different from the spectrum in liquid [76, 77],

The QE is evaluated as follows: for each photo-multiplier we compute the expected number of photons due to each α source via a Monte Carlo simulation, assuming infinite Rayleigh scattering and absorption lengths. We extract the experimental quantities by fitting the α-data in gas: since the average number of photons expected at each PMT is very low (sometimes less than one) and the pedestal width is of comparable size when expressed in photo-electron units, we fit the data by using the convolution of a Poisson function with a Gaussian, representing the contribution of the pedestal (Figure 7.7). Data points are plotted versus Monte Carlo predictions: the expected linear relation is well verified (see Figure 7.8) for a large number of PMTs. The slope of the fitted straight line represents our estimate of the QE. The distribution of the measured quantum efficiencies is shown in Figure 7.9. To get a better evaluation of the QEs several runs of α-sources in cold gas

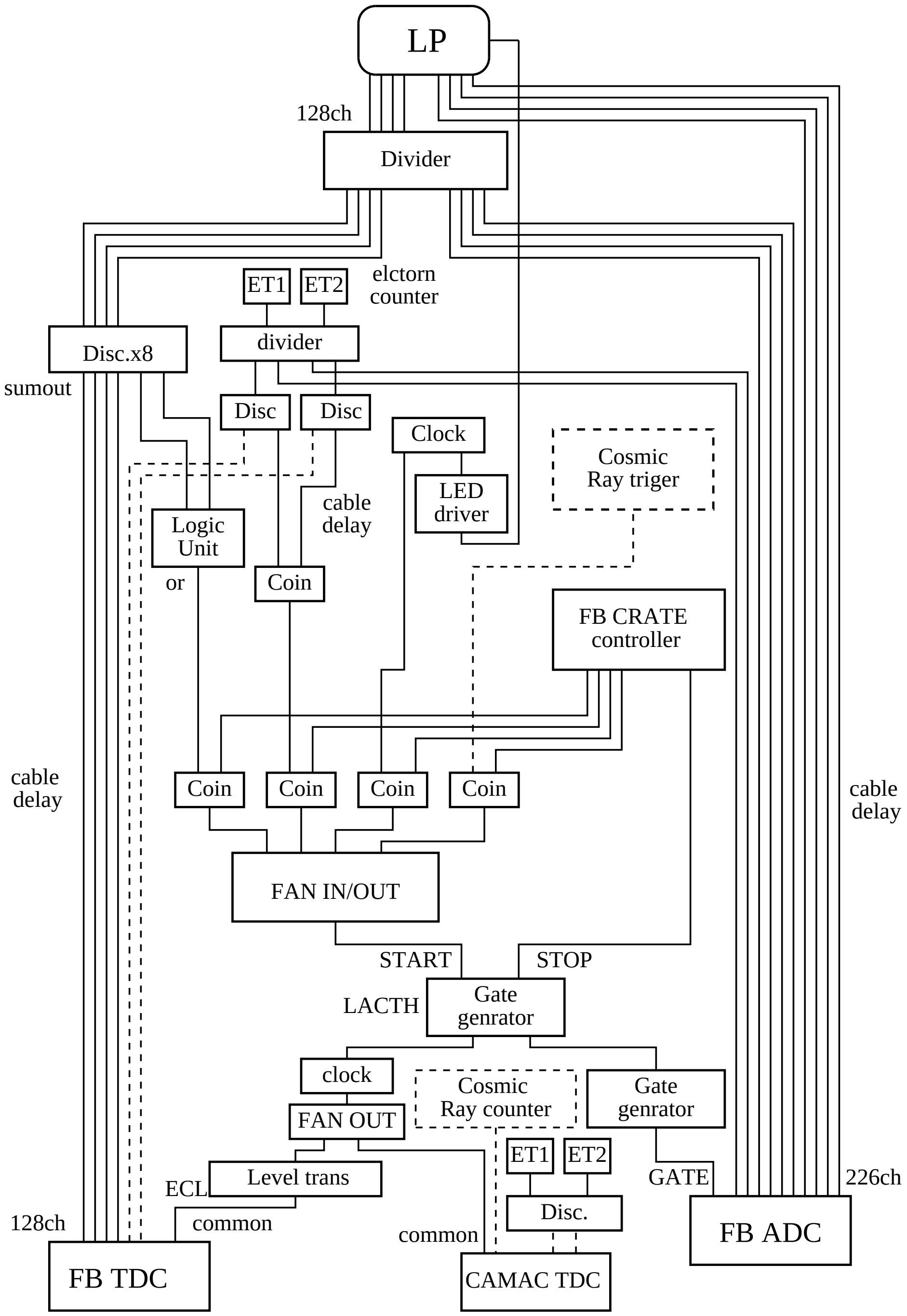

Figure 7.6: Schematics of the DAQ for most of the LP tests

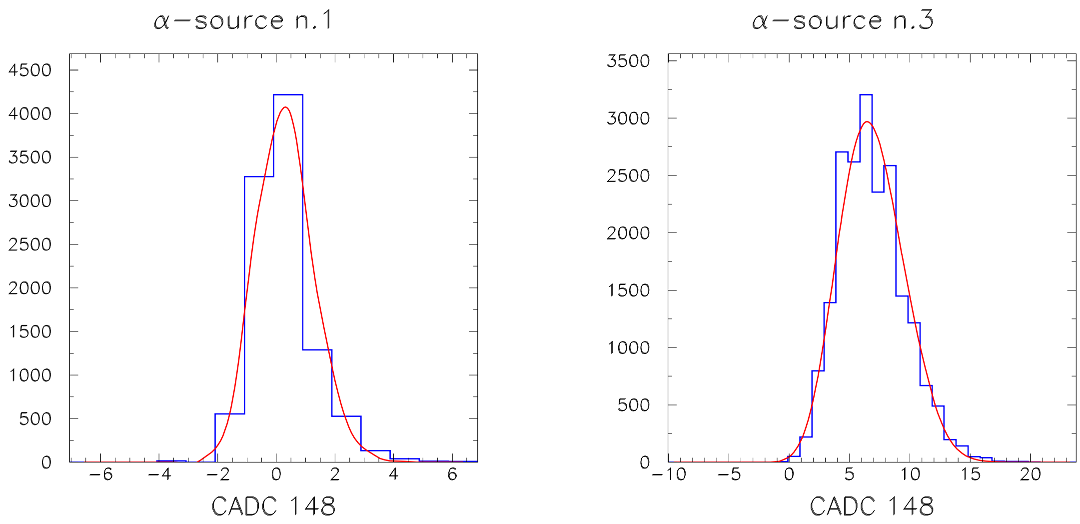

Figure 7.7: Examples of Poisson+Gaussian fits to the PMT charge distributions.

are used. The position of the sources was changed at the beginning of 2003 hence for each PMT up to 8 α-source positions can be included for the QE extraction, provided that a certain care is taken in putting all different runs together.

There are PMTs showing evident deviations from linearity for a low number of expected photoelectrons. This effect does not seem to be caused by differences in the α-sources, in fact different sources seen at the same angle show the same pattern of deviation from linearity. It is therefore plausible that there are systematics which are not properly taken into account in the simulation (*e.g.* reflection on PMT windows for large incidence angles) which cause these effects. Taking into account the Fresnel reflection on PMT windows, helps in reducing these effects and in restoring a linear relation.

We estimate that this procedure cannot give the QEs to better than $20 \div 30\%$ for these PMTs: the average uncertainty, on the other hand, can be estimated by comparing, PMT by PMT, the quantum efficiencies extracted with the method above in different runs, separated by a long time period (months) in which the calorimeter has been evacuated and re-filled, and moreover the position of the alpha sources was changed (and the LP moved from Japan to Switzerland!). An example of such a comparison is shown in Figure 7.10*a*. Figure 7.10*b* shows the distribution of the QE difference over QE sum for the same data. On average the QEs are consistent within few percents in average.

Modeling the α-sources is a critical issue for determining the QEs, and furthermore the number of points is limited. For this reason an alternative procedure is necessary for the precise knowledge of the PMT quantum efficiencies in the final experiment. A dedicated test station is being built and installed in Pisa to perform such measurements, together with characterization measurements for each PMT. The PMT test station will be the subject of Chapter 11.

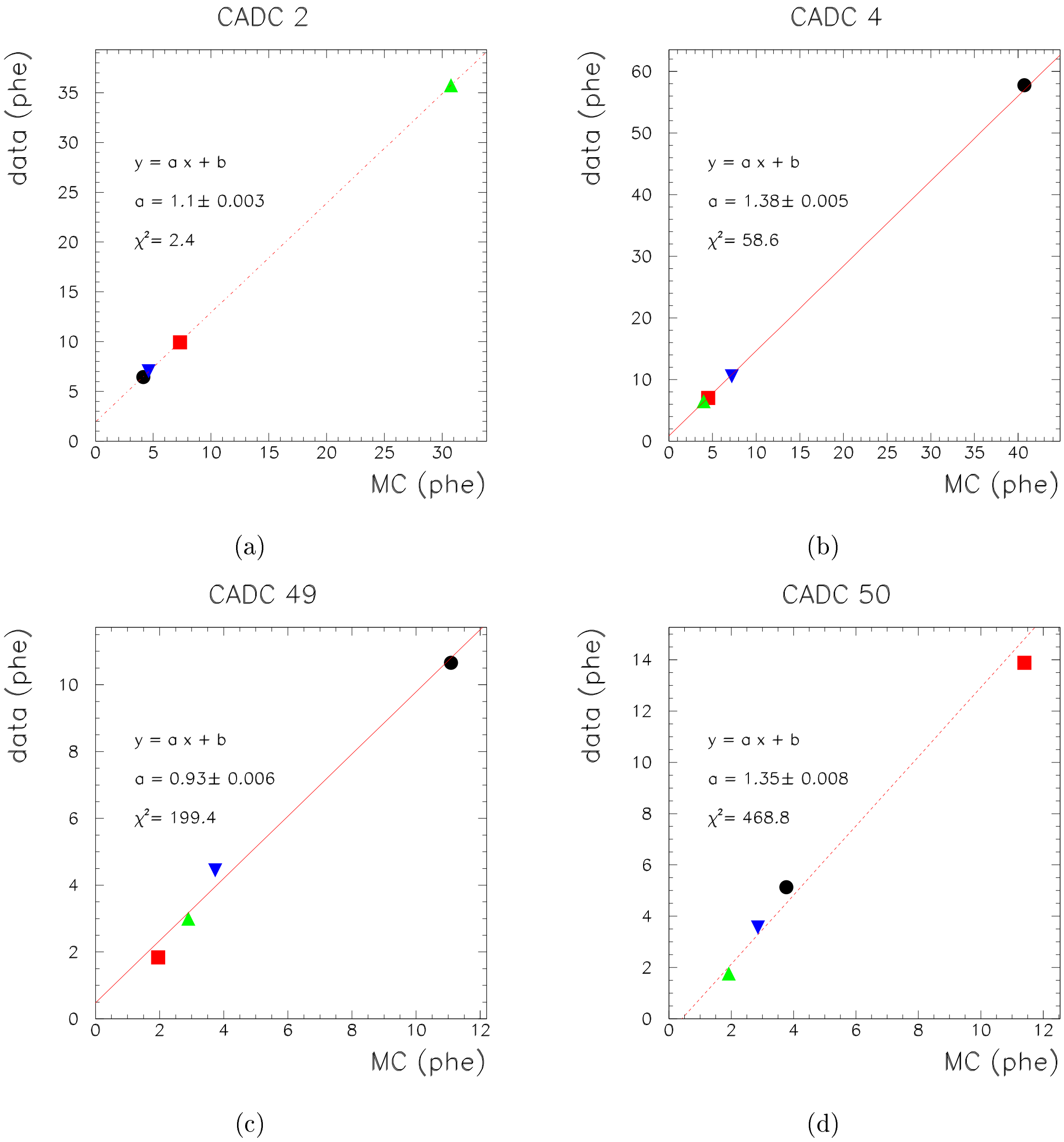

Figure 7.8: Examples of linear fits to extract the PMTs quantum efficiencies. The linear relation is pretty well verified even if there are some distortions for small number of photoelectrons. In the MC a nominal QE of 5% is included, therefore the fitted value a is the “true” quantum efficiency in units of 5%.

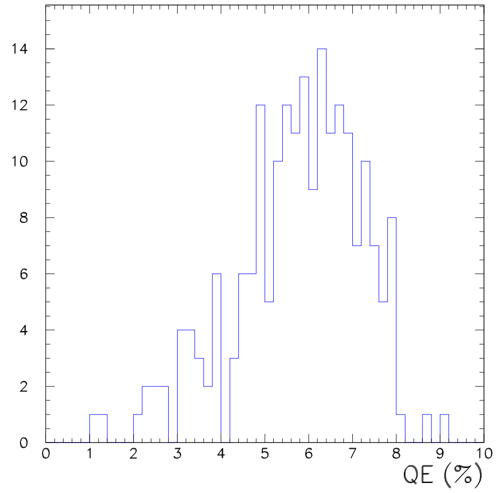

Figure 7.9: The distribution of the measured quantum efficiencies for all the PMTs.

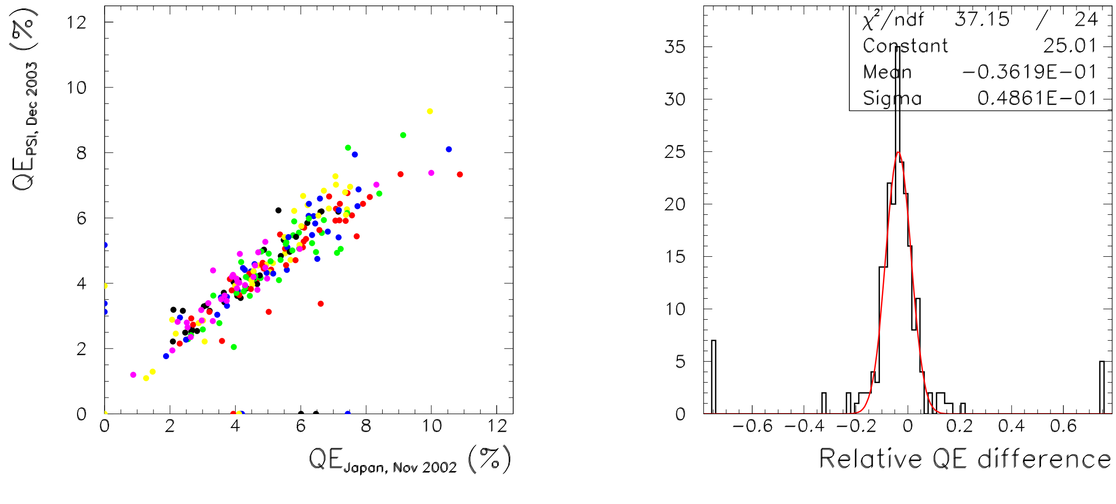

(a) (b)

Figure 7.10: (a) Comparison of the quantum efficiencies obtained with the stated method in two different periods; (b) the quantity $QE(1) - QE(2)/QE(1) + QE(2)$ is plotted and fitted with a Gaussian, whose sigma is 5%.

Another possibility that has been explored to limit the way unknown reflections affect the QE determination, is to put inside the calorimeter thin metal wires with $\alpha-$sources electro-deposited in several hot-spots. These wires have already been installed in the LP and will be tested in a forthcoming beam period (fall 2004).

7.3.4 Gain calibration

The gain of each PMT is measured at least twice a day, during normal operation, using the following procedures.

Let N be the average number of photoelectrons seen when a certain amount of light impinges on the PMT; if the PMT current output and the ADC integration are linear the ADC counts corresponding to the anode charge q is linear with the number of photoelectrons;

$$q = gN + q_0, \tag{7.1}$$

where g is the gain and q_0 the pedestal. For a given light intensity N obeys a poissonian statistics (which can be approximated with a gaussian if $N > 10$). The variance of the charge distribution is linear with N:

$$\sigma^2 = g^2 N + \sigma_0^2, \tag{7.2}$$

σ_0 being the r.m.s. of the pedestal distribution[2].

From Eqs.(7.1) and (7.2) we obtain

$$\sigma^2 = g(q - q_0) + \sigma_0^2. \tag{7.4}$$

By varying the light intensity, both the average charge and its variance should scale accordingly. The gain for each PMT is obtained by a linear fit of σ^2 vs q as in (7.4).

Implementation

LEDs were used in the detector as a tunable light source for gain measurement. The diode current could be varied by using a CAMAC LED driver (CAEN C529) triggered by a TTL pulse at 100 Hz. The LED driving pulse amplitude is remotely controlled via DAC settings of the LED driver, to scan the light intensity in 5 steps, as shown in Figure 7.11. For each step, a pre-set number of events is accumulated into a histogram; a gaussian fit is made to this histogram from which the average charge and variance are extracted (see Figure 7.12a).

In order to let all the PMTs see enough photoelectrons for the Gaussian approximation to be valid, we flashed simultaneously pairs of LEDs on opposite faces and had therefore four possible LED pair choices. By choosing different LED sets we could explore the charge linearity over the complete ADC range (see Figure 7.12(right)).

[2] Eq.(7.2) is obtained by neglecting the intrinsic PMT resolution of the single phe pulse. The inclusion of this effect slightly modifies this formula which becomes:

$$\sigma^2 = (g^2 + \sigma_g^2)N + \sigma_0^2, \tag{7.3}$$

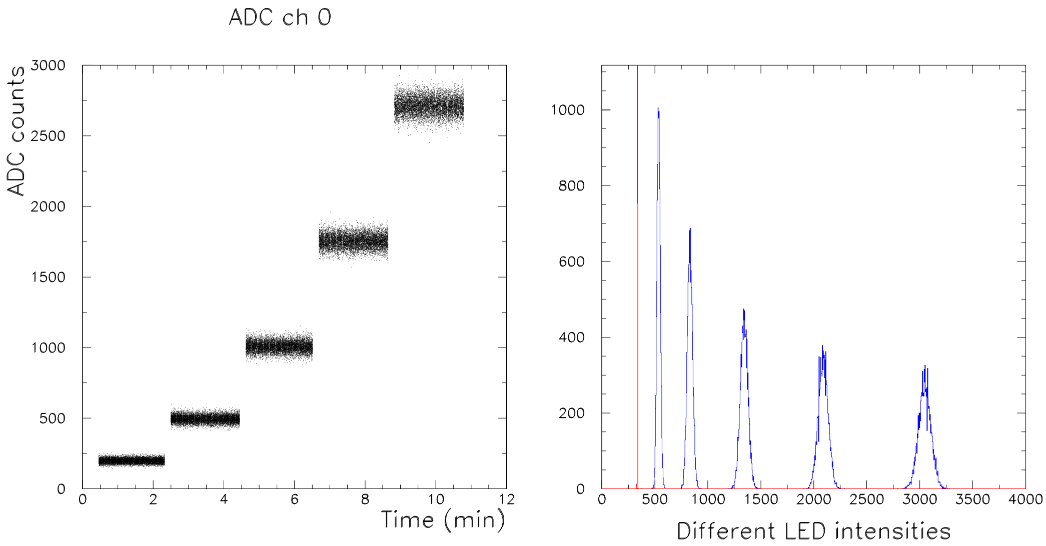

Figure 7.11: ADC spectrum of one channel (PMT 0) following the different LED intensities.

Stability checks

The linear dependence on both q and σ^2 on the number of photoelectrons is satisfied if the LED is stable.

LED intensity fluctuations during single runs (10 minutes, short–term variations) would increase the variance of the charge distribution, therefore making additional terms appear in Eq.(7.2), while the average charge would not be affected. The linear relation of Eq.(7.4) would therefore be no longer valid.

If LED fluctuations were instead sufficiently slow so as to change only the average number of photoelectrons from run to run (long–term variations) eq.(7.4) would still hold and the gain determination would not be affected.

Short-term stability

In Figure 7.13 we show the distribution of the estimated total number of photo-electrons[3] for a particular LED. Since the RMS of this distribution is less than 1% of its average we estimate that LED (short–term) intensity fluctations are below this value.

We therefore decided to keep also the statistical error below 1% in the gain determination by collecting 10,000 events for each LED intensity (less than 2 minutes at a rate of 100 Hz). The plot used for the gain determination of a particular PMT is shown in Figure 7.14(left).

where σ_g is the resolution on the single phe. We note that the even with this additional term the variance is linear with the number of photoelectrons.

[3]For a 10^6 gain one ADC channel corresponds to 1.25 photoelectrons

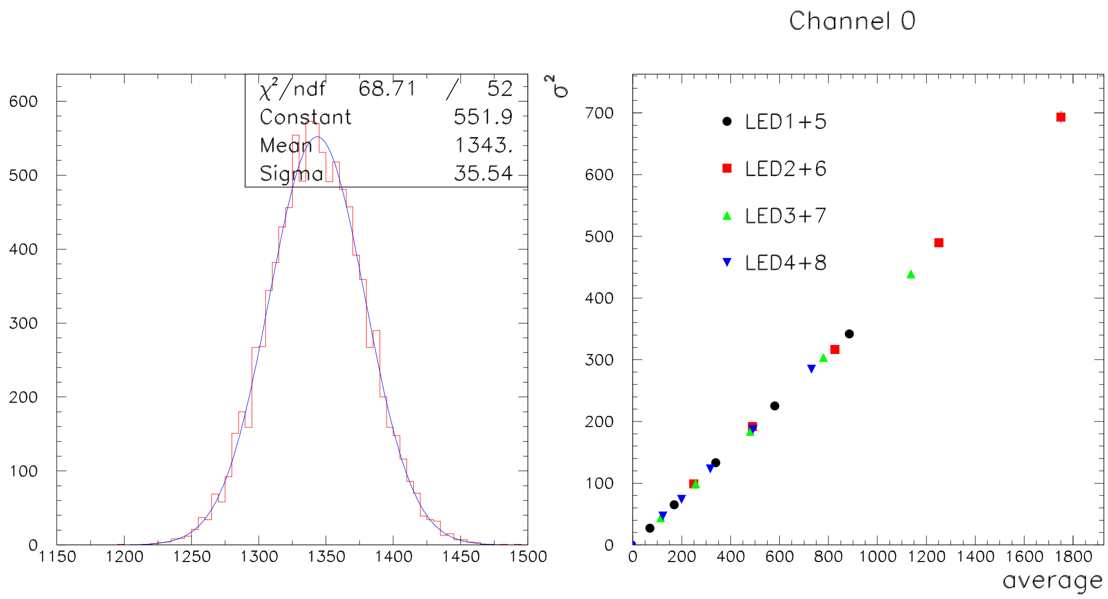

Figure 7.12: (Left) Gaussian fit to one ADC spectrum. (Right) Charge values obtained for PMT 0 by flashing one LED pair at a time. Linearity seems to hold all over the ADC range.

In Figure 7.14(right) we also show the distribution of the gain error as determined from the fit for all the PMTs. The compatibility with the expected statistical error in the gain determination is a further hint on the validity of the linear relation 7.4.

The stability of the gain determination for a particular LED pair was also checked by looking at the distribution of the ratio of the gain determined in two consecutive runs by flashing the same LED pair. The RMS of this distribution (shown in Figure 7.15) is 1.5%.

LED intensity long–term stability

We monitored the PMT signals for about two hours after turn-on. During this period we flashed LED's 1 and 5 (placed on the right and left side of the prototype entrance window respectively) and took data at regular intervals (one run every 5 minutes); during each of these runs we collected 1000 events for each LED setting. The average charge for one PMT as a function of time is shown in Figure 7.16: it varies with a period of $\sim$ 1 h and $\sim$ 10% in amplitude.

All the PMTs exhibit the same behaviour as can be seen in figure 7.17(left). This slow, coherent behaviour, which could be due to slow changes in the driver input, should not, as previously said, influence our gain determination: in figure 7.17(right) we show the gain evaluated for the same PMT of Figure 7.16 which is stable within error during the same period of time (these runs where taken with low statistics, 1000 events, hence the uncertainty on the gain determination is larger).

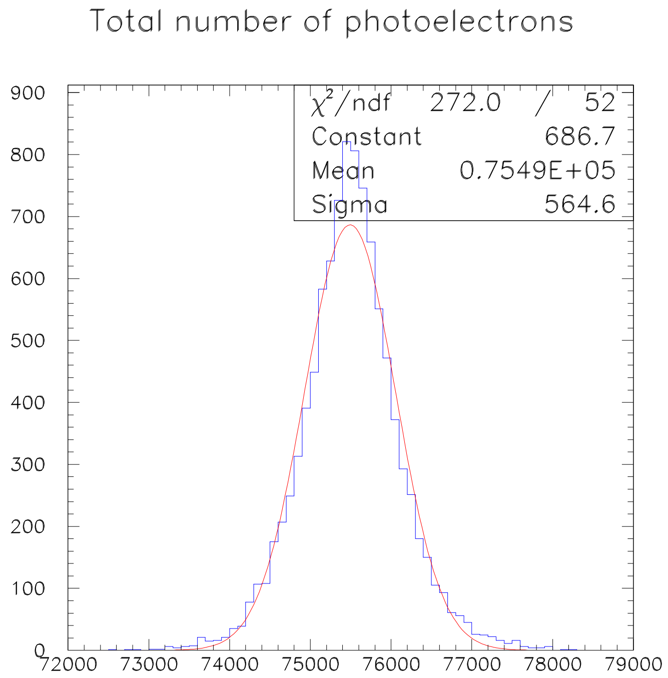

Figure 7.13: Total number of photoelectrons recorded for a particular LED intensity. Its RMS is less than 1%.

Accuracy of the method

The method accuracy was determined by flashing in turn all the four LED pairs and extracting the average gain for each PMT and its standard deviation. In Figure 7.18a we plot for each PMT the standard deviation of the gain distribution. This quantity is typically between 1% and 4%. PMTs with higher fluctuations (i.e. RMS>5%) have been checked one by one and exhibit different problems (large pedestal, bad cabling,...). An example of a PMT with a problem in the ADC readout is shown in Figure 7.18b.

Gain stability

Gains were determined about twice per day during data taking with the large prototype and could therefore be followed for long periods of time. In fig 7.19 we show the gains of two photomultipliers for a period of about one month.

The Large Prototype PMTs gains were measured with a simple and fast procedure. The uncertainty on the gain determination was estimated to be less than 4% for all PMTs. This uncertainty should be sufficient for reaching a systematic error on the energy determination of 52.8 MeV photons due to the gain knowlededge below 1%.

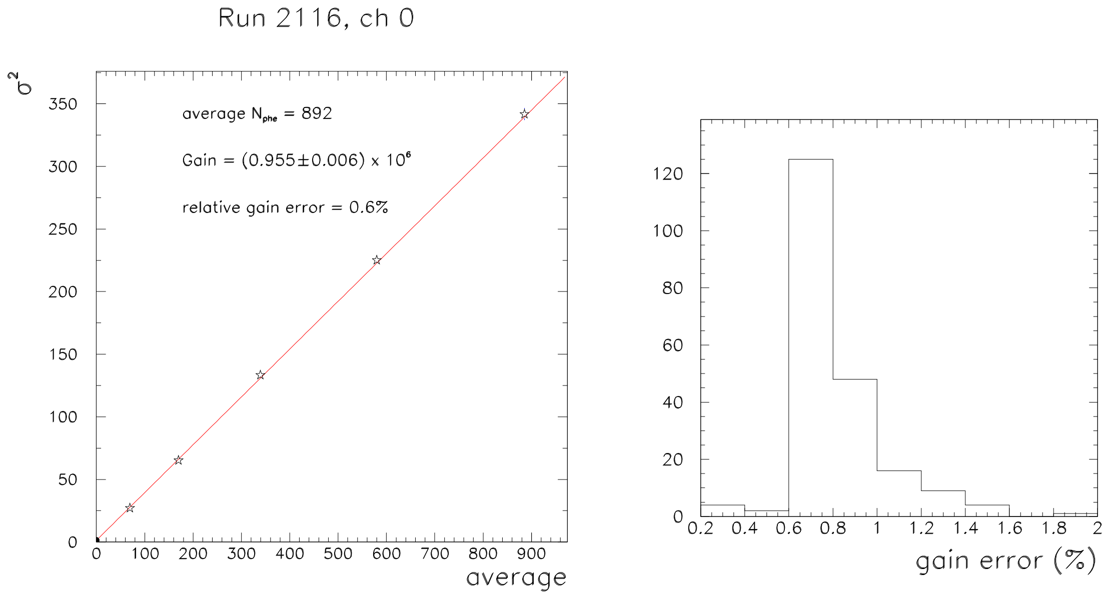

Figure 7.14: Determination of the gain for a particular PMT by using 10000 events per peak (left) and distribution of the error in the gain determination (right).

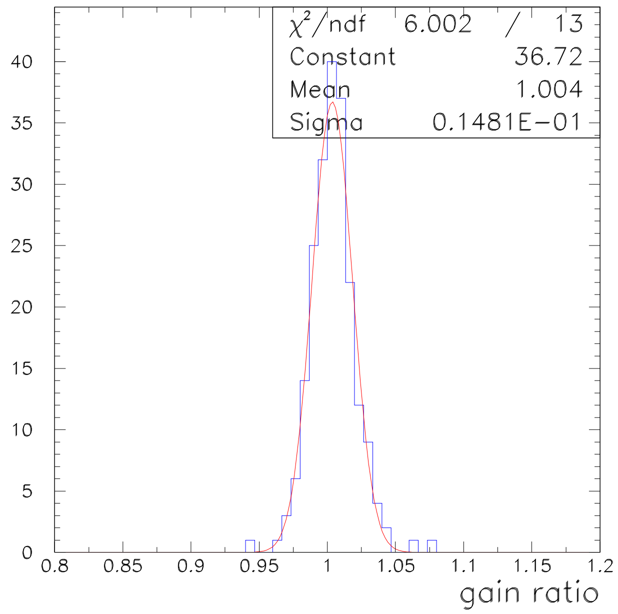

Figure 7.15: Ratio of the gain obtained in two consecutive runs, flashing the same pair of LED.

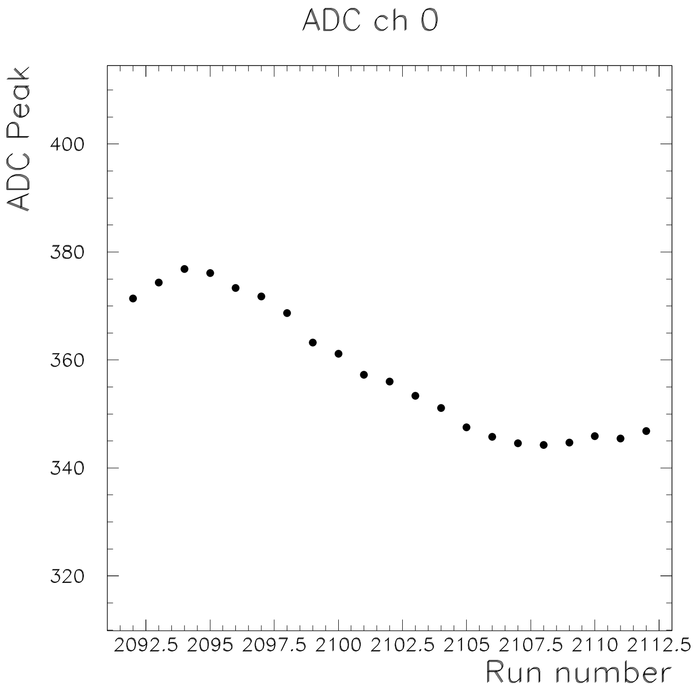

Figure 7.16: Time variation of the ADC peak for PMT 0.

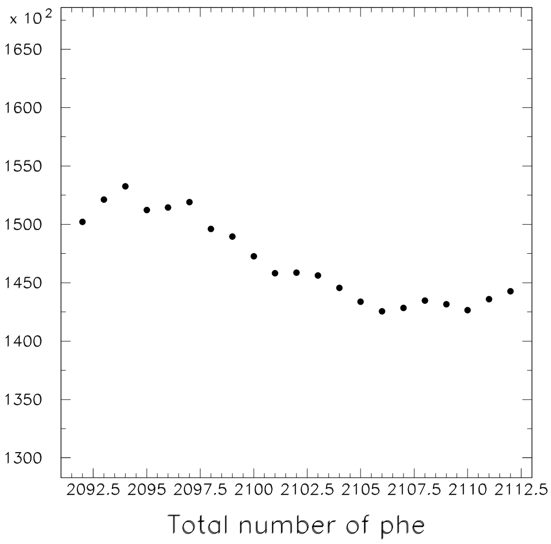

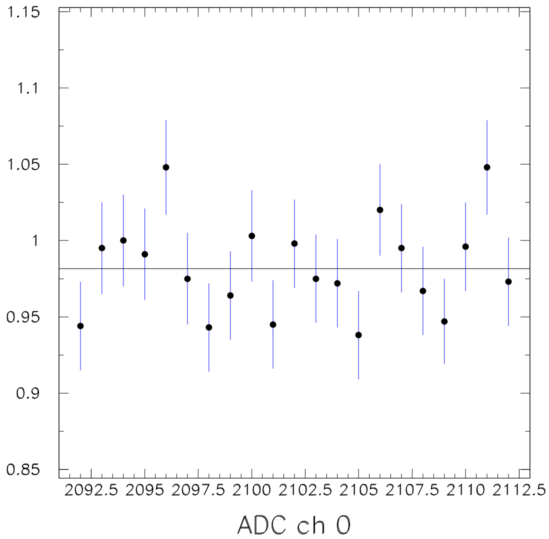

Figure 7.17: (Left) Total number of phe's as a function of time: (right) gain variation for PMT 0.

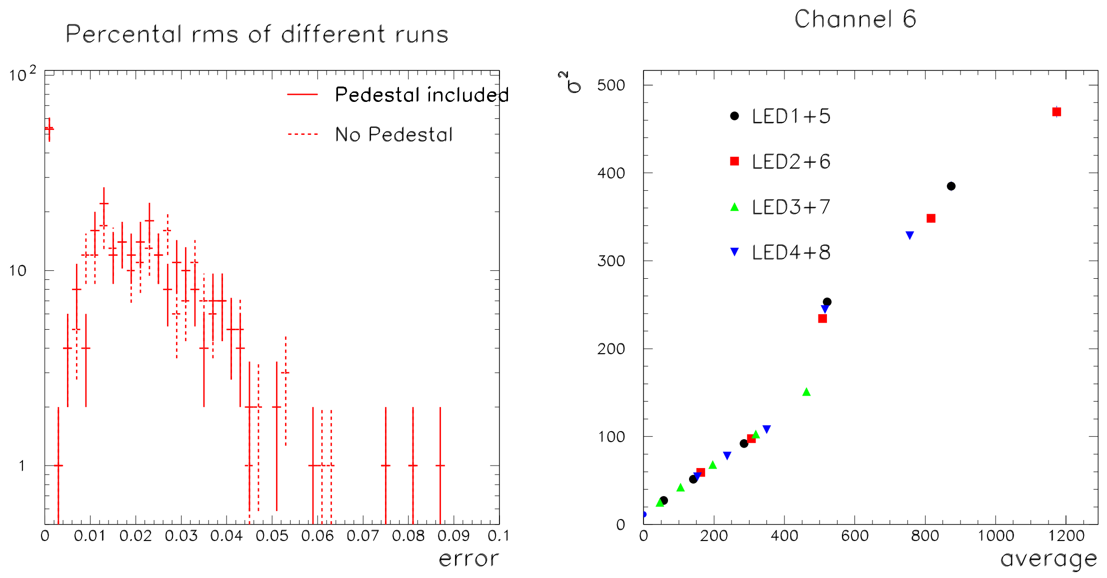

(a) (b)

Figure 7.18: (a) Distribution of the RMS of the gain for four runs taken with four different LED pairs; (b) A PMT which exhibit a bad behavior.

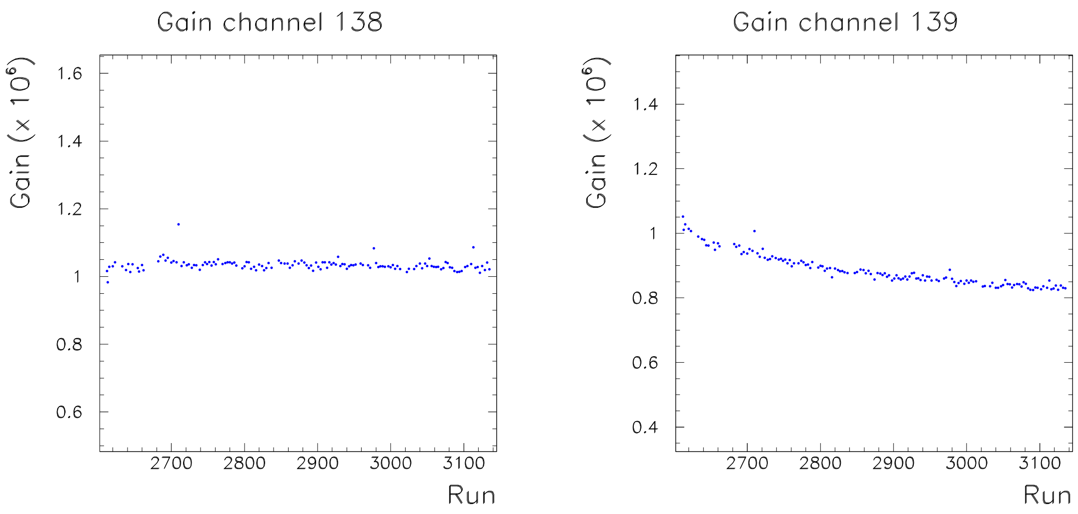

Figure 7.19: Gain of two photomultipliers for a period of about one month

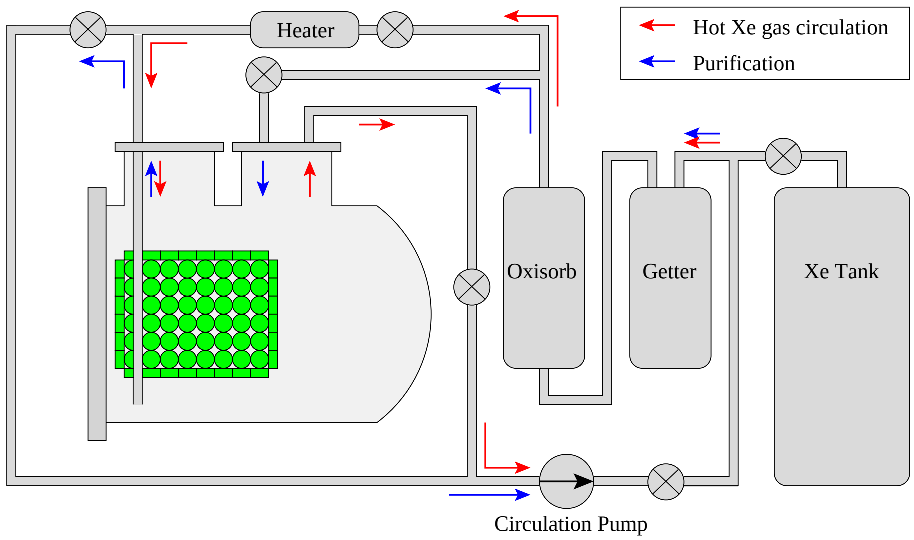

Figure 7.20: Schematic diagram of the circulation/purification system installed during LP tests.

7.4 Physics measurements during normal operation

In the first stages of the large prototype operation, a strong absorption of scintillation light was found by studying α-source events in liquid Xe. After systematic studies on the residual gas before the liquefaction, by means of mass spectroscopy and build-up tests (*i.e.* pressure increase with time after a period of evacuation), we found that a possible explanation was that water was desorbed from the G10 holder and/or acrylic fillers into the LXe.

We introduced a circulation–purification system, shown schematically in Figure 7.20. Liquid Xe was evaporated, pumped by a diaphragm pump through an Oxisorb cartridge and a molecular filter [95, 94], and condensed back into the cryostat. The flow rate of gaseous Xe was approximately 500 cm^3/min, hence a whole volume could be circulated in a month time.

We used cosmic-ray muons as well as α-source data to monitor the light yield during circulation. Three pairs of trigger counters (TC1, TC2 and TC3) were placed above and below the vessel to select vertical muons (Figure 7.4). The purification was performed continuously for over 1200 hours. In Figure 7.21*a* the relative light increase for PMTs at two different distances from the α-source is shown. In Figure 7.21*b* the light collected by all PMTs for vertical muons is shown as a function of time.

To systematically study the purification process we carried out various tests, such as stopping or increasing the circulation flow rate, by-passing the purification line etc. We reached a stable configuration after one month (700 hours) of purification.

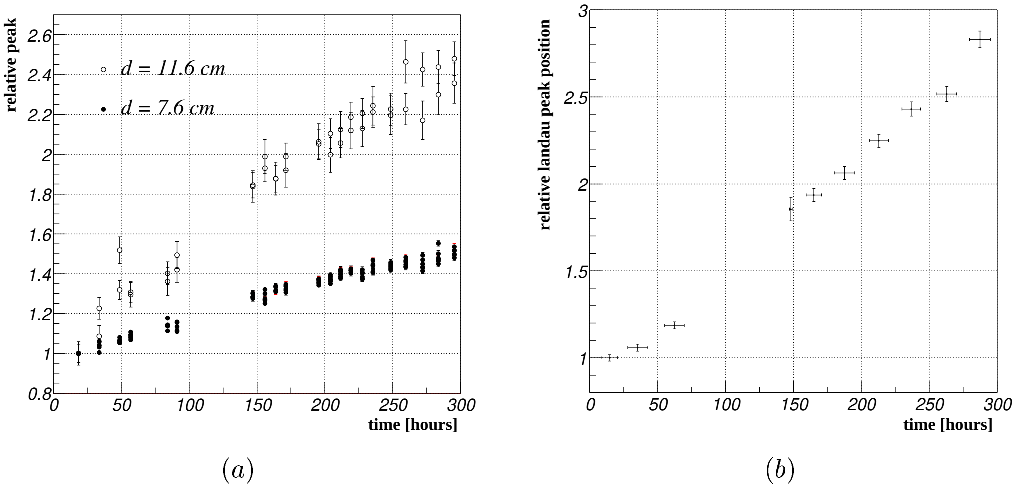

Figure 7.21: (a) Light yield improvement for alpha events observed by PMTs located at 7.6 cm and 11.6 cm away from alpha sources (left). (b) The light yield for cosmic ray events.

7.4.1 Absorption length estimate

The attenuation length was evaluated by using α-source data: the light collected by each PMT, normalized to unit solid angle, was plotted against the PMT-source distance. The distribution in gaseous Xe is consistent with a constant function, hence attenuation in GXe is negligible.

The attenuation in liquid Xe is due to both absorption and Rayleigh scattering. The output of each PMT was compared either to the one expected from the Monte Carlo simulation with no absorption and variable λ_{R}, or to the signal seen with gaseous Xe, and then plotted against the PMT-source distance.

Figures 7.22a and b show the distributions at the beginning of the purification (black circles) after two weeks of purification (red squares) and after one month of purification (blue stars). The initial absorption length was estimated to be of the order of 7 cm, while after one month purification the distribution is consistent with no absorption. An exponential fit to the distribution allows us to extract a lower limit for the absorption length (related to the slope of the function) and to compare the measured light yield (related to the intercept at zero) with values in literature. The correlation of these variables is shown in Figure 7.23b where the two lines are the 68% and 95% confidence level contours, which give the values shown in Table 7.2: at 90% CL the light absorption length is $\lambda_{\mathrm{Abs}} > 95$ cm. It is apparent that the sensitivity on λ_{Abs} is limited by the dimension of the large prototype (50 cm).

After the successful purification of the liquid Xe under detector operational conditions, efforts have been focused on reducing the initial amount of water contamination in the vessel, and on improving the purification speed.

We replaced most of the acrylic parts with Teflon parts in a clean room, to suppress out-gassing

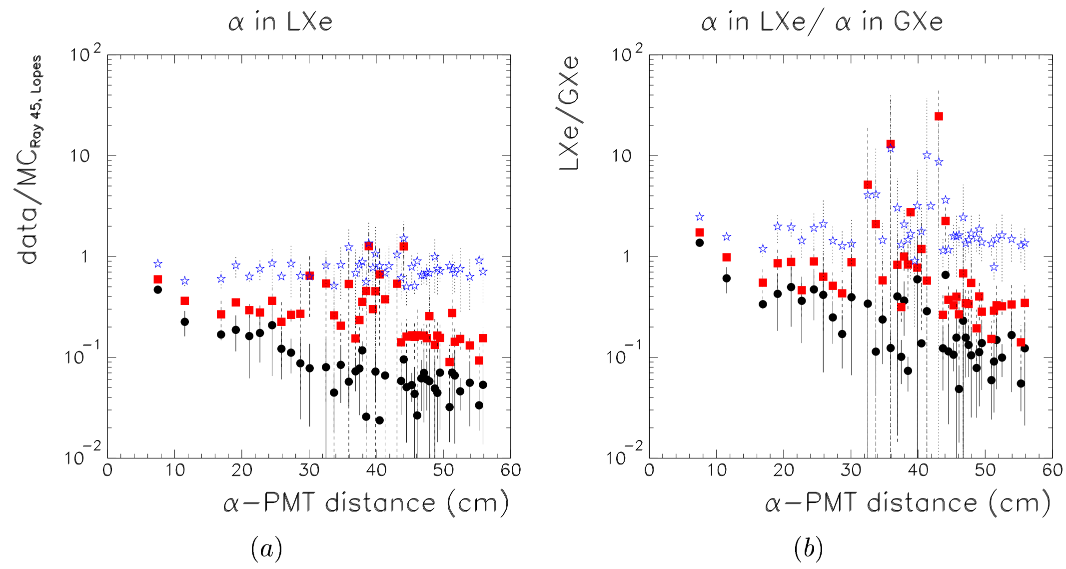

Figure 7.22: Comparison of alpha data in liquid Xenon to Monte Carlo simulation (a) and to alpha data in cold gaseous Xenon (b) for three different runs: before the purification (circles), after two weeks of purification (squares), and after one month of purification (stars).

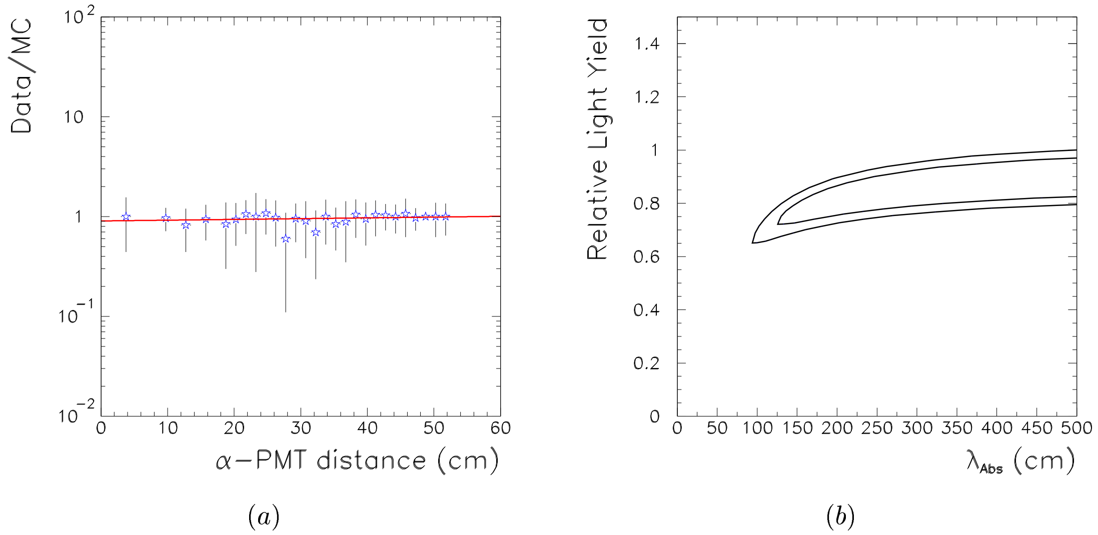

Figure 7.23: (a) A typical distribution used to evaluate Xe purity (absorption length and light yield) during the large prototype normal operation; (b) The confidence regions at 68% and 95% confidence level for λ_{Abs} and for the light yield.

CL	λ_{Abs} (cm)	Light Yield (phe/MeV)	W_{ph}^{α} (eV)
68%	> 125	37500^{+3000}_{-7000}	27^{+5}_{-2}
95%	> 95	37500^{+4000}_{-10000}	27^{+7}_{-3}

Table 7.2: Typical measured values for the absorption length lower limit and for the light yield for alpha sources.

in the inner chamber, resulting in an initial λ_{abs} of 30 cm in subsequent tests.

We developed a liquid-phase purification system with a fluid pump to increase the purification efficiency that will be tested at the end of year 2004. In such a system the circulation speed could be increased up to 100 l/hour of liquid Xe, corresponding to 830 l/min in gas, more than one thousand times faster than the present system.

7.4.2 Light yield for α and γ

We measured the different light yield of liquid Xe for photons and α-particles. An Am/Be source was placed directly in front of the entrance window of the large prototype. The Am/Be source produces neutrons with an energy spectrum that extends up to 10 MeV, and a photon of 4.44 MeV, which comes from the de-excitation of the daughter carbon nucleus. We recorded simultaneously the signal from this photon together with the signal coming from the α-sources placed inside the prototype. The two signals could be separated using a topological cut, which selects the signal from the α-sources thanks to their easy position identification. Using the 4.44 MeV gamma to set the energy scale and assuming linearity in this energy range (the energies of the α-source and of the AmBe gamma-ray are not much different), the energy of the α-source peak is found to be overestimated. Taking into account the energy loss of alpha particles in the thin gold coating the light yield for α sources is found to be $(18 \pm 2)\%$ larger than that for electrons. This, together with the measurement of the absolute light yield for the alpha sources gives, assuming negligible absorption,

$$W_{ph}^{\alpha} = (27 \pm 2)\ \mathrm{eV} \tag{7.5}$$

$$W_{ph}^{e} = (32 \pm 3)\ \mathrm{eV}. \tag{7.6}$$

7.4.3 Radioactive background

As a by-product of the data acquisition of α-source runs with high PMT gain ($g = 5 \times 10^6$) we were able to observe events due to environmental radioactivity.

Since there was no specific trigger for such events, an off-line selection was needed to disentangle the α-source signal from the low-energy environmental background. A geometrical cut was made to select events which were reconstructed at a z (depth inside the detector) not consistent with the position of the alpha sources. In this way we selected events whose reconstructed positions, projected on the front face, are uniformly distributed. This can be seen from Figure 7.24. In the

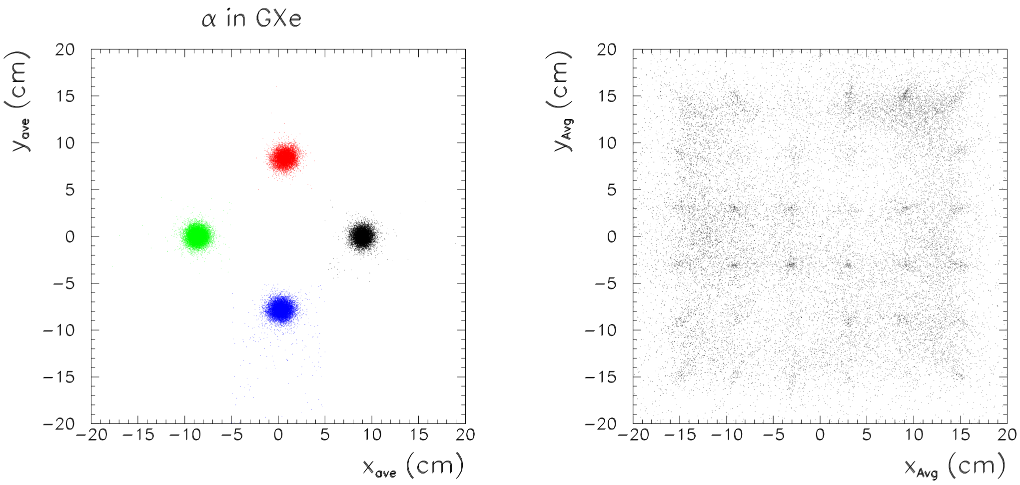

(a) (b)

Figure 7.24: Distribution of the reconstructed event position projected on the front face for (a) α-source events and (b) radioactive environmental background

energy spectrum of such events (Figure 7.25) we see the presence of two major peaks which can be identified with the lines coming from Tallium (2.614 MeV) and Potassium (1.461 MeV) decays. The energy scale was set using the α-source peaks as a reference, taking into account that for an α-source on the wall the light seen by the LP is half of the light that the same source would produce if placed at the detector center; Monte Carlo simulation confirms this naive expectation.

The radioactivity peaks are not very prominent even though other peaks seem to appear. The number of events is not sufficient to extract the prototype resolution at these energies but this is the first time that such a signal is observed with a liquid Xe scintillation calorimeter.

7.5 Conclusion

The successful operation of a liquid Xe calorimeter prototype has been described. The necessary issue of Xe transparency to self-scintillation light has been experimentally addressed and an absorption length $\lambda_{\mathrm{Abs}} > 95$ cm has been achieved. We now turn to the performances of such a device as a 52.8 MeV photon detector.

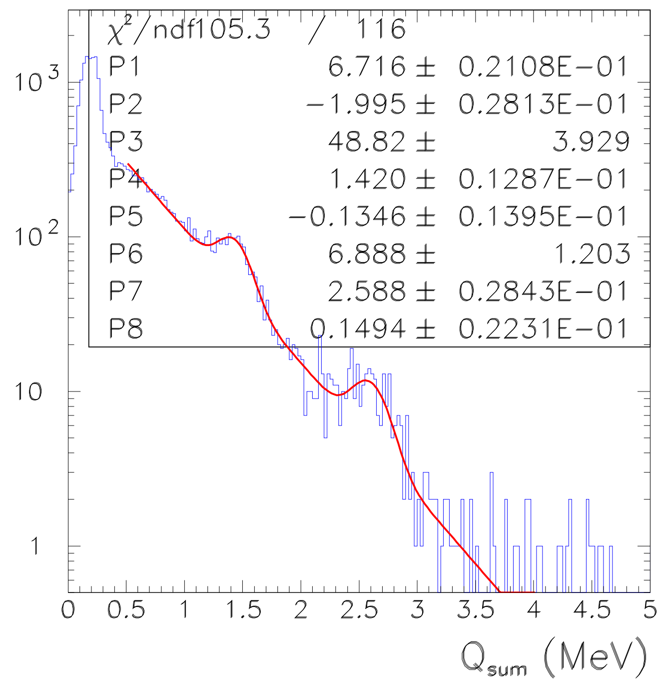

Figure 7.25: Energy spectrum of radioactive background events

Part III

The charge exchange test at PSI

Chapter 8

Production of monochromatic photons

8.1 Introduction

The validation of a new detector requires tests in a condition close to that envisaged for its utilization in experiment. We have seen in the previous Chapters the response of the large prototype to α-sources, cosmic ray muons and low energy gammas. There is the need to test the response of the large prototype with photons in an energy range comparable to $m_{\mu}/2 \sim 52.8$ MeV and to make a comparison with the Monte Carlo simulation predictions, in order to gain the necessary knowledge to design the final MEG experiment calorimeter.

The experimental issue of obtaining photons in the correct energy range can be addressed in many ways. We will briefly review in the following sections various ways of obtaining such photons, spending much detail on the actually applied technique, namely the measurement of photons coming from π^0 decays from π^- charge exchange on protons.

8.2 Production of "monochromatic" high energy photons

The production of monochromatic photons of energy in the correct range ($\sim$ 50 MeV) is of paramount importance to estimate both the energy and the timing resolution of the large prototype. Of course the measured energy spectrum, representing the response function to a δ-function excitation, immediately gives the energy resolution of the detector, if the incoming photon is monochromatic.

In the case of the MEG liquid xenon calorimeter, as in all similar devices, such a response is not a pure Gaussian but exhibits a tail on the left side (see, *e.g.* Figure 6.15) due to unavoidable energy leakage, determined by the finite size of the detector and, ultimately, by low energy photons and electrons which are backscattered and lost for good. The FWHM of this distribution is what we quote as our "resolution" but the difference between the high- and low- energy tails is worth some more remarks: we are searching for events at the energy spectrum end-point, 52.8 MeV, so we select the signal region as centered to the 52.8 MeV peak; the right-tail resolution (σ_R) is linked to the probability that a photon of lower energy is reconstructed in this signal region (*i.e.* background enters in the game) while the lower energy tail (σ_L) is related to the probability that a photon of the correct energy is degraded outward the signal region (*i.e.* we loose a good photon).

It is important to notice that one could, in principle, shift the left edge of the signal region towards higher energies, reducing the number of background photons at the price of reducing the efficiency on the signal and requiring a longer running time.

For a timing resolution measurement, the monochromaticity of the photon is not stringent but the capability of identifying the photon production time and place becomes crucial. We will review some techniques for producing high energy gammas with these requirements in mind: radioactive sources, inverse Compton scattering, tagged electron beam and π^0 decay.

8.2.1 Photons from radioactive decays

The most common sources of mono-energetic γ-rays are radioactive sources such as, *e.g.*, $^{60}_{27}$Co (E_γ = 1.173 MeV and 1.333 MeV, τ =5.271 y) whose photons come from de-excitation of internal nuclear levels of the daughter $^{60}_{28}$Ni nucleus. Because of the peculiar origin of these photons their energy is limited to few MeVs for isotopes whose lifetime allows easy handling. Furthermore, the higher the energy of the photon, the shorter the lifetime of the radioactive isotope.

Photons from nuclear level de-excitation of higher energy must be sought for in bombarding (for instance with protons or neutrons) a suitable target. Examples of such reactions are:

- ^{7}Li(p,$\gamma_{19.6}$)^{8}Be, together with ^{19}F(p,α)^{16}O* $\rightarrow^{16}$O+$\gamma_{6.1}$, in which 17.6 MeV and 6.1 MeV photons can be obtained by bombarding a LiF target with $\sim$ 500 keV protons [97];

- ^{58}Ni(n,γ)^{59}Ni* $\rightarrow^{59}$Ni+$\gamma_{9.0}$ which happen, among others with the emission of lower energy photons, for thermal neutron capture on Nickel.

Care must however be taken to guarantee the presence of a line, by keeping the background photons at a negligible level.

8.2.2 Compton backscattering of LASER beams

This technique was first developed in late 60s [98] after an idea of Arutyunyan and Tumanian [99] and, independently, by Milburn [100], who pointed out that Compton scattering of LASER light against high energy electrons can produce γ-ray beams. In the scattering process, depicted in Figure 8.1, a LASER photon of energy k_1 strikes a relativistic electron of energy E with a relative angle $\theta_1 \approx 180°$. If θ and θ_2 are the values of the photon scattering angles with respect to the

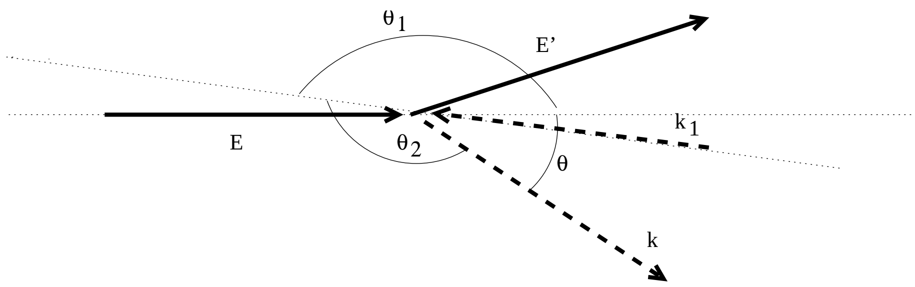

Figure 8.1: The kinematics of Compton scattering in flight

incoming electron and photon beams respectively, the energy of the final photon k is

$$k = k_1 \frac{1 - \beta \cos\theta_1}{1 - \beta\cos\theta + \frac{k_1}{E}(1 - \cos\theta_2)} \tag{8.1}$$

where β is the electron velocity in units of the speed of light c [101]. With a relativistic electron source, $\beta \sim 1, \theta_1 \approx \theta_2 \approx 180°$ and $\theta \sim 0$, Equation (8.1) may be rewritten as

$$k = E\frac{z}{1+z+x} \qquad \begin{cases} z = \dfrac{4Ek_1}{m^2} \\ \\ x = (\theta\gamma)^2 \end{cases} \tag{8.2}$$

hence the maximum photon energy $k_{\max}$ is obtained for $x = 0$ (back-scattered photons) and the uncertainty on the outcoming photon energy is limited by the collimator size. If $\Delta\theta$ is the half aperture of the collimator the fractional energy resolution of the collimated beam is given by

$$\frac{\Delta k}{k_{\max}} = \frac{k_{max} - k}{k_{\max}} \approx \frac{x_{\text{coll}}}{1 + z + x_{\text{coll}}} \tag{8.3}$$

which is small provided that $x_{\text{coll}} = (\Delta\theta\gamma)^2 \ll 1$, *i.e.* the electron energy is not too high, and the angular divergence of the electron beam σ'_x is also negligible ($\sigma'_x \ll 1/\gamma$) otherwise it dominates the achievable angular collimation.

To give an order of magnitude for the various quantities mentioned in this section we can refer to the LASER-Compton Backscattering Facility available at the TERAS storage ring at ETL, Tsukuba, where a tunable Nd:YLF LASER is shot against 800 MeV electrons ($\sigma'_x \sim 0.15$ mrad). The energy attainable for different LASER overtones are summarized in Table 8.1. In a typical situation in which a 3 mm ϕ collimator is placed a few meters downstream the interaction point its contribution to the energy definition is of a few percents. A measurement with a Ge high-resolution spectrometer in this situation showed a 2.6% resolution FWHM at 10 MeV which is scaled to $\sim$ 10% at 40 MeV [102].

The backscattering facility at ETL was used for the first tests of the large prototype [103, 64]. For the aforementioned reason it was not possible to extract the LP resolution (FWHM), because the lower energy tail was dominated by the angular divergence of the electron beam. It was however

	λ (nm)	k_1 (eV)	k (MeV)
1st	1053	1.13	~ 10
2nd	527	2.32	~ 20
3rd	351	3.50	~ 30
4th	265	4.64	~ 40

Table 8.1: Main parameters of the ETL-LCS photon beam.

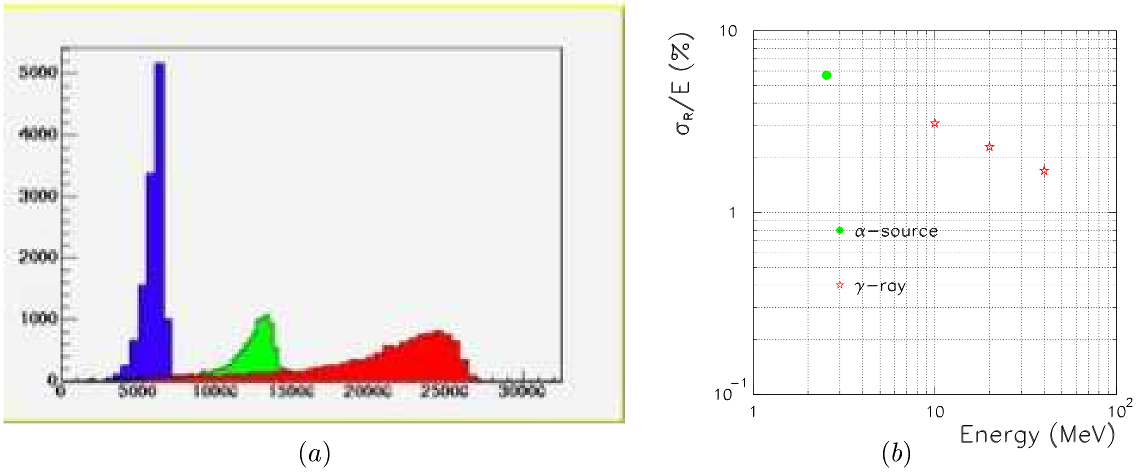

(a) (b)

Figure 8.2: (a) Q_{sum} spectrum of the 10 MeV, 20 MeV and 40 MeV photon from the ETL backscattering facility as seen by the large prototype (from ref. [103]); (b) Energy dependence of the high energy tail of the distribution (σ_R).

possible to gain information on σ_R and on LP position resolution. In Figure 8.2*a* we show the the photon peaks as recorded by the LP at the energies of 10, 20 and 40 MeV and in Figure 8.2*b* the Gaussian width of the right-hand tail is plotted as a function of the energy. It has the correct dependence on the number of photoelectrons collected, and a resolution (σ_R!) of $(1.2 \pm 0.2)\%$ is expected at 52.8 MeV.

The position resolution was measured by collimating the incoming photon using a lead brick with a 1 mm bore. Ten representative positions were tested, *e.g.* the PMT center, the mid-point of two PMTs, the mid-point of four PMTs etc. The algorithm described in the Monte Carlo chapter was used to extract the position resolution for each set-up. An average of the obtained values, which takes the relative probabilities of the various incidence positions into account, yields a $\sigma_x \approx \sigma_y \approx (3.4 \pm 0.2)$ mm [103].

8.2.3 Tagged electron beams

Another commonly used method for obtaining high energy photons consists in passing an electron beam of well-defined momentum through a thin target causing electrons to emit bremsstrahlung photons. The positron momentum at the target exit is eventually measured by a magnetic spectrometer. It is possible to associate to each photon an energy, by means of of the conservation of the electron plus photon 4-momentum, hence the name "tagged" photon beam. In this way there is, strictly speaking, no monochromatic photon but the energy of the produced gammas can be known at a better-than-percent level, depending on the electron momentum and momentum measurement setup.

8.2.4 Photons from π^0 decays

The neutral pion decays electro-magnetically in two photons with a branching ratio of 98.8%. The photons are emitted back-to-back in the π^0 rest frame with an energy of

$$E_\gamma^* = \frac{m_{\pi^0}}{2} \simeq 67.5 \text{ MeV}.$$

Once observed in the laboratory frame, where the π^0 moves with velocity β, both the photon's energy and direction are changed due to relativistic aberration and Doppler-shift. Indicating the center-of-mass quantities with an asterisk the result of a Lorentz transform to the laboratory frame gives (see Figure 8.3)

$$E_{1,2} = \gamma \frac{m_{\pi^0}}{2} (1 \pm \beta \cos\theta^*) \tag{8.4}$$

and the relative angle between the two photons in the laboratory frame is given by

$$\cos\xi = \frac{\gamma^2(\beta^2 - \cos^2\theta^*) + \sin^2\theta^*}{\sqrt{\sin^2\theta^* + \gamma^2(\beta + \cos\theta^*)^2}\sqrt{\sin^2\theta^* + \gamma^2(\beta - \cos\theta^*)^2}}. \tag{8.5}$$

A minimum angle exists in the laboratory frame between the directions of the two photons.

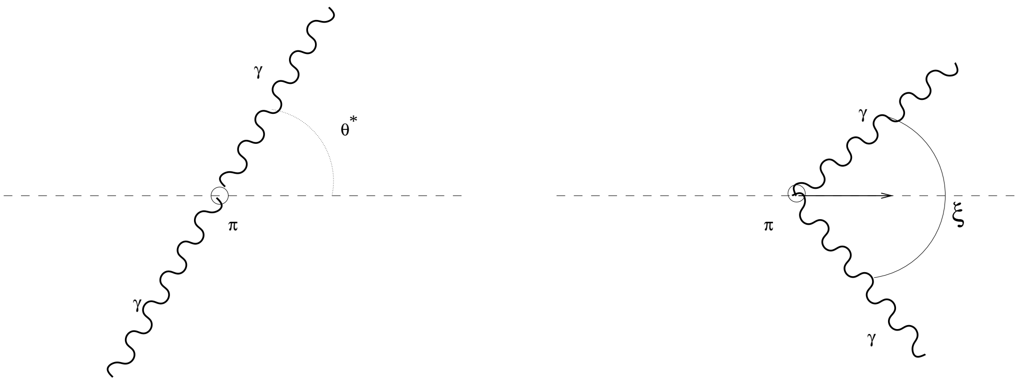

Figure 8.3: Kinematics of the π^0 decay in the center-of-mass frame (left) and in the laboratory frame (right).

As it is readily seen by differentiating Equation (8.4), the energy spectrum of the two photons in the laboratory frame

$$\frac{\mathrm{d}N}{\mathrm{d}E} = \frac{\mathrm{d}N}{\mathrm{d}\cos\theta^*} \cdot \frac{\mathrm{d}\cos\theta^*}{\mathrm{d}E} \tag{8.6}$$

is flat (the decay is isotropic in the pion rest frame, *i.e.* $\mathrm{dN/dcos}\,\theta^*$ is constant), and has a box shape between the energies

$$E_{\mathrm{Min}} = m_{\pi^0}\sqrt{\frac{1-\beta}{1+\beta}} \qquad E_{\mathrm{Max}} = m_{\pi^0}\sqrt{\frac{1+\beta}{1-\beta}}. \tag{8.7}$$

A strong correlation exists between the photon's opening angle and energies. In particular the extremal energies are obtained for photons which are emitted at 180° in the laboratory, that is along the π^0 flying direction.

This strong correlation between energy and opening angle can be used to precisely define the energy of one photon by tagging the direction of the opposite one.

The charge exchange reaction

Low momentum neutral pions can be obtained from π^- captured at rest on the protons present in a suitable target such as, for instance, hydrogen. The details of the slowdown process of π^- in hydrogen have been discussed in considerable detail by Wightman [104]. The significant sequence of processes is as follows.

1. Slowdown of the fast meson by the ordinary stopping power mechanism ($\sim 10^{-10}$ sec);
2. Slowdown by collisions with orbital electrons with velocity comparable to that of the meson (10^{-12} sec);
3. Capture of the meson in an outer orbit leading to an excited π^- H^+ system [105];

4. Reduction of energy of the neutral π^- H^+ system to the lowest quantum state. This latter process is not radiative but is due to collisions of the neutral system with other hydrogen molecules ($10^{-10} \div 10^{-9}$ sec).

In liquid or high pressure hydrogen the over-all time to enter the K shell is sufficiently short to compete effectively with the $\pi - \mu$ decay time (2.6×10^{-8} sec). Capture in flight, on the other hand, is considerably less probable, and its lifetime is of the order of $10^{-4} - 10^{-5}$ sec [106].

The reactions which then happen at rest are:

$$\pi^- p \rightarrow \gamma n \tag{8.8}$$
$$\pi^- p \rightarrow \pi^0 n. \tag{8.9}$$

Equation (8.8) is called "radiative capture" of π^- on protons and produces monochromatic photons with energy $E_\gamma = 129.4$ MeV together with monochromatic neutrons with kinetic energy $T_n \sim 8.9$ MeV. Note that the mean binding energy of the pionic hydrogen is equal to -0.37 ± 0.08 keV [107] and can be neglected in what follows.

Reaction (8.9) is called "charge exchange" reaction and produces monochromatic π^0s with kinetic energy $T_{\pi^0} = 2.88$ MeV ($\beta \simeq 0.203$) which immediately decay yielding a box-shape spectrum of photons with energies

$$54.9 \text{ MeV} < E_\gamma < 82.9 \text{ MeV}$$

The relative branching ratio between processes (8.9) and (8.8) is called the "Panofsky ratio" [106], and its value is $P = 1.546 \pm 0.009$ [108].

The correlation between the two photons energy and direction in reaction (8.9) is depicted in figure 8.4. From the figure it is apparent that in a configuration where a coincidence between two detectors placed on either side of the π^0 production target is required, even a modest collimation ($\Delta\theta < 5°$) is sufficient to define the energy of the least and most energetic photons (54.9 MeV and 82.9 MeV respectively) to better than percent level. The energy of the softer photon is extremely similar to that expected in a $\mu \rightarrow e\gamma$ decay.

This method of producing high energy photons was chosen to measure the resolution of the large prototype in a test performed at the PSI. In the following sections we will describe the steps, from kinematical consideration to the real detector and target configuration, that were necessary to accomplish the relevant choices in the realization of the test, such as, *e.g.*, the choice of the beam settings, of the π^- target, of the opposite side detector, etc.

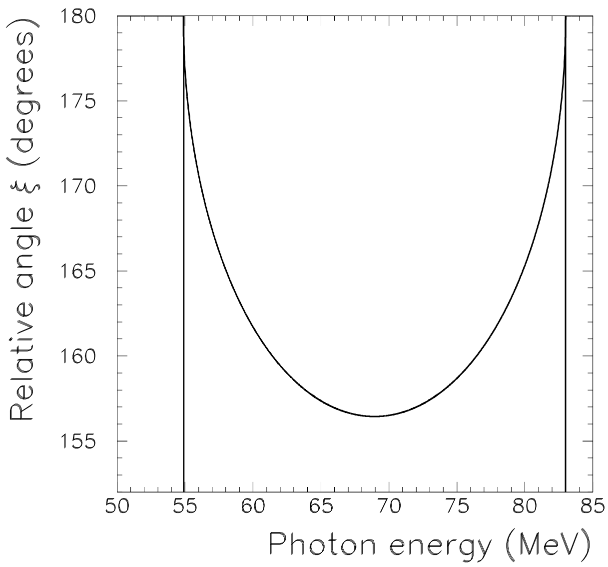

Figure 8.4: Correlation between the energy of the two photons from the $\pi^0 \to \gamma\gamma$ decay and their relative angular separation ξ in the laboratory frame.

Chapter 9

The charge exchange test setup at PSI

9.1 Introduction

The charge exchange test was performed at PSI between the months of September and December 2003. The large prototype was brought to the πE1 beam line, branching from the E-target of the PSI primary proton beam line. We recall that 590 MeV/c protons hit a 6 cm thick graphite target and secondary particles coming from proton interactions are extracted by magnetic elements.

The set-up for the charge exchange test is depicted in Figure 9.1. The incoming π^- beam is stopped in a liquid hydrogen target, after passing a beam counter $S1$ and a graphite moderator. The large prototype is placed on one side of the target at a distance of 115 cm from its geometrical center. Opposite to it a segmented NaI crystal calorimeter is used to measure the direction and energy of the second particle (photon or neutron). Two lead collimators are placed in front of both detectors to limit the solid angle acceptance of the system in order to define the energy of the detected photons. The effective acceptance for back-to-back photons was calculated to be $\sim 5 \times 10^{-5}$.

In the following sections we will describe the beam line and target, the NaI detector and the trigger and DAQ system. The next Chapter will deal with the data analyses.

9.2 Beam line configuration

The πE1 beam line, represented schematically in figure 9.2, delivers high intensity pion and muon beams with momentum ranging from 10 to 500 MeV/c. The particles from the thick-target station are extracted in the forward direction at an angle of 8°. In order to obtain a large angular acceptance, half quadrupoles with pole tip radii of 20 cm are used as the first focusing elements of the beam line. Two optical modes of operation are available:

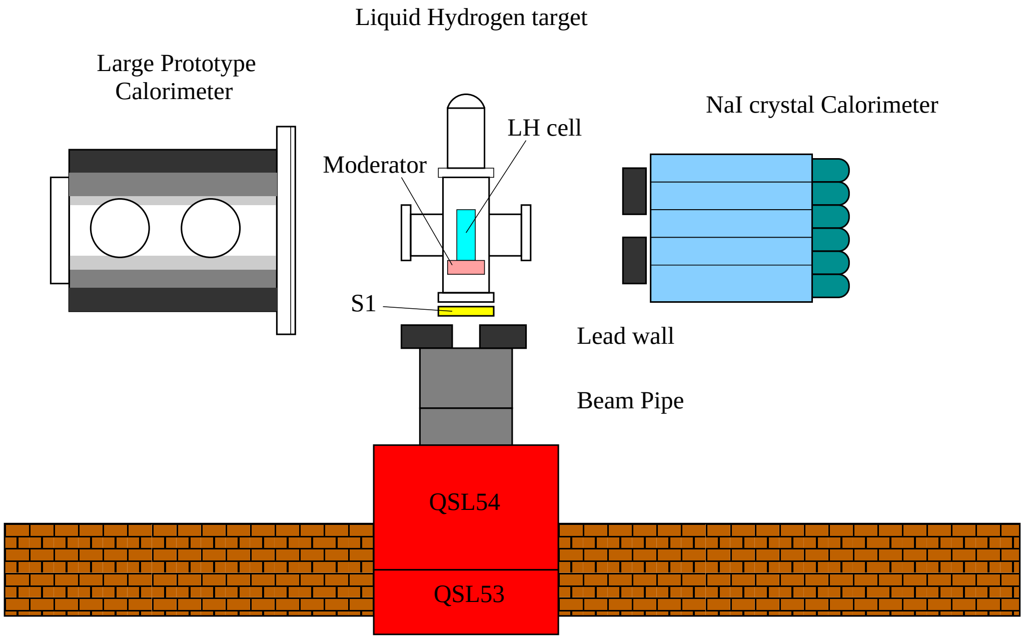

Figure 9.1: The set-up for the autumn 2004 charge exchange test at PSI.

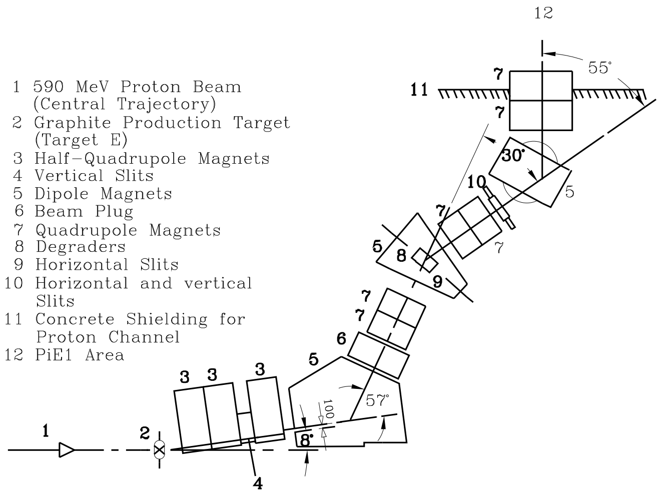

Figure 9.2: Magnetic elements of the πE1 beam line.

	Mode A	Mode B
Length (m)	16	16
Max Momentum (MeV/c)	280	500
Solid angle (msr)	32	13
Momentum acceptance (FWHM)	7.8%	8.0%
Momentum resolution (FWHM)	0.8%	0.26%

Table 9.1: Characteristics of the πE1 beam line in mode A (high flux) or mode B (high momentum resolution).

Mode A provides high fluxes with low momentum resolution. Its momentum is limited by the focusing strength of the first quadrupoles to values lower than 280 MeV/c;

Mode B is a low acceptance, high momentum resolution version up to momenta of 500 MeV/c.

The main characteristics of the two operation modes are summarized in Table 9.1. There are three slits in the beam line to control either beam intensity by reducing the angular acceptance of the beam, or the momentum band acceptance and hence the momentum resolution of the transported beam, and a set of variable thickness carbon degraders.

The measured pion and electron fluxes shown in figure 9.3, taken from the PSI users' guide [109], are higher than the presently available beam intensities for low energy pions because of different magnet settings in the main proton beam line [110].

The beam line was tuned to transport particles of 110 MeV/c momentum. The choice of this value is dictated by several factors: on one hand the higher the momentum, the higher the π^- flux. On the other hand, pions of higher momentum have a larger range and range straggling in liquid hydrogen. It is in fact the range straggling that determines the containment of the stopped π^- into the target: for low momentum particles it is given by the sum of two contributions [111]:

$$\Delta R \propto \left\{ \left[\left(\frac{200 m_e}{M} \right) f \left(\frac{E}{Mc^2} \right) \right]^2 + \left(3.5 \frac{\Delta p}{p} \right)^2 \right\}^{1/2} p^{3.5}, \tag{9.1}$$

where M is the target nucleus mass, f is the Symon function and Δp is the momentum spread of the beam.

The first part comes from the straggling of a monochromatic beam, while the second is the contribution due to the momentum bite of the beam. The overall straggling is proportional to $p^{3.5}$.

The momentum of $\approx$ 110 MeV/c is of particular interest also because it allows a better separation of the pions from the other unwanted particles in the beam, namely muons and electrons, the latter being the dominant content of the beam (see figure 9.3). A way to distinguish pions from other particles is to exploit their different phase with respect to the radio frequency signal from the accelerator: all secondary particles are produced by proton interactions on the carbon target, which happen with a $\approx$ 50 MHz frequency (one proton bunch every 19.75 ns) within the bunch time spread, which is actually less than 1 ns. Secondaries eventually reach the experimental areas, located at the beam line end, at different times, according to their velocity.

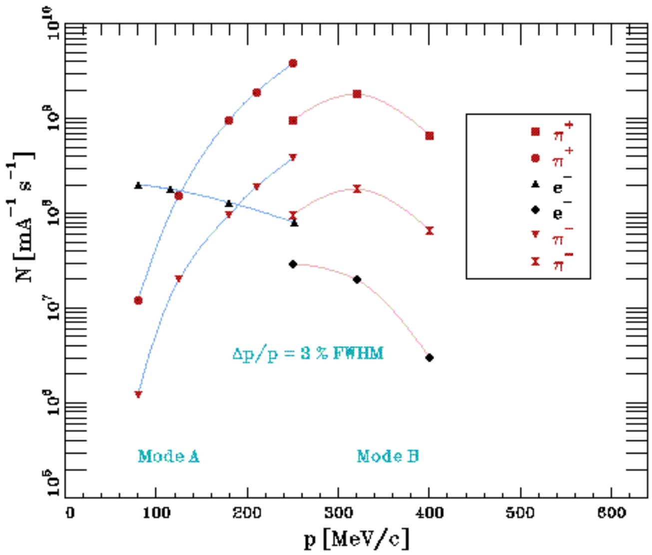

Figure 9.3: Particle fluxes in the $\pi E1$ beam line as reported in the PSI users' guide [109].

Indicating with t_π, t_μ and t_e the time-of-flight of the three particles at the end of the $\pi E1$ beam line, whose length $L \sim 15$ m, their momentum dependence is given by

$$t_{\pi,\mu,e} = \frac{L}{v_{\pi,\mu,e}} = \frac{L}{c} \frac{\sqrt{p^2_{\pi,\mu,e} + m^2_{\pi,\mu,e}}}{p_{\pi,\mu,e}}. \tag{9.2}$$

In figure 9.4 we plot the arrival time differences for the three pairs of particle, $\Delta t_{e\mu}$, $\Delta t_{\pi\mu}$, $\Delta t_{e\pi}$. For a momentum choice of $\sim$ 110 MeV$/c$, electrons and muons reach simultaneously the $S1$ counter, while the pions have an almost maximum delay of $\sim$ 8 ns, which allows their easy identification.

This technique allows for π^- tagging but does not reduce the number of contaminant particles. To accomplish this, the different momentum loss of particles transversing a material is used: a carbon degrader of 4 mm thickness is placed at the center of the ASY51 dipole magnet (element number 8 in figure 9.2). Electrons loose 2 MeV kinetic energy while pions suffer a ≈ 5 MeV slow-down. The magnets of the second half of the beam line are tuned on a lower momentum, hence the pions are transported to the target area while electrons are defocussed and eventually lost.

With such accomplishments the ratio of pions to electrons is reduced from an initial value of 15 to a fairly good value of 0.83, keeping a flux of 8×10^5 π^-/sec.

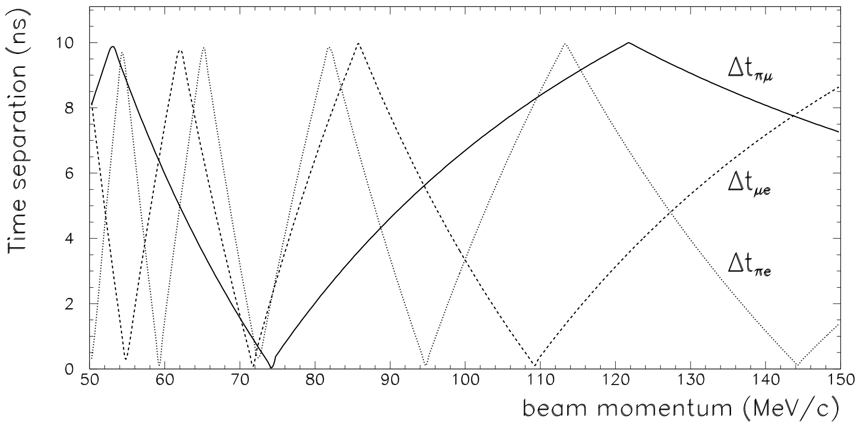

Figure 9.4: Time-of-flight separation for various beam particle types within a 19.75 ns window versus momentum, for a beam counter $S1$ distance of 15.3 m. At 110 MeV/c muons and electrons arrive simultaneously and are separated by 8 ns from the pions. This is in absence of the intermediate degrader in the ASY51 magnet.

9.3 Target

A liquid hydrogen target was chosen to have π^- undergo the charge exchange reaction. In principle any proton-rich target, such as polyethylene $(CH_2)_n$, can be used to moderate and capture π^-. On such materials the π^- can be captured either by the proton or by the other parasitic nucleus. A simple model for meson capture on nuclei shows that the probability of being captured by a nucleus of charge Z is proportional to Z, times the value at the origin of the (1s) wave function of the $\pi-$nucleus mesic atom, which is proportional to Z^3. Therefore the overall probability of being captured by the parasitic nucleus is larger by a factor Z^4. A more complete treatment of the problem [112], which involves consideration also of the slow-down process, the de-excitation of the mesic atom to the ground state and of the quantum statistics of the nucleons, shows that the probability of being captured by the "wrong" nucleus is proportional to Z^3, and this relation is well obeyed by most hydrogenate compounds, as can be seen from Figure 9.5.

For a polyethylene target, for instance, the fraction of stopped pions which undergo charge exchange on protons is approximately 1%, the rest being captured on carbon, with consequent production of secondary particles most of which are photons.

A liquid hydrogen target is therefore a necessary device in order to make a clean measurement. We used an hydrogen target which is schematically represented in figure 9.1. The target cell is a cylinder of 4 cm diameter and 9 cm length, placed with its axis parallel to the incoming beam, inside a cross shaped vacuum chamber with thin (100 μm) mylar entrance and side windows. Its active volume is 125 cm^3 and the hydrogen is liquefied and kept cold by a GM refrigerator. The

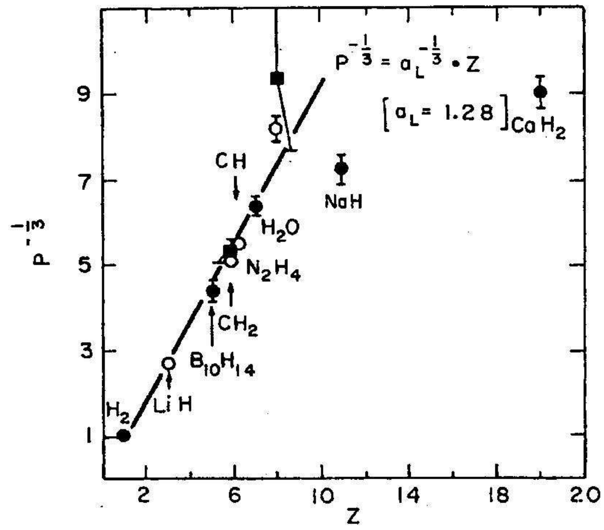

Figure 9.5: Relative probability P for a negative pion impinging on hydrogen compounds, of being captured by the H atom; as explained in the text this is roughly proportional to $1/Z^3$ (after [112]).

range of 107 MeV/c pions[1] in liquid hydrogen is 35 cm and the range straggling is $\Delta R \sim 1.26$ cm. The configuration (position and thickness) of the moderators in front of the target was optimized from the results of a Monte Carlo simulation [113] and range curve measurements. One of such range curves is shown in Figure 9.6: an increasing number of isotropic graphite slabs (3.3 mm thick each, density 1.75 g/cm^3) was placed before the liquid hydrogen target. The rate of S1$\oplus$NaI coincidences was measured, as well as the rate of the S1$\oplus$NaI$\oplus$LXe ones. Assuming that the rate of events in the detectors is dominated by photons coming from the π^- charge exchange, the maximum rate is obtained for the maximum number of stopped pions.

In the final configuration a 2.6 cm thick graphite moderator (density 1.75 g/cm^3) was placed directly in front of the target cell, inside the vacuum chamber, in order to reduce the beam divergence due to multiple scattering and to stop the π^- in the target center. It was estimated that 99% of the pions stop in the target volume.

With the angular acceptance reported in section 9.1, the expected (and measured) rate, at full beam intensity, of back-to-back photons was 5 Hz.

9.4 The NaI detector

An array of 64 modules of NaI(Tl) was used to detect the γ-ray coincident with that detected by the large prototype. We will describe its geometry, the calibration procedure and its performance.

[1]The π^- are slowed down from the initial 110 MeV/c momentum by the carbon degrader placed at the center of the ASY51 dipole magnet.

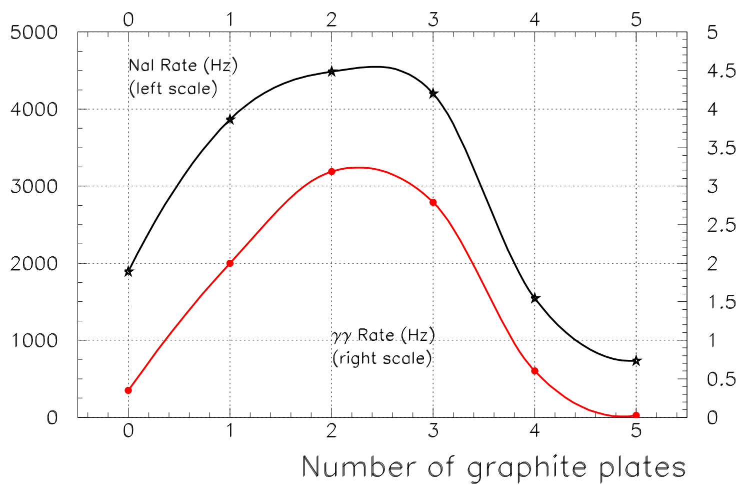

Figure 9.6: Curve of the rate of S1⊕NaI (left scale) and S1⊕NaI⊕LXe (right scale) coincidences, as a function of the number of thin isotropic graphite slabs placed as a moderator in front of the hydrogen target.

9.4.1 Description

Figure 9.7 shows the detector, made of 64 bars ($63.5 \times 63.5 \times 406$ mm^3) of NaI(Tl) Polyscin© scintillator [114]. The detector is assembled to form an 8×8 array encased in an air-tight container. The lateral and rear walls of this box are of 19 mm aluminum plates. To limit the absorption, the front wall is made of a 0.5 mm thick steel sheet. In the backplate, the light is transmitted through Pyrex windows and 60 mm long Plexiglas light guides to the photo-multiplier tubes (Phillips PM2202). Each module is optically isolated from its neighbors by a layer of optical reflector and subsequent wrapping in an aluminized mylar foil. The anode pulses are transmitted to the acquisition through tri-axial cables. The pulse of each crystal is sent to a CAMAC ADC (LeCroy LRS2249W).

9.4.2 Calibration

High energy photons interacting in the detector generate an electromagnetic shower, the energy of which is distributed over several modules of the array. The overall performances of the detector depend therefore on the development of the shower and on the characteristics and inter-calibration of the single channels. To achieve an optimal energy resolution three steps where necessary: a reduction of the common noise, a crystal inter-calibration and a suitable algorithm for the energy summation over several crystals.

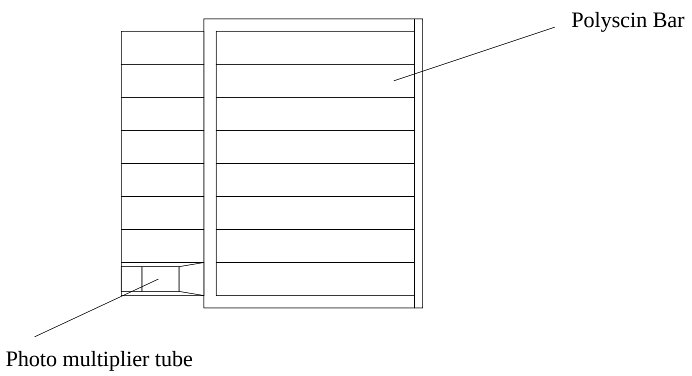

Figure 9.7: Schematic cross section of the NaI detector.

Common noise subtraction

Although the signals of all crystal are transmitted through tri-axial cables to the acquisition a correlation in the amplitude of the various modules charge is still visible, possibly due to non-shielded noise or fluctuations in the PMT or ADC power supply, as apparent, for instance, from Figure 9.8a where the correlation between the pedestal of two crystals is shown. To overcome this problem a common-noise subtraction algorithm was applied [115]: the average pedestal of all crystals is computed from those modules which are below a 0.4 MeV equivalent threshold on a event-by-event basis, and this average is subtracted from all channels ("second pedestal correction"). In this way the single pedestal widths shrink on average from $5 \div 6$ ADC channels to $2 \div 3$.

Crystal inter-calibration

The crystal inter-calibration proceeded in two steps. A primary calibration used cosmic ray muons and was refined with the photons coming from the π^0 decay. For the rough calibration, cosmic rays were triggered by the eight pairs formed by the topmost and the bottommost crystal in each array column. In this way vertical cosmic rays passing through all eight crystals in each column were selected. The rate for such events was about 0.1 s^{-1}. The Landau distribution was fitted for each crystal and the peak position for all histograms was used as the inter-calibration constant. This procedure is based on the fact that all crystals are spanned in an equal manner by cosmic rays. This is true for a pure vertical muon beam, but in the real case, due to the natural angular spread of the muons, crystals in the middle of the column are hit mostly in the central part, therefore different crystals are probed differently. To overcome this oddity we used π^0 photons, triggered back to back, to inter-calibrate the central modules: we required the coincidence between the NaI array and the xenon calorimeter prototype, selecting the 83 MeV photon in the latter. The crystal with the maximum charge was selected and its charge recorded. The position of the peaks of such histograms was set to be equal by appropriate calibration constants. Such constants were coded in the off-line analysis programme and used to compute the NaI energy sum.

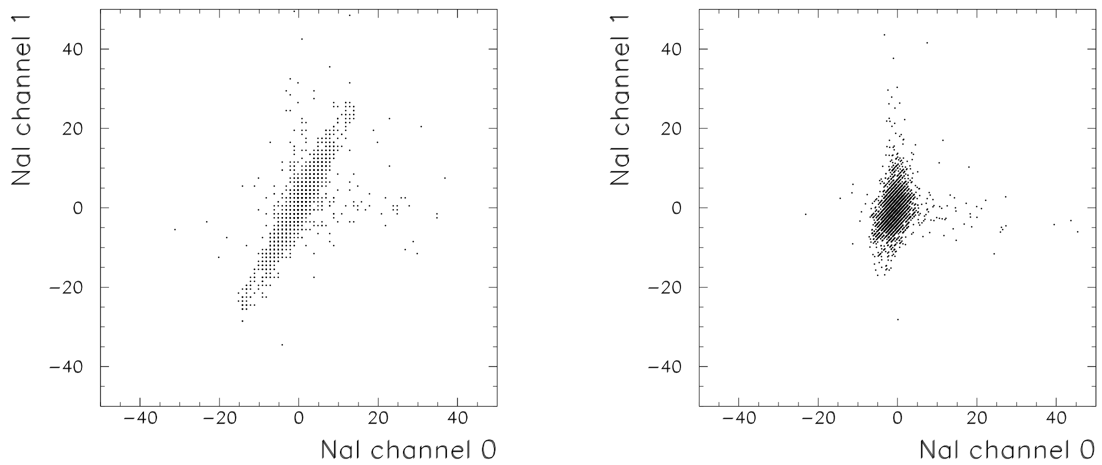

(*a*) (*b*)

Figure 9.8: (*a*) Correlation between the pedestal values of the output of two crystals. In (*b*) the same plot is shown after the common noise correction.

Energy summation algorithm

The amplitude recorded on all channels hit by the electromagnetic shower is used to estimate the photon energy: however, in order to reduce the pile-up occurring in multiple detection, we restrict the summation to a cluster C defined by the following algorithm: C includes the element of the detector which received the maximum energy, and all the elements, above a 0.4 MeV threshold, connected to another member of the cluster, by a side or by the corner. Thus

$$E = \sum_{i \in C} E_i, \tag{9.3}$$

where E_i are the corresponding energies, deduced from the ADC counts using the calibration factor and a pedestal value for each channel.

9.4.3 Performance

The resolution obtained in this way is fairly good, as well as the linearity, in fact the peak position is well reproduced. In figure 9.9*a* the 54.9 MeV peak is plotted. In figure 9.9*b* the resolution (sigma) is plotted as a function of the reconstructed energy. For comparison the raw resolution at 55 MeV obtained with no common noise subtraction and summing the contribution of all calibrated crystals amounts to $\sim 10\%$.

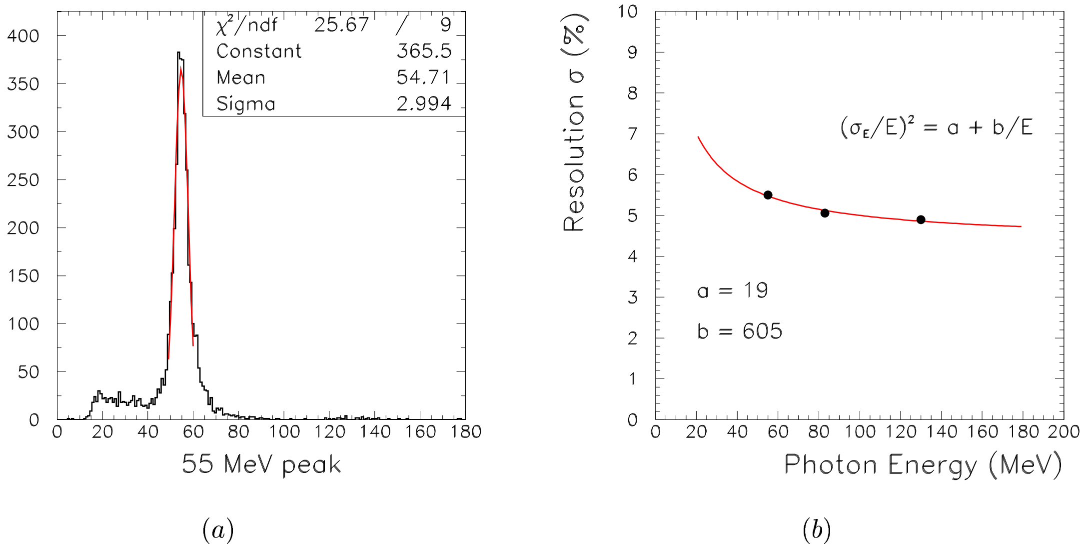

Figure 9.9: (*a*) Example of fit to the 55 MeV photon peak as measured by the NaI array after applying the corrections explained in the text; in (*b*) the resolution is plotted as a function of the energy.

The dependence of the resolution σ upon the energy E can be parameterized as [116]

$$\left[\frac{\sigma_E}{E}(\%)\right]^2 = a + \frac{b}{E}. \tag{9.4}$$

The E^{-1} term arises from statistical fluctuations in the emission of scintillation photons and their absorption on the photo-cathode. The parameter a accounts for systematic fluctuations. Our best fit is obtained with $a = 19$ and $b = 605$.

Chapter 10

Energy and timing measurement

10.1 Set up

10.1.1 Mechanics

As shown in Figure 9.1 the π^- beam was stopped in the liquid hydrogen target, after passing the $S1$ scintillation counter and the graphite moderator. A 10 cm diameter lead collimator was placed in front of the calorimeter prototype, while a 10×10 cm^2 square window selected photons impinging on the center of the NaI detector. Furthermore, the LP front face was covered, apart from the entrance window, by paraffin blocks and boron-loaded polyethylene slabs, in order to moderate and capture neutrons, that are present in the experimental area during the measurement.

Another counter, formed by two thin scintillator foils (Bicron BC404) read by two fast PMTs each and glued to a 3 mm thick lead foil, could be mounted in front of the NaI, to convert photons and provide the signals for timing resolution measurements.

The studies for a specific filler to be placed between the PMT bleeder circuit and the honeycomb window were not finished, therefore no filler was used: xenon could leak in the space between the honeycomb window and the PMT bleeder circuits of the front face PMTs: photons had therefore to cross an additional 5 mm layer of liquid Xe before entering the calorimeter wall, deteriorating the efficiency and the resolution of the photon energy reconstruction: this in fact consisted in an additional 0.15 X_0 to be crossed by the photons impinging the center of the calorimeter.

10.1.2 Electronics

The ADC signals of all LP PMTs are sent to an active splitter, developed for the MACRO experiment [117]: one part of the splitted signal is sent to the FastBUS CIAFB ADCs after a 200 ns delay, and a part is sent to the CAMAC discriminators (PHILLIPS PS7106 and LeCroy LRS2249W).

Monte Carlo simulations of the LP energy spectrum from the charge-exchange photons showed that the central PMTs of the front face receive most of the light of each event. If photons interact in front of one PMT, its corresponding ADC channel saturates. To extend the dynamic range the signals of the central PMTs of the front face are additionally split, and a part is attenuated by a factor of 10 or 3, depending on the PMT position.

The PMT signals are discriminated at a threshold of 10 mV and the discriminated signals are sent to FastBUS, CAMAC and VME TDCs (LRS1875A, PS7186H and CAEN V775) the first two having a 25 ps, the latter 50 ps least count resolution. CAMAC and VME TDCs are operated in *common stop* mode, while FastBUS TDCs can be operated only in *common start* mode, hence a delay line is inserted between them and the discriminators.

10.1.3 DAQ

The acquisition program was based on the MIDAS framework [118], developed at PSI, running on a MS Windows 2000 machine. Data are written in a binary stream and subsequently analyzed offline to obtain PAW ntuples or root trees.

10.1.4 Trigger configuration

Besides the usual pedestal, alpha, LED and cosmic-ray trigger (the latter also including the aforementioned trigger for cosmics crossing the sodium iodide) a special trigger for the LP was implemented for this test to be able to select the π^0 photons: the analog sum of 8 central PMTs of the front face and of 4 central PMTs of the back face was computed, and a threshold corresponding to ~ 1 MeV was set on this sum. The insertion of the back face PMTs was needed to trigger events in which the photon does not convert near the front face.

NaI photon trigger was provided by discriminating the analog sum of the signals of the 4 central NaI PMTs, in a way similar to that used for the LP. Charge and timing information for the $S1$ counter was recorded, as well as the TDC of the radio frequency.

Three photon trigger modes where available: two *one-arm* triggers ($S1\otimes$NaI and $S1\otimes$ LXe) to study the complete photon spectrum in either detector, and a *two-arms* trigger ($S1\otimes$ NaI $\otimes$ LXe) used to select back-to-back photons, to perform energy and timing measurements. The signal timing was set so that $S1$ was the last signal in most events, therefore determining the coincidence timing.

Thanks to the presence of the RF signal in the data stream it is possible to distinguish offline pions from electrons from their different arrival time, as it is clearly visible from Figure 10.1a. The $\pi^- - e^-$ time difference with respect to the RF is ~ 7 ns as expected for 107 MeV particles (cfr. Figure 9.4). The incoming π^- have the $S1$ timing between 13 and 16 ns, while the RF timing between 13 and 18 ns, *i.e.* events in region b in Figure 10.1b. The other shadows in the figure are caused by accidental coincidences, in which the $S1$ signal does not stop the TDC counting (hence being a constant) but is randomly-distributed within the 19.75 ns time window, though maintaining a correct phase with RF (*i.e.* $RF - S1 =$ particle time of flight = constant, as in c for pions and d for electrons).

Figure 10.2a shows a spectrum in the LXe taken with the one-arm trigger (note the low energy

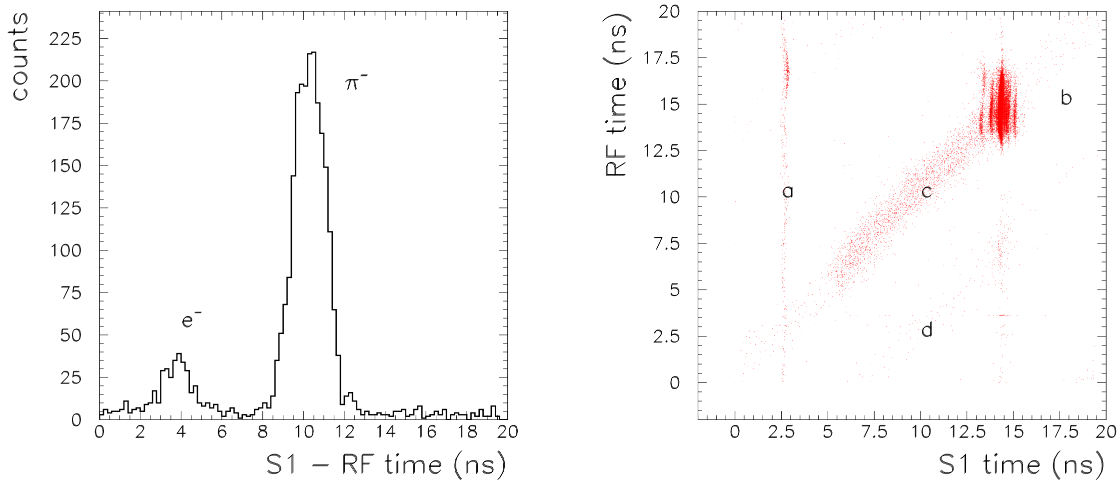

(*a*) (*b*)

Figure 10.1: (*a*) Difference in the arrival times of pions and electrons on the $S1$ reference counter; (*b*) distribution of the triggered events in the $RF - S1$ diagram; the different events in the various regions are explained in the text;

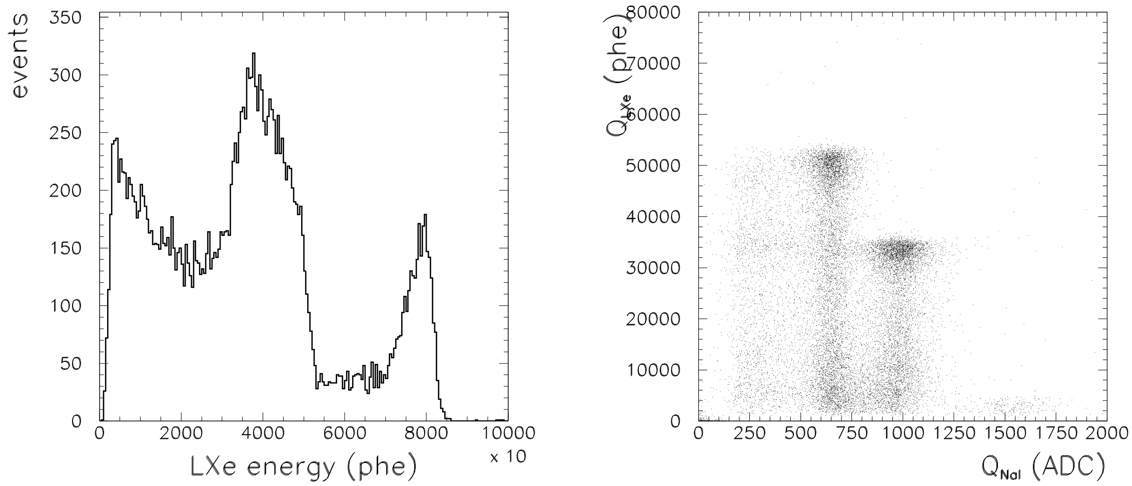

(*a*) (*b*)

Figure 10.2: (*a*) Spectrum recorded by the liquid xenon calorimeter prototype with the one-arm trigger; (*b*) correlation between the energy recorded in the liquid xenon calorimeter and in the NaI for a typical two-arms trigger run.

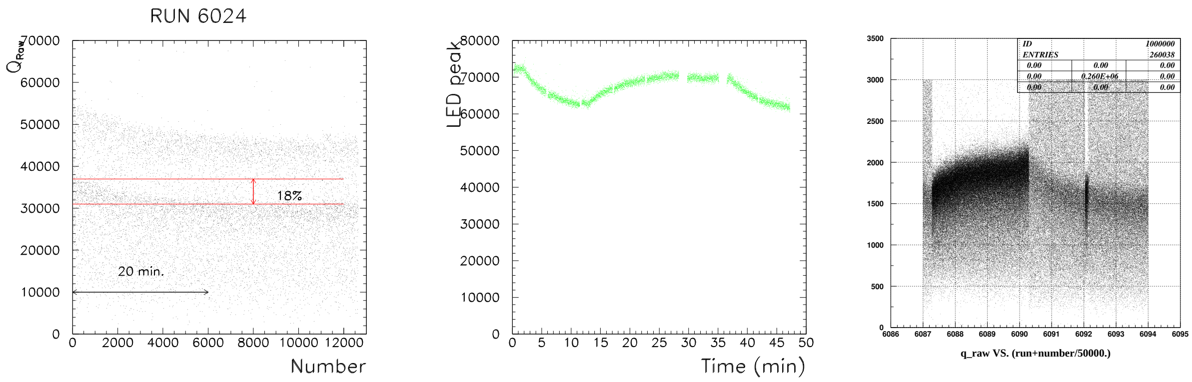

(a) (b) (c)

Figure 10.3: Variation of the recorded number of photoelectrons as a function of time after opening the beam shutter for $\gamma\gamma$ events (a); the same behavior is observed also within an LED run (b) in which the beam shutter was opened ($t = 2$ min) closed ($t = 12$ min) and opened again ($t = 37$ min); (c) shows the same behavior in an α-source run, where the background due to low energy photons is also apparent.

tail due to charge exchange neutrons) while in Figure 10.2b we show the signals in LP and NaI detectors for a two-arms trigger run. The presence of the two anti-correlated peaks at 55 MeV and 83 MeV is clearly visible.

10.2 Energy resolution of the Large Prototype

10.2.1 Background-induced PMT problems

During the first days of data taking it was noticed that, after opening the beam shutter that allows π^- and other particles to enter the experimental area, the signals coming from the LP exhibited a systematic drift towards lower values, with a characteristic time of the order of few minutes. This behavior was observed both in the two back-to-back γ-lines (Figure 10.3a) and in the α-source line (Figure 10.3c). We were able to reproduce the effect also with LED signals. Figure 10.3b shows the sum of all PMT outputs in a LED run, as a function of time when the shutter was open and subsequently closed. After measuring PMT gains and quantum efficiencies in beam-on and beam-off configurations we discovered that while the PMT gains were almost unaffected, the average charge recorded by each PMT was substantially lower in the beam-on configuration, both at 178 nm (light from the α-source) and at visible wavelength (light from the LEDs) as shown in Figure 10.4a and 10.4b. Furthermore the variation for each PMT was consistent for both wavelengths (Figure 10.4c).

These measurements are therefore consistent with an overall change in the photo-electron emission or collection efficiency which takes place at low temperature when the photo-multipliers are

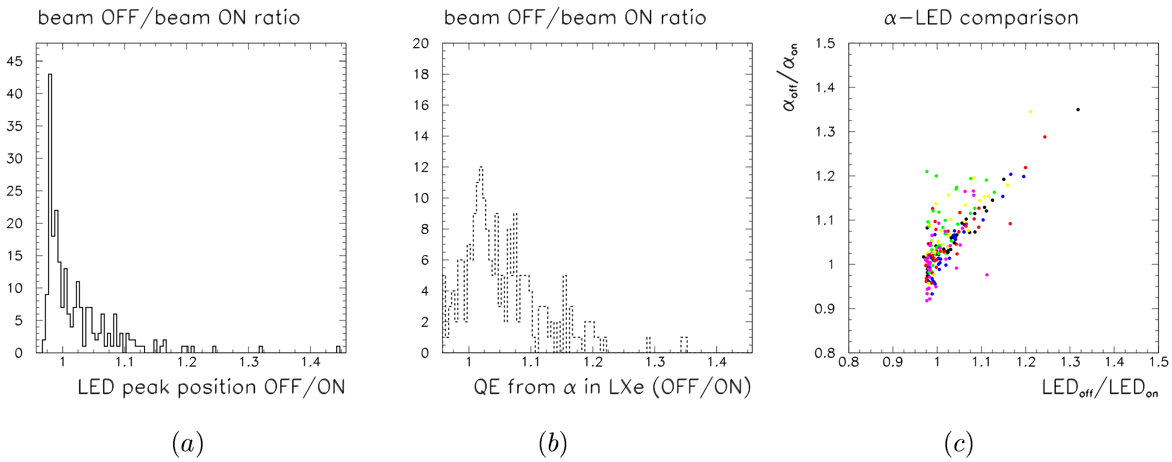

Figure 10.4: (a) distribution of the ratio of the position of the LED peak as recorded by each PMT with beam off and beam on; (b) distribution of the ratio of the quantum efficiencies determined with beam off and beam on; (c) correlation between the LED peak variation and the QE variation in the beam off/beam on situations.

illuminated at a high light level. In fact in the beam-on configuration there is a few kHz background of low energy photons (see Figure 10.3c). We could mimic the effect, in absence of beam, by flashing a LED whose output was equivalent to the observed background. This effect was reduced (though not eliminated) by lowering the π^- beam intensity, by means of a slit placed on the beam line (element number 9 in Figure 9.2).

This effect was attributed to an increase of the photo-cathode resistivity at low temperature. Systematic studies were then carried out at the PMT test facility in Pisa and Tokyo, which helped to better understand and solve this problem by means of constant interaction with HAMAMATSU Photonics, Inc. Those studies will be presented in the next Chapter.

The charge exchange runs, taken with a beam intensity reduced by a factor of ≈ 5, yielded a two-arms trigger rate of ≈ 1 Hz. The liquid hydrogen target has been essential because with other materials the rate of stopped pions would not have been sufficient to perform the measurement in a reasonable time, needing, in case of polyethylene for instance, a time larger by a factor of 100, as seen in the previous Chapter. For each run we measured gain and α-source peak with the beam shutter closed. We then opened the shutter and waited more than half an hour to allow the PMTs to stabilize. We measured their gain and α-peak again; the new gains were used for calibration while the quantum efficiencies were multiplied by a factor computed by using the LED pulse shift, being this measurement well correlated to the α-peak shift, but more precise, as visible, for instance, from Figure 10.4c.

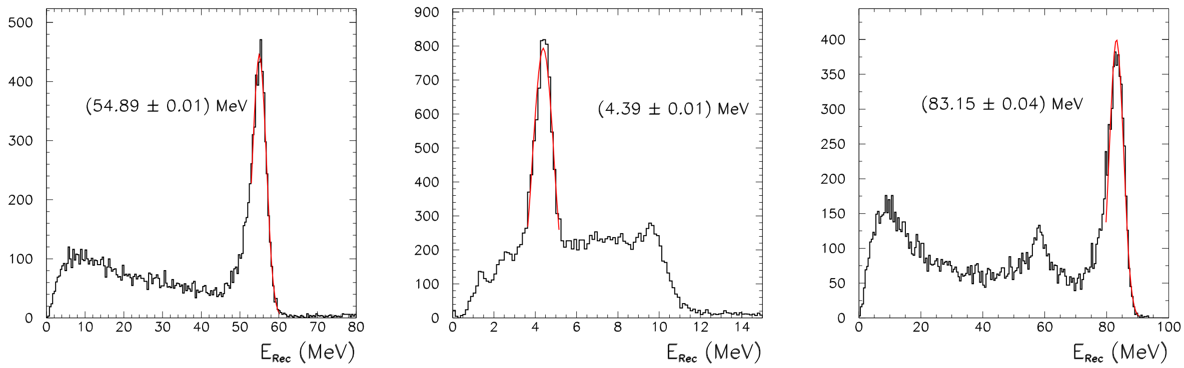

(a) (b) (c)

Figure 10.5: Energy reconstructed with the linear method using a single set of coefficients. By calibrating the energy scale to the 54.9 MeV photon (a), both the 4.4 MeV photon of an AmBe source (b) and the 83 MeV photon from the π^0 decay (c) are correctly reconstructed.

10.2.2 Energy measurement

The average PMT gain set for the energy measurement was $g = 10^6$. The liquid xenon purity was constantly checked in the usual way with α-sources and found to give always $\lambda_{\mathrm{Abs}} > 1$ m.

The extraction of the energy information from the ADC values of all PMTs required the following steps:

- pedestal subtraction;
- the saturated ADCs, if any, were replaced by the corresponding attenuated channel, corrected by a multiplicative factor extracted, on a run-by-run basis, comparing the non-saturated values in both channels;
- the ADC value of each PMT was transformed in the corresponding number of photoelectrons, taking gain, quantum efficiency and ADC least count into account;
- the number of photo-electrons (n_{phe}) for each PMT was used to compute the total number of photoelectrons for quick analyses (Q_{sum}) and as the input for the reconstruction program based on the linear fit (see Chapter 6).

The linear fit method (Section 6.7.1) was used to extract the photon energy E_{Rec} for each event, while the position of the photon conversion $\{x_{\mathrm{fit}}, y_{\mathrm{fit}}, z_{\mathrm{fit}}\}$ was determined by a MINUIT fit of the light distribution on the PMTs of the front face (Section 6.6.1). We selected photons whose interaction point was within the collimator acceptance ($\sqrt{x_{\mathrm{fit}}^2 + y_{\mathrm{fit}}^2} < 5$ cm).

By using a single set of coefficients for all the events, and setting the energy scale to reproduce the 54.9 MeV peak at the correct position (roughly corresponding to 32 000 photo-electrons), we

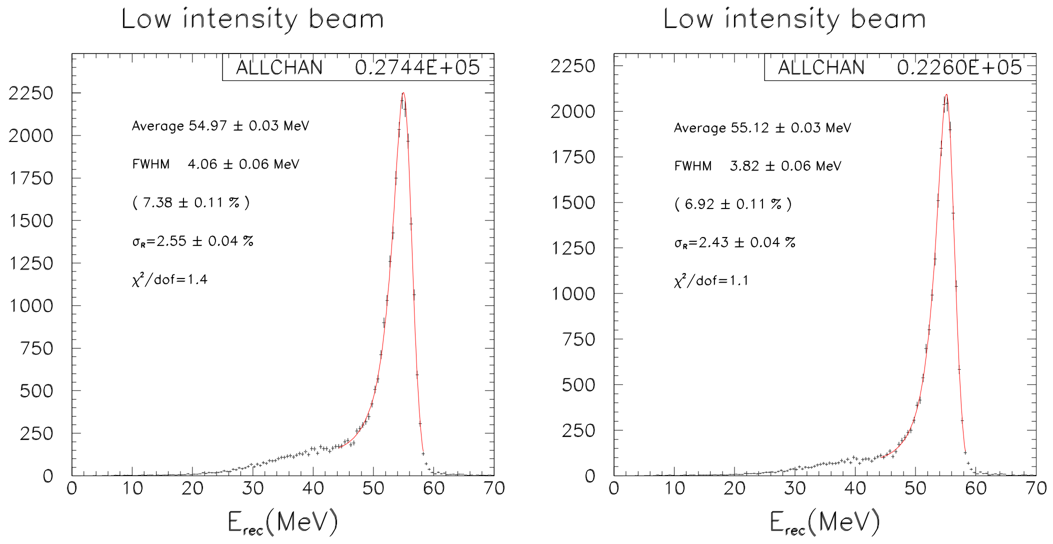

(a) (b)

Figure 10.6: The fits to the 54.9 MeV energy peak, without position cuts, without (a) and with (b) the 2.5 cm depth selection.

verified that the energy exhibits a good linearity, as can be seen from the fact that both the AmBe source 4.4 MeV γ-ray energy and the 83 MeV π^0 photon energy are correctly reproduced (Figure 10.5).

If we select the 55 MeV peak in the LP by requiring the 83 MeV photon in the NaI with no cuts other than the "π^- region" in the $S1 - RF$ diagram, the obtained FWHM is $(7.4 \pm 0.1)\%$, $\sigma_R = 2.5\%$. This is reduced to $(6.9 \pm 0.1)\%$, $\sigma_R = 2.4\%$ if a cut on the depth of the γ-ray conversion point is set (distance from the wall larger than 2.5 cm) this cut retaining 82% of the events (Figure 10.6). Monte Carlo simulations show in fact that this cut is necessary to get rid of the photons converting *before* entering the xenon active volume.

This result is, however, not completely satisfactory since we expected, from the Monte Carlo simulations a resolution around 4% FWHM. It is true that the linear method is strongly dependent on how well the detector is known and modeled. The information coded in the Monte Carlo is, to our knowledge, the one which best reproduces all other measurements performed so far.

As a next step the Monte Carlo simulation was used to extract the average expected charge for each PMT, and a new set of quantum efficiencies was computed by comparing those values to the observed energy distributions. We applied the linear reconstruction to event sub-samples, dividing the collimator surface in 3×3 sub-regions. With the same cuts as before (π^-, 55 MeV peak and depth$>$ 2.5 cm) the resolution ranges from $(4.7 \pm 0.2)\%$ to $(5.5 \pm 0.3)\%$ (see Figure 10.7). The peak in each sub-region is slightly shifted, with the consequence that, when the whole incidence region is spanned, the 54.9 MeV peak is smeared and the resolution worsens.

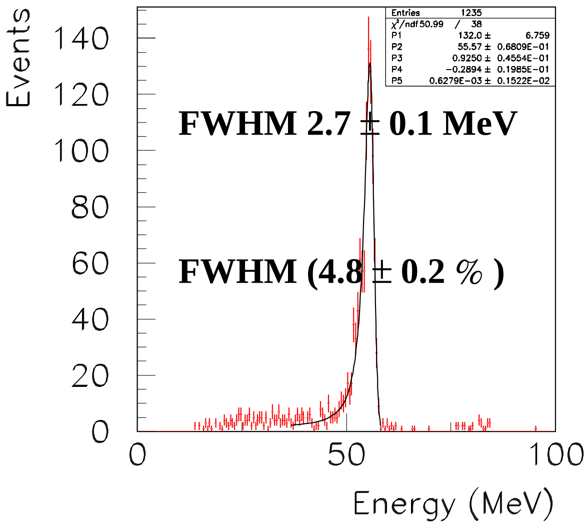

Figure 10.7: A representative fit to the 54.9 MeV energy peak, performed on an event subsample selected in position.

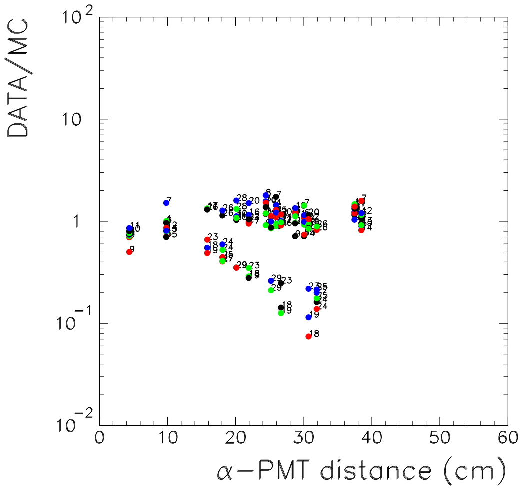

(a)

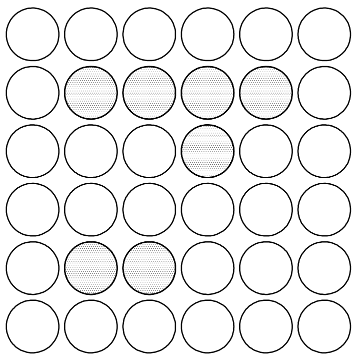

(b)

Figure 10.8: (a) ratio of observed to expected $\alpha-$source light seen by the PMTs of the front face as a function of the PMT-source distance; in (b) the PMTs which belong to the lower population are shaded.

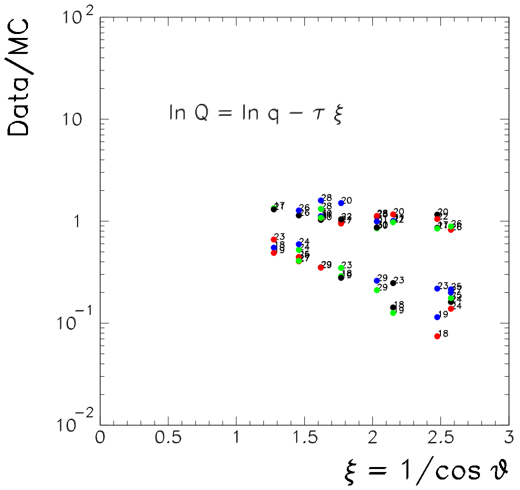

Figure 10.9: The dependence of the observed to expected light ratio of Figure 10.8a is plotted as a function of the average incidence angle of the scintillation light, and it is found to be quite consistent with the predictions of Equation (10.2).

After a thorough investigation, we came to the conclusion that the ultimate reason for this effect is the poor knowledge of PMT quantum efficiencies and the bad behavior of some PMTs of the front face at low temperature. This can be seen by looking at the signals of the front face PMTs in α-source runs. If we plot, for those PMTs, the ratio between the observed and the expected number of photoelectrons as a function of the PMT-source distance (Figure 10.8a) we clearly distinguish two populations: the upper one is the expected distribution for large absorption length, but there is a group of photo-multipliers (shaded in Figure 10.8b) which exhibit a strange behavior: these PMTs (which are among the ones with the lowest QEs) show a larger absorption of scintillation light. The dependence of the observed/expected ratio on the average incidence angle of the scintillation light from the α-sources is plotted in Figure 10.9, and is consistent with a strong absorption of scintillation light by the photo-cathode[1]. In fact if we call λ the photo-cathode absorption length ($\lambda \sim t$, the photo-cathode thickness) for a photon impinging at an angle θ from the normal to the PMT surface the effective quantum efficiency $Q(\theta)$ is the "true" quantum efficiency q at normal incidence times an attenuation factor:

$$Q(\theta) = q\, e^{-\frac{t}{\lambda \cos\theta}} \tag{10.1}$$

$$\ln Q(\theta) = \ln q - \frac{t}{\lambda}\frac{1}{\cos\theta}, \tag{10.2}$$

which seems to be well obeyed by those "bad" PMTs.

[1]To help reducing the photo-cathodic resistivity at low temperature for those PMTs, R6041Q, a thin Mn layer was deposited below the photo-cathode. The thickness of this layer is difficult to control and heavily affects the UV quantum efficiency [119].

Of course one cannot push much further those considerations: taking this angle-dependence of the quantum efficiency into account is impossible. The quoted energy resolution is our best result and every effort must be put in the improvement and selection of the photo-multipliers for the final calorimeter.

10.3 Timing resolution measurement

The time coincidence between the high-energy photon detected by the calorimeter and the positron detected by the drift chambers and timing counter device is essential in reducing the accidental background. The two particles are required to be generated in the target at the same time within the experimental resolutions of the timing counter and of the LXe device. We saw in Chapter 4 that the resolution of the timing counter is $\sim$ 100 ps FWHM. A comparable timing resolution is therefore envisaged for the photon detector, since the ultimate rejection power on the background is determined by the combined performances of the two devices.

It is interesting to notice, looking for instance at Table 3.1, that the foreseen timing resolution represents the major improvement of the MEG experiment over the previous $\mu^+ \to e^+\gamma$ searches.

10.3.1 Principle of the measurement

The timing T_0 of the photon generation on the target is the time at which the parent muon decays. Photons within the calorimeter acceptance travel, with the speed of light c, towards the detector, where they interact at a position $\vec{R}_{\rm int} = \{\rho_{\rm int}, \theta_{\rm int}, \phi_{\rm int}\}$. The scintillation light travels towards the calorimeter surface with a speed $c/n_{\rm Xe}$ ($n_{\rm Xe}$ being the liquid Xe refractive index) where it is collected at a time $T_{\rm coll}$ by the photo-multiplier tubes and recorded by the electronics chain after some delay $T_{\rm PMT} + T_{\rm dly}$ where $T_{\rm PMT}$ is the transit time of electrons in the PMT and $T_{\rm dly}$ is some fixed delay due to cables, electronics etc...

The decay time T_0 is therefore related to the time T_i^{tw} at which the $i-$th PMT, at position $\vec{P}_i$, exceeds a fixed threshold in the following way (see Figure 10.10):

$$\begin{array}{cccccccccc} T_0 = & T_i^{tw} & - & \dfrac{\rho_{\rm int}}{c} & - & \dfrac{|\vec{R}_{\rm int} - \vec{P}_i| n_{\rm Xe}}{c} & - & T_{\rm PMT} & - & T_{\rm dly} \\ & (i) & & (ii) & & (iii) & & (iv) & & (v) \end{array} \tag{10.3}$$

where the superscript (tw) means that T_i is already corrected for the time-walk effect. It is well known, in fact, that the time of arrival of signals coming from the photo-tubes, defined as the time at which a signal exceeds a fixed threshold, is correlated with the pulse height: this can be well modeled [120, 121] as

$$T^{tw} = T^m - \frac{W}{\sqrt{q}} \tag{10.4}$$

where T^{tw} is the corrected time, t^m is the measured time, q is the integrated charge of the PMT signal and W is a correction parameter determined by data fitting.

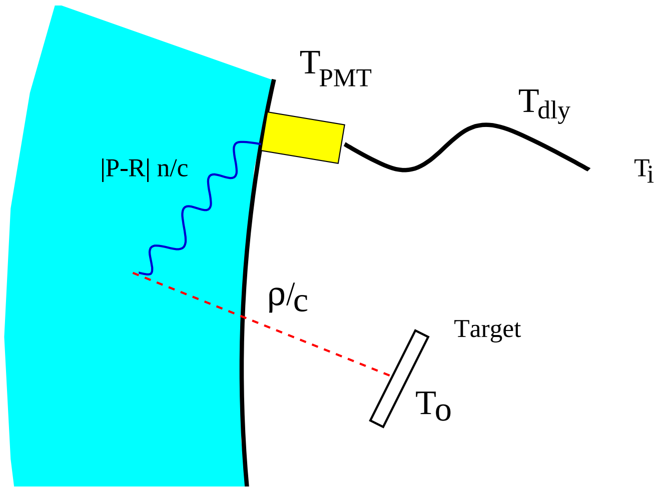

Figure 10.10: Schematic view of the various terms contributing to the photon timing measurement

T_0 is affected by fluctuations in the various terms of the right side of Equation (10.3):

1. Uncertainty on the photon conversion position $\sigma_{\vec{R}_{\rm int}}$ directly affects terms number (ii) and (iii); in the particular case of our test with photons coming from the π^0 decays, term (ii) includes also the lack of knowledge of the π^- capture position inside the liquid hydrogen target. Assuming the values given by the Monte Carlo optimization of the target ($\sigma_{\rm transv}$ = 5 mm, $\sigma_{\rm long}$ = 11 mm) it gives a contribution of $\sigma_{\pi^-} \approx 43$ ps;

2. The transit time spread of the PMTs affects term (iv): these fluctuations are proportional to $\sigma_{stt}/\sqrt{N}$ where $\sigma_{stt} \approx 200$ ps is the single electron transit time spread of the R6041Q PMTs and N is the number of photo-electrons seen by the i-th PMT; the $\sqrt{N}$ arises from the Gaussian distribution of the transit time of electrons along the dynode chain;

3. Fluctuations in the cable length and/or electronics, *e.g.* due to temperature variations, affect term (v).

Furthermore, in Equation (10.3) the photon conversion and the emission of Xe scintillation photons are assumed to be simultaneous events, while the scintillation photons are emitted with an exponential distribution with a time constant (in case of γ-initiated e.m. shower, cfr. Chapter 5) $\tau_{\rm rec} \approx 45$ ns. The fluctuation on the emission time of a single scintillation photon with such an exponential distribution is

$$\sigma_t^2 = \langle t^2 \rangle - \langle t \rangle^2 = \tau_{\rm rec}^2. \tag{10.5}$$

In case of emission of N scintillation photons the scintillation timing is determined by the earliest emitted photon, whose distribution is given by[2]:

$$\mathcal{P}(t_{\rm min}){\rm d}t_{\rm min} \propto e^{-Nt_{\rm min}/\tau_{\rm rec}}{\rm d}t_{\rm min} \tag{10.6}$$

[2]In the case $N = 2$ this is easily seen as follows: the joint probability of obtaining two scintillation photons at

hence the fluctuation in case of N emitted photons[3] scales with N and not with $\sqrt{N}$:

$$\sigma^2_{t_{\min}} = \langle t^2_{\min} \rangle - \langle t_{\min} \rangle^2 = \frac{\tau^2_{\rm rec}}{N^2}. \tag{10.7}$$

Terms in Equation (10.3) can be divided in two groups: those which are linked to the physics $(i), (iv), (v)$, and those which are linked to the geometry $(ii), (iii)$. The "intrinsic" timing resolution $\sigma_{\rm intr}$ can be measured by dividing the PMTs in two independent groups and estimating the width of the distribution of the difference of the measured timing in each group. In this way, the position of the π^- and photon conversion point cancels out.

We can therefore assume that the liquid Xe calorimeter timing resolution is given by

$$\sigma^2_t \approx \sigma^2_{\rm pos} + \sigma^2_{\rm intr}. \tag{10.8}$$

Since an uncertainty on one of the coordinates of the conversion point of 0.5 cm contributes for $\sigma^2_{\rm pos} \approx 0.5$ cm $\times$ 33 ps/cm $\times\, n_{\rm LXe} \approx 25$ ps to the total timing resolution, a comparable intrinsic resolution is needed in order to obtain an overall timing below 100 ps FWHM.

To measure the absolute timing resolution, one the other hand, we must know the time at which the π^0 decays, hence we need to measure the opposite side photon with a certain precision. Since the NaI is too slow to give a good timing, a lead/BC404 reference counter was placed in front of it. This counter is made of two thin ($50 \times 50 \times 10$ mm^3) Bicron BC404 plastic scintillators ($\tau = 2.1$ ns) read on both sides by two fast PMTs (Hamamatsu R5505) for a total of 4 PMTs. A 3 mm lead radiator (0.54 X_0) was placed in front of this counter.

10.3.2 Measurement of the "intrinsic" timing resolution

Events from two-arm trigger runs at high gain ($g = 5 \times 10^6$) were analyzed for the timing resolution measurement. We selected events entering the LP through the thin Al window, $\sqrt{x^2_{\rm fit} + y^2_{\rm fit}} < 5$ cm and evaluated the timing resolution as a function of the number of photo-electrons. This is essential since the final detector will have PMTs with a higher quantum efficiency (20% on average instead of 5%).

The time distribution of each TDC channel is broadened by the time-walk dependence and by fluctuations in the photon conversion position. An iterative procedure is used to calculate the correction factors:

---

time t_1 and t_2 is given by

$$\mathcal{P}(t_1, t_2)\mathrm{d}t_1\mathrm{d}t_2 \propto \exp(-t_1/\tau)\exp(-t_2/\tau)\mathrm{d}t_1\mathrm{d}t_2.$$

The distribution of the arrival time of the first photon $t_{\min}$ is the sum of two identical contributions obtained for $t_1 < t_2$ and $t_1 > t_2$. In both cases the distribution of $t_{\min}$ is given by

$$\mathcal{P}(t_{\min})\mathrm{d}t_{\min} \propto \int_{t_2 > t_1} \mathcal{P}(t_1, t_2)\mathrm{d}t_2 = \int_{t_1}^{\infty} \mathcal{P}(t_1, t_2)\mathrm{d}t_2 \propto \exp(-2t_1/\tau)\mathrm{d}t_1.$$

The generalization in case of N scintillation photons is straightforward.

[3]Note that here N is the ***total*** number of scintillation photons, not the number of photo-electrons on a single PMT as in the case of $T_{\rm PMT}$.

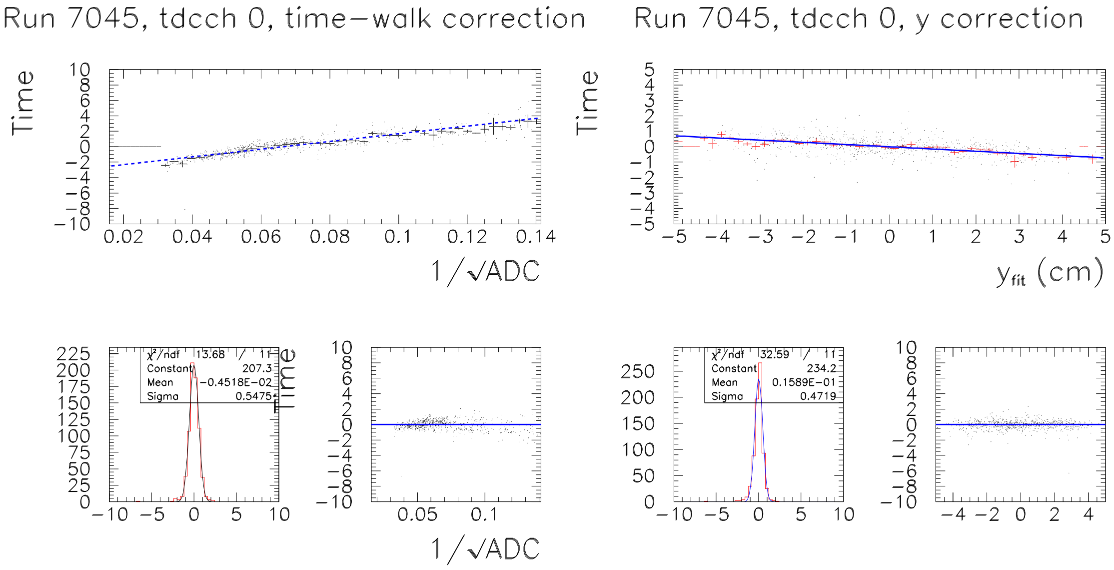

(a) (b)

Figure 10.11: (a) The time-walk correction for a typical photo-multiplier; (b) the timing distribution of the same channel after the correction.

1. the time recorded by each TDC channel is corrected for its amplitude dependence (10.4). The correlation follows fairly well the $\frac{1}{\sqrt{Q_i}}$ dependence as can be seen from Figure 10.11a;
2. the resulting time is corrected for the reconstructed γ-conversion position dependence[4] (x, y, z), by a phenomenological linear relation (Figure 10.11b);
3. items (1) and (2) are repeated until no further dependence is observed;
4. the TDC values are multiplied by the TDC least count to have their values in nanoseconds.

The corrected time distribution of each PMT is fitted with a Gaussian function and its width σ_i is recorded and used as a weight in subsequent average operations. Due to the γ position selection the light seen by each PMT is almost constant and the width of the distribution reflects the fluctuation in the number of detected photo-electrons: the smaller the photo-electrons, the larger the σ_i's.

We divided the PMTs in two groups, called "left" and "right", according to their geometrical position, and evaluated the weighted average time in each group T_L and T_R. We considered as the intrinsic time resolution the width of the distribution of the quantity

$$\hat{T} = \frac{T_L - T_R}{2}. \tag{10.9}$$

We divided the photon spectrum in five regions of increasing number of photo-electrons and computed the timing resolution for each. The intrinsic time resolution as a function of the number

[4]This was necessary because we divided the PMTs into "left" and "right" PMTs, hence the difference $t_L - t_R$ is still dependent on the γ conversion point .

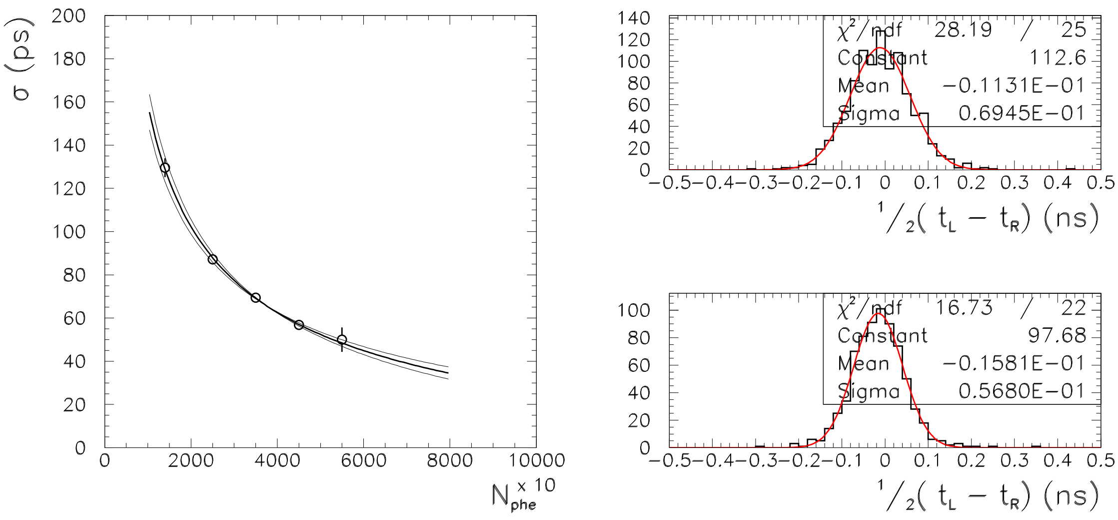

(*a*) (*b*)

Figure 10.12: (*a*) Intrinsic time resolution as a function of the number of photoelectrons. The number of photo-electrons detected for a 52.8 MeV photon is 35000 in case of 5% PMT quantum efficiency. For 20% PMT QE this number could exceed 100000 photo-electrons. The fit with the function explained in the text is shown, together with its 1σ band. (*b*) Two of the distributions fitted to obtain the values in the left plot.

of photo-electrons is shown in Figure 10.12*a*, while Figure 10.12*b*, shows two representative fits to the $1/2(t_L - t_R)$ distribution. The obtained resolutions are in good agreement with a fitted dependence of the form

$$\sigma = a + \frac{b}{\sqrt{N_{\rm phe}}} \tag{10.10}$$

which is superimposed to the plot together with its 1σ region of variation of the fitted parameters. A correction to the left-most point $N_{\rm phe}$ was applied, in order to account for the fact that in this region not all the PMTs are above the TDC threshold, hence the effective number of photo-electrons used for timing reconstruction is a 5% lower than the measured one. The expected number of photo-electrons in the final detector for a 52.8 MeV γ ranges from 100 000 to 120 000 according to the new quantum efficiencies. We can therefore estimate an intrinsic resolution of $\sigma_{\rm intr} = 20 \div 30$ ps at 52.8 MeV. If we want to estimate the LXe timing resolution (Equation 10.8) we have to fold the intrinsic and the geometrical resolutions, extracted from data and Monte Carlo simulations. Assuming $\sigma_{\rm pos} = 25$ ps in each coordinate, this amounts to

$$\sigma_t \simeq 45 \div 55 \text{ ps}, \tag{10.11}$$

i.e. $(105 \div 130)$ ps FWHM, which, combined with the timing counter resolution (Chapter 4) gives an expected timing resolution of $(144 \div 160)$ ps FWHM.

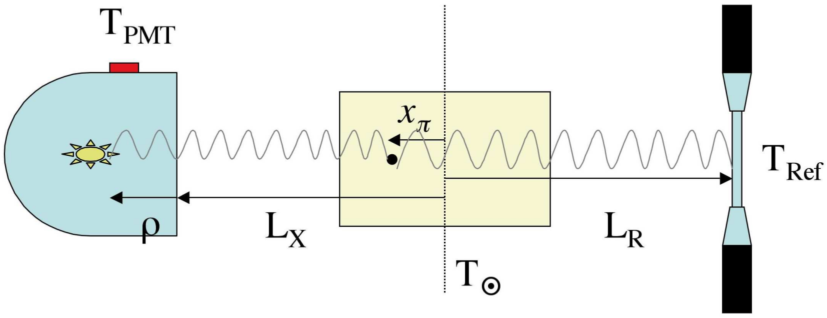

Figure 10.13: Scheme of the $\pi^0 \to \gamma\gamma$ detection to illustrate the contribution of the uncertainty on the π^0 conversion position.

10.3.3 Measurement of the absolute timing resolution

The absolute timing resolution is defined as the width of the distribution of the weighted sum of all the PMT times. We referred each timing to the plastic scintillator sandwich timing. We used for this purpose the quantity

$$T_{\rm ref} = \frac{T_1 + T_2 + T_3 + T_4}{4}, \tag{10.12}$$

where T_i is the time-walk corrected timing of the $i-$th PMT of the reference counter. The contribution of $T_{\rm ref}$ to the resolution, estimated by the width of the distribution of

$$\tilde{T} = \frac{T_1 + T_2}{2} - \frac{T_3 + T_4}{2}, \tag{10.13}$$

which has a $\sigma_{\rm ref}$ of (61 ± 1) ps.

We must note that in this case there is no cancellation of the γ conversion position, nor of the π^0 decay position inside the liquid hydrogen target; instead, the uncertainty on the latter contributes twice: Figure 10.13 shows an exaggerated scheme of the $\pi^0 \to \gamma\gamma$ detection. If we call $T_\odot$ the decay time of a π^0 at the center of the target, the time recorded by a PMT on the liquid xenon detector due to photons coming from a π^0 decaying at a position x_π is

$$T_{\rm PMT} = T_\odot + \frac{L_{\rm X}}{c} - \frac{x_\pi}{c} + \frac{\rho}{c} + (iii) + (iv) + (v) \text{ as before} \tag{10.14}$$

while

$$T_{\rm Ref} = T_\odot + \frac{L_{\rm R}}{c} + \frac{x_\pi}{c} \quad \Rightarrow \quad T_\odot = T_{\rm Ref} - \frac{L_{\rm R}}{c} - \frac{x_\pi}{c}, \tag{10.15}$$

hence

$$T_{\rm PMT} = T_{\rm ref} + \frac{L_{\rm X} - L_{\rm R}}{c} - \frac{\mathbf{2}x_\pi}{c} + \ldots \tag{10.16}$$

where we understand why the uncertainty on the π^0 decay position contributes twice.

We performed the same analysis used for the intrinsic time resolution, apart from the obvious replacement of the sum of the PMT timings instead of their difference. The results are shown

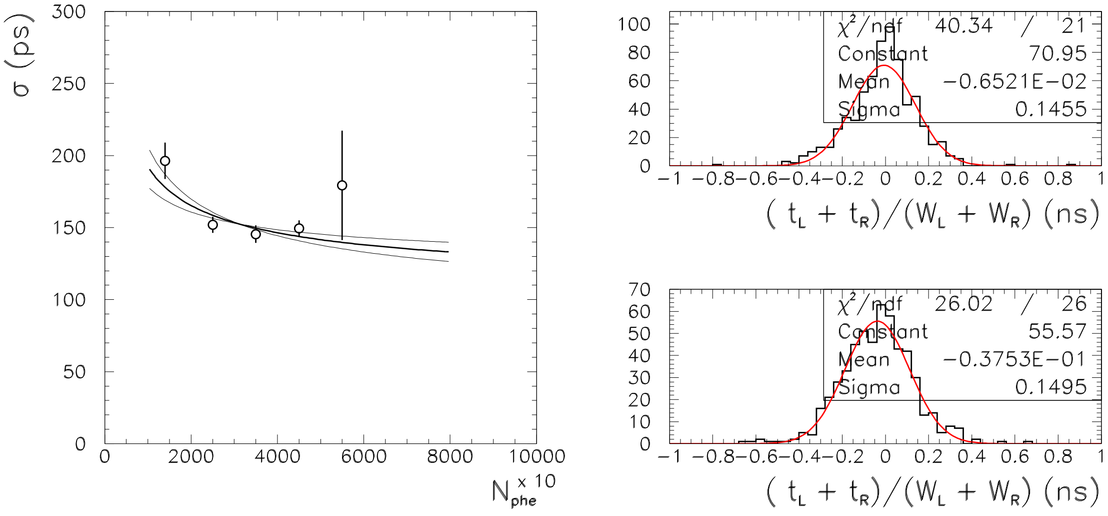

(*a*) (*b*)

Figure 10.14: (*a*) Absolute time resolution as a function of the number of photoelectrons. The fit with the function explained in the text is shown, together with its 1σ band. (*b*) Two of the distributions fitted to obtain the values in the left plot.

in Figure 10.14. We note that the resolution does not improve with the photo-electron statistics and reaches a plateau of $\approx (130 \pm 10)$ ps. It is a clear sign that the resolution is dominated by the contributions of the reference counter and of the π^0 and γ decay position (called here $\sigma_{\rm space}$). They amount, in fact, to

$$\begin{aligned}
\sigma^2_{\rm space} &= \sigma_x^2 + \sigma_y^2 + \sigma_z^2 + \sigma^2_{\rm Ref} + (2\sigma_\pi)^2 && (10.17)\\
&\approx 3 \times (25)^2 + (61)^2 + (2 \times 43)^2 \text{ ps} && (10.18)\\
&\approx 114 \text{ ps.} && (10.19)
\end{aligned}$$

The contribution of the π^0 decay and of the reference counter can be subtracted from (130 ± 10) ps to estimate the absolute timing resolution

$$\sigma_{\rm Abs} = (75 \pm 20) \text{ ps}, \tag{10.20}$$

which automatically includes the uncertainty in the photon conversion point. Also for this measurement is essential to refer to a larger number of photo-electrons because of the new PMTs with higher QEs. A new measurement of the resolution is foreseen with the LP equipped with the new PMTs.

10.4 Conclusion

In this Chapter we have shown the results of the energy and timing resolutions of the liquid xenon calorimeter large prototype, measured with photons at an energy close to 52.8 MeV. For the energy resolution measurement we had to cope with several factors related to the PMT quantum efficiencies: their dependence on beam intensity was reduced by operating the $\pi E5$ beam at a lower current; furthermore several PMTs of the front face had a particularly low QE and exhibited a behavior which is still not well understood. We could, anyway, partly correct for these effects obtaining an energy resolution of $\sim 5\%$ on the 10 cm diameter region at the detector center.

The intrinsic timing resolution has been shown to have a $1/\sqrt{N_{\rm phe}}$ dependence and a $\sigma_{\rm intr} = (20 \div 30)$ ps is envisaged at 52.8 MeV with improved quantum efficiencies. The measurement of the absolute timing resolution, on the other hand, was dominated by factors unrelated to the liquid xenon calorimeter and gives a timing resolution of (75 ± 20) ps sigma once the beam contributions are subtracted.

An issue that proved to have an utmost importance was the knowledge of the behavior at low temperature and high rate of each PMT that will be installed in the experiment. It is for this purpose that a cryogenic PMT test facility was assembled in Pisa as explained in the following Chapter. The last Chapter will summarize the implications of the so far obtained resolutions on the MEG experiment sensitivity.

Chapter 11

The PM test facility

11.1 Introduction

We assembled and operated a cryogenic facility at INFN Pisa with the initial idea to measure the main characteristics of the photo-multipliers, such as quantum efficiency, gain-voltage curve etc., before their installation in the final calorimeter, in a known and controlled geometry. After the discovery of the rate dependence of the PMT response, during the charge exchange test, it proved to be of invaluable help in understanding the phenomenon and in the rapid solution of the problem.

11.2 Description of the facility

The guide line in designing and building the test facility was the safety in xenon handling: especially we wanted to limit the possibility of an accidental xenon leak.

The facility is schematically drawn in Figure 11.1: it is all made of stainless steel standard and custom ultra high vacuum components; it is composed of an inner volume, called the "jar": a 10 cm diameter stainless steel cylinder, capable of containing 2 ℓ of liquid xenon, placed inside a larger cylinder (25 cm diameter) which is evacuated for thermal insulation. A hollow copper tube, soldered on the inner jar, embeds the copper cooling coil for the liquid nitrogen flow. On top of this tube, four power resistors can be heated to regulate the copper temperature. A CF-100 cross communicates with the active volume and with the outer environment through two gate valves: gas xenon can be poured or extracted from the cross and from the jar independently.

A large storage tank, the "reservoir", is connected directly to the jar, through an Oxisorb cartridge, that can be optionally by-passed: should anything happen to the liquid xenon causing its temperature to rise, making it boil, the vapor is free to flow harmlessly to the reservoir that, thanks to its huge volume ($\approx 600\ \ell$), limits the overall pressure to less than 2 bar.

Inside the jar where Xe is liquefied, a PMT (the "lower PMT", or "reference PMT") is supported by an aluminum holder suspended by means of stainless steel rods to the top flange, in order to

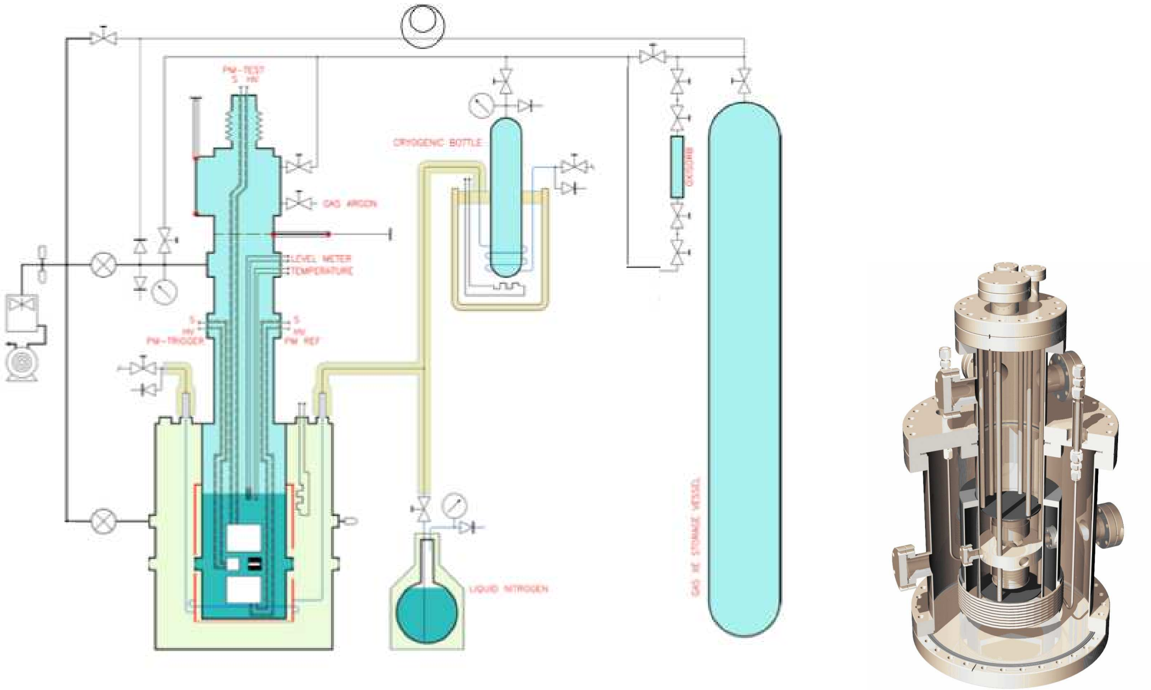

(*a*) (*b*)

Figure 11.1: (*a*) Schematic drawing of the cryostat system used to test PMTs at low temperature; (*b*) Cross section of the active volume of the cryostat.

minimize the thermal input. Another photo-multiplier (the "upper PMT", or "measured" PMT) can be inserted, and displaced, by a linear actuator. A special holding system was designed in order to be able to exchange the upper PMT without evaporating the xenon, the procedure being as follows:

1. the linear actuator is moved in upward position to bring the upper PMT at the center of the cross, the internal gate valve is closed and the gas xenon in the cross is pumped to the reservoir via a clean scroll pump, evacuating the cross;

2. warm nitrogen is poured into the cross to heat up the PMT;

3. the external gate valve is opened and the PMT is replaced. High voltage and signal cables are connected, and the rail-and-spring system which holds the upper PMT is replaced in position;

4. the external gate valve is closed and the cross evacuated;

5. gas xenon is poured again, the internal gate valve is opened and the linear actuator brings the new PMT to the measurement volume.

The lower PMT holder accommodates three blue LEDs and an $\alpha-$source stand, where an ^{241}Am source is placed such in a way as to be at the same distance from each PMT. A custom capacitive level meter, made of four $20 \times 180 \times 0.5$ mm^3 copper plates held 150 μm apart by Teflon spacers, is used to measure the amount of liquid xenon present in the jar. A quartz fiber points towards the lower (reference) PMT and it is used to transmit the light from an external nitrogen laser (Laser Scientific, Inc. VSL 337LRF, $\lambda = 337$ nm) whose stability is monitored by an external PMT. Two PT100 platinum resistors are used to monitor the temperature of the lower PMT holder ($T_{\rm in}$) and of the copper tube ($T_{\rm out}$).

11.3 Operation

We operated the facility with gaseous argon and gaseous or liquid xenon. Argon was used to test the photo-multipliers well below the Xe boiling and melting temperatures. Xe is liquefied by flowing liquid nitrogen through the cooling pipe. It takes typically 20 minutes to start liquefaction and one additional hour to have 1 ℓ of liquid xenon. When the desired amount of xenon is reached, the temperature of the copper tube is controlled by heating the four power resistors. A typical liquefaction cycle is shown in Figure 11.2.

A LabView program controls the temperatures, level and heating power through the same slow control bus, developed at PSI, used in the large prototype and in the final experiment (Midas Slow Control Bus, MSCB [122]). A special MSCB module gives the appropriate heating power on the basis of the set temperature to keep a stable operating condition. The typical temperature fluctuations of the liquid xenon are of the order of ± 0.3 °C (see Figure 11.3).

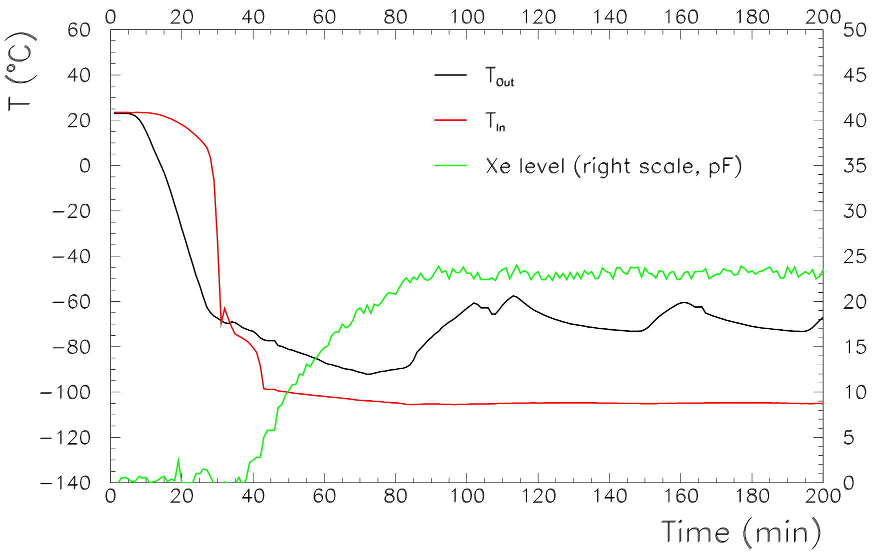

Figure 11.2: Typical behavior of inner and outer temperature for a liquefaction of xenon. The level of xenon is also indicated, as measured, in pF, by the capacitance level meter.

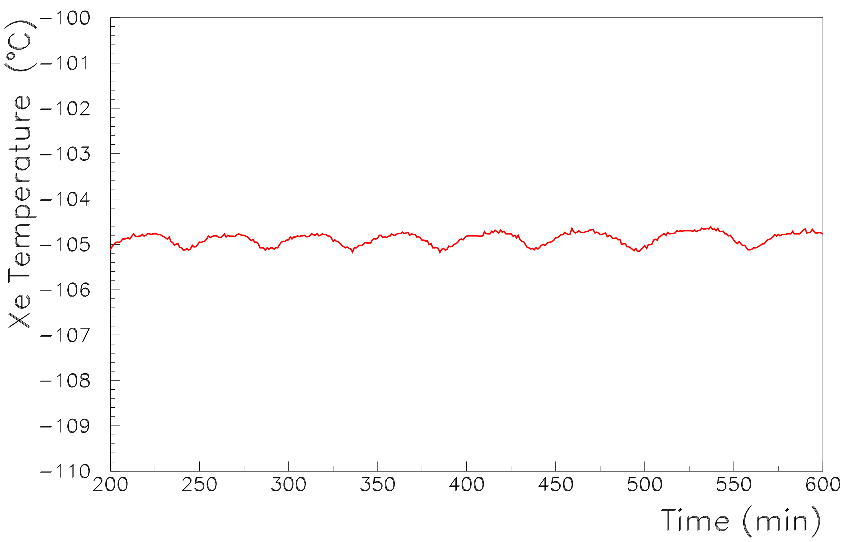

Figure 11.3: Typical inner temperature fluctuation during a PMT test in liquid Xenon

11.4 Measurements

11.4.1 Set up and procedure

LEDs can be flashed by two different pulsers: a Wavetek waveform generator and a Berkeley Nucleonics pulser. Both can provide driving pulses of some Volts, few ns wide with the desired stability. PMTs were powered by a CAEN NIM power supply (N470). The acquisition system is based on a VME crate driven by a Motorola 68030 based computing unit running the OS-9 operative system, and ancillary NIM electronics. The PMT anodic signals are sent to a NIM fan-out. One copy is discriminated, used for trigger purposes and sent to a VME TDC (CAEN V488). Another copy of the signal is sent through a delay line to a VME ADC (V465).

The typical measurement cycle consists in a determination of the gain of the 2 PMTs (one LED is flashed at different amplitudes as for the large prototype) followed by pedestal run and illumination test: one LED (the "biasing" LED) is flashed at a fixed intensity but at different rates to provide the desired illumination and anodic current, while the signals of another LED (the "measuring" LED) flashed at a 50 Hz frequency, are recorded by the acquisition. During a typical run, lasting roughly 15 minutes, the biasing LED is switched on for a certain time and then switched off again, to see its effect on the PMT response.

11.4.2 The PMTs under test

We tested three kinds of photo-multipliers: their mechanical structure is the same (case, dynode structure, bleeder circuit) but with different photo-cathodes:

R6041Q Is the type which has been installed in the large prototype so far. Its photo-cathode is K−Cs−Sb, and a thin Mn layer is evaporated between the photo-cathode and the quartz window to help reducing the resistivity at low temperature. Some difficulties in evaporating this layer yielded PMTs with low QEs and large spread in QE values [119];

R9288 This model was developed to overcome the difficulties with the Mn layer and to provide larger quantum efficiencies. The uniform Mn layer is replaced by a mesh of aluminum strips, and the photo-cathode composition is different: Rb−Cs−Sb. Hamamatsu asserts that the typical QE at 178 nm for this PMT model is $\approx 20\%$;

R9288-MOD We had only two samples of this model which was developed on our request to further reduce the resistivity at low temperature. It is identical to R9288 but with an aluminum mesh twice as dense as the previous model.

11.4.3 Biasing current consideration

The choice of the anodic current range to be used in the tests was dictated by the fact that we want to test the PMTs in a situation as close as possible to that in which they will operate.

The average anodic current will be determined, in the experiment, by the rate of low energy photons; there will be two main sources of such photons: the $\mu^+ \to e^+\nu\bar{\nu}\gamma$ radiative decay and the capture of thermal neutrons on Xe. γs from the radiative muon decay have, on average, an energy of 8 MeV. The expected rate is of the order of the μ^+ stopping rate times its branching ratio. Only 10% of those photons will be in the calorimeter angular acceptance, hence the number of scintillation photons generated, per second, inside the calorimeter at a full intensity muon beam will be

$$N_\gamma \simeq 40\,000 \left(\frac{\text{phe}}{\text{MeV}}\right) \times 8\ \text{MeV} \times 10^8\ \mu^+/\text{sec} \times 10^{-2} \left(\frac{\gamma}{\mu^+}\right) \times 10\% \simeq 3.2 \times 10^{10}. \tag{11.1}$$

Taking an average of 20% QE and 30% PMT coverage of the calorimeter, at a gain of $g = 10^6$ this amounts to a current per PMT of

$$I_a(\text{radiative}) = \frac{N_\gamma \times QE \times \text{Coverage} \times g \times e}{N_{\text{PMT}}} \simeq 0.4\ \mu\text{A}, \tag{11.2}$$

where e is the electron charge.

The number of thermal neutrons in the $\pi E5$ area has been measured [123] to be $15n/\text{sec}/\text{cm}^2$. Thermal neutrons are captured ($\lambda_{\text{Cap}} \sim 3$ cm) by Xe nuclei which emit an energy of 9 MeV, shared typically among several photons. Assuming that half of this energy is contained in the calorimeter a calculation analogous to the previous one gives

$$I_a(\text{neutrons}) \simeq 3\ \mu\text{A}. \tag{11.3}$$

Note that the bleeder circuit current at normal operation is roughly 60 μA. The neutron flux envisaged for the final experiment is high and their screening must be studied. In the charge exchange test we estimated the anodic current due to thermal neutrons to be of the order of 1 μA. It is for this reasons that we studied the PMT response in a range $(1 \div 4)$ μA. Neutron field measurements are being done with a Bonner Sphere detector and with NaI activation, and are planned in the experimental area after the beam line setup is complete.

11.4.4 Results

We tested the PMTs in Ar gas and in liquid Xe. The test in Ar enabled us to explore a wider temperature range, while the tests in liquid Xe insured a condition as close as possible as the final one. While the temperature control in liquid xenon is relatively simple, the temperature stabilization in gaseous argon required a few hours. Figure 11.4a shows the output of a R6041 PMT at $-105\ °C$, the normal operation temperature of the liquid xenon detector (the pressure at which the liquid is kept is larger than 1 atm), while a LED, producing an anodic current of 0.8 μA is switched on and off. The effect is dramatic and reproduces what observed during the charge exchange test. To quantify the effect we fit the resulting histogram (see Figure 11.6a) with an exponential relaxation

$$\mathcal{A}(t) = a + be^{-t/\tau}, \tag{11.4}$$

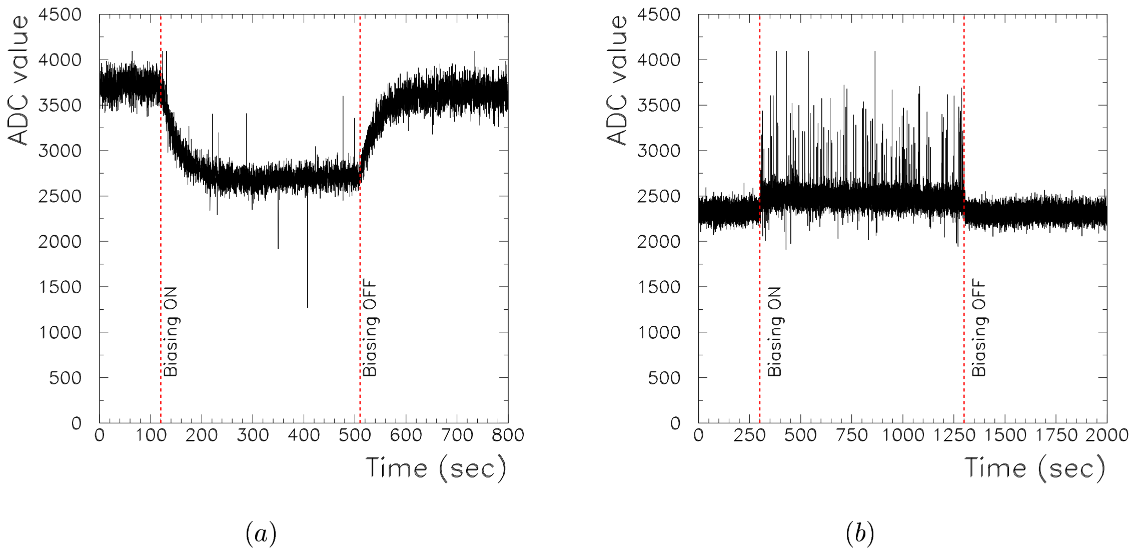

Figure 11.4: LED amplitude measured by a R6041Q PMT during a biasing test at -105 °C (a) and at room temperature (b)

and quote as "relaxation factor", defined as the fraction of the original amplitude at which the PMT sets, the plateau/peak ratio given, in the notation of Equation 11.4, by

$$\frac{\text{Plateau}}{\text{Peak}} = \frac{a}{a+b}.$$

The relaxation factor is almost $\sim 75\%$ for this PMT! Notice that the same PMT at room temperature is completely insensitive to the biasing (Figure 11.4b) but for a small over-linearity, due to the fact that the biasing current is not negligible with respect that drained by the bleeder circuit[1] [124]. The gain has in fact been measured with and without biasing, and the difference accounts for the observed increase in signal height.

Figure 11.6 shows the relaxation factor for two R9288 PMTs over a wide range of temperatures, and at several anodic currents, taken in gas Ar. Figure 11.6a shows a typical exponential fit, while Figure 11.6b summarizes the response of several tested photo-multipliers at an anodic current of 4 μA. The PMT with serial number TB0171 was sent back to Hamamatsu for a check and they discovered that the Al mesh was not perfectly grounded for this PMT. The other photo-multipliers show a safe behavior down to temperature of -110°C. The red star in Figure 11.5a shows the old type PMT for comparison.

The results for the two samples of the double grid PMTs (ZA1980 and ZA1985) are also shown: they do not show any misbehavior in the liquid xenon temperature range ($-105 \div -108$ °C). We unfortunately had the possibility to test only two PMTs of this type.

[1]We solved this problem for future PMTs by inserting two Zener diodes to stabilize the voltage across the two last dynodes

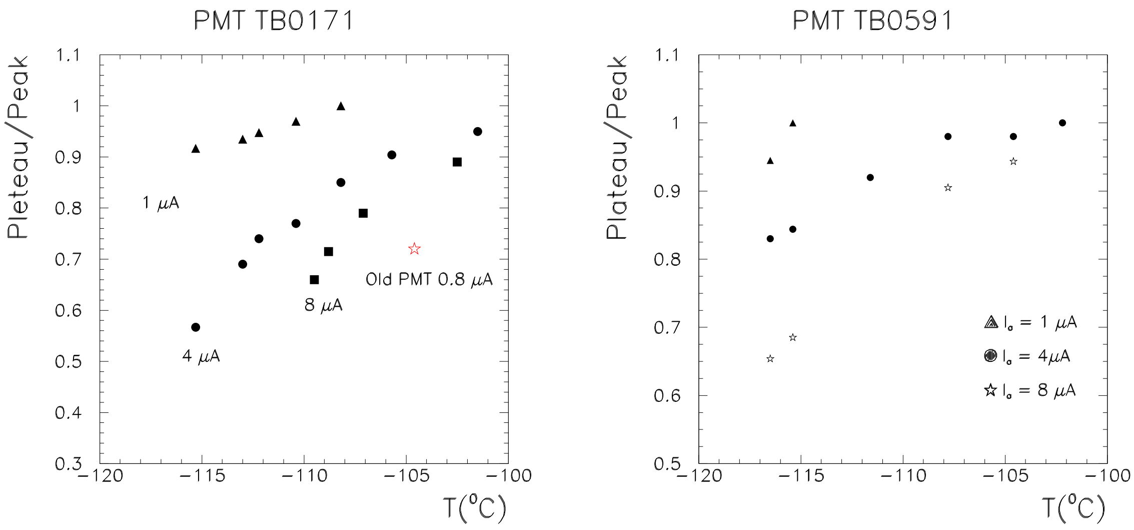

(a) (b)

Figure 11.5: Plateau/Peak ratio as a function of the temperature for different biasing currents for two single Aluminum mesh PMTs. The red star shows the behavior of a R6041Q PMT.

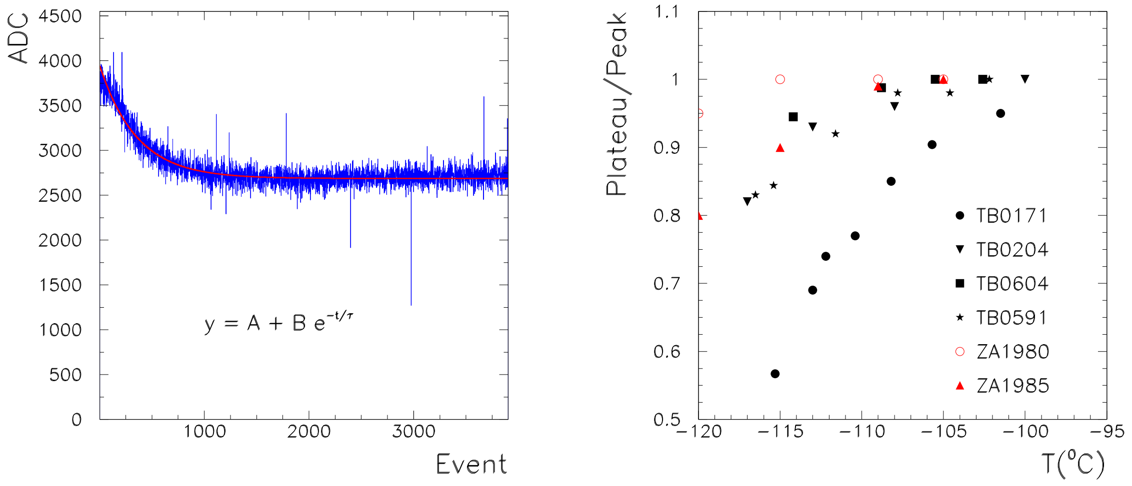

(a) (b)

Figure 11.6: (a) A typical exponential fit of the PMT behavior; (b) Summary plot for several single-aluminum mesh photo-multipliers (TB series) and the two samples of the double-aluminum mesh PMTs (ZA series).

11.5 Conclusions

We are confident that the single aluminum grid and, better, the double aluminum grid PMTs solve the problems observed during the charge exchange test, and will be suitable for operation in the final experiment. To confirm this statement they will be installed and tested in the large prototype in a forthcoming test-beam period.

Chapter 12

The MEG experiment sensitivity

12.1 Introduction

The last Chapter of this thesis deals with the question: what did we learn from the previous reported measurements? How do the resolutions obtained affect the MEG experiment sensitivity?

Clearly the resolutions measured for the photon detector were obtained with the large prototype in a geometric condition which is different from the final one mainly in two respects: the final calorimeter has a curved shape and has a larger volume, hence it is more sensitive to light absorption effects. Anyway the results obtained for the resolutions are comparable to the Monte Carlo expectations, hence we are confident that the same algorithms applied to the curved geometry can be trusted. Moreover it was shown that the ultimate resolutions of the two devices were comparable.

12.2 Preliminary remarks

We define the *sensitivity* of the MEG experiment to the branching ratio of the $\mu^+ \to e^+\gamma$ decay as the 90% confidence level (CL) upper limit in case of no event observed during the running period. For a given branching ratio $B_{\mu^+\to e^+\gamma}$, the number of observed events can be written as

$$N_e = R_\mu T \frac{\Omega}{4\pi} \epsilon_e \epsilon_\gamma \epsilon_{\rm cut} B_{\mu^+\to e^+\gamma} \tag{12.1}$$

where R_μ is the muon stop rate, T is the measuring time, Ω is the detector solid angle (we assume identical values for the photon and positron detectors), ϵ_e and ϵ_γ are the positron and photon detection efficiencies (we assume $\epsilon_e \approx 0.9$, $\epsilon_\gamma \approx 0.65$ due to the probability of gamma conversion in the materials before the liquid Xe volume, whose thickness amounts to 0.44 X_0) and $\epsilon_{\rm cut}$ is the efficiency of the selection cuts. Those cuts can be applied on the reconstructed positron energy (E_e) photon energy (E_γ) opening angle ($\theta_{e\gamma}$) and relative timing ($t_{e\gamma}$), and define the signal region.

It is clear that the selection cuts must be chosen so as to keep the background within this region

Quantity	resolution	value	uses MC	uses data
Photon detector energy resolution	δy	0.035		$\surd$
Positron energy resolution	δx	0.006	$\surd$	
Relative timing resolution	$\delta t_{e\gamma}$	105 ps	$\surd$	$\surd$
Relative angle resolution	$\delta\theta_{e\gamma}$	23 mrad	$\surd$	$\surd$
"	δz	0.012	$\surd$	

Table 12.1: The resolutions on the various kinematical quantities of the positron-photon pair used to compute the expected sensitivity of the MEG experiment to the $\mu^+ \to e^+\gamma$ branching ratio. See the text for details.

at a negligible level, and are therefore dependent on the detector resolutions. If we choose to apply 90% efficient cuts on the four quantities (corresponding to 1.4 FWHM for Gaussian-distributed variables) $\epsilon_{\mathrm{cut}} = (0.9)^4 = 0.66$. For sake of convenience, we define the branching ratio for which the observed number of events is exactly $N_e = 1$, all the other quantities being known, as the single event sensitivity (SES) of the experiment.

As we stated in Chapter 3 the background is dominated by accidental coincidences of Michel positrons, close to the spectrum endpoint, with high energy photons from muon radiative decay or positron annihilation-in-flight.

We can make those statements more quantitative now, on the basis of the detector resolutions, and, in particular, on the basis of the energy and timing resolutions of the liquid xenon detector, obtained from the charge exchange test.

The resolutions used in what follows are summarized in Table 12.1, the naming conventions being the same of Chapter 2 (δ means the half-width of a 90% efficient region).

- The photon energy resolution $\delta y = 0.035$ arises from a 90% efficient cut on a photon distribution with a 5% FWHM, which is the result obtained at the charge exchange test;
- The e^+ energy resolution value, $\delta x = 0.006$ is taken from Chapter 4;
- The relative timing resolution, $\delta t_{e\gamma} = 105$ ps, is the average of the range quoted in section 10.3.2, and is given by the convolution of the measured timing resolution of the LP and timing counter (including the contribution of the position resolution);
- The relative direction resolution is computed by folding the drift chamber resolution (12 mrad) with the curved calorimeter expected resolutions ($\sigma_\phi = 7$ mrad, $\sigma_\theta = 6.5$ mrad, see Figure 6.11, confirmed by the measurement at TERAS): two collinear but opposite vectors have been randomly displaced according to those resolutions, and their relative angle $\theta_{e\gamma}$ has been computed. The 90% efficient cut on the $\pi - \theta_{e\gamma}$ distribution is given by $\delta\theta_{e\gamma} = 0.023$ mrad (see Figure 12.1);

With these resolutions in mind we compute the expected background, and then state the required muon flux and running time to perform a sensitive search for the $\mu^+ \to e^+\gamma$ decay.

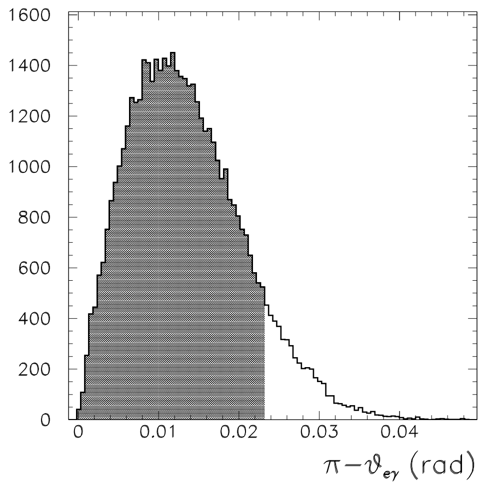

Figure 12.1: 90% efficient cut on the distribution of the positron-photon relative angle $\pi - \theta_{e\gamma}$.

12.3 Physics background evaluation

As observed in Section 3.3.1 the physics background branching ratio can be computed from the $\mu \to e\gamma\bar{\nu}\nu$ decay width. Two forms exist, depending on whether the angular resolution is better or worse than the energy ones ($\delta z \lesseqgtr 2\sqrt{\delta x \delta y}$). In either case the contribution to the background is negligible, as clear observing Figure 12.2a and b. In our situation $\delta z = 0.012 < 2\sqrt{\delta x \delta y} = 0.028$, hence we must refer to Figure b. The contribution of the physics background to the branching ratio is therefore $< 3 \times 10^{-15}$.

12.4 Accidental background evaluation

The contribution of accidental coincidences has been shown in Section 3.3.2 to be

$$B_{acc} = R_\mu \cdot (2\delta x) \cdot \left[\frac{\alpha}{2\pi}(\delta y)^2(\ln(\delta y) + 7.33)\right] \times \left(\frac{\delta\theta^2}{4}\right) \cdot (2\delta t). \qquad (12.2)$$

We want to keep the number of expected accidental background events, given by B_{acc} divided by the single event sensitivity[1], at the level of $N_{acc} \sim 0.5$ events. Figure 12.3a shows B_{acc} as a function of the photon and positron energy resolution for a muon rate of 2.2×10^7 μ/sec, while Figure 12.3b shows the expected number of background events as a function of the muon stopping rate R_μ and measuring time T, for the resolutions quoted in Table 12.1.

[1]This number therefore scales with $(R_\mu)^2$.

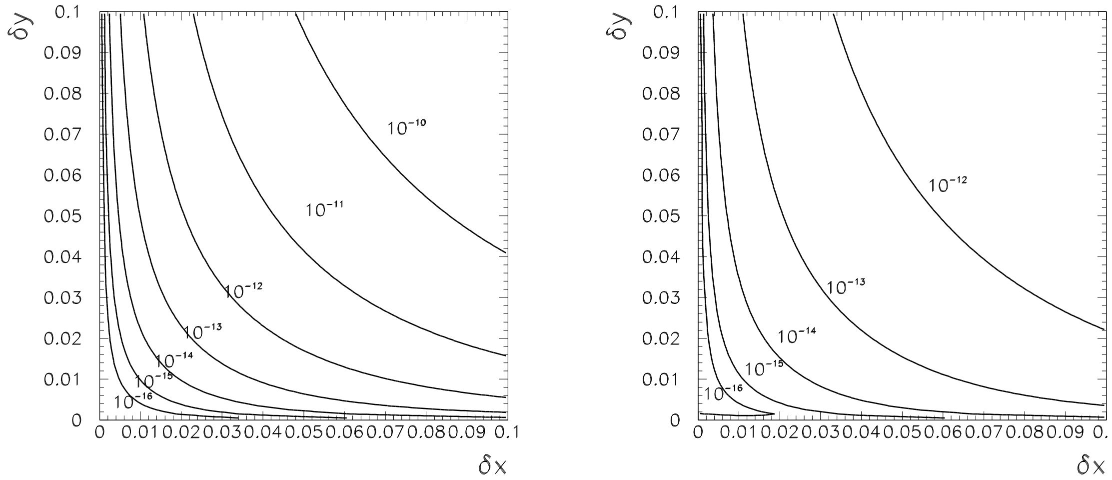

(a) (b)

Figure 12.2: Computation of the dependence of the physics background branching ratio on the positron and photon energy resolutions in the case $\delta z > 2\sqrt{\delta x \delta y}$ (a) and $\delta z < 2\sqrt{\delta x \delta y}$ (b). To obtain this latter plot we assumed $\delta z = 0.012$.

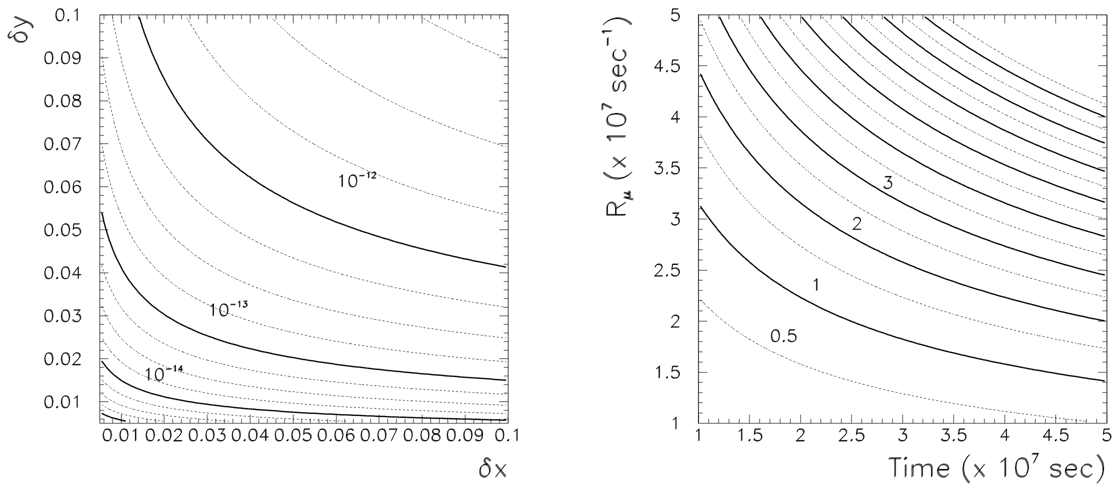

(a) (b)

Figure 12.3: (a) B_{acc} as a function of the photon and positron energy resolution at $R_\mu = 2.2 \times 10^7$ sec^{-1}; (b) Number of expected background events as a function of the muon stopping rate R_μ and measuring time T, for the resolutions quoted in Table 12.1.

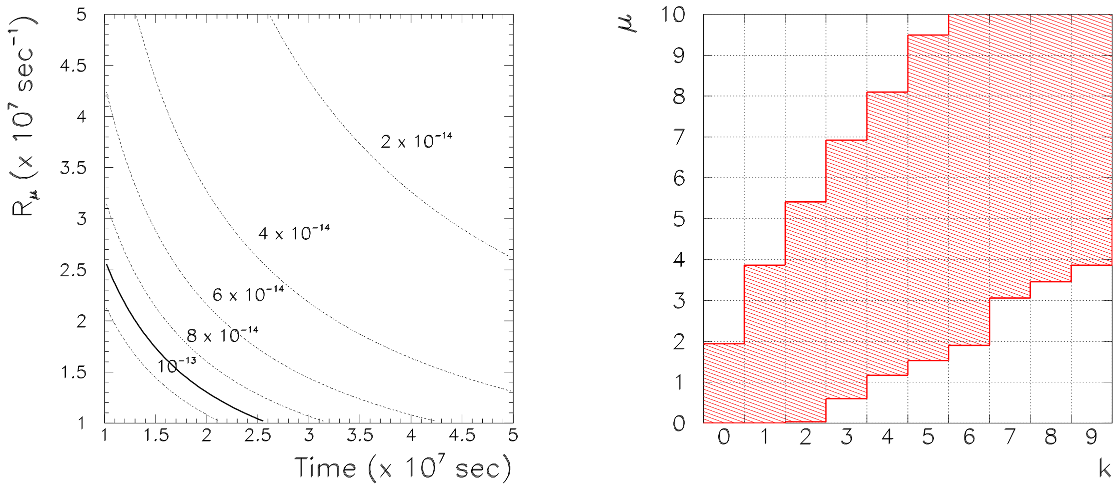

(*a*) (*b*)

Figure 12.4: (*a*) Single event sensitivity as a function of the muon rate and of the running time; (*b*) the 90% frequentist confidence band for the average μ of a Poisson process when a number k of events is observed, in the presence of a background of 0.5 events.

12.5 Contribution of photon pile-up

Since the calorimeter is a homogeneous volume there is the possibility that two, or more, low energy photons entering the liquid xenon volume are reconstructed as a single high-energy photon. Waveform digitization and event reconstruction will help in reducing this background. A Monte Carlo simulation [61] shows that the contribution of the pile-up photons which are not distinguished by the waveform digitization is to increase the number of background events by $10 \div 15\%$ for a muon rate of $R_\mu = 10^8$/sec.

12.6 Sensitivity to the $\mu^+ \to e^+\gamma$ decay

Once we accept the value of 0.5 background events, we can move along the dotted line marked 0.5 on Figure 12.3*b*. The choice of the values of R_μ and T is dictated by a compromise between the need to perform the experiment in a reasonable time and having a good single event sensitivity. The single event sensitivity (which does not depend on the resolutions) is shown in Figure 12.4 as a function of the muon rate and of the running time. A comparison of Figure 12.3*b* and Figure 12.4*a* shows that a reasonable choice, $R_\mu = 1.2 \times 10^7$ μ/sec, $T = 3.5 \times 10^7$ sec, yields a SES of 6×10^{-14}. It is clear that, due to the R_μ^2 dependence of the accidental background, for a given number of accepted background events it is more convenient to run for a longer time at a lower beam intensity, because the SES increases.

We must emphasize that $= 6 \times 10^{-14}$ is *not* the sensitivity to the $\mu^+ \to e^+\gamma$ decay as defined at the beginning of this Chapter. In fact we must compute the 90% confidence level band and extract the limit on the $\mu^+ \to e^+\gamma$ decay in case of no candidate observed.

In Figure 12.4*b* we show the confidence band calculated, in a frequentist framework using the Feldman-Cousins ordering prescription [125], for a Poisson-distributed signal over an expected background of 0.5 events. In case of no candidate observed ($k = 0$ on the $x-$axis) the 90% CL region yields $N_{\mu^+ \to e^+\gamma} < 1.98$ that, at a SES of 6×10^{-14} implies a limit on the $\mu^+ \to e^+\gamma$ branching ratio of

$$BR(\mu^+ \to e^+\gamma) < 1.2 \times 10^{-13} \quad @90\% \text{ CL.} \tag{12.3}$$

From the same plot one sees that a discovery can be claimed at this CL after an observation of at least three candidates, in which case the limit would be

$$4.2 \times 10^{-14} < BR(\mu^+ \to e^+\gamma) < 4.2 \times 10^{-13}.$$

12.7 Importance of detector stability

It is clear that the number of background events entering the signal region can vary in case of time dependence of the detector resolutions, *e.g.* given by a time-dependent attenuation length for the scintillation light in xenon. It is therefore necessary to have a continuous and reliable monitoring system of all the experimental resolutions involved in the determination of the signal region. For the liquid xenon calorimeter several possibilities are envisaged and/or under test, which allow a survey of the detector in an energy range as large as possible:

- In the low energy region (5.5 MeV) α-source spots deposited on thin wires could be used to measure the PMT quantum efficiencies and the liquid xenon attenuation length. This possibility is a unique feature of a liquid calorimeter, in which a source can be directly mounted in the active volume. Four tungsten wires with two ^{210}Po sources each are presently mounted in the large prototype and will be tested soon. Polonium was chosen for the first tests, despite its short half-life (138 days) because of some difficulties in ^{241}Am deposition, which are now solved. Cobalt discs or wires are planned to be tested, too;
- In the intermediate energy region, the activation of materials immersed in LXe, by means of thermal neutrons, moderated from a neutron generator or intense AmBe source could produce photon lines of some MeVs (see, *e.g.* section 8.2.1);
- In the high energy region measurements of photons from π^0 decays from π^- charge exchange in a LH_2 target are planned. Since this measurement requires the temporary replacement of the polyethylene target with a liquid hydrogen one, which costs some effort and time, the possibility is being studied of installing a LH_2 cell behind the detector, hit by π^- from a parallel beam line. In this way the calibration could be performed as frequently as desired;

The possibility of having different ways of calibration and monitoring, complementary to each other, is of extreme importance for the experiment.

Conclusion

Five years have passed since the approval of the MEG proposal by the PSI scientific committee; during this time major improvements have been made towards the building of the experiment whose ambition is to improve the present limit on the $\mu^+ \to e^+\gamma$ decay branching ratio by two orders of magnitude. Pushing the limit to such a level is of extreme importance: an evidence for the decay would be a clear signal of new physics beyond the Standard Model, and a negative result will constrain the possible extensions of the model, ruling out most of their free parameter space.

A first big step was the demonstration of the capability to guarantee a sufficient xenon transparency to its scintillation light, by means of a suitable purification system. After that the operation of the presently largest liquid xenon calorimeter in the world allowed us to test procedures and solutions for designing the final form of the calorimeter.

The test of the prototype with photons at an energy close to 52.8 MeV, on a PSI beam line, was of paramount importance, because we could operate in a condition very similar to the final one, and we could test a calibration method (the charge exchange reaction on a liquid hydrogen target) that will be present for the MEG curved shape calorimeter. It also allowed the realization of problems concerning the PMT operation at high rate and low temperature, and we are confident that this problem is now solved for future PMTs.

The results obtained are slightly worse than expected, both for energy and for timing resolution. The experimental setup was not ideal, especially for the poor understanding of the behavior of some PMTs. Even with this results we showed that the sensitivity of the MEG experiment is still two orders of magnitude below the present limit.

A new test beam is in preparation to repeat the energy and timing measurements with charge exchange photons, and a new calibration method has been implemented, namely the introduction in the calorimeter of α-sources deposited on thin tungsten wires: a calibration method that is unique to this device.

In the meanwhile the experiment commissioning schedule is being completed: the COBRA magnet is already in the $\pi E5$ area, and the beam line is waiting for its final element, the beam transport solenoid, to be delivered at PSI at the beginning of the next year. The year 2005 will see also the assembly of all the experiment detectors: the drift chambers and the timing counter, and the manufacturing of the xenon calorimeter cryostat, in which the PMTs will be installed in autumn and winter. The trigger and DAQ system production will proceed in parallel, in order to guarantee the commissioning of the full detector as soon as the beam will be available in 2006. A two years data taking period ($2006 \div 2007$) is then foreseen.

Bibliography

[1] R. Barbieri, "The Standard Model of Electroweak Interactions", IFUP-TH06/95, and references therein.

[2] A. di Giacomo, "Lezioni di Fisica Teorica", Edizioni ETS (1992) Pisa

[3] S. Weinberg, "The Quantum Theory of Fields", Cambridge University Press (2000) Cambridge

[4] R. N. Mohapatra, "Unification and Supersymmetry", 2^{nd} edition, Springer-Verlag, New York (1992)

[5] L. B. Okun, "Leptons and Quarks", North-Holland Publishing Company, Amsterdam (1982)

[6] B. T. Cleveland *et al.*, "Measurement Of The Solar Electron Neutrino Flux With The Homestake Chlorine Detector," Astrophys. J. **496**, 505 (1998).

[7] Y. Fukuda *et al.* [Super-Kamiokande Collaboration], "Measurement of the solar neutrino energy spectrum using neutrino electron scattering," Phys. Rev. Lett. **82**, 2430 (1999) [arXiv:hep-ex/9812011].

[8] Y. Suzuki [Super-Kamiokande Collaboration], "Solar Neutrino Results From Super-Kamiokande," Nucl. Phys. Proc. Suppl. **77**, 35 (1999).

[9] D. Kielczewska [SUPER-KAMIOKANDE Collaboration], "Neutrino Oscillations At Super-Kamiokande," Nucl. Phys. Proc. Suppl. **81**, 133 (2000).

[10] W. Hampel *et al.* [GALLEX Collaboration], "GALLEX solar neutrino observations: Results for GALLEX IV," Phys. Lett. B **447**, 127 (1999).

[11] J. N. Abdurashitov *et al.* [SAGE Collaboration], "Measurement of the solar neutrino capture rate with gallium metal," Phys. Rev. C **60**, 055801 (1999) [arXiv:astro-ph/9907113].

[12] M. Apollonio *et al.* [CHOOZ collaboration], "Search for neutrino oscillations on a long base-line at the CHOOZ nuclear power station" Eur. Phys. J. C**27**, (2003) 331 [arXiv:hep-ex/0301017]

M. Apollonio *et al.* [CHOOZ collaboration], "Limits on neutrino oscillations from the CHOOZ experiment", Phys. Lett. B **466** (1999) 415

[13] Q. R. Ahmad *et al.* [SNO Collaboration], "Measurement of the charged of current interactions produced by ^{8}B solar neutrinos at the Sudbury Neutrino Observatory," Phys. Rev. Lett. **87**, 071301 (2001) [arXiv:nucl-ex/0106015].

[14] M. Maltoni *et al.* "Status of global fits to neutrino oscillations", preprint `hep-ex/0405172`

P. Creminelli, G. Signorelli and A. Strumia, "Frequentist analyses of solar neutrino data," JHEP **0105**, 052 (2001) [arXiv:hep-ph/0102234].

[15] H. Georgi, in *Particles and Fields*, ed. C. E. Carlson, AIP (1975)

[16] Fritsch and Minkowski, Ann. Phys. **93** (1975) 193

[17] M. L. Brooks *et al.* [MEGA Collaboration], "New limit for the family-number non-conserving decay $\mu^+ \to e^+\gamma$", Phys. Rev. Lett. **83**, 1521 (1999) [arXiv:hep-ex/9905013].

[18] M. Ahmed *et al.*, "Search for the lepton-family-number nonconserving decay $\mu^+ \to e^+\gamma$," Phys. Rev. D **65** (2002) 112002 [arXiv:hep-ex/0111030].

[19] Bellgardt, U., *et al.*, 1988, Nucl. Phys. B **229**, 1.

[20] Wintz, P., 1998, in *Proceedings of the First International Symposium on Lepton and Baryon Number Violation*, edited by H.V. Klapdor-Kleingrothaus and I.V. Krivosheina (Institute of Physics Publishing, Bristol and Philadelphia), p.534.

[21] Willmann, L., *et al.*, 1999, Phys. Rev. Lett. **82**, 49.

[22] Edwards, K.W., *et al.* (CLEO Collaboration), 1997, Phys. Rev. B **55**, R3919.

[23] K. Abe *et al.* [Belle Collaboration] "Search for $\tau \to \mu\gamma$ decay at Belle," KEK PREPRINT-2001-79 (2001) *Prepared for the 20th International Symposium on Lepton and Photon Interactions at High Energies (LP 01) Rome, Italy, 23-28 Jul 2001*

[24] Bliss, D.W., *et al.*, 1998, Phys. Rev. D **57**, 5903.

[25] Krolak, P., *et al.*, 1994, Phys. Lett. B **320**, 407.

[26] Ambrose, D., *et al.* (BNL E871 Collaboration), 1998, Phys. Rev. Lett. **81** 5734.

[27] Lee, A.M., *et al.*, 1990, Phys. Rev. Lett. **64**, 165.

[28] L. Bellantoni *et al.* [KTeV collaboration], Proc. 36th Rencontres de Moriond (Les Arcs, France) 10-17 Mar 2001 [arXiv:hep-ex/0107045]

[29] Akers, R., *et al.* (OPAL Collaboration), 1995, Z. Phys. C **67**, 555.

[30] Abreu, P., *et al.* (DELPHI Collaboration), 1997, Z. Phys. C **73**, 243.

[31] L. J. Hall, V. A. Kostelecky and S. Raby, "New Flavor Violations In Supergravity Models", Nucl. Phys. B **267**, 415 (1986).

[32] R. Barbieri and L. J. Hall, "Signals for supersymmetric unification," Phys. Lett. B **338**, 212 (1994) [arXiv:hep-ph/9408406].

[33] R. Barbieri, L. J. Hall and A. Strumia, "Violations of lepton flavor and CP in supersymmetric unified theories," Nucl. Phys. B **445**, 219 (1995) [arXiv:hep-ph/9501334].

[34] Y. Kuno and Y. Okada, "Muon decay and physics beyond the standard model," Rev. Mod. Phys. **73**, 151 (2001) [arXiv:hep-ph/9909265].

[35] J. Hisano, T. Moroi, K. Tobe and M. Yamaguchi, "Exact event rates of lepton flavor violating processes in supersymmetric SU(5) model," Phys. Lett. B **391**, 341 (1997) [Erratum-ibid. B **397**, 357 (1997)] [arXiv:hep-ph/9605296].

[36] P. Ciafaloni, A. Romanino and A. Strumia, "Lepton flavor violations in SO(10) with large tan beta," Nucl. Phys. B **458** (1996) 3 [arXiv:hep-ph/9507379].

[37] J. Hisano and D. Nomura, "Solar and atmospheric neutrino oscillations and lepton flavor violation in supersymmetric models with the right-handed neutrinos," Phys. Rev. D **59**, 116005 (1999) [arXiv:hep-ph/9810479].

[38] K. Hagiwara *et al.* [Particle Data Group Collaboration], "Review of particle physics," Phys. Rev. **D 66**, 010001 (2002).

[39] H. N. Brown *et al.* [Muon g-2 Collaboration], "Precise measurement of the positive muon anomalous magnetic moment," Phys. Rev. Lett. **86**, 2227 (2001) [arXiv:hep-ex/0102017].

[40] J. Hisano and K. Tobe, "Neutrino masses, muon $g-2$ and lepton-flavour violation in the super-symmetric see-saw model", Phys. Lett. B **510**, 197 (2001) [arXiv:hep-ph/0102315].

[41] S. H. Neddermeyer and C. D. Anderson, "Note On The Nature Of Cosmic Ray Particles," Phys. Rev. **51**, 884 (1937).

[42] H. Yukawa, Proc. Phys. Math. Soc. Jap. **17**, 48 (1935)

[43] M. Conversi, E. Pancini and O. Piccioni, "On The Disintegration Of Negative Mesons," Phys. Rev. **71**, 209 (1947).

[44] E. P. Hincks and B. Pontecorvo, "On The Absence Of Photons Among The Decay Products Of The 2.2-Microsecond Meson," Can. J. Res. **28A**, 29 (1950), reprinted in S. M. Bilenky *et al.* (editors) "Bruno Pontecorvo" Società Italiana di Fisica (1997)

[45] Lokonathan, S. and J. Steinberger, "Search for Improbable Muon Decays" Phys. Rev. **98**, 240 (1955).

[46] Feinberg, G., Phys. Rev. **116**, 1482 (1958)

[47] Danby, G., J.M. Gaillard, K. Goulianos, L.M. Lederman, N. Mistry, M. Schwartz, and J. Steinberger, Phys. Rev. Lett. **9**, 36 (1962)

[48] P. Depommier *et al.*, "A New Limit On The $\mu^+ \to e^+\gamma$ Decay," Phys. Rev. Lett. **39**, 1113 (1977).

[49] A. van der Schaaf, R. Engfer, H. P. Povel, W. Dey, H. K. Walter and C. Petitjean, "A Search For The Decay $\mu^+ \to e^+\gamma$", Nucl. Phys. A **340**, 249 (1980).

[50] W. W. Kinnison *et al.*, "A Search For $\mu^+ \to e^+\gamma$", Phys. Rev. D **25**, 2846 (1982).

[51] R. D. Bolton *et al.*, "Search For Rare Muon Decays With The Crystal Box Detector," Phys. Rev. D **38**, 2077 (1988).
R. D. Bolton *et al.*, "Search For The Decay $\mu^+ \to e^+\gamma$", Phys. Rev. Lett. **56**, 2461 (1986).

[52] Fronsdal, C., and H. Überall, Phys. Rev. **118**, (1959) 654.

[53] Eckstein, S.G., and R.H. Pratt, Ann. of Phys. **8**, (1959) 297.

[54] Y. Kuno and Y. Okada, "$\mu \to e\gamma$ Search with Polarized Muons," Phys. Rev. Lett. **77**, 434 (1996) [arXiv:hep-ph/9604296].

[55] S. Parker, H. L. Anderson and C. Ray, "Search for the decay $\mu^+ \to e^+\gamma$", Phys. Rev. **133** B768 (1964).

[56] S. Frankel *et al.*, "New Limit on the $e + \gamma$ Decay Mode of the Muon", Phys. Rev. Lett. **8** 123 (1962).

[57] H. P. Povel *et al.*, "A New Upper Limit For The Decay $\mu^+ \to e^+\gamma$" Phys. Lett. B **72**, 183 (1977).

[58] A.E. Pifer *et al* "A high stopping density μ^+ beam" NIM 135 (1976) 39

[59] H-W. Reist *et al.* "Development of a low-momentum "surface" muon beam for LAMPF", NIM 153 (1978) 61

[60] J. D. Bowman *et al.*, "Upper Limit For The Decay $\mu^+ \to e^+\gamma$", Phys. Rev. Lett. **42**, 556 (1979).

[61] A. Baldini, [MEG Collaboration], "The MEG experiment: search for the $\mu^+ \to e^+\gamma$ decay at PSI" at `http://meg.psi.ch/docs/prop_infn/nproposal.ps.gz`

[62] TRANSPORT - *A Computer Program for Designing Charged Particle Beam Transport Systems*, K.L. Brown *et al.* CERN Yellow Report 73-16, (1973);

[63] Decay TURTLE - *A Computer Program for Simulating Charged Particle Beam Transport Systems, including Decay Calculations* K.L. Brown and Ch. Iselin, CERN Yellow Report 74-2 (1974);
Graphics versions of both Programmes by U. Rohrer PSI-Report (1980).

[64] T. Mori *et al.*, Search for $\mu \to e + \gamma$ down to 10^{-14} branching ratio, proposal to PSI (1999) R-99.05.01

[65] MEG Collaboration, "Test measurements for the MEG drift chambers" in PSI Annual Report (2003), also at http://meg.pi.infn.it/docs/index.html

[66] G. Signorelli, "Towards a $\mu^+ \to e^+\gamma$ experiment", Pretesi per il passaggio al terzo anno di Perfezionamento della Scuola Normale Superiore (2002) unpublished.

[67] MEG Collaboration, "MUEGAMMA timing counter prototype test", PSI Annual Report (2001)

[68] F. Gatti, "Status of the MEG timing counter", February 2004, available at http://meg.psi.ch/docs

[69] T. Doke and K. Masuda, "Present status of liquid rare gas scintillation detectors and their new application to gamma-ray calorimeters" Nucl. Instr. Meth. **A420** (1999) 62

[70] C. Rubbia, CERN EP Internal Report 77-8 (1977)

[71] E. Conti *et al.* [EXO Collaboration], "Correlated fluctuations between luminescence and ionization in liquid xenon," Phys. Rev. B **68** (2003) 054201. arXiv:hep-ex/0303008.

[72] P. K. Lebedev and V. I. Pryanichnikov, "Present and Future production of Xe and Kr in the former USSR", Nucl. Instrum. Meth. A **327** (1993) 222.

[73] P. Belli *et al.* "Liquid Xenon scintillators" Nucl. Instr. Meth. **A310** (1991) 150

[74] A. S. Schlüsser *et al.*, "Observation of excimer luminescence from electron-excited liquid Xenon", Appl. Phys. Lett. **77** (2000) 1

[75] E. Morikawa *et al.*, "Ar, Kr and Xe excimer luminescence: from the dilute gas to the condensed phase", J. Chem. Phys. **91** (1989) 1469

[76] J. Jortner *et al.*, "Localized excitations in condensed Ne, Ar, Kr and Xe", J. Chem. Phys. **42** (1965) 4250

[77] N. Schwenter, E.-E. Koch and J. Jortner, "Electronic Excitations in Condensed Rare Gases", Springer-Verlag, Berlin 1985

[78] N. J. Basov *et al.*, J. Luminescence 1/2 (1970) 834

N. J. Basov *et al.*, JETP Lett. **12** 329

[79] J. B. Gerardo and A. W. Johnson, "Photoattenuation in the extreme red wings of Xe and Kr resonant lines", Phys. Rev. **A 10** (1974) 1204

[80] L. D. Landau, E. M. Lifshitz, "Electrodynamique des milieux continus", 12 ed. MIR Moscow (1990)

[81] G. M. Seidel, R. E. Lanou and W. Yao, "Rayleigh scattering in rare-gas liquids" Nucl. Instrum. Meth. A **489** (2002) 189 [arXiv:hep-ex/0111054]

[82] A. Baldini *et al.*, “Liquid Xe scintillation calorimetry and Xe optical properties” arXiv:physics/0401072.

[83] L. M. Barkov *et al.* Nucl. Instr. Meth. **A379** (1996) 482

[84] J. D. Jackson, *Classical Electrodinamics*, 3rd ed. (1998) Wiley

H. Frohlich, *Theory of dielectrics*, Oxford University Press, New York (1957) 2nd edition.

[85] K. Watanabe E. Inn and M. Zelikoff, “Absorption coefficients of oxygen in the vacuum ultraviolet” J. Chem. Phys. **21** (1953) 1026

[86] The tabulated data are taken from the NASA web site http://uvisun.msfc.nasa.gov/GG/GG34-ECHAR/oldhome.html

[87] IUPAC Subcommittee on Gas Kinetc Data Evaluation - Data Sheet POx1, available at http://www.iupac-kinetic.ch.cam.ac.uk

[88] The tabulated data are taken from the Oregon Medical Laser Center, http://omlc.ogi.edu/spectra/water/ and references therein.

[89] IUPAC Subcommittee on Gas Kinetc Data Evaluation - Data Sheet PHOx1, available at http://www.iupac-kinetic.ch.cam.ac.uk

[90] K. Watanabe and M. Zelikoff, “Absorption coefficients of water vapor in the vacuum ultraviolet” J. Opt. Soc. Am. **43** (1953) 753

[91] The GEANT physics simulation reference manual, v. 3.21 (1994) CERN Library Long Writeup W5013

[92] S. Belforte *et al.*, *SVT Technical Design Report*, CDF note 3108 (1994); CERN EP report 81-12/ReV.

[93] T. Haruyama, “A pulse-tube refrigerator fo the PSI MUEGAMMA experiment”, MUEGAMMA (2000) available at http://meg.pi.infn.it, and KEK-PREPRINT-2002-102

[94] MONO TORR PS15 Series, SAES Pure Gas, Inc. 4175 Santa Fe Road San Luis Obispo, California, 93401 USA.

[95] Oxisorb, Messer Griesheim GmbH, Dusseldorf, Germany.

[96] A. Beer G. Critin and G. Schuler, NIM A234 (1985) 294

[97] R. L. Carrington *et al.*, Nucl. Instr. Meth. **163** (1979) 203

[98] C. Bemporad *et al.*, Phys. Rev. **138** (1965) B1546

[99] F. R. Arutyunyan and V. A. Tumanian, Phys. Lett. **4** (1963) 176

[100] R. H. Milburn, Phys. Rev. Lett. **10** (1963) 75

[101] D. Babusci *et al.*, "Polarised and tagged gamma-ray Ladon beams", Riv. Nuovo Cim. **19** (1996) 1

[102] H. Ohgaki, H. Toyokawa, K. Kudo, N. Takeda, T. Yamazaki, "Generation and application of Laser-Compton gamma ray at ETL", NIM **A455**, 54-59 (2000)

[103] K. Ozone, University of Tokyo PhD thesis, in progress.

MEG Collaboration, "Recent developments of the MEG liquid Xenon photon detector", PSI Annual Report (2003)

[104] A. S. Wightman, Phys. Rev. **77** (1950) 521

[105] E. Fermi and E. Teller, Phys. Rev. **72** (1947) 399

[106] W. K. H. Panofsky, R. L. Aamodt and J. Hadley, Phys. Rev. **81** (1951) 565

[107] J. F. Crawford *et al.*, Phys. Rev. D**43** (1991) 46

[108] J. Spuller *et al.*, "A remeasurement of the Panofsky Ratio", Phys. Lett. **67B** (1977) 479

[109] Paul Scherrer Institut, PSI Accelerator Facilities Users' Guide, (1994) available from the PSI secretatiat. Information available also from the PSI web site `http://www.psi.ch`

[110] P-R. Kettle, private communication.

[111] B Rossi, "High energy particles", Prentice-Hall, New York (1952)

M. G. Payne "Energy Straggling of Heavy Charged Particles in Thick Absorbers", Phys. Rev. **185** (1969) 611

[112] J. A. Bistirlich *et al.*, Phys. Rev. C **5** (1972) 1867.

[113] A. Papa, Tesi di Laurea Universitá di Pisa (2004), unpublished

[114] A. Bay *et al.*, "A Modular NaI(Tl) Detector for Intermediate Energy Photons", Nucl. Inst. Meth. **A271** (1988) 497

[115] E. Frlež, D. Počanić, S. Ritt, Nucl. Inst. Meth. **A463** (2001) 341 [arXiv:hep-ex/0009042]

[116] Birks, "Theory and practice of scintillation counting" New York (1964)

Breitemberg, Progr. Nucl. Phys. **4** (1956) 56.

[117] M. Ambrosio *et al.* [MACRO collaboration] "The MACRO detector at Gran Sasso", Nucl. Instr. Meth. Phys. Res. A **486** (2002) 663

[118] The MIDAS Online and Analysis Framework, `http://midas.psi.ch`

[119] HAMAMATSU Photonics, Inc. Private communication.

[120] W. B. Atwood, "Time of flight measurements" SLAC-PUB-2620 (1980)

[121] W. Braunschweig *et al.*, "A large area time-of-flight system with a resolution of 0.5 ns FWHM" NIM **134**, 261 (1976)

[122] The Midas Slow Control BUS, `http://midas.psi.ch`

[123] MUEGAMMA collaboration, "Update and supplement to the Letter of Intent R-98-05.0", (1999) available at http://meg.pi.infn.it

[124] S–O Flyckt and C. Marmonier editors, "Photomultiplier Tubes: principles and applications", Photonis Brive, France, (2002)

[125] G. J. Feldman and R. D. Cousins, Phys. Rev. D **57** (1998) 3873

Acknowledgments

Writing a PhD thesis, or at least working on it, takes a non-negligible part of one's life, especially if he or she is young, and especially if he or she is an experimental physicist. It is therefore impossible to recognize all the acknowledgments to whom deserves them, but anyway I shall try.

First of all I would like to thank the MEG Pisa group, whence I learned the meaning of working in a group and not only with the single group members: Carlo Bemporad, whose immense knowledge and experience guided me through those years; Roberto Pazzi who taught me how much one can enjoy making physics and Marco Grassi who taught me how much physics one can make, and enjoy it; Franco Sergiampietri, who introduced me to the beauty of turning ideas into reality; Fabrizio Cei and Donato Nicolò, whom, being closer to me in age, I could constantly question without shame on whatever physics topic I was struggling with, and get an answer, most of the times correct! Alessandro Baldini is named for last only because he deserves a special thanks: he has all these qualities together and is able to show each one at the correct time, which I tried to learn; but furthermore had the most difficult task of being my advisor. Guido Gozzano's verses are dedicated to these gentlemen: after years of searching for supernovae which would not explode or neutrinos which would not oscillate, they deserve to carry out an experiment in which something pops out!

I cannot forget my junior colleagues, Stefano Giurgola and Angela Papa, the first working at his *PhD thesis and the second starting soon, hopefully followed by young Nicolino.*

It was amazing to work with all the physicists of the MEG collaboration, but a particularly warm thanks goes to Satoshi Mihara and Wataru Ootani who, together with Ryu, Hajime and Kenji, helped me surviving in Japan and introduced me in the Japanese way of life.

But as I was saying the PhD covers so much of one's life, and I had the fortune to share my years as a student with my friends at the Scuola Normale: in particular Paolo, Alberto, Fabio, Arianna and Andrea. It is really true what Andrea wrote in his *acknowledgments: I learned more from our discussions at the* mensa *(and around Pisa) than from the many books I read.*

My being away from home during my studies would have been much more difficult without the love and patience of my parents and of my sister. But above all it would not have been the same without Silvia: I do not really know how to thank her for her love and support.

Needless to say that the work in an experimental physics thesis is never the work of an individual, but of a group instead in which I enjoyed to be: the merits are everybody's, the mistakes mine.

Non amo che le rose
che non colsi.

(G. Gozzano, da *I Colloqui*)